Department of Physics and Astronomy
Ghent University (BE)
&
Department of Physics
LERMA-CY Cergy Paris Université (FR)

The role of carbonaceous dust in the ISM as a catalyst for the formation of molecules and grain growth

by

Grieco Francesco

A thesis submitted in fulfilment of the requirements for the

double degree:

Doctor of Science: Astronomy at Ghent University
&
Doctor of Earth and Universe Sciences at CY Cergy Paris Université

ACADEMIC YEAR 2023 - 2024

Author - PhD candidate:
Francesco Grieco

Supervisors:
Prof. Dr. Ilse De Looze
Department of Physics and Astronomy
Ghent University

Prof. Dr. François Dulieu
Department of Physics
LERMA-CY Cergy Paris Université

JOINT EXAMINATION BOARD

Internal from UGent:
Prof. Dr. Maarten Baes
Department of Physics and Astronomy, Ghent University

External designated by CYU:
Dr. Jennifer Noble
Department of Physics, Aix-Marseille Université

Externals:
Prof. Dr. Asunción Fuente
Centro de Astrobiología, CSIC-INTA
Prof. Dr. Serena Viti
Leiden Observatory, Leiden University

Chair:
Prof. Dr. Toon Verstraelen
Center for Molecular Modeling, Ghent University

Summary

This Thesis presents a comprehensive study of the interaction between dust grains and various gas-phase species in the ISM. The main results involve the use of surfaces like ices and coronene, a surface that resembles polycyclic aromatic hydrocarbons (PAHs), with gas-phase H and O elements. We investigate how dust grains can catalyze the formation of new molecules through processes like adsorption, diffusion, surface reactions and desorption in typical ISM conditions.

The Thesis includes three experimental Chapters (4, 5 and 6), performed at LERMA-CYU by using the FORMOLISM setup, that are complemented by two theoretical studies (Chapters 8 and 9), conducted with `Cloudy` and `Nautilus` codes at UGent. The experiments focus on the role that different dust grain surfaces and ice layers have on the Binding Energies (BEs) of molecules (Chapter 4), on the experimental formation of H_2 on coronene up to 250 K (Chapter 5) and on the formation of solid water on dust at temperatures up to 85 K (Chapter 6). Several astrophysical implications are also discussed.

The results presented in Chapter 5 show how H_2 can form in molecular clouds with dust temperatures >20 K and this is extremely relevant to explain the efficient H_2 and star formation in high redshift galaxies. Chapter 6 gives new insights on the formation of icy mantles that could be forming at higher temperature than previously demonstrated, being a significant way to explain the gas-phase elemental O depletion observed in such conditions. Moreover, the disappearance of PAHs in the transition from diffuse to dense clouds could be explained by the dust grains starting to be covered by ice layers. In Chapter 8 we study the effect of the high temperature experimental H_2 formation on PAHs on the location of the dissociation front (DF) in a classical PDR picture, by modelling it with `Cloudy`. From a basic implementation of the experimental results of Chapter 5 in the code, it has been challenging to quantify such effect. This underlines how a lot of work still needs to be done on models to better match observations. In Chapter 9 some questions regarding O depletion in translucent clouds and grain growth introduced in Chapter 6 are addressed with `Nautilus`. By using an innovative strategy, we were able to reproduce C and O depletions in translucent cloud conditions by locking them in two separate surface species upon adsorption, reproducing the molecular structure ratio of organic carbonates.

This Thesis shows the incredible catalytic nature of PAHs and their capacity to enable chemisorption processes for the formation of molecules at high dust temperatures. This is an important result that can be linked to the new discoveries reporting the possibility of having grain growth at lower n_H.

Samenvatting

Dit proefschrift rapporteert over een uitgebreide studie van de interactie tussen stofdeeltjes en verschillende gasdeeltjes in het interstellaire medium. De belangrijkste resultaten van deze studie betreffen het gebruik van stofoppervlakken zoals ijs en coroneen (deze laatste vertoont gelijkenis met polycyclische aromatische koolwaterstoffen of, in het kort, PAHs) met elementaire H en O deeltjes. We onderzoeken hoe stofdeeltjes de vorming van nieuwe moleculen kunnen katalyseren door processen zoals adsorptie, diffusie, oppervlaktereacties en desorptie onder typische ISM-omstandigheden.

Het proefschrift omvat drie experimentele hoofdstukken (Hoofdstuk 4, 5 en 6), uitgevoerd in LERMA-CYU met behulp van de FORMOLISM-opstelling, die worden aangevuld met twee theoretische studies (Hoofdstukken 8 en 9), uitgevoerd met de `Cloudy` en `Nautilus` codes aan de UGent. De experimenten richten zich op de rol die verschillende stofoppervlakken en ijslagen hebben op de bindingsenergieën (BEs) van moleculen (Hoofdstuk 4), op de experimentele vorming van H_2 op coroneen bij temperaturen tot 250 K (Hoofdstuk 5) en op de vorming van vast water op het stofoppervlak bij temperaturen tot 85 K (Hoofdstuk 6). Diverse astrofysische implicaties worden eveneens besproken.

De resultaten gepresenteerd in Hoofdstuk 5 tonen aan hoe H_2 kan worden gevormd in moleculaire wolken met stoftemperaturen >20 K, wat van groot belang is voor het verklaren van de efficiënte vorming van H_2 en stervorming in sterrenstelsels op hoge roodverschuiving. Hoofdstuk 6 biedt nieuwe inzichten in de vorming van ijsmantels die bij hogere temperaturen kunnen ontstaan dan eerder aangetoond, wat een significante manier kan zijn om de waargenomen depletie van elementair O in het gas onder dergelijke omstandigheden te verklaren. Bovendien kan de verdwijning van PAHs in de overgang van diffuse naar dichte gaswolken worden verklaard door de bedekking van stofdeeltjes met ijslagen. In Hoofdstuk 8 bestuderen we het effect van de experimentele H_2-vorming bij hoge temperaturen op PAHs op de locatie van het dissociatiefront (DF) in een klassiek PDR-model aan de hand van `Cloudy` modellen. Uit onze basisimplementatie van de experimentele resultaten van Hoofdstuk 5 in de code blijkt dat het een uitdaging is om dit effect te kwantificeren. Dit resultaat benadrukt hoeveel werk er nog nodig is aan modellen om beter overeen te komen met observaties. In Hoofdstuk 9 worden enkele vragen met betrekking tot O depletie in transparante wolken en de groei van stofdeeltjes, geïntroduceerd in Hoofdstuk 6, bestudeerd aan de hand van de `Nautilus` code. Door gebruik te maken van een innovatieve strategie waren we in staat om C en O depleties in transparante wolk condities te reproduceren door deze twee elementen te incorporeren in twee afzonderlijke oppervlakte-elementen wanneer een adsorptie proces plaatsvindt, en waarbij de moleculaire samenstelling van organische carbonaten werd gereproduceerd.

Het proefschrift toont de ongelooflijke katalytische aard van polycyclische aromatische koolwaterstoffen (PAHs) en hun capaciteit om chemisorptieprocessen voor de vorming van moleculen bij hoge stoftemperaturen te ondersteunen. Dit is een belangrijk resultaat dat kan worden gekoppeld aan de nieuwe ontdekkingen die wijzen op de mogelijkheid van stofaangroei bij lagere $n_{\rm H}$.

Acknowledgements

This Thesis is the fruit of an extraordinary team work over the past 4 years. Years of doubts and successes, falls and rises, many smiles, which are now coming to an end and they seem to have flown away in the blink of an eye.

I could never start without acknowledging my supervisors. Prof. François Dulieu, tout a commencé dans ton labo à Cergy où J'ai toujours trouvé les réponses à mes doutes, les incitations à mes hésitations et un groupe avec lequel partager mon quotidien, pas seulement scientifique. Merci à tous, à tout le groupe pour leur soutien et présence constante. Un merci tout particulier à Julie et Shreya pour leur amitié sincère et leurs mots amicaux qui ont fait la différence dans mon parcours et mon séjour au LERMA.

Mijn dank gaat dan ook uit naar Prof. Ilse De Looze. Een wetenschappelijke gids en morele steun, altijd bereid om mij te pushen om te verbeteren. Bedankt om mij altijd met een glimlach te verwelkomen, om mij zoveel te leren en om mij altijd te vertrouwen, voor jullie stiptheid en extreme professionaliteit en emotionele intelligentie. I also thank the entire group at Ghent University for the evenings, the experiences, the welcoming spirit that is never taken for granted.

I thank both my supervisors for believing in me from the beginning and throughout this journey. I arrived here with an unorthodox scientific path, I had a thousand doubts, but I tried with all my heart and you have always shown me appreciation, thank you.

I acknowledge all the people and collaborators I have met during my Thesis and every single one that, even through a simple chat, has contributed to my scientific improvement and, especially, my personal one.

I want to thank the entire Joint Examination Board for agreeing to be part of it and for taking the time to read this Thesis, for all the questions that will be asked and the corrections that will be made. I thank you because all this can only make me grow.

Ringrazio la mia famiglia, le mie origini, le mie radici, la mia terra. Ho apprezzato il mio valore, quindi il vostro, con il privilegio di riconoscermi guardandomi da un ramo lontano, ma sempre con le spalle coperte dal vostro sostegno. Grazie per avermi capito, aspettato, accettato nei miei cambiamenti e scoperte, decisioni, grazie per avermi supportato e, come sappiamo, sopportato.

Ai miei amici di sempre, ai ritorni felici ed alle braccia aperte all'arrivo, al tempo che non basta mai ed all'evolversi di noi senza allontanarci. Alle videochiamate mute, ai pettegolezzi nell'etere. Grazie.

To my crazy happy family all over Europe, a constant support in every corner of the world. Thank you for putting up with my exuberance, thank you for the advices and teachings, thank you for allowing me to trample half the world together. I am, today, many more things thanks to you.

I really want to acknowledge and thank the family I found in Ghent, in Nieuwpoort:

Marga and her ecosystem made of Iris, friends, animals, her sensitivity for every single living creature. For all the small talks around a coffee that can do deep only with a bottle of prosecco, for all the things you thought me in these years. I will never forget the first welcome soep you made for me with so much love, it made me feel at home from the beginning. For all the discussions that could have lasted forever. You, your creativity and curiosity, your brightness and critical look on the world have inspired me so much. Ik ben dankbaar dat ik de kans heb gehad om iemand als jij te ontmoeten. Bedankt voor alles.

Mas não termino sem agradecer à minha joia rara, o meu verdadeiro e feliz apoio. Não sei como você conseguiu aguentar meus delírios, meus momentos mais sombrios, minhas inseguranças. Um sorriso pela manhã, um abraço sincero, uma referência nesses quatro anos. Com você tudo é possível, tudo se resolve, juntos tudo parece fácil. Você acreditou e acredita em mim quando eu nunca acreditaria, você enche o ar de alegria e serenidade. Você é uma pessoa especial e me sinto sortudo por ter você comigo, continuaremos caminhando juntos pelo mundo. Ao sorriso da minha vida, muito obrigado.

Contents

List of Figures

List of Tables

Abbreviations & Symbols

FORMOLISM	FORmation of MOLecules in the ISM
LERMA	Lab d'Etudes du Rayonnement et de la Matière en Astrophysique
CYU	CergY University
UGent	Ghent University
ISM	InterStellar Medium
FUV, UV	Far-, UltraViolet
MC	Molecular Cloud
PAH	Polyciclic Aromatic Hydrocarbons
HII, HI	Ionized, neutral atomic Hydrogen
CII	Ionized Carbon
OI	Neutral Atomic Oxygen
CNM	Cold Neutral Medium
WIM, WNM	Warm Ionized, Neutral Medium
HIM	Hot Ionized Medium
$A_{\mathbf{V}}$	Total Visual Extinction in magnitudes
$n_{\mathbf{H}}$	H column density
IR	InfraRed
NIR	Near InfraRed
MIRI	Mid InfraRed Instrument
TC	Translucent Cloud
PDR	Photon-Dominated Region or Photo-Dissociation Region
RF	Radiation Field
IF	Ionization Front
DF	Dissociation Front
UIR	Unidentified InfraRed bands

UIB	Unidentified Infrared Bands
AIB	Aromatic Infrared Bands
SED	Spectral Energy Distribution
BGs	Big Grains
VSGs	Very Small Grains
SNe	SuperNovae
AGB	Asymptotic Giant Branch
$M_{\odot}$	Solar Mass
JWST	James Webb Space Telescope
ISO	Infrared Space Observatory
BE	Binding Energy
S	Sticking coefficient
$E_{\mathbf{phys}}$	Physisorption Energy
$E_{\mathbf{chem}}$	Chemisorption Energy
$E_{\mathbf{S}}$	Sticking Energy
$E_{\mathbf{k}}$	Kinetic Energy
$E_{\mathbf{diff}}$	Diffusion Energy
$E_{\mathbf{des}}$	Desorption Energy
$E_{\mathbf{b}}$	Binding Energy
$\tau_{\mathbf{des}}$	Residence time
$r_{\mathbf{des}}$	Desorption rate
$\mathbf{k}_b$	Boltzmann constant
QT	Quantum Tunneling
$\mathbf{T}_c$	Critical Temperature
$\mathbf{T}_s$	Surface Temperature
$\mathbf{T}_{grain}$	Grain Temperature
$\mathbf{T}_{dust}$	Dust Temperature
$\mathbf{T}_{peak}$	Peak Temperature
ER	Eley-Rideal
LH	Langmuir-Hinshelwood
UHV	Ultra High Vacuum
OFHC	Oxygen Free High Conductivity
FTIR	Fourier Transform InfraRed spectroscopy

RAIRS	Reflection Absorption InfraRed Spectroscopy
QMS	Quadrupole Mass Spectrometer
MCT	Mercury Cadmium Telluride detector array
OAE, OAP	Off Axis Ellipsoidal, Parabolic mirror
TPD	Temperature Programmed Desorption
DED	During Exposure Desorption
EPR	Electronic Paramagnetic Resonance
HOPG	Highly Oriented Pyrolytic Graphite
ASW	Amorphous Solid Water
PCI	PolyCrystalline Ice
ML	MonoLayer
m/z	mass/charge ratio detected with the QMS
c/s	counts per second (QMS detection signal)
A	Pre-exponential factor in the Polanyi-Wigner equation
TST	Transition State Theory
HH	Harmonic oscillator approximation
QM	Quantum Mechanical
ALMA	Atacama Large Millimeter/submillimeter Array telescope
NOEMA	NOrthern Extended Millimeter Array telescope
D, H, O, C, N	Atomic Deuterium, Hydrogen, Oxygen, Carbon, Nitrogen
M2, M4	2 m/z, 4 m/z referred to D, D_2
M16, M32	16 m/z, 32 m/z referred to O, O_2
CMB	Cosmic Microwave Background
SFR	Star Formation Rate
SEM	Standard Error of the Mean
BKG	BacKGround
TMC	Taurus MC
COMs	Complex Organic Molecules
U	Ionization parameter
J-layer/species	Surface layer/species for the grain structure in the 3-phase `Nautilus`
K-layer/species	Mantle layer/species for the grain structure in the 3-phase `Nautilus`
XO	O-bearing non-desorbing sink molecule
XC	C-bearing non-desorbing sink molecule

Dedicated to my nonni

Chapter 1

General introduction to Astrochemistry

1.1 The InterStellar Medium

The cycle of stellar evolution and destruction is the very core of the chemical variety and life we have in the InterStellar Medium (ISM). Heavy elements are synthesized in the inner part of stars during their lifetime to be afterwards expelled into the ISM during their death and other processes. Those elements constitute the gas and the solid dust we observe and they are responsible for the chemical complexity in the ISM. The ISM is a dynamic environment that represents all the matter between stars in a galaxy, besides dark matter. This medium is not homogeneous and it can have very different physical and chemical conditions depending on the regions where it is located. Strong is the influence of temperature and density, but also the presence and strength of radiation, turbulence, magnetic fields and cosmic rays. Most of the chemical species are formed through gas-phase reactions while some need catalytic support from dust grains to undergo reactions allowing the formation of new molecules. Until now, more than 300 molecules have been detected in the interstellar medium or circumstellar shells [CDMS, 2024]. The chemistry of the ISM becomes relevant in regions where the UV photons sourced from galactic stars are partially shielded by H-atoms, defining what we call Molecular Clouds (MC). Thus, stars evolve in a cycle that starts from the gravitational collapse of dense clouds until the return to the ISM through the remnants of stars at their death. Interstellar regions contain mainly a mixture of gas and dust (99% and 1% in mass respectively). 98% of its gas mass is made up of hydrogen (70%) and helium (of about 28%), while the rest (of about 2%) consists of carbon, oxygen and heavier

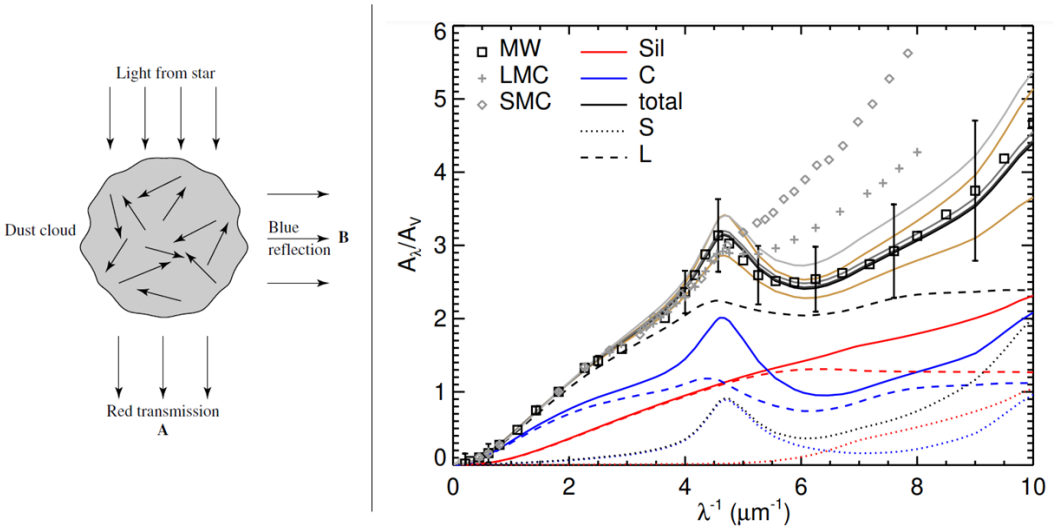

FIGURE 1.1: Left (from Paron [2018]): An interstellar cloud containing significant amounts of dust along with the gas (a dust cloud) can both scatter and absorb light that passes through it. The amount of scattering and absorption depends on the number density of dust grains, the wavelength of the light, and the thickness of the cloud, grain size and properties. Since shorter wavelengths are affected more significantly than longer ones, a star lying behind the cloud appears reddened to observer A. Observer B sees the scattered shorter wavelengths as a blue reflection nebula. Right (from Dubois et al. [2024]): extinction curve obtained from the fiducial G10LG simulation at 400 Myr for the total dust content (black solid), and the contribution from carbonaceous (blue, C), silicate (red, Sil) grains, and small (dotted, S) and large grains (dashed, L). The extinction curves at different times (100, 200, 300, and 400 Myr) are shown from light to dark grey scales. The scatter of the extinction curves from the simulation are the brown solid lines.The extinction from the Milky Way (MW), Large Magellanic Cloud (LMC), and Small Magellanic Cloud (SMC) are shown as labelled in the corresponding panel, with the typical estimation of the scatter.

elements (so-called metals). One can see that up to half of the heavier elements compresses to form dust [De Vis et al., 2019], thus constituting only 1% of the total mass of the ISM. Even if so little, dust is a crucial element in the cyclic evolution of stars. A star is born out of gas and dust in the ISM and, during its lifetime and death, a large fraction of material can return to the ISM through stellar winds and explosive events. Subsequently, the next generations of stars come from this already processed material. The gaseous matter can be studied by using spectroscopic observations, whereas the dust particles are more difficult to study for their intrinsic spectroscopic congestion and because of the scattering of the radiation emitted by stars and absorption of the blue end of the spectrum. One has to imagine that dust represents objects capable of obscuring the stars behind. The cumulative effect of scattering (out of the line-of-sight) and absorption of starlight happening in the ISM is defined as interstellar extinction. Figure 1.1 gives an idea of the role of dust in interacting with a source of light such as a star (right panel) and a typical extinction curve for different grain types and sizes (left panel).

Extinction depends on the size distribution of the grains present on the line of sight, their mineral composition and the wavelength of the emitted light. An extinction curve represents the quantity of light absorbed and scattered as a function of its wavelength. Understanding this curve is necessary to determine the spectrum emitted by a source whose light passes through a portion of ISM before reaching us. Thus, the extinction curve is an interesting diagnostic tool for examining the nature of dust grains. Since the extinction curves are wavelength-dependent, longer wavelengths are not absorbed as strongly as the blue light, for example. Extinction curves can therefore give us some information on dust composition by showing "bumps", the UV slope and other characteristic features. The strength of the characteristic band in the UV at 217.5 nm has been considered a proof of the existence of graphite and/or polycyclic aromatic hydrocarbons (PAH) [Draine, 1989, Lin et al., 2023], one of the major components of interstellar dust. PAHs are also responsible for a series of infrared emissions observed between 3.3 (C-H stretching) and 12 μm and even at longer wavelengths. More information about another main component of interstellar dust comes from dark absorption bands at 9.7 μm and 18 μm in the near-infrared which can be associated with SiO-based structures, also known as silicates. The features of extinction curves can be reproduced by considering dust as made up of grains of carbon containing molecules, graphite and PAHs, together with silicates, with sizes that range from tenths of nanometers to microns. More details about PAHs are given in a dedicated Section (1.3.1.6), since they are the main type of surfaces studied in this Thesis.
[Herbst, 1995, Paron, 2018, Lequeux, 2005, Carroll and Ostlie, 2017]

As mentioned before, the ISM gas and dust can be found in different density and temperature ranges. The main phases of the ISM are the Cold Neutral Medium (CNM), the Warm Ionized and Neutral Medium (WIM and WNM) and the Hot Ionized Medium (HIM). The most interesting phase for our study is the CNM since, depending on physical (T between 10-100 K) and chemical conditions (from $n_{\mathrm{H}} \approx 10^{1-2}$ cm^{-3} to $\approx 10^{3-6}$ cm^{-3}) it can contain a variety of cloud types. The WNM (T $\approx 10^3$ K, $n_{\mathrm{H}} \approx 1$ cm^{-3}) is in pressure equilibrium with the CNM and it is considered to set its boundaries, it is made up of neutral atomic hydrogen (HI) while the WIM has slightly higher temperature ranges but more diffuse ionized gas (T $\approx 10^4$ K, $n_{\mathrm{H}} \approx 0.1$ cm^{-3}), visible in HII regions. The HIM constitutes the intercloud medium or coronal gas, it contains very hot (T $\approx 10^7$ K) and diffuse gas mainly composed of ionized species ($n_{\mathrm{H}} \approx 10^{-3}$ cm^{-3}). The CNM contains clouds that can therefore be classified as diffuse or dense, from atomic to molecular. Diffuse clouds possess gas densities in the range 10 - 1000 cm^{-3}, low extinction in the visible, and temperatures in the range 50 - 100 K. The dense clouds, also called molecular, are the densest part of the ISM with an average temperature of 10 K, with a gas density of 10^{3-6} cm^{-3} and large visible extinction. Since dense clouds

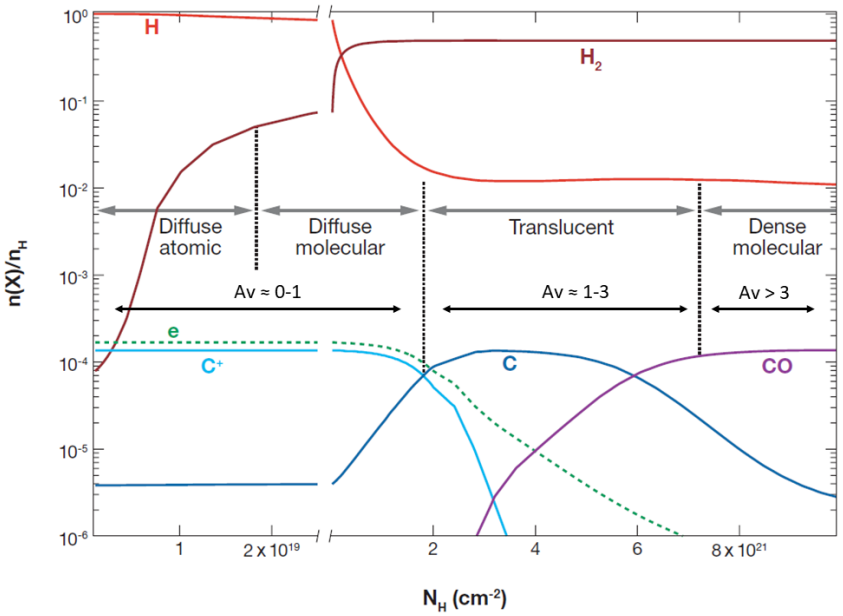

FIGURE 1.2: Classification of interstellar clouds types. From Snow and McCall [2006].

are shielded from primary UV sources that would contribute to the ionization of H and to the photodissociation of H_2, most of the hydrogen will be in its molecular form, H_2. Clouds between these two limiting cases, dense and diffuse, are defined as translucent and this specific transition environment is crucial for the onset of the ice mantles on the dust grains. A scheme of different regions and related main parameters is given in Figure 1.2 and more details in the following section (1.2).
[Caselli and Ceccarelli, 2012, Mateo-Marti et al., 2019, Snow and McCall, 2006]

1.2 Interstellar Clouds

1.2.1 Diffuse Clouds

Diffuse clouds extend from being totally exposed to radiations, for the vicinity to the interstellar source, to regimes where this field attenuates. In the first case we define those clouds as diffuse atomic ones, environments where hydrogen is neutral and atomic, while other atoms such as carbon, with ionization potentials lower than hydrogen, can still be fully ionized. Low extinction sightlines are typical of diffuse atomic gas, regions with low density ($\approx 10 - 100$ cm^{-3}) and temperatures of up to hundreds K. Further away from the radiating source, we approach a diffuse MC regime. Here the H_2 does not dissociate anymore, thus the hydrogen in molecular form increases, but carbon can still be ionized and almost all the CO will still photodissociate. A typical steady-state condition that provides such shielding is a diffuse atomic cloud layer surrounding the

molecular one. Most sightlines crossing diffuse molecular clouds will also cross diffuse atomic gas, therefore a diffuse cloud can be observed within a range of visual extinction of $A_V < 2$ mag. In this molecular regime the densities are slightly higher than the atomic ones (up to 500 cm^{-3}) and, together with the presence of H_2, this permits the chemistry to start increasing in complexity. The main available molecules are here observed in absorption in the UV/visible (e.g., CO, CH, CN), in the IR (CO, H_2, H_3^+), and at mm wavelengths (e.g. HCO^+, OH).
[Lequeux, 2005, Snow and McCall, 2006]

1.2.2 Translucent Clouds

When we reach local environments where carbon starts to transition from its ionized form to its atomic or molecular (CO) form, we encounter regions of the clouds that have been defined as Translucent Clouds (TC). There is a co-existence of carbon forms at visual extinction of $1 < A_V < 5$. Here the chemistry starts to actively involve C and CO and this sets the boundaries of the very dense clouds, where carbon is only found in its molecular form. Thus, sightlines with $A_V > 1$ are candidates for hosting translucent clouds. However, higher values of A_V do not necessarily imply the presence of translucent material, but such A_V values could simply be justified by the presence of multiple diffuse molecular clouds along the line of sight. In this Thesis we will address the TC seen as protagonists for the scientific problems concerning oxygen depletion and the onset of the ice mantle. Both those processes should be happening in the transition from diffuse to dense clouds and they have both been a hot astrochemical topic in the last decades.
[Corby et al., 2018, Snow and McCall, 2006, Burgh et al., 2010, van Dishoeck and Black, 1989]

1.2.3 Dense Clouds and Star formation

With increasing extinction, the chemistry changes completely and we enter environments defined as dense molecular clouds. Here the main source of ionization are cosmic rays and the chemistry depends on the main and stable molecular forms: CO and H_2. This regime is characterized by lines of sight with $A_V > 5$ and they are observed by IR absorption and mm emission. As already mentioned, the densities are higher and the dust temperature drops to a few tens of Kelvin or below. These temperatures make the chemistry happening on grains very relevant since the adsorption of species on surfaces is favored at lower temperatures. The first and main molecules detected by their rotational transitions have been CO, NH_3, H_2O, and H_2CO. Dense clouds also represent

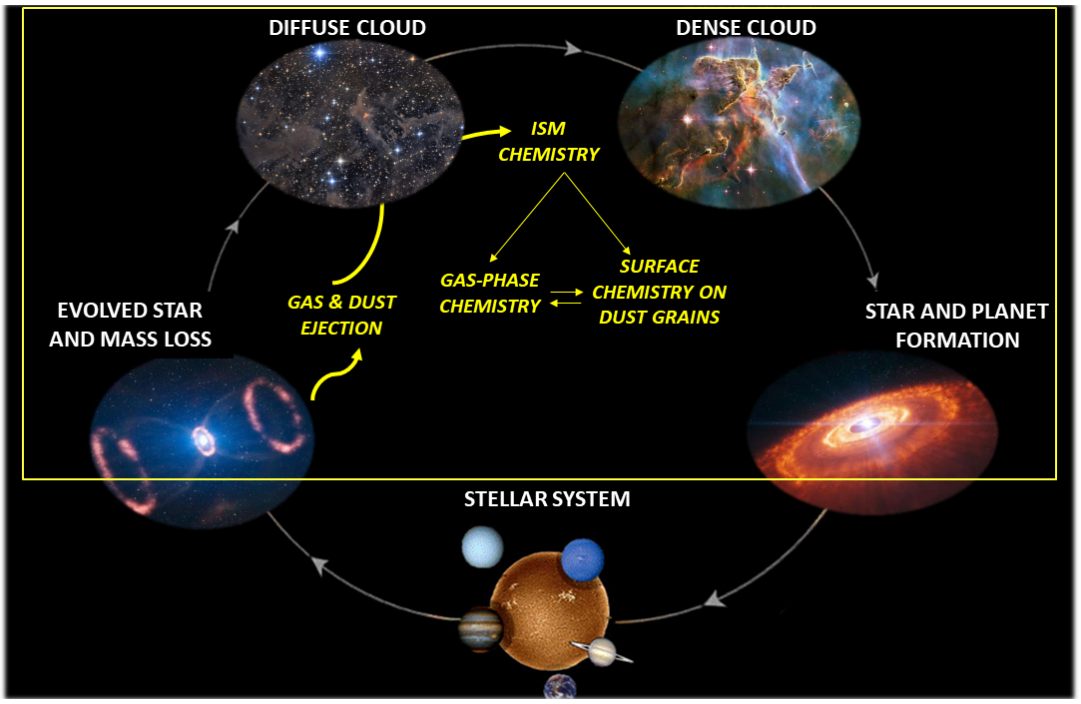

FIGURE 1.3: The cycle of matter in space: the loop of stellar life. Picture edited from an original by Mateo-Marti et al. [2019].

an important step towards star formation and they allow the transition from diffuse gas-phase chemistry to surface chemistry, underlying the role of dust grains catalyzing the formation of new species. H_2 is one of the main cooling agents able to influence star formation and its main formation route depends on dust grains as catalysts with maximum efficiency in cold molecular cloud conditions. When an interstellar cloud approaches a certain mass, it can undergo the formation of a protostellar system through its collapse and self-gravitation. A schematic overview of the processes involving MCs is displayed in Figure 1.3.
[Solomon and Klemperer, 1972, Herbst and Klemperer, 1973, Weinreb et al., 1963]

1.2.4 PDRs

PDR is the abbreviation of Photo-Dissociation or Photon-Dominated Region, a part of the ISM where the UV Radiation Field (RF, energies between 6 eV $<$ photon energy $<$ 13.6 eV) is capable of photo-dissociating molecules. The radiation decreases while going deeper into the molecular clouds and different physical-chemical stages of PDRs are usually defined through the visual extinction. Observationally, it is possible to easily study those regions because of strong [CII] and [OI] lines, at 158 and 63 μm respectively, as well ro-vibrational H_2 lines and aromatic bands from the grains in the mid-IR. A picture of a typical PDR structure is given in Figure 1.4. Chemically, in the parts that are the closest to the radiation source, hydrogen is ionized (H^+, HII

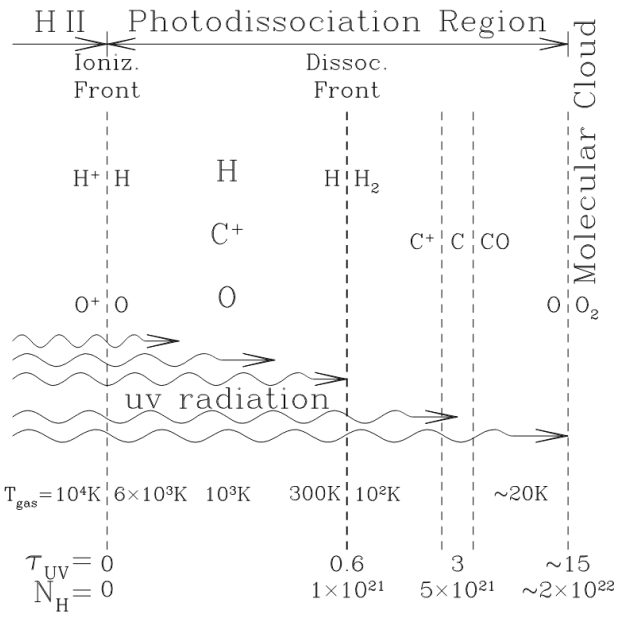

FIGURE 1.4: Schematic diagram showing the different zones in a PDR by Draine and Bertoldi [2000].

region), afterwards it is in its atomic form (H) and only further away from the radiation source it recombines to form H_2. The first front is called the ionization front (IF), while the dissociation one (DF) defines the H to H_2 transition at A_V around 0.2. In a similar way, carbon firstly goes from C^{++}, in the HII region, to C^+ in the outer parts to afterwards recombine with electrons to form C at A_V around 1. Only deeper in the cloud carbon will be molecularized into CO. Oxygen is almost everywhere in its atomic state and its abundance depends on the C to CO transition, that is not a sharp one at all. Every transition and front represents a certain coexistence of ionized, atomic and molecular forms of all the species. The chemistry in these regions depends on the high temperatures and the photons that are able to trigger photoelectric effects on dust grains and to excite H_2 molecules. Grains get heated by UV-photons absorption and they are only able to cool down through the emission in the IR continuum and with typical aromatic bands in the mid-IR. Many models for PDRs have been constructed since the first detection of the infrared cooling lines in the 70's. Sternberg and Dalgarno [1995] present a comprehensive overview of the chemical processes happening in these regions. In the review by Hollenbach and Tielens [1999] they stress on the crucial location of the DF since it is considered to be extremely important in PDRs because molecular hydrogen formation and its excitation can trigger many other chemical reactions and form new species. The so-called Unidentified InfraRed emission bands (UIR) are routinely detected in the strongly illuminated parts of the PDR and it has been understood that the chemical nature of such emissions comes from carbonaceous grains, typically aromatic hydrocarbon materials. [Duley and Williams, 1981, Allamandola et al., 1985, Puget and

Leger, 1989, Tielens, 2008]
The aromatic C-H stretching bands give rise to emission at 3.3, 8.6 and 11.3 mm while the 6.2 and 7.7 mm bands are due to C-C stretching modes. The assignment of such bands to a specific molecular structure has been under discussion for several years, but there is now agreement on identifying PAHs as the most probable source. Allamandola et al. [1985] provides an abundance for PAHs of about 10^{-7} relative to hydrogen, considering that they should absorb about 5% of the total IR flux and they have an average size of 50 C atoms. The study of PDRs has therefore underlined how the presence of far-UV photons can affect the processes of the ISM. The models describing those regions are applicable to very diverse environments.

1.3 Dust Grains and molecules

1.3.1 Dust Grains

To understand the lifecycle of the dust, it is important to consider the physical and chemical processes taking place in the cosmic environments. The diffuse ISM evolves into translucent clouds and then into cold, dense interstellar molecular clouds. Dense clouds collapse into denser cores forming central stars. Central stars at the end of their life (evolved stars) expand and, finally, release their shells into the ISM re-introducing dust in the diffuse interstellar medium. Dust is one of the fundamental players in these processes. When dust enters the ISM, it can be destroyed and re-condensed, traveling through diffuse and dense clouds, proto-stellar envelopes and so on. The exact formation pathways of interstellar dust remain a scientific discussion [Galliano et al., 2021]. First steps of dust formation are thought to occur via gas-phase reactions in high-temperature circumstellar envelopes of evolved stars [Nanni et al., 2013, Ventura et al., 2012, Maercker et al., 2014]. After their formation, dust grains are pushed away by radiation pressure into the ISM, where they can undergo destruction by supernova shocks [Slavin et al., 2015]. Only a part of the dust produced by stars survives into the ISM. However, observations show a high concentration of dust grains in the ISM. Thus, an efficient formation mechanism is required to explain the difference between stellar formation and interstellar destruction rates [Potapov and McCoustra, 2021, Draine, 2009].
As mentioned before, dust grains are omnipresent in the interstellar medium. Despite their low abundance, they play a crucial role in many aspects of the evolution of the interstellar medium. They have a great influence on the radiative transfer in the Galaxy. They absorb about half of the stellar radiation in the UV and visible before re-emitting it at longer wavelengths in the IR, submillimeter and millimeter wavelength domains in the form of thermal emission [Viaene et al., 2016, Driver et al., 2006]. Furthermore,

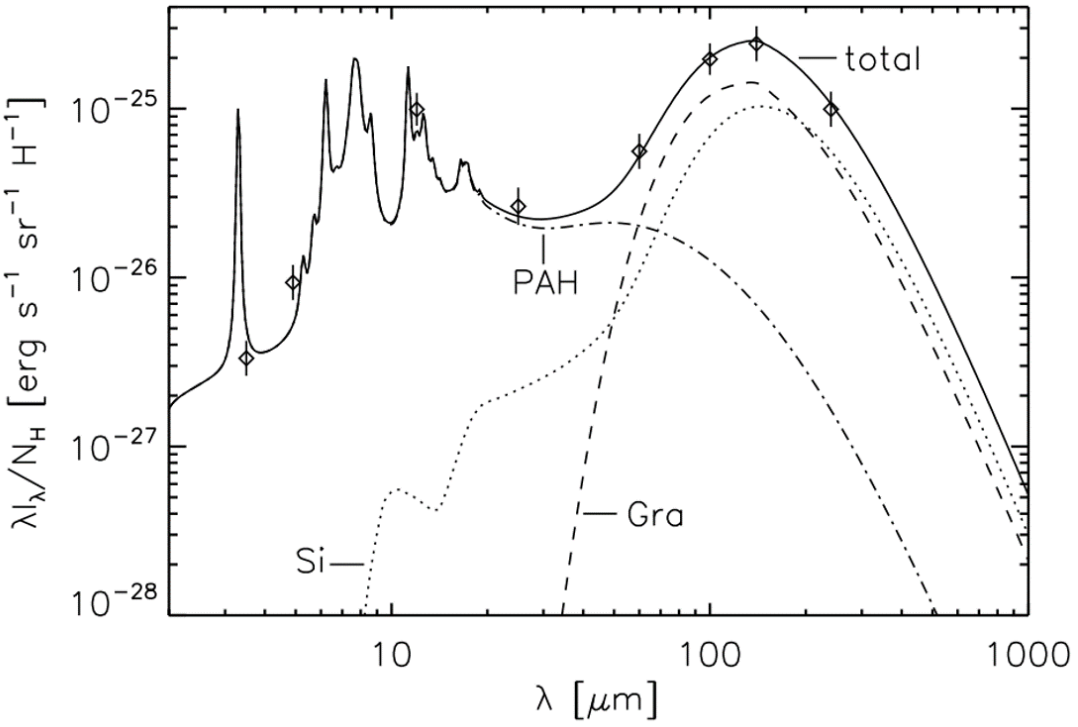

FIGURE 1.5: The dust and PAH emission SED for the diffuse ISM at high Galactic latitude (solid line) calculated using the model described in Popescu et al. [2011]. Here are also plotted the COBE data (symbols with error bars). These are given as an average of the data from the North ecliptic pole field and the Lockman Hole field Arendt et al. (1998) and are further colour corrected. The contributions of the different dust compositions to the total model SED are as follows: Si (dotted line), Gra (dashed line), PAH (dashed-dotted line). SED taken from Popescu et al. [2011].

dust grains are important players in heating the interstellar medium, on the one hand through the photoelectric effect and on the other hand by collisions with the gas atoms in dense environments.

As already mentioned at the beginning of this Chapter, different emission and/or absorption features give us insights on the major components and main constituents of the observed dust grains. In general, they are considered to be mainly made of silicates and/or carbonaceous materials. The usual assumed ratios between the two families of dust grains are $\approx$ 70 % for Si-bearing grains and $\approx$ 30 % for the C-bearing ones [Jones et al., 2013, 2017, Draine et al., 2007]. The smallest dust grains, PAHs, deserve a special mention. The fraction of dust mass in the form of PAHs strongly correlates with metallicity, thus the value may vary for different samples, but several studies have tried to give quantitative constraints to account for the correct percentage. Draine et al. [2007], Aniano et al. [2020] studied a sample of galaxies obtaining a % of PAHs in the range 0.4 - 4.7 (higher values found for higher metallicities) with respect to the total dust mass. One has also to consider that PAHs have incredibly small sizes, compared to other grains populations, with a mean value of 50 C atoms, they therefore dominate

the surface/volume ratio and have a strong role in the interaction with the gas-phase [Lin et al., 2023].

To account for extinction and interstellar emission, Desert et al. [1990] proposed a separation into three populations of grains of increasing sizes, giving rise to IR emission at increasing wavelengths. The characteristics of these emissions depend on the nature and size of the grains: large grains, very small grains and PAHs in order of decreasing grain size. Large grains (BGs) have sizes greater than 15 nm with a maximum size at least greater than a hundred nanometers to account for extinction. BGs dominate the emission from 100 μm to 1 mm. Very small grains (VSGs) are here needed to account for the emission between 20 and 100 μm, usually a population of small carbonaceous grains with sizes of order of 1.2 to 15 nm is used. PAHs are aromatic and carbon-based compounds with sizes from 0.4 to 1.2 nm, more details are given in a separate section (1.3.1.6). In Figure 1.5 one can see a typical Spectral Energy Distribution (SED) in emission for the diffuse ISM and it shows how different features belong to different dust compositions.

1.3.1.1 Dust formation and destruction

The different mechanisms for dust formation, size increase or decrease, and eventual destruction, depend on the environment, and physical conditions. As said before, nucleation of dust grains is not considered to happen in the ISM, but most of the grain seeds and metals must come directly from stars. These stars also contribute to an important dust destruction mechanism ("astration"), since they also require grains for their formation process. By considering only stellar dust production sources (SNe and AGBs), it appears difficult to account for the bulk of the dust mass observed in galaxies [De Looze et al., 2020, Galliano et al., 2021, Draine, 2009]. Accretion of metals onto dust grains in dense ISM clouds could be the key to explain the large amounts of interstellar dust. Many physical processes behind "grain growth" in the interstellar medium remain unclear. Once in the ISM in fact, dust in a diffuse cloud can fragment through shattering processes [Hirashita and Yan, 2009] or be affected by supernovae (SNe) shocks. In a dense environment, dust can undergo coagulation, mostly if in neutral phases, or condensation, by accretion of elements from the gas-phase to build up a refractory grain mantle and icy layers. Figure 1.6 gives a schematic view of all the possible directions and pathways that dust can take during its evolution, as a function of the environment. It is important to stress on the fact that the nature of the grain (carbonaceous or Si-based) completely affects the reactions and processes happening on the different dust surfaces. A brief overview about the main mechanisms involved in dust evolution is given below,

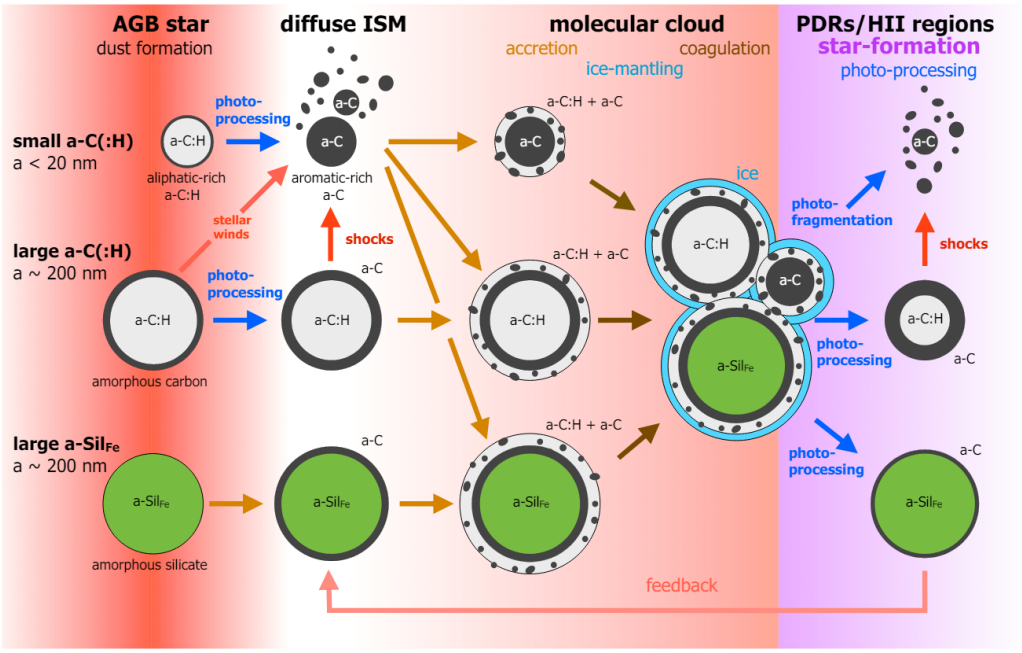

FIGURE 1.6: Figure taken from Jones et al. [2013]. Schematic view of all the possible evolutionary tracks of insterstellar dust in its lifecycle. The red zone reflects the density, n_{H}, and the violet one represents high G_0 radiation fields. The picture corresponds to a specific dust model and it is only taken as a qualitative example.

in order to afterwards move to the actual growth processes of dust particles.
[Slavin et al., 2015, Kirchschlager et al., 2022, De Looze et al., 2020, Jones et al., 2013]

1.3.1.2 Processes affecting grain sizes and size distribution

Dust fragmentation depends on the amount of kinetic energy of two colliding particles. If the relative velocity between grains is high enough, they would not clump together or scatter, but rather break up to form smaller fragments. This process results in an increase of the small grain abundance and it is mainly efficient for turbulent gaseous media or in SN shock waves.
Coagulation mainly concerns neutral grains in cold or warm environments. When grains find each other in high density regions, such as MC cores, they have the possibility to clump together, conserving the total mass but increasing the number of large grains. Coagulation makes a contribution only when a sufficient fraction of the grains has reached a sufficient size to make the rate high enough. So far, we have considered coagulation and fragmentation as processes that directly affect grain sizes and their distribution, but they conserve the mass while changing the total available surface area for further processes happening on grains. The size distribution of available dust grains in a specific region strongly affects the amount of available surface, thus the condensation rate.
The last main mechanism that is relevant for the dust lifecycle, before describing the

processes triggered by SNe, is grain condensation. In denser and colder environments, where high molecular densities contribute to radiation shielding and low temperatures prevent sublimation from the grains, the accretion of molecules on the grain becomes important. In these conditions cold dust grains can grow by accretion of condensing species on their surface. The timescale of an efficient condensation process in a MC core is shorter than its lifetime (a few 10^7 years). Condensation is an important replenishment mechanism, but the average grain size is not much affected.
[Mattsson, 2016]

1.3.1.3 SNe and dust

Supernovae can destroy both pre-existing grains by the SN blastwave (i.e. the forward shock) and newly formed dust by the reverse shock [Slavin et al., 2015, 2020, Jones et al., 1996, Silvia et al., 2010]. In general, these processes are crucial to understand galactic dust evolution. Supernova generated shock waves are responsible for most of the destruction of dust grains in the interstellar medium (ISM). Grains can be destroyed in shocks by thermal and non-thermal (inertial) ion sputtering, shattering (mostly for larger grains) and vaporization caused by grain-grain collisions.
Because of the shock, the magnetic field increases, the grains accelerate and the heating of the gas (for non-radiative shocks) enhances the sputtering of small grains resulting in a reduction of the dust mass and a change of the grain size distribution shape. Average shock speeds range between hundreds and thousands of km/s. Grain destruction timescales by SNe events is of the order of a few 10^8 yr [Slavin et al., 2015, Kirchschlager et al., 2022, Jones and Nuth, 2011], while the grain supply from AGB stars has a timescale longer than 100 Myr. Another growth mechanism explaining this discrepancy, like chemical accretion on grain surfaces, should therefore exist.
The efficiency of dust destruction strongly depends on the rate of grain shattering, due to grain-grain collisions, ion sputtering, the ISM structure and on the environment (dense or diffuse) where the SN goes off. There are still many questions trying to understand to what extent the dust formed in supernovae (SNe) will actually survive the passage of the shocks and be mixed into the interstellar medium (ISM).
Also a reverse shock (shock wave collapsing back toward the origin of the supernovae explosion) is potentially able to destroy newly formed dust material. In this case, the processes involved are grain charging, sputtering and grain-grain collisions. The fraction of grains destroyed by a reverse shock depends on the morphology of the ejecta as well as on the surrounding medium (to decide whether a reverse shock will form and at which point in time). The most important factors are the composition and size distribution of the grains, the properties of the SNe and its environment. There are several studies

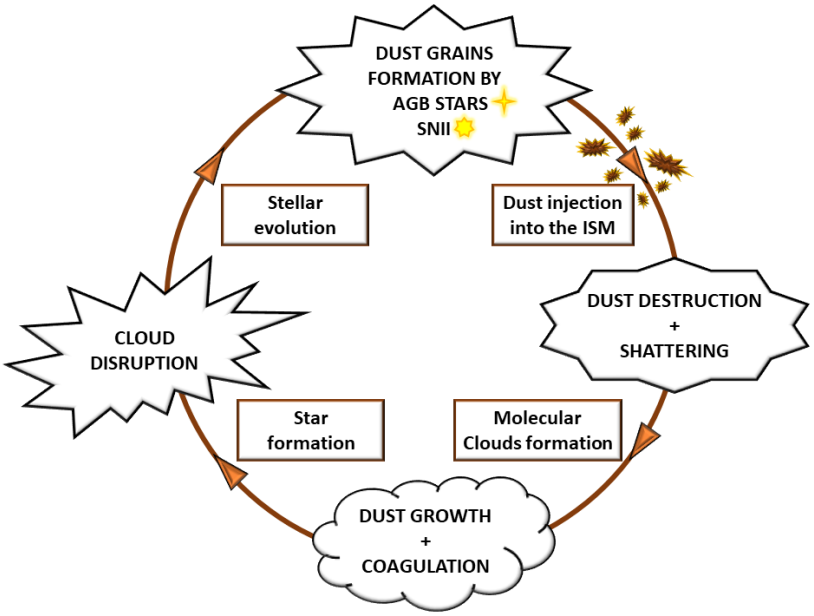

FIGURE 1.7: Simplified schematic evolution of dust in galaxies.

showing the dust survival of silicates with respect to carbon dust (10 - 30% and 20 - 40% respectively) with smaller radii being the most affected by destruction [Micelotta et al., 2016]. Grain-grain collisions and sputtering are synergistic in determining the surviving dust budget in supernova remnants. Since an alternative to star supply is needed as dust production, a proposed and now largely accepted mechanism for dust grain growth is the accretion of elements under interstellar conditions. Laboratory experiments have supported efficient formation of silicate and carbon grains of small size (nm) at low temperatures [Rouillé et al., 2015, 2020]. Figure 1.7 shows a simplified picture of the overall dust production/destruction mechanisms and its participation to the lifecycle of stars.
[Slavin et al., 2015, Kirchschlager et al., 2022, 2019, Micelotta et al., 2016, Potapov and McCoustra, 2021, Rouillé et al., 2015, 2020]

1.3.1.4 Grain growth: elemental accretion & depletion

Observationally, the existence of grain growth is considered to be an important process that explains the positive correlation between the depletion of elements and the gas density [Jenkins, 2009]. The dust-to-gas ratio increases with the density, proving the more efficient accretion of gas-phase metals on dust in denser ISM conditions [Roman-Duval et al., 2022, Clark et al., 2023]. Another proof relies on the proportional trend of the dust-to-gas and dust-to-mass ratios increasing with the metallicity and suggesting that grain growth is an important way to account for dust production at redshifts at least up to 6.3 [Konstantopoulou et al., 2024].

Understanding the composition and the main elements participating in the growth of dust is therefore a crucial aspect in this field. Measurements of the elemental depletions provide another perspective on interstellar dust. The elemental depletions show that in interstellar clouds most of the elements with low condensation temperatures such as Si, Fe and Mg are in dust grains. For the two most abundant elements, C and O, the situation is not easy to analyze since comparison of their fractions in the gas and in the dust is not trivial. Infrared and submillimeter observations of dust emission are important tools to provide further information about the composition of interstellar dust as a function of size. Populations of molecular sized particles and small grains are observed by their mid-infrared emission bands. Grain growth by accretion of gas-phase metals contributes to the formation of a refractory material mantle and this is believed to happen in the cold diffuse ISM [Zhukovska et al., 2016, 2018]. In a more dense environment, in the transition from translucent clouds to dense molecular ones, we observe the onset of an ice mantle around the refractory core via physisorption and chemisorption. As already mentioned, two processes can actually lead to the increase in size and mass of grains in interstellar clouds: coagulation, where two low velocity grains collide and stick together, and chemical accretion. The first process will form more porous grains consisting of various sub-grains with different composition that can reach micrometre sizes (see the recent work by Dartois et al. [2024]), whereas the second process will result in accretion of the abundant species, namely H, O, C, N, but also Fe, Mg, Si onto grain surfaces. Only at lower temperature and in specific environments, a formation of an ice mantle around the refractory core takes place. In fact, here small molecules such as water, CO, CO_2, ammonia, methane, methanol adsorb on grain surfaces and, together with newly synthesized molecules, they build icy mantles around the grains. H_2O represents more than 60% of the present molecules. The ice layers promptly desorb when exposed to UV radiation and temperatures higher than 150 K [Ferrara et al., 2016].

All the layers accreting on the grain, from the refractory material to the ice mantle, have the importance of removing species from the gas phase and representing a catalytic surface for further synthesis of new molecules on the grain that may afterwards desorb and come back to the gas component. The composition of the mantle strongly depends on the environment.

Gas-phase species arriving on the surface of a grain can bond by physisorption or chemisorption (see Chapter 2). Different types of grains also change the energies involved in all these processes even for the same species. Dust in the interstellar medium is thus subject to modifications, accretion and both constructive and destructive processing. The interstellar dust composition and size distribution is therefore a balance between the formation, growth and destruction processes operating in interstellar media. Having binding energy values, insights on desorbing species and reactions happening on

the surface, comparison with observations and models can give more details on the life-cycle of dust and ISM evolution (see also Barlow [1978]). For what we have understood until now, the growth of dust grains by accretion of gas-phase metals is now widely assumed to be an important process in the interstellar medium (ISM). Observations such as the positive correlation of depletion with gas density [Jenkins, 2009] are now well explained by grain growth and studies on galaxy evolution consider grain growth a needed addition to their models. As said before, in dense gas accretion is very efficient and it has to be taken into account. Here dust grains form icy mantles, rather than directly accreting refractory elements, which are rapidly photo-desorbed when exposed to ultraviolet (UV) radiation [Ceccarelli et al., 2018, Ferrara et al., 2016]. A low density condition makes accretion more inefficient, and this is still a problem in traditional models. Potential ways have been identified in order to avoid this problem, finding that the observed patterns for some elemental depletions, for example, were well-reproduced. There are also different ideas on the elemental depletions comparisons: efficient accretion of gas-phase metals by small, negatively charged dust grains has been proposed as an explanation for elemental depletion patterns observed in the CNM [Zhukovska et al., 2016, 2018]; other authors propose that the accretion of C^+ and S^+ can be enhanced in TCs where particles are expected to be negatively charged [Ruffle et al., 1999, Cazaux et al., 2022, Fuente et al., 2023]. Meanwhile, relatively high levels of depletion in the CNM, rather than being a sign of efficient grain growth, can also be considered indicative of the survival of dust grains in initially highly depleted material from a (presumably) denser phase of the ISM. Other authors propose that
[Priestley et al., 2021, Boogert et al., 2015, Ceccarelli et al., 2018, Boulanger et al., 2000]

1.3.1.5 Carbonaceous grains

Dust rich in silicon, metals and oxygen are believed to originate in C-rich AGB and red supergiants, while carbonaceous dust should be coming from carbon stars (AGB, see next section (1.3.1.6)). All stars with initial masses in the range of 1-8 $M_\odot$ (solar masses) pass through an asymptotic giant branch (AGB) phase. AGB stars eject large amounts of processed gas into the ISM, having a predominant role in describing abundances of chemical species. The AGB stars are efficient dust producers too, since their winds provide the right thermodynamic conditions for the condensation of gas-phase species into solid particles. Late AGB phases are the most relevant to assess grain production yields and the mechanisms behind those processes can be unveiled by comparing observations of post-AGB stars and dust formation modelling [Tosi et al., 2023]. Depending on the metallicity, the dust population mixture from AGB stars can be more or less dominated by carbon grains [Zhukovska and Henning, 2013]. One has to take into account that the

overall dust mass produced by AGB stars over cosmic time scales is usually way lower than the one observed in specific clouds, making the hypothesis of the grain growth by accretion in the ISM possibly being very relevant in such conditions [Srinivasan et al., 2016].
[Tosi et al., 2023, Nanni et al., 2013, 2014, Ventura et al., 2013, Ventura and Limongi, 2014, Zhukovska and Henning, 2013, Desert et al., 1990]

1.3.1.6 PAHs

The most important types of grains/surfaces for this study are Polycyclic Aromatic Hydrocarbons (PAH). These are carbonaceous compounds made up of carbon and hydrogen atoms arranged in such way to build aromatic rings and C-H bonds. They are characterized by aromatic emission bands (C-H and C-C modes linked to the aromatic core), extinction in the UV, and they are considered responsible for the excess of absorption at 217.5 nm. PAHs constitute a family of molecules composed of at least two aromatic rings to which hydrogen atoms are attached. There are two classes of PAHs depending on the compactness of the aromatic structure: cata-condensed PAHs, if the carbon atoms are in no more than two rings, and peri-condensed, if carbon atoms are part of three rings. In all experiments presented in this thesis, the coronene molecule ($C_{24}H_{12}$, Figure 1.8) was used to mimic the observed PAHs in the ISM. Coronene is a centrally peri-condensed PAH composed of 24 carbon atoms, where all the carbon atoms located at the edge of the structure are bonded to a hydrogen atom. Because of the close resemblance to the interatomic carbon-carbon bond length of graphite (around 1.40 Å), it is often used as a graphite model. PAHs were first identified in the ISM in 1984 by Leger and Puget [1984] and Allamandola et al. [1985], to account for the emission of Unidentified Infrared Bands (UIB), subsequently called Aromatic Infrared Bands (AIB). They contain up to 20% of the total interstellar carbon, making them the most abundant interstellar molecules after CO and H_2. PAHs are considered to have a size between 50 and 150 carbon atoms to explain the emission of UIBs. Smaller PAHs are thought to be photo-dissociated, while larger PAHs will instead begin to form carbon clusters kept together by weak forces, and ultimately, nanoscale carbon grains. The aromatic infrared bands are observed in the infrared spectrum in a large number of interstellar objects. Variations in the positions, line widths and relative intensities of these bands are observed from one studied object to another.
Several questions still stand nowadays regarding the lifecycle of PAHs. They should be forming in the envelopes of carbon-rich evolved stars such as AGBs and post-AGBs, but the timescale of their destruction by SNe and UV fields seems to be shorter than the production provided by such stars [Sandstrom et al., 2010]. Thus, other production

mechanisms may need to be considered, such as in situ formation in the ISM, or a top-down formation route where PAHs are created as the fragments of larger carbonaceous grains [Chastenet et al., 2019, Sandstrom et al., 2010].

There is a correlation between the mass fraction of PAHs and metallicity, since a decrease of their emission has been observed in low-metallicity environments [Gordon et al., 2008, Galliano et al., 2021]. It is unclear what causes the weak PAH emission observed in low-metallicity environments. Sandstrom et al. [2010] also found a lower PAH fraction in diffuse ISM, compared to the amounts found in dense clouds, possibly explained by either the presence of destruction events in diffuse MC or the possible formation mechanisms in dense clouds.

In general, it is not very clear whether in low-metallicity regions or more diffuse environments the smaller fraction of PAHs is caused by a harder radiation field or there simply is a reduced formation efficiency. New discoveries on PAHs have been made with JWST. Large C-dust reservoirs at high redshifts have been found with the detection of the 217.5 nm bump [Witstok et al., 2023]. New results also report the possibility to spatially resolve and better distinguish between the light coming from small and large dust grains, stars and hot dust. The 3.3 μm small-PAHs emission feature has been used as a tracer of dust grain fractions [Spilker et al., 2023, Chastenet et al., 2023, Sutter et al., 2024]. The work published by Spilker et al. [2023] represents the highest redshift detection of PAH emission so far.

JWST is now providing the highest quality IR data ever obtained and this allows the community to have access to more details regarding the AIBs, among other important information. Because of the relevance that PDRs and PAHs have in this Thesis, the recent work carried out by the PDRs4All team (Chown et al. [2024], Peeters et al. [2024], Habart et al. [2024]), reporting the most updated mid-IR observations of the Orion Bar, is highly relevant for this Thesis and is briefly summarised here. They provide a zoom-in of the typical AIBs (3.3, 6.2, 7.7, 8.6, 11.2, 12.7 μm), but most importantly they observe a decrease of about 40% for the 3.3/11.2 intensity ratio in the atomic region of the PDR, while going from the dissociation fronts to the HII region. This pushes the size distribution of PAHs towards larger species in those regions, implying that small PAHs with less than 50 carbon atoms most probably undergo photolysis and photoprocessing, depending on the strenght of the FUV. This is in agreement with previous studies showing that PAH sizes increases while approaching the illuminating source. Thus the PAH size strongly depends on the radiation field and, in its proximity, the photochemical processes promote the destruction of small PAHs while they unable the formation of more stable species [Knight et al., 2021]. A similar situation is applicable to very diffuse environments while, in denser regions, smaller PAHs can survive, coagulate and they are also expected to be condensed onto dust grains [Wakelam and Herbst, 2008, Rapacioli et al., 2005, 2006].

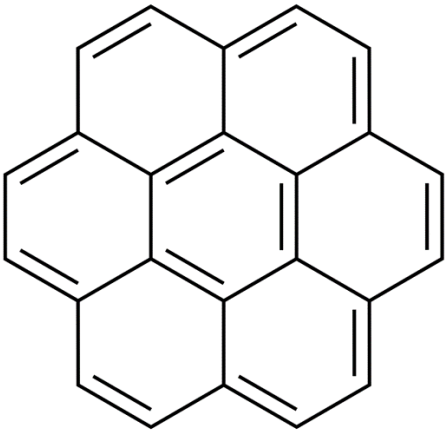

FIGURE 1.8: Coronene chemical structure.

[Draine, 2009, Leger and Puget, 1984, Allamandola et al., 1985, Joblin et al., 1992, Allain et al., 1996, Tielens and Hagen, 1982, Rapacioli et al., 2005, 2006, Salama et al., 1996]

1.3.1.7 Interstellar ices

When dust is observed in front of a bright IR source, it is possible to observe many other bands characteristic of different solids. These solids are known as ices forming mantles onto grains when densities are sufficiently high and temperatures are low enough to allow the condensation of gas species onto dust. These ices are formed by condensation of interstellar molecules onto sufficiently cold grains, and they can be modified by chemical reactions. The deposition of an ice mantle onto grains increases their size and changes the visible and IR extinction curves in molecular clouds. This phenomenon can be ignored in the diffuse medium where grains are too warm to allow for efficient ice condensation, but it becomes important in molecular clouds. In general, the deposition and formation of the very first layers of the ice mantle is considered to be starting in translucent regions of molecular clouds. More details on these aspects are given in Chapter 6. These mantles are destroyed when molecular clouds are disrupted, either through thermal evaporation, or through photodesorption (by the absorption of a UV photon), or through the prompt dissipation of accumulated chemical energy. The icy mantles of interstellar grains are made up of different molecules and the most abundant species are H_2O, CO, CO_2, H_2CO, CH_4, CH_3OH, NH_3 with water being the major component. In general, these molecules freeze on the surface of the grain from the gas phase, however the composition

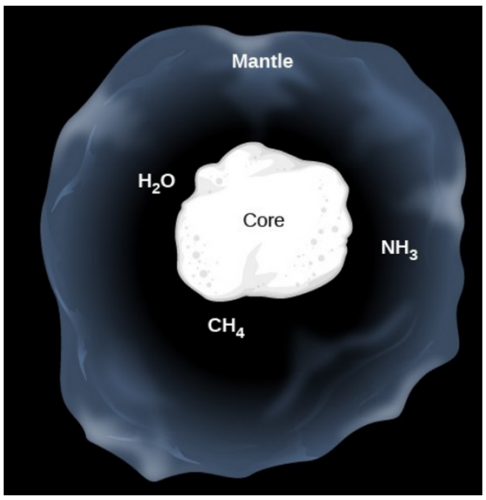

FIGURE 1.9: Scheme of an icy mantle around the refractory core of a dust grain from https://www.collegesidekick.com/study-guides/astronomy/cosmic-dust.

of the mantle does not reflect the composition or abundance of the gas phase since the reactions forming most of the complex species containing O, C and N happen on the surface through grain chemistry processes (see a typical ice mantle representation in Figure 1.9). Water, which is the dominant species of ice, is produced by a succession of hydrogenation of oxygen atoms which are adsorbed on the surface of the grains. Water molecules deposited on a surface form different structures depending on the temperatures and pressure under which it is formed. For a temperature above 160 K, ice has a hexagonal crystal structure. If the surface temperature is between 130 K and 160 K, the water ice has a crystalline cubic shape. For a temperature below 130 K, ice is amorphous. Amorphous ice mainly has two forms, between 100 to 130 K, it is in compact form (non-porous ice) because the molecules can still rearrange themselves a little. Below 100 K, ice is amorphous and porous. In this case molecules coming from the gas phase are immediately stuck where they adsorb on the grains, forming networks of pores with a complex morphology. The transitions between the different shapes are clearly visible on a water TPD (Temperature Programmed Desorption) curve by the appearance of stages. The experimental study in Chapter 4 shows, uses and describes experimental results of amorphous compact ices and crystalline ones.
[Oba et al., 2009, Gibb et al., 2004, Tielens and Hagen, 1982, Petrenko and Whitworth, 2002]

1.3.2 Molecules in the ISM

The first interstellar molecules have been identified in the early 1940s, namely CH and CN, and with the development of millimeter telescopes in the 70s, a lot of interest shifted towards the denser and darker regions. To date we consider two main processes causing the rich chemistry observable in the ISM: gas-phase reactions and reactions happening on the surface of grains. When we observe the diffuse ISM, we notice that almost all the molecules lay in the ground electronic and vibrational states. The rotational excitation is associated to collisions with other molecules (mainly H and H_2) and to radiative processes. In general, most of the physical and chemical processes that occur in diffuse clouds are the same ones that operate in dense clouds, with the main difference being that photo-processes play an important role only in diffuse cloud chemistry. In dense clouds the large dust extinction suppresses them and the presence of molecular hydrogen makes collisions more relevant. As already mentioned before, radio observations have resulted in the identification of more than 300 molecules [CDMS, 2024] with different degrees of complexity, from diatomic molecules such as H_2 and CO, to tri-atomic ones like H_2O and H_3^+ and very long organic molecular chains such as $HC_{11}N$. The main factors affecting the chemical nature of the ISM are the density and the temperature of the available gas together with its composition and the type and concentration of dust grains in the specific cloud. The main constituent of molecular clouds is H_2 and its formation strongly depends on the presence of dust grains. It is therefore likely that those surfaces provide important catalytic effects for the formation of other species as well, namely CH, NH, OH, CH_2, CO, CO_2, and H_2O. The surface/grain chemistry is not the only one playing an important role in the chemical complexity within clouds, but many molecules show formation pathways only possible in the gas-phase. A notorious example is the formation of the hydroxyl molecule (OH) that can be synthetized through reactions involving atomic and molecular ions. The chemistry of diffuse and dense clouds has been reviewed by van Dishoeck [1998]. In the following Sections the focus is on two important molecules for the overall ISM chemistry: H_2 and H_2O. Reactions on the surfaces of the dust particles promote indeed the formation of molecules, especially of H_2, and other hydrogen-rich species like H_2O. Besides representing the main characters of the research developed through this PhD, H_2 is the most abundant molecule of the ISM and the cooling agent needed to start star formation processes. H_2O represents the main component of interstellar ices, locking up most of the available oxygen and creating icy mantles around dust grains influencing the whole chemistry in the transition from diffuse towards denser clouds.
[Snow and McCall, 2006, Carroll and Ostlie, 2017].

1.3.2.1 Molecular hydrogen

H_2 is the most abundant molecule in the Universe and plays a crucial role in the processes regulating star formation and the evolution of galaxies. Its formation on dust grains initiates the chemistry of interstellar gas and it is a major contributor to the cooling of astrophysical media. H_2 is a symmetrical homo-molecular species without dipole moment, therefore direct observations of H_2 have always been challenging: the electronic transitions occur in the UV region, to which the Earth's atmosphere is opaque, and all the high temperature ro-vibrational transitions within the electronic ground state are quadrupolar, thus faint. This section is organized as an historic overview of the main scientific steps taken towards understanding the physical-chemical processes of molecular hydrogen in the ISM and the progress made from its first detection. Space-based missions in the mid-IR such as *Spitzer* and *ISO* have been crucial in detecting the rotational lines, providing new understandings about molecular hydrogen in space. The gas-phase production of H_2 is considered to be too low, most of it is therefore thought to be formed on the surface of dust grains [Gould and Salpeter, 1963]. Besides theoretical and experimental studies unveiling the different formation processes, observations can provide estimates of the several rates for different ISM regions. Regarding IR observations, before *ISO* (1995), only few ro-vibrational lines of H_2 had been observed, towards Galactic shocks and PDRs, planetary nebulae, and in some instances the nuclei of active galaxies (first studies by Shull and Beckwith [1982] and Fischer et al. [1987]). The first observations of the pure rotational lines of H_2 in the zero vibro-eletronic state were done in 1991, from the ground and towards the Orion bar [Parmar et al., 1991]. ISO was able to cover wavelengths in the range 2 – 200 μm, thus several pure rotational lines of H_2 have been observed, helping in studying the links between molecular hydrogen, dust and other gas components. Studies combining observations from *ISO* and ground-based telescopes allowed to have new information about H_2 formation rates under several physical conditions. Habart et al. [2004] found efficient H_2 formation at gas temperatures above 300 K, meaning that physisorption (see Chapter 2) is not the only processes involved in its formation on dust grains, but chemisorption (see Chapter 2) involving strongly bound H-atoms is required. The efficient H_2 formation under those conditions, where H atoms scan the surface finding a previously chemisorbed one, seems to depend on the presence of very small grains (VSG, r $<$ a few 10 nm) in PDRs and aromatic dust particles (PAHs, r $<$ 1 nm). Several works have addressed this topic both in the laboratory [Joblin, 2001] and observationally [Le Coupanec, 1998]. The role of VSGs in molecular hydrogen formation processes and their emission between 15 and 40 μm has been understood through the IR *Spitzer* Space Telescope launched in 2003.
Spitzer has provided spectroscopic observations and has given more insights into the H_2 physics in PDRs. Those studies also revealed that the observed column densities of

rotationally excited H_2 were way higher than model predictions. An approach to reduce this difference was proposed to introduce an enhancement in the H_2 formation rate, since the line intensities depend strongly on it and it affects the location of the dissociation fronts in PDRs. Despite enhancing the formation rate, the PDR models keep giving too low intensities. Several explanations were given, such as the possibility of having H_2 gas at a higher temperature than previously thought or predicted by models. [Habart et al., 2004]

New insights have come with the James Webb Space Telescope (JWST). In the inner region of the Orion Nebula, it has been able to provide the newest and sharpest images ever. New details regarding the description of hydrogen in the transitions between the ionization and dissociation fronts of PDRs are now available. The observations provide a more detailed spatial resolution of the AIBs, showing how the PDR edge is steep and it is followed by a warm atomic layer reaching the DF, defined by multiple ridges [Peeters et al., 2024]. By following the H_2 lines, a new and more complex DF structure has been found, where the H to H_2 transition is at stake. With *JWST* [Habart et al., 2024], they were for the first time able to spatially resolve the emission profiles of the high rotationally and vibrationally excited H_2 lines [Peeters et al., 2024]. There are also new studies detecting hot H_2 without a cold counterpart in CO with *JWST* MIRI and they are now focusing on understanding how the formation of H_2 is possible in these conditions.

[Habart et al., 2005, 2011, 2024, Appleton et al., 2023].

Trying to explore all the ranges of temperatures at which molecular hydrogen can be efficiently formed on dust grains thus represents an important research topic in this field. Experiments and models such as the ones presented in this thesis can provide important references for the interpretation of the new JWST data.

1.3.2.2 Water in the ISM

Water represents one of the most important molecules in the whole universe, playing a fundamental role from terrestrial life to interstellar processes. It is made up of the first and the third most abundant elements, namely H and O. The same historic approach used for H_2 is adopted in this section. After its discovery as vapor in the Orion Nebula in 1969, its general chemical formation pathway was established and considered to involve both gas-phase and solid-state chemistry, but many related processes were still not fully understood. Thanks to the detection of water in several regions by the *Herschel* Space Observatory, we have a now a better description of water chemistry in space. [Van Dishoeck et al., 2013]

Because of the presence of a strong molecular dipole, water shows strong pure rotational,

vibrational and electronic transitions. H_2O can exist either in the gas-phase or as ice and its chemistry involves three main formation routes: low-temperature (< 100 K) ion-neutral chemistry; high-temperature neutral-neutral chemistry; surface chemistry. Gas-phase water can also undergo destruction through reactions involving ions such as H_3^+, HCO^+, C^+, H^+, He^+ and via photo-induced processes. Besides the pure gas-phase formation processes of water molecules, it is extremely important to account for the reaction happening on grains at lower temperatures. Surface chemistry is indeed the way for gas-phase species to interact with dust grains through accretion and desorption processes, thermally (sublimation) and non-thermally (mainly photo-desorption). From observations of water ices in molecular clouds [Whittet et al., 2011], it is now well known that ices form in regions of molecular clouds where the A_V is around 3. For lower extinction values, the interstellar UV fields contribute to efficient photo-desorption of the species landing on the dust grain surfaces thus preventing the icy mantle formation. Water ice is, after H_2, one of the most important molecules formed on grain surfaces at low temperatures. Ice chemistry is therefore another approach to understand the depletion of abundant species such as oxygen from the gas-phase by accretion on dust. The processes involving the formation of water ices on grain surfaces can also be distinguished between the chemistry of diffuse and translucent clouds, namely the reactions happening on dust itself (silicates and/or amorphous carbon), and the ones happening in colder and denser regions where oxygen and other species accrete on pre-existing ice layers. The chemistry of water on dust grains has been mainly investigated because of its importance not only for the onset of the icy mantles during dust cycles and stellar evolution, but also in relatively new fields such as Astrochemistry and Astrobiology that aim to uncover the origin and the future of life in the universe.
[Van Dishoeck et al., 2013, Caselli and Ceccarelli, 2012]

1.4 Introduction to Thesis structure and projects

This Thesis represents a surface astrochemical study of reactions happening on dust grains. Specifically, the main part is dedicated to experiments run at LERMA-CYU using the FORMOLISM (FORmation of MOLecules in the ISM) setup, where we were able to use surfaces such as amorphous ice, simulating icy mantles, and coronene, a PAH-like structure. The gas-species interacting with those surfaces are mainly hydrogen and oxygen and we have tried to answer very simple questions with eventually high impact. The three Chapters reporting experimental studies and results (Chapters 4, 5, 6) come from three different already published articles. The two main experimental Chapters (5 and 6) are also followed up with theoretical studies carried out at UGent using `Cloudy` and `Nautilus` codes, respectively Chapters 8 and 9, to provide an interpretation for

some the experimental work.

The Thesis starts with a general introduction to the world of Astrochemistry (Chapter 1). The aim is to cover the main astrochemical aspects and processes relevant to the research carried out in this PhD: the composition of the ISM, with the diverse environments and phases, and the molecular clouds; the main processes related to the dust lifecycle, together with the role of those surfaces as catalysts for the chemical reactions and adsorption processes; some details about the most abundant molecules of the ISM that are also the main characters of this Thesis, namely H_2 ad H_2O.

Chapter 2 presents some theoretical elements of surface physics and surface chemistry in order to create a theoretical basis to afterwards go into the details of the experimental setup and to make a link with the astrochemical reactions involving the dust grain surfaces described in Chapter 1.

Chapter 3 gives a detailed description of the different components of the FORMOLISM setup at LERMA-CYU. This chapter also describes the experimental methods used to carry out the experiments: TPD (Temperature Programmed Desorption) and DED (During-Exposure Desorption). The main results section of this manuscript starts with Chapter 4.

This is the first experimental Chapter containing the first published study of this PhD. This chapter is mainly used here as an example and introduction to FORMOLISM, experimental techniques and configurations. It is also an input to add some theoretical aspects to this Thesis and show how experiments allow to extract Binding Energies (BEs) through appropriate fittings.

The second chapter reporting experimental results is Chapter 5. This is taken from the second publication of this PhD journey. This Chapter shows the experimental results concerning the high temperature atomic recombination of hydrogen on PAH-like structure, where those surfaces act as catalysts. The study is framed in an introduction that links H_2 to star formation and it discusses the astrophysical implications of such results.

The last experimental publication is reported in Chapter 6: by adding oxygen to the experimental setup we were able to form icy mantles at higher temperatures than previously reported. A general introduction and discussion of icy mantles, translucent clouds and oxygen depletion is reported within this Chapter.

From here on starts the modelling/theoretical part of the Thesis. Chapter 7 is a general introduction to the main codes used in astrochemistry with a brief description of the ones used in this Thesis. Chapter 8 represents in fact the theoretical follow-up of the results presented in Chapter 5. By using the `Cloudy` model, we tried to study the effects of high-temperature H_2 formation on the location of the dissociation front of a PDR by implementing the formation of molecular hydrogen on carbonaceous grains at higher temperatures.

Chapter 9 is the very last project of this PhD. With the `Nautilus` code, we tried to

go deeper into the scientific question marks regarding translucent clouds, already introduced in Chapter 6. In this study we tried to reproduce the translucent regions of a few molecular clouds and, by following the strategy of Jones and Ysard [2019], we tried to develop a sink molecule that would account for the observed oxygen depletion eventually resulting in grain growth, before the onset on the icy mantle.
Finally, the conclusions are presented in Chapter 10. This last one represents a brief summary of the goals achieved, it briefly discusses possible applications to astrophysics, but it also gives a personal point of view on the future perspectives for such topics.

Chapter 2

Theory Background

2.1 Surface Physics

The experimental methods used in this Thesis are designed to study the effect of the interaction of molecules and/or atoms in the gas phase on a solid phase. There are three main processes describing such a system and they concern the landing of the species on the surface (adsorption), the diffusion on the chosen substrate and the eventual desorption (return to the gas phase).
Each process strictly depends on the nature of the species involved and on the temperature chosen for the experiments. Moreover, the dynamics and the reactivity of molecules/atoms can be studied in two different regimes: sub-monolayer and multilayer. A monolayer is when a one-molecule-thick layer covers the entire surface, after which the following landing species will adsorb on the just-formed layer and not on the original surface anymore. The actual interaction between a gas-phase species and a surface is therefore usually studied through the physical-chemical description of the sub-monolayer regime, which is the goal of our study.

2.1.1 Adsorption

The first process concerning the landing of gas-phase species on the surface is adsorption. Depending on the nature and type of systems this can lead to two main interactions: physisorption and chemisorption. Physisorption is involved when only weak bonding between molecules/atoms and the surface take place. We are thus talking about van der Waals-type forces without significant redistribution of electron densities between the molecule and the surface. Chemisorption involves instead the formation of an actual chemical bond, with a relevant rearrangement of electron densities, that will strongly

link the adsorbate to the substrate. As for all long-distance weak forces, the potential describing physisorption is a combination of attractive (Van Der Waals) and repulsive (Pauli repulsion) parts. The resulting potential is a typical Lennard-Jones potential:

$$V_{\mathrm{LJ}}(r) = 4\epsilon \left(\left(\frac{\sigma}{r}\right)^{12} - \left(\frac{\sigma}{r}\right)^{6} \right); \tag{2.1}$$

where r is the distance between two interacting particles, ϵ is the depth of the potential well (usually referred to as "dispersion energy", strength of interaction), and σ is the distance at which the particle-particle potential energy V is zero (often referred to as "size of the particle"). The Lennard-Jones potential V_{LJ} has its minimum at a distance of $r = r_{min} = 2^{1/6} \cdot \sigma$.

In this case the nature of the adsorption does not require activation and it is therefore very fast, it is described as totally reversible and non-dissociative. Thus, it can act at longer distances making the multilayer regime possible. The typical binding energy of a physisorption process is about 10-400 meV (100-5000 K/k_b). If chemical bonds are formed, the type of potential now includes dissociation and it is better described through a Morse potential:

$$U(r) = D_\epsilon \left[1 - e^{-\alpha(r-r_e)} \right]; \tag{2.2}$$

where D_ϵ is the depth of the potential well relative to the dissociated atoms, α is its range (inversely proportional to the width of the potential well), and r_e the equilibrium distance.

Chemisorption usually forms bonds with energy of 1-10 eV. Since chemisorption is defined as the formation of chemical bonds between landing species and surface upon adsorption, this puts several constraints in order for this to be possible: the presence of active sites on the surface, the reactivity of the impinging species and the overcoming of the activation barrier are almost always needed to initiate the reaction. If the chemisorption process provokes the dissociation of the landing species, this newly formed chemical bond can also be responsible for the formation of new molecules by the encounter of other reactants through surface diffusion, thus resulting in an irreversible process. Chemisorption involves higher energies than physisorption and it needs the active role of the surface, thus it is a process happening only in the sub-monolayer regime. Figure 2.1 gives a visual representation of the potential energies involved in chemisorption and physisorption processes as a function of the distance of an atom approaching the surface. The experiments run in the course of this PhD and the results presented in this Thesis show the joint impact of these processes since some are facilitated under certain conditions rather than others. While physisorption is always at work, the best example of chemisorption is given in Chapter 5.

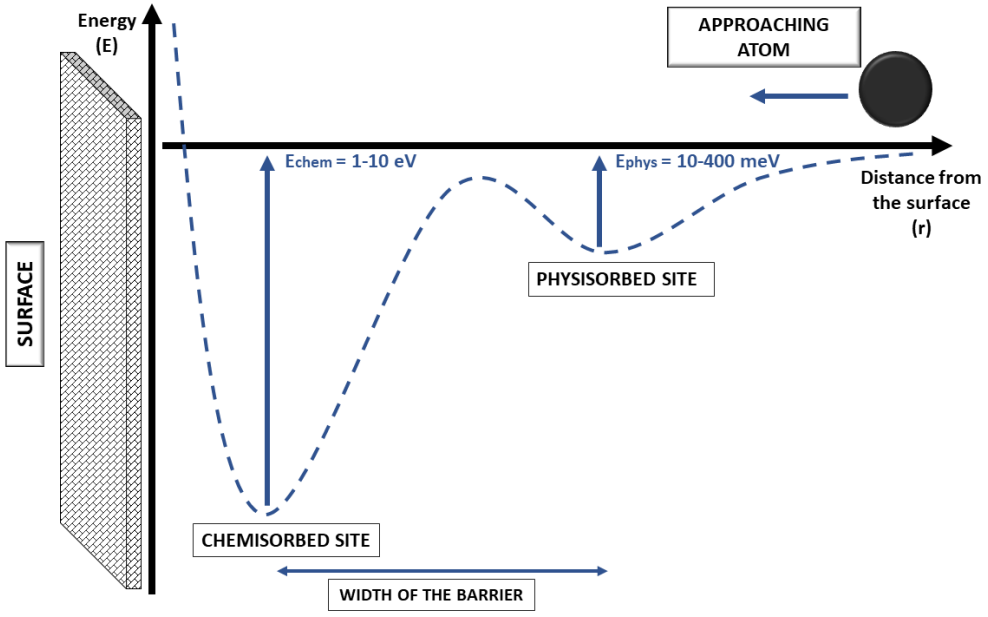

FIGURE 2.1: The interaction between an atom adsorbate and a surface site as a function of the distance to the surface: weak physisorbed sites (Van der Waals interaction, E_{phys}) and chemisorbed sites (chemical bond, E_{chem}). The physisorption potential has been assumed to be a Lennard-Jones potential, whereas chemisorption is described by a Morse potential.

2.1.1.1 Sticking coefficient

When a gas-phase molecule arrives at the surface, there is a certain probability that this will stick, adsorb and eventually diffuse and desorb. This is expressed by the sticking coefficient (S) in the range 0 - 1, where the limits correspond to no adsorption and complete adsorption of all incident molecules, respectively. S depends on the temperature of the system, the surface coverage and its structure. From an energetic point of view, S represents how fast the energy of gas phase atoms is transferred to the surface. There is a simple way to approximate it in experiments:

$$S \propto \frac{E_s}{E_s + E_k}; \tag{2.3}$$

Where E_S is the sticking energy (physisorption) and E_k the kinetic energy of the gas species.

The sticking coefficient varies only for big ranges of surface T ($\approx$ 600K) and since we run experiments in ranges of $\leq$ 200 K we consider it constant for each studied system. In general, if the E_S is significantly bigger than E_k, the sticking coefficient is approximately considered to be equal to 1. One has to keep in mind that E_S corresponds to the physisorption binding energy E_b [Kruegel, 2003]. The binding energy strongly depends on the kinetic energy of the adsorbing molecule and its nature, but most importantly on the type of surface (composition and local conditions). Given the fact that a surface shows

a distribution of possible binding sites and a molecule can diffuse before desorption, the description of the energies involved in the desorption of a species from a specific surface should always be considered as a distribution of binding energies as well [Minissale et al., 2022].
Details of each set of experiments are given in every experimental Chapter.

2.1.2 Surface diffusion/migration

The motion of an adsorbed particle on a surface is described by the laws of surface diffusion. In most of the cases, the mobility is enabled by thermal activation and its path defines a random walk. If the species on the surface are distributed in such a way to define a concentration gradient, the adsorbed particles will therefore move towards sites of low concentration and this situation, that does not concern our experiments, is better described by the Fick's laws. Thus, from an atomic scale, our system is made up of adsorbed species located in a specific site of a surface with the possibility, if thermal activated, to undergo a site-to-site random hopping. The mean-square displacement of the hopping species in time t is given by:

$$\langle r^2 \rangle = \nu \cdot a^2 \cdot t; \tag{2.4}$$

where a is the jump distance (i.e., the adsorption site spacing) and ν the frequency of hops. Note that $\nu \cdot t$ gives the number of hops.
It is also convenient to define a diffusion coefficient as the ratio between $\langle r^2 \rangle$ and the time of hopping multiplied by the number of neighboring available sites (z):

$$D = \frac{\langle r^2 \rangle}{z \cdot t} = \frac{\nu \cdot a^2}{z}; \tag{2.5}$$

where z depends on the type of diffusion and on the solid structure of the surface.
When a species adsorbs onto a site, it finds itself located in a certain well, with a precise oscillation frequency ν_0, where the barrier height is essentially the diffusion energy (E_{diff}). The hopping frequency is therefore defined as the possibility for a species to hop to another site:

$$\nu = \nu_0 \cdot exp(\frac{-E_{diff}}{k_b T}); \tag{2.6}$$

where k_b is the Boltzmann constant and T is the temperature of the surface. Moreover, one has to take into account that E_{diff} can also be expressed as a fraction of the desorption energy (E_{des}), with a ratio that depends on the species and surfaces involved (Minissale et al. [2016]).
In fact, the diffusion energy is usually way lower than the desorption one, but slightly

higher than k_bT. Different types of diffusion can also happen depending on the coverage and the landscape of the surface. In the first case we have two main diffusion conditions: tracer or chemical diffusions. For low coverages, we would observe a tracer diffusion, where there is no interaction between adsorbed species. Here particles are considered to have an independent random walk. For high coverages, we talk about chemical diffusion with non-negligible interaction between diffusible particles. In this case, adsorbed species could have a diffusion with a certain dependence on the concentration gradient and thus the scientific description can be achieved by using Fick's laws. Depending on the surface landscape, we can distinguish between intrinsic diffusion, if there are no traps/defects for diffusing species, or mass transfer diffusion if the process is affected by the generation and/or trapping of diffusing species by inhomogeneities of the surface. Finally it is important to stress on the several possible diffusion mechanisms: hopping, atomic exchange, tunneling and vacancy.

- Thermal Hopping
  As already briefly mentioned, this is a thermally activated diffusion mechanism allowing an adsorbed particle to go from an equilibrium-state adsorption site to the next one. Despite being the simplest, it gives a good general description of various real systems.

- Atomic Exchange
  It is a place exchange mechanism between two atoms. An adsorbed atom replaces another one which will therefore move to the very next site. During this diffusion mechanism, all the involved atoms show a high coordination number. Sometimes it is energetically more favorable than simple hopping.

- Tunneling
  Quantum tunneling (QT) represent the migration by which a small mass species can cross an energy potential barrier if the latter is low and thin enough. In this case, this mechanism physically substitutes the thermal hopping resulting in the same effect. Nevertheless the QT diffusion is always dominated by the thermal diffusion, above a certain critical temperature T_c.

- Vacancy
  This mechanism appears relevant on a surface where the majority of atomic sites are occupied and the species move controlled by the formation and migration of vacancies.

2.1.3 Desorption

Desorption is the process by which a pre-adsorbed species gains enough energy to cross the activation barrier to return to the gas-phase. Desorption is mainly of two types: thermal and non-thermal. The latter is a non-equilibrium process in which the temperature of the system is not the main phenomena allowing desorption. Non-thermal desorption can be important under specific ISM conditions. The main non-thermal mechanisms are: electron or ion impact-stimulated desorption, photo-desorption, chemical desorption.
When an atom or a molecule is ejected from a grain/solid-state surface due to the impact of particularly energetic ions or electrons, the process is referred to as sputtering. In this case, the particles have kinetic energies higher than the usual thermal ones. Extensive ion sputtering is one of the processes caused by SNe-generated shock waves. Electron sputtering of ices is, instead, widely studied for the production of gas-phase species from icy surfaces in the ISM [Johnson et al., 2013].
Photo-desorption is the mechanism by which the absorption of a UV photon by a molecule adsorbed on a surface results in its desorption or in the desorption of a nearby species (direct or indirect processes respectively) [Bertin et al., 2013]. Many studies focus on the role of UV photo-desorption of ices (see Öberg et al. [2009,]). Regarding chemical desorption, it concerns the possibility for a newly formed molecule to desorb because of the excess of exothermic energy that does not dissipate on/through the surface [Dulieu et al., 2013].
Only thermal desorption is relevant to the experiments presented here.

2.1.3.1 Thermal desorption

From a thermodynamic point of view, thermal desorption is a process where thermal and chemical equilibrium are achieved at each time step, therefore describing an overall metastable equilibrium that evolves linearly. From a kinetic side, one can define the desorption rate as the number of particles desorbing from a unit surface area per unit time. The reverse of the rate is the residence time, defined as follows:

$$\tau_{des} = \nu_0^{-1} \cdot e^{\frac{E_b}{k_b T_s}}; \tag{2.7}$$

with ν_0 being the oscillation frequency of a species in a site (approximately the vibration the surface lattice is $\approx 10^{13}$ s^{-1}), E_b is the binding energy and T_s the surface temperature. A better description of ν_0 can be found in the review by Minissale et al. [2022].
If we assume that all the adsorbed species occupy identical sites and there is no interaction among them, the desorption rate can be expressed as a function of surface coverage,

by using the Polanyi-Wigner Equation:

$$r_{des} = -\frac{d\theta}{dt} = k_n \cdot \theta^n; \tag{2.8}$$

where n is the so-called order of the desorption (see Figure 3.2, Section 3.3.2) and θ is the surface coverage. The desorption rate constant k_n can be expressed by using the Arrhenius equation as general expression for T-dependent chemical reaction. A better description of the study of desorption rates by using the Arrenhius equation and the importance of the pre-exponential factor are given in Chapter 4 by giving an example of experimental results and their analysis.

2.2 Surface Chemistry

As already said in the introduction, chemical reactions happening on dust grains play an important role in explaining abundances of observed species in the ISM, since they are crucial surfaces onto which gas-phase species can land and eventually react. In this terms, the surface is catalyst that can speed up or facilitate reactions. There are two main mechanisms to explain the formation of new species by the interaction of gas-phase species with a given surface. Both of them require the adsorption of, at least, one species on the surface to make the reaction possible.

2.2.1 Eley-Rideal

In this mechanism, proposed in 1938 by D. D. Eley and E. K. Rideal, only one of the molecules is already adsorbed and the other one reacts with it upon arriving from the gas phase. It is similar to what would happen in the gas-phase. It is a non-thermal surface mechanism because it leads to a reaction between a thermally adsorbed surface species and a reactant which has not been thermally accommodated to the surface yet. It is also possible that the landing particle does not adsorb on the surface at first impact, but it dissipates its energy by hopping on the surface until finding a reactant already thermalized, located far from the impact site. This is the hot atom mechanism, similar to the dynamic of the ER one, but of about one order of magnitude higher in terms of total reaction rate.

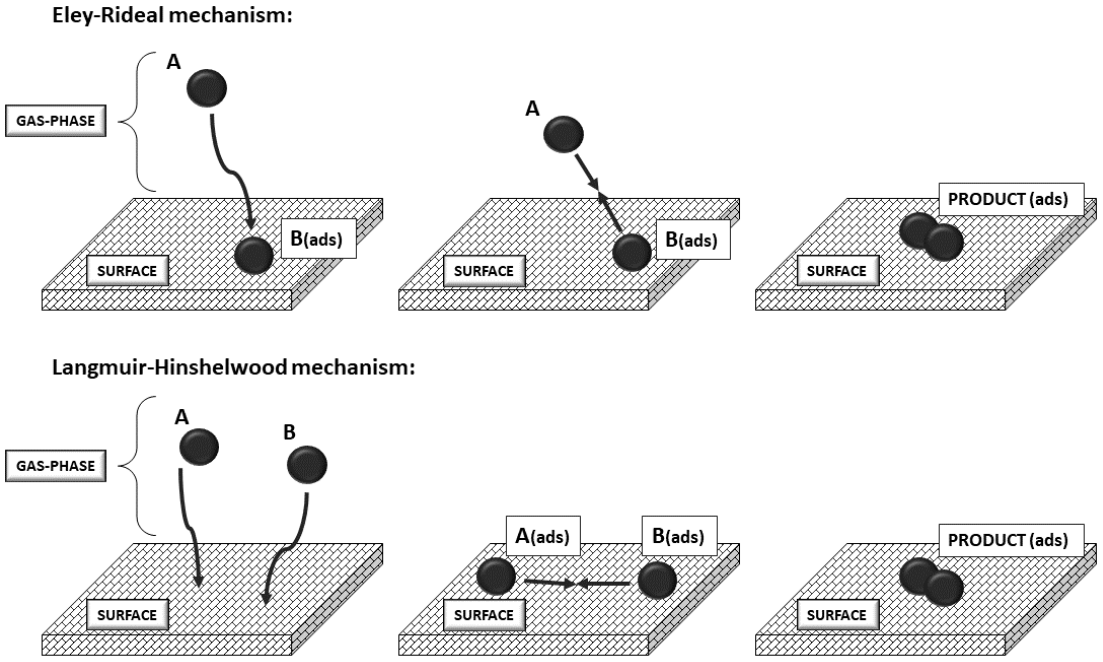

FIGURE 2.2: Representation of Eley-Rideal & Langmuir-Hinshelwood mechanisms.

2.2.2 Langmuir-Hinshelwood

This mechanism concerns the formation of molecules when two reactants are already adsorbed on the surface. The LH mechanism is a thermal surface mechanism because both reactants are thermalized but at least one of them should be mobile, having enough energy to diffuse and migrate to encounter the other one. Thus, the reaction may not be the only limiting step, but also the diffusion of the species on the surface.

[Wang and Gomer, 1979, Antczak and Ehrlich, 2010, Roger, Martinazzo et al., 2004, Oura et al., 2004]

Chapter 3

Experimental Setup: FORMOLISM

The experiments were conducted at LERMA-CYU, laboratory in the Physics Department of the Université de Cergy-Paris (France), by using the FORMOLISM setup. The acronym stands for FORmation of MOLecules in the InterStellar Medium and it aims to reproduce and to study relevant astrophysical reactions happening on dust grains in specific physical conditions. FORMOLISM is an equipment made up of an UltraHigh Vacuum (UHV) chamber (base pressure of $\approx 1 \times 10^{-11}$ mbar) containing an oxygen-free high-conductivity (OFHC) copper sample holder/surface with diameter of 1 cm and a base temperature of 300 K. This surface is located in the middle of the chamber and attached to a closed-cycle He cryostat (Advanced Research Systems 4K DE-210SB cryocooler coupled to a ARS-10HW compressor). The connection to the cryostat allows to scan temperatures from a few Kelvins up to hundreds. It enables to study the adsorption of species from the gas phase, their reactions, and related mechanisms happening on the surface as well as to reach desorption temperatures. The copper sample holder can also be covered with other substrates based on the scientific question that is addressed during the specific experiment, without affecting the temperature. Surfaces such as graphitic and carbon pellets or silicates represent usual composites glued on the copper, but FORMOLISM also allows to directly deposit ice through an ad-hoc microcapillary array system, locally injecting water vapour. Those surfaces thus become the new stage mimicking dust grains on which gas-phase species will land, eventually react and desorb. Molecules and atoms arrive through two main beams by regulating the initial pressure of injection. The beams are collimated towards the surface. The dissociation of molecules into atoms is made possible by forming a plasma in the source zone. The latter is cooled down by a flux of compressed air constantly circulating around the tube to minimize the eventual recombination of the atomic species and to reduce the discharge temperature of

the cavity, resulting in a cold plasma. Finally, the detection of the incoming beams and, most importantly, the processes occurring on the surface upon gas-phase species interactions is realized by IR and mass spectrometry. FORMOLISM is in fact equipped with both a Bruker Tensor 27 Fourier transform infrared spectrometer (FTIR) to study the adsorbed/formed species in situ, set up in a reflection-absorption infrared spectroscopy (RAIRS) configuration, and a Quadrupole Mass Spectrometer (QMS). In the present thesis, only the rotatable QMS has been used to characterize the composition of the beams entering the UHV chamber and to detect, study and measure the desorption of each species from the surface into the gas phase as a function of temperature [Congiu et al., 2012, Amiaud et al., 2007, Minissale, 2014].
Over the years FORMOLISM has been used to address and answer several astrophysically relevant experimental questions, here we provide an overview of typical laboratory projects.

- Physics and chemistry on the surfaces of interstellar dust grains: reactions and energies involved.
- Study of interstellar ices: formation and morphology.
- Thermal and non-thermal processes coupling gas and solid phases.
- IR spectroscopy analysis of molecules formed on interstellar grains and the prediction of their reaction pathways.

The specifics of each FORMOLISM component, together with more details about the experimental configurations, are given in the following Chapters (4, 5, 6). Figure 3.1 shows a schematic picture of the setup with its most relevant parts.
In the following sections we describe the main FORMOLISM components:
3.1. The UltraHigh Vacuum (UHV) main chamber and sample holder;
3.2. Two triply differentially pumped beamlines and microwave cavities;
3.3. The Quadrupole Mass Spectrometer (QMS).

3.1 UHV main chamber, sample holder and surfaces

The UHV main chamber is a stainless steel cylinder with radius of 15 cm and height of 120 cm, that is able to reach values of about 10^{-11} mbar by using a system made up of a cryopump, a titanium sublimation pump, a turbo molecular pump and an ion pump, with a residual molecular/atomic density of about a few 10^6 cm^3. One has to consider that, in

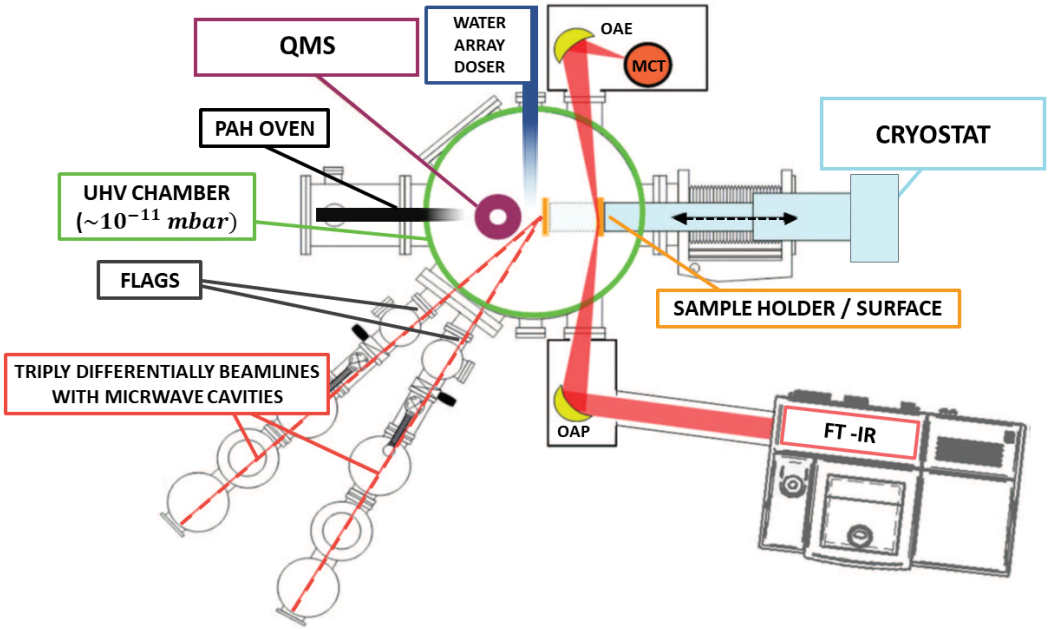

FIGURE 3.1: Schematic top-view of the FORMOLISM set-up taken from Congiu et al. [2012] where MCT is the liquid-nitrogen-cooled Mercury Cadmium Telluride detector; OAE and OAP are the Off-Axis Ellipsoidal and Parabolic mirros rispectively; PAH stands for Policyclic Aromatic Hydrocarbon and the FLAGS are mechanical choppers that can be rotate in order to block or reduce the flux in the beams.

practice, it is impossible to exactly reproduce astrophysical conditions of p= 10^{-14} mbar (Williams and Herbst [2002]) for both the vacuum system and for the experimental time that each study would require. However, the pressure of FORMOLISM, coupled with the possibility of reaching very low temperatures, is enough to get rid of the pollutants that would strongly interfere with the experiments. One has to keep in mind that, at a H_2O partial pressure of about 10^{-10} mbar and a surface temperature of 10 K, our system would need more than 5000 minutes to get the sample holder covered with 1 ML of water vapour.

The sample holder that is placed in the main chamber represents the main surface for the reactions to occur. The sample holder is connected to a He closed cycle cryostat with a specifically designed interface that allows the surface to cool down and heat from a few Kelvins up to 800 K. The temperature is measured using a calibrated silicon-diode sensor and a Au-Fe/Cromel K-type thermocouple attached to the sample holder. A simple controller unit, Lakeshore 340 [1], is used to regulate the temperature by varying the power of the heater, controlling the changes and following the experiments upon careful calibration of the parameters. The temperature can be controlled to ±0.2 K and measured with an accuracy of ±1 K. An important aspect concerns the fact that the sample holder is placed at the same height of the beamlines, in order to better receive

[1]The Lakeshore 340 is a control unit that enables the remote control of some parameters in FORMOLISM. Specifically, this unit allows the regulation of the temperatures and the heating rates by which the surface is heated or cooled down

the eventual species, and it can be moved back and forth with respect to the center of the chamber depending on the type of experiments. The translation plate to which the copper surface is connected is remotely controlled and it is used to achieve specific configurations to respond at best to various experimental requests such as depositing water ices through a built-in channel, checking the beamlines' composition with the QMS or to better position the surface depending on the rotation of the QMS used in the experiment.

Last but not least, it is important to mention that the copper sample holder is not the actual surface used to mimic reactions in the ISM, there is in fact the possibility to glue pre-made samples (usually silicates or graphite-like ones), directly deposit water ices or carbon-based structures such as PAHs. For each mentioned surface there is a protocol that has to be followed to allow the correct experimental procedure and the absence of pollution in the chamber. If pre-made surfaces are used, it is important to follow a step-by-step procedure in order to clean the surface before putting it inside the setup and to operate several de-gazing and heating cycles. Different glues also respond to several experimental parameters such as the temperatures involved and the type of surface sample. The main chamber is also equipped with a microchannel doser used to make water ice films on the sample surface. Water is contained in a small vial located outside the chamber and it can diffuse into it via a microcapillary array. The water diffuser can be moved and placed in front of or above the sample holder, depending on whether we want a direct ice deposition or whether we want to mimic the growth of ice on the surface by spraying water in the whole chamber (background deposition) above the sample. Moreover, the temperature on the surface can be chosen, changed, and controlled in order to go from a more or less compact ice to an amorphous or crystalline one. More details on specifics about the deposition of different ices are given in Chapter 4. When water is sent directly through the doser, by opening the leak valve, the local pressure reaches about 10^{-6} mbar, while the residual pressure into the chamber goes up only to a few 10^{-9} mbar. This is explained by the distance between the diffuser and the cold surface being smaller than the mean free path of H_2O so most of water molecules will deposit on the sample holder (or on the cryostat). The original UHV is afterwards reached again by waiting about one hour. For the background deposition, longer times are required to deposit the same amount of ice layers. For a pressure in the chamber that reaches a few 10^{-8} mbar, a monolayer ($\approx 10^{15}$ molecules cm^{-2}) is grown in around 5 minutes. The expression of the flux Φ is given below:

$$\Phi = \frac{v \cdot n}{4} = \frac{P}{4KT} \cdot \sqrt{\frac{8KT}{\pi \cdot m}}; \tag{3.1}$$

Where P and T are respectively pressure and temperature of the chamber, m is the mass on the impinging molecules, v is the molecular mean velocity and n the molecular

number density.
FORMOLISM also provides a PAH-oven that allows the sublimation of a chosen molecular powder, previously placed inside, towards the sample holder creating a whole new surface. Once the sublimation temperature of the chosen species is obtained, the oven is brought in front of the sample holder (distance of about 3 cm) and the valve is opened. For both the ice and the PAH depositions, the number and type of layers deposited can be tuned by varying time and distance from the sample holder.
Specifics on how each of the surfaces is chosen, glued, or deposited are given in the protocol description for every study/experiment/Chapter.
[Minissale, 2014, Minissale et al., 2016, Ferrero et al., 2022]

3.2 Beamlines and microwave cavities

FORMOLISM is equipped with two beamlines that are the channels by which the molecules/atoms are collimated into the main chamber and eventually land on the surface previously placed on the sample holder. The atoms/molecules are usually sent at a temperature slightly above the room temperature (< 350 K) and they reach the surface at an angle of either 40° or 57°, depending on the chosen beamline. The resulting kinetic energy perpendicular to the surface is therefore reduced. The beamlines are triply differentially pumped and aimed towards the sample holder. They are basically three vacuum chambers connected together by tight diaphragms of 3 mm diameter. Firstly, from an external vial containing the sample, the injection pressure is ≈ 1 mbar and we reach $\approx 10^{-5}$ mbar in the expansion chamber (first stage). The second stage is defined by a pressure of 10^{-8} and the flux arrives in the main chamber with an usual pressure increase of about few 10^{-11} mbar. The beamlines are always kept under vacuum and they can be detached and separated from the main chamber by two valves. Between the third diaphragm and the main chamber there is a mechanical chopper/plate, called "flag", that can be used to block or reduce the flux, depending on the type of experiment. In order to achieve atomic beams by injecting molecules through the beamlines, the latter are also equipped with a surfatron (microwave) cavity and a power supply (up to 300 W at 2.45 GHz). Each atomic beam is therefore produced by a RF (radio-frequency) dissociation of the molecules in a compressed-air Pyrex tube placed in the cavity in which a water circuit cools down the metallic parts. Decreasing the discharge temperature by creating a cold plasma is essential to avoid total recombination of the atoms. In fact, even though the dissociation rate is never 100%, it is possible to maintain the atomic beams over the whole experimental session. The dissociation rate is measured by the quadruple mass spectrometer in the main chamber and more details are given for each

experimental study (Chapters 4, 5, 6).
[Pirronello et al., 1997, Minissale, 2014, Grieco et al., 2024]

3.3 QMS and experimental methods (TPD and DED)

3.3.1 QMS

All the detections and results presented in the experiments of this Thesis are obtained through Quadrupole Mass Spectrometer (QMS) analyses. The QMS is made up of 3 main parts: an ionizer (an electron-bombarding system using thermal emission from a hot tungsten filament), a mass filter (discrimination zone) and the ion detector. When the molecules/atoms that we target to detect enter the QMS, they are firstly ionized and therefore accelerated toward the mass filter. This is composed of 4 metallic rods where voltage combination of direct and radio frequency components are applied between adjacent and opposite rods. This allows the species to be selected according to their mass charge ratio (m/z), which is technically fixed. The ion detector is a Channeltron (electron multiplier) that converts the output current into a digital signal. A software allows to monitor, record and follow the number of a given species arriving at the QMS. Together with the QMS, the Lakeshore temperature controller, which remotely controls and changes the temperature of the surface, can be launched, allowing more complex analyses. In particular, it is possible to study the dependence between the desorption temperatures of a species and the type of surface used for the experiments. The QMS is located on the top part of the chamber and it can be vertically translated in order not to interfere with the beam deposition on the surface (maintained above the surface) or moved at the same height as the beams and sample holder. It can also be rotated to allow detection of the beamlines themselves, their composition and possible dissociation rate, as well as the species desorbing from the surface, if it is moved to face the sample holder. In the upper position, the QMS is used to analyze the abundances of residual gases in the main chamber. Different types of experiments can be run by using the QMS, coupled with varying the temperature of the surface. The setups used in this study are TPD (Temperature Programmed Desorption) and DED (During Exposure Desorption) experiments.

3.3.2 TPD

Thermal Programmed Desorption is an important method to study thermal desorption of atoms and molecules from the sample holder. In TPD experiments molecules and atoms are deposited on the surface at a temperature low enough to unable their sticking. The

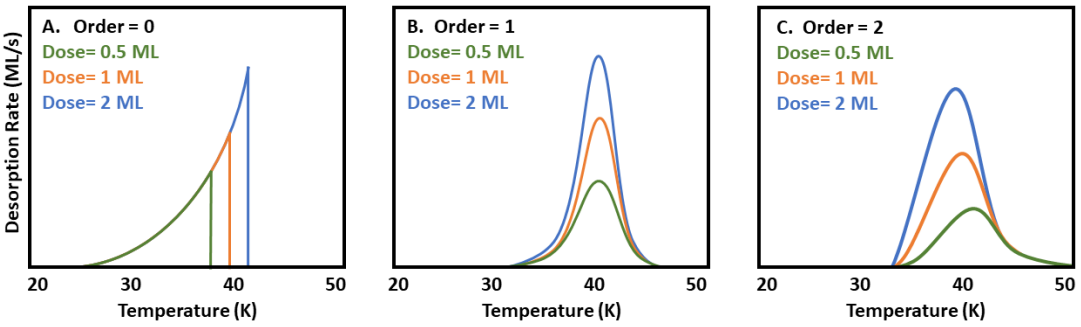

FIGURE 3.2: Representative thermal desorption profiles with varying initial surface coverage/dose.

system is afterwards heated with a linear ramp to observe the desorption of molecules from the sample surface. When the surface reaches a specific temperature (desorption temperature), the energy transferred to the adsorbed species causes their desorption into the gas phase. During the operated TPD experiments, the temperature T is increased linearly with time from the initial temperature T_0. Temperature and time are related by:

$$T = T_0 + \beta \cdot t; \tag{3.2}$$

Where $\beta = dT/dt$ is the heating rate in units of K/sec.

Different desorption profiles are possible, depending on the number of reactants necessary to activate the desorption (kinetic order). Figure 3.2 displays three different TPD profiles corresponding to the zero, first, and second order n of the desorption kinetics.
The typical zero order (n = 0) profile reflects a desorption that does not depend on the coverage. The first-order (n = 1) profile corresponds to the thermal desorption of molecules adsorbed on the surface, the desorption peak is asymmetric and its position does not change with the coverage. For the second order (n = 2) profile, the peak positions shift towards low temperatures when the coverage increases, the reaction rate is thus proportional to the concentrations of the reactants. More details about the desorption kinetics are given in the Desorption Section (2.1.3) of Chapter 2 and more practical specifics and examples are given in Chapter 4.

3.3.3 DED

In case of DEDs, we monitor the signal during the deposition phase with the QMS rotated to allow the beam to reach the sample and to have a certain detection of species already desorbing or reacting upon arrival on the surface. In general, DEDs are useful

when the species, arriving from the gas phase or newly formed on the surface, are unable to thermalize on the surface, and they are released into the gas phase. The best example is given for the formation of H_2 at high temperatures in Chapter 5.
[Abdi-Salam, 2019, Thanh, 2018, Minissale, 2014]

Chapter 4

Acetaldehyde binding energies: a coupled experimental and theoretical study

The following Chapter is taken from the first publication of this PhD Thesis [Ferrero et al., 2022]. For this study, several groups have collaborated in order to combine the expertise of LERMA-CYU in astrochemical experiments with their theoretical simulations (performed by Ferrero, S. at Universitat Autonoma de Barcelona) to draw important conclusions. The published paper is therefore divided in exactly two parts. This Chapter will report mainly on the experimental side of the article with a little section (4.5.3) dedicated to the comparison with the simulations run by Ferrero, S. This work can be seen as an important step in the PhD to gain knowledge in managing the FORMOLISM set-up, building the scientific independence for the next projects, being able to run experiments, getting the best results and analyzing data. This Chapter is also used to introduce and specify in more depth a few concepts already introduced previously in the manuscript: the importance of the pre-exponential factor in the Polanyi–Wigner equation, the difference among the possible interstellar ices structures and how to use the experimental results to extract BEs (binding energies) through fitting.

The undersigned PhD student has been the one performing the entire experimental procedure: protocols (together with Prof. F. Dulieu), experiments, fitting to extract the binding energies and results and their interpretation (together with the other co-authors of the paper [Ferrero et al., 2022]).

4.1 Abstract

Acetaldehyde is one of the most common and abundant gaseous interstellar complex organic molecules, found in cold and hot regions of the molecular interstellar medium. Its presence in the gas-phase depends on the chemical formation and destruction routes, and its binding energy (BE) governs whether acetaldehyde remains frozen onto interstellar dust grains or not. In this work, we report a combined study of the acetaldehyde BE obtained via laboratory TPD (Temperature Programmed Desorption) experiments and theoretical quantum chemical computations. BEs have been measured and computed as a pure acetaldehyde ice and as mixed with both polycrystalline and amorphous water ice. Both calculations and experiments found a BE distribution on amorphous solid water that covers the 4000–6000 K range, when a pre-exponential factor of $1.1 \times 10^{18} s^{-1}$ is used for the interpretation of the experiments. We discuss in detail the importance of using a consistent couple of BE and pre-exponential factor values when comparing experiments and computations and when introducing them in astrochemical models. Based on the comparison of the acetaldehyde BEs measured and computed in the present work with those of other species, we predict that acetaldehyde is less volatile than formaldehyde, but much more than water, methanol, ethanol, and formamide. We discuss the astrochemical implications of our findings and how recent astronomical high spatial resolution observations show a chemical differentiation involving acetaldehyde, which can easily be explained as due to the different BEs of the observed molecules.

4.2 Introduction

Acetaldehyde (CH_3CHO) was one of the first polyatomic molecules discovered in the interstellar medium (ISM) [Gottlieb, 1973, Fourikis et al., 1974]. It is a rather common interstellar molecule, found in warm and cold environments. For example, it is abundant in hot cores [e.g. Blake et al., 1987, Csengeri et al., 2019, Law et al., 2021] and hot corinos [e.g. Cazaux et al., 2003, Manigand et al., 2020, Yang et al., 2021, Chahine et al., 2022], protostellar molecular shocks [e.g. Lefloch et al., 2017, De Simone et al., 2020, Codella et al., 2020] and young disks [e.g. Codella et al., 2018, Lee et al., 2019]. Against the theoretical expectations, acetaldehyde is also present in cold prestellar cores [e.g. Bacmann et al., 2012, Vastel et al., 2014, Scibelli and Shirley, 2020]. Finally, acetaldehyde is detected in comets [Crovisier et al., 2004, Le Roy et al., 2015, Biver et al., 2021], where the measured relative abundance with respect to methanol is similar to that found in hot corinos [e.g. Bianchi et al., 2019, Drozdovskaya et al., 2019]. Several experimental and theoretical studies have focused on the acetaldehyde formation routes both in the gas-phase and on the grain-surfaces. Charnley [2004] first proposed that acetaldehyde is

synthesised in the gas-phase via the reaction of the ethyl radical (CH_3CH_2) with atomic oxygen (O). Subsequently, Skouteris et al. [2018] found that acetaldehyde could be a daughter of ethanol (CH_3CH_2OH), while Vasyunin et al. [2017] proposed a synthesis from methanol (CH_3OH) reacting with CH. Finally, publicly available astrochemical reaction networks [KIDA and UMIST: Wakelam et al., 2012, McElroy et al., 2013, respectively] also report an ionic route via the protonated acetaldehyde (CH_3CHOH^+), which is in turn formed from dimethyl ether (CH_3OCH_3) reacting with H^+. Vazart et al. [2020] has reviewed all these reactions from the theoretical and experimental point of view and concluded that only the first two routes are viable (i.e. involving CH_3CH_2 and CH_3CH_2OH, respectively), while the last two (i.e. those involving CH_3OH and CH_3CHOH^+) are inefficient in the ISM conditions. Finally, the observed correlation between the derived abundances of acetaldehyde and ethanol in warm and hot sources is in favor of acetaldehyde being the ethanol daughter [Vazart et al., 2020]. For the grain-surface formation routes, the situation is more debated. Since the end of the last millennium, experiments have found that acetaldehyde is formed in UV-illuminated ices consisting of water, CO, methanol and methane [e.g. Hudson and Moore, 1997, Bennett et al., 2005, Öberg et al., 2010, Martín-Doménech et al., 2020] or other components [e.g. Chuang et al., 2021]. Triggered by these experiments, Garrod and Herbst [2006] proposed the formation of acetaldehyde from the combination of the radicals HCO and CH_3 on the dust grain icy surfaces, when the grain temperature increases enough to make the two radicals mobile. However, a first study by Enrique-Romero et al. [2016] suggested that the reaction of the two radicals on an amorphous water ice surface actually does not end up into the formation of acetaldehyde but rather into carbon monoxide (CO) and methane (CH_4). Subsequent and more accurate studies confirmed that the acetaldehyde formation on amorphous water surfaces may or may not occur and is always in competition with the CO + CH_4 formation [Rimola et al., 2018, Enrique-Romero et al., 2019, 2020]. Similar conclusions were reached when considering the reaction on CO-rich ices [Lamberts et al., 2019]. Finally, the most recent theoretical study by Enrique-Romero et al. [2021] found that the efficiency of the formaldehyde formation by the coupling of HCO and CH_3 is a strong function of the grain temperature and the diffusion energies of the two radicals, with the possibility to being practically zero if their mobility is relatively large (i.e., a diffusion/BE ratio less than 0.3). In agreement with these theoretical predictions, a very recent and sophisticated study by Gutiérrez-Quintanilla et al. [2021] found no formation of acetaldehyde on an amorphous water ice enriched with HCO and CH_3. In their experiment, Gutiérrez-Quintanilla et al. [2021] trapped radicals, formed via photolysis of methanol ice, in an argon matrix at 14 K and identified them via Electronic Paramagnetic Resonance (EPR) spectroscopy. Once liberated from the matrix, the various radicals combined giving rise to several species, but not acetaldehyde. More

recently, non energetic processes on the grain surfaces have been found to possibly produce acetaldehyde in CO-rich ices [e.g. Fedoseev et al., 2022]. Adding confusion to this situation, Hudson and Ferrante [2020] noticed that the IR bands, on which the identification (frequencies) and quantification (band strengths) of acetaldehyde in the various experiments relied, were often incorrect. Finally, this work also emphasized the almost impossibility for astronomical observations to be able to identify frozen acetaldehyde. Whatever the formation mechanism, either in the gas-phase or on the grain surfaces, acetaldehyde would freeze onto the cold dust grain mantles and would be removed from them only when the dust temperature reaches the acetaldehyde sublimation temperature, which is governed by its binding energy (BE: sometimes it is also called desorption energy) to the water ice, and its pre-exponential factor (see the Section 4.5.1). Please note that the sublimation temperature can be reached due to both thermal and non-thermal processes, such as the desorption caused by the interaction of the cosmic-rays, which permeate the Milky Way, with the dust grains. In the latter case, for example, only a fraction of the grain is heated up and acetaldehyde would be desorbed if the reached temperature is larger than its sublimation temperature. Therefore, in practice, whether acetaldehyde is in the gas-phase (where it can be observed via its rotational lines) or frozen onto the grain mantles (where it has not been detected so far) is completely governed by its BE. Moreover, BE always enters in an exponential form, so that its accurate estimation is essential to properly assess whether and how much acetaldehyde would be gaseous. So far, there are very few specific studies on the acetaldehyde BE. To our best knowledge, Wakelam et al. [2017] is the first theoretical study, but it only considered one water molecule to simulate the interstellar water ice. These authors found a BE equal to ∼5400 K. Recently, Corazzi et al. [2021] reported an experimental study of the BE on olivine surfaces covered by an ice of pure acetaldehyde or mixed with water. They found that the acetaldehyde BE on a mixture of iced water-acetaldehyde is 3079 K, substantially different from the Wakelam et al.'s estimate. In a very recent combined theoretical and experimental study, Molpeceres et al. [2022] obtained, for the desorption of acetaldehyde on non-porous amorphous solid water surfaces, the values of 3624 and 3774 K, respectively. These values are relatively similar to the Corazzi et al's value, but still far from that of Wakelam et al.'s one. There is, therefore, a need to clarify the origin of this difference as well as to improve both experimental and theoretical estimates. In this work, we combine state-of-the-art experimental (temperature programmed desorption, TPD) and theoretical (quantum chemical computations) techniques with the aim to provide possibly the most accurate estimate of the acetaldehyde BE on water ice, simulating at best the ISM conditions.

4.3 Methods: FORMOLISM configurations and experimental protocols

For the specific purposes of this study, the sample holder, hosted in the UHV chamber and connected to the cryostat, has been covered with a highly oriented pyrolytic graphite (HOPG, ZYA-grade) sample. The HOPG is a model of an ordered carbonaceous material, carbon atoms in a hexagonal lattice, mimicking some aspects of interstellar dust grain analogues. The HOPG grade (10 mm diameter-2 mm thickness) was firstly dried in an oven at about 100°C for two hours, and then cleaved several times in air using the "scotch tape" method at room temperature to yield several limited defects and step edges [Chaabouni et al., 2020]. The HOPG was glued directly onto the copper finger and dried in ambient conditions for about an hour before inserting it in the chamber and closing the set up. Once high vacuum is reached ($<10^{-7}$ mbar) in few minutes the sample is dried under vacuum during 3 hours at 350 K. Then the HOPG sample and the whole system is baked out at 100°C for a few days in order to remove any adsorbed contaminants and to reach the UHV base pressure. Before starting any experiment, the system is slowly heated up to 720 K to maximise the degassing rate and ensure a very clean sample surface. The CH_3CHO (Sigma Aldrich, purity higher than 99.5%) molecular beam is prepared in a triply differentially pumped beam-line aimed at the sample holder. It is composed of three vacuum chambers connected together by tight diaphragms of 3 mm diameters. Molecular pressure injected in the gas line is of about 1.4 mbar. In the expansion chamber (first stage) the pressure is in the 10^{-5} mbar range, while in the main chamber the rise of the pressure is not measurable ($<10^{-11}$ mbar). The CH_3CHO on HOPG experiments have been used as reference and preliminary studies before investigating the desorbing behaviour of the molecule on two different D_2O ice substrates formed on the sample. In this study, we have deposited CH_3CHO molecules on HOPG by using only one beam-line oriented at 57° relatively to the surface of the sample, while D_2O ice films have been deposited on HOPG by using a separated channel and a micro-capillary array doser moved close to the sample holder. It allows to control the ice deposition rates and to avoid to raise the pressure in the whole chamber. The two different D_2O ices are, respectively, compact non-porous amorphous deuterated water (ASW-c) and (poly)crystalline deuterated ice (PCI). ASW-c is formed when the sample is held at 110 K, while PCI layers have been formed by depositing D_2O at 110 K, heating until 150 K with a ramp rate of 5 K/min and waiting for few minutes to be sure that the crystallization has happened, as detected by the change in the desorption rate [Speedy et al., 1996]. For both ices, about 30 monolayers (ML) have been deposited on HOPG while the pressure in the main chamber never exceeded 5×10^{-8} mbar. After the CH_3CHO deposition phase at 45 K, we used the TPD technique by warming-up the

sample and detecting the desorbing species from the surface through mass spectrometry. TPD were obtained from 45 to 220 K for the CH_3CHO on HOPG experiments and only to 140 K for the CH_3CHO on water ice ones, in order to avoid D_2O desorption after 150 K. In all cases, a linear heating rate of 12 K/min has been programmed to heat up the sample. Because of the poor thermal contact between the sample holder and the copper block, the temperatures registered during the TPD were re-calibrated by depositing different gases of known BEs (O_2, Kr, D_2O). The accuracy is about 1 K for the values of temperature below 125 K and 0.2 K for the ones above. The actual new ramps obtained after calibration are taken into account in the simulations and analyses. With the QMS, the same molecule can be detected in different m/z corresponding to the fragmentation of the parent molecules after the electron impact (here at 30 eV). The main fragments under study here are m/z=44 (molecular mass of CH_3CHO^+) and m/z=29 (HCO^+, the main fragment of acetaldehyde). The desorption and degree of crystallization of D_2O ice films have been followed through the signal of m/z=20.

4.4 Experimental Results

Experiments on HOPG have been used mainly as reference, in order to understand the behavior of the acetaldehyde adsorption and the deposition time needed to have a monolayer on the substrate. Seven measurements corresponding to increasing deposition times (1, 1.5, 3, 4, 5, 6, 12 minutes) have been carried out on HOPG to study the evolution of the TPDs from a sub-monolayer regime to a multilayer one. Figure 4.1 shows only four TPD curves belonging to four different deposition times using the same first stage pressure to introduce a constant flux of CH_3CHO in the system. There are two main features appearing in the graph: a low temperature peak between 105-110 K, and a second peak centered around 117.5 K. At low deposition times, only the peak at higher temperature appears (black and red curves corresponding to 1.5 and 3 minutes). It initially increases in intensity with coverage but saturates for longer depositions. After 6 minutes of deposition, the low temperature peak clearly appears. The TPD after 12 min deposition shows both peaks equally intense, although the low temperature peak is slightly broader. The high temperature peak is attributed to the sub-monolayer regime and is first populated, and, when the monolayer is saturated and the multilayer regime starts, the second peak at lower temperature appears. By following the TPD experiments on HOPG, a monolayer of molecules on the substrate is believed to form after $\approx$ 4 minutes of deposition. We define this time to calibrate the rest of the analyses. As HOPG and ASW-c have about the same surface density of sites, the same time deposition is used to characterise the coverage on ice, and to derive the BEs of CH_3CHO as a function of the coverage. In order to derive the BEs on HOPG and on

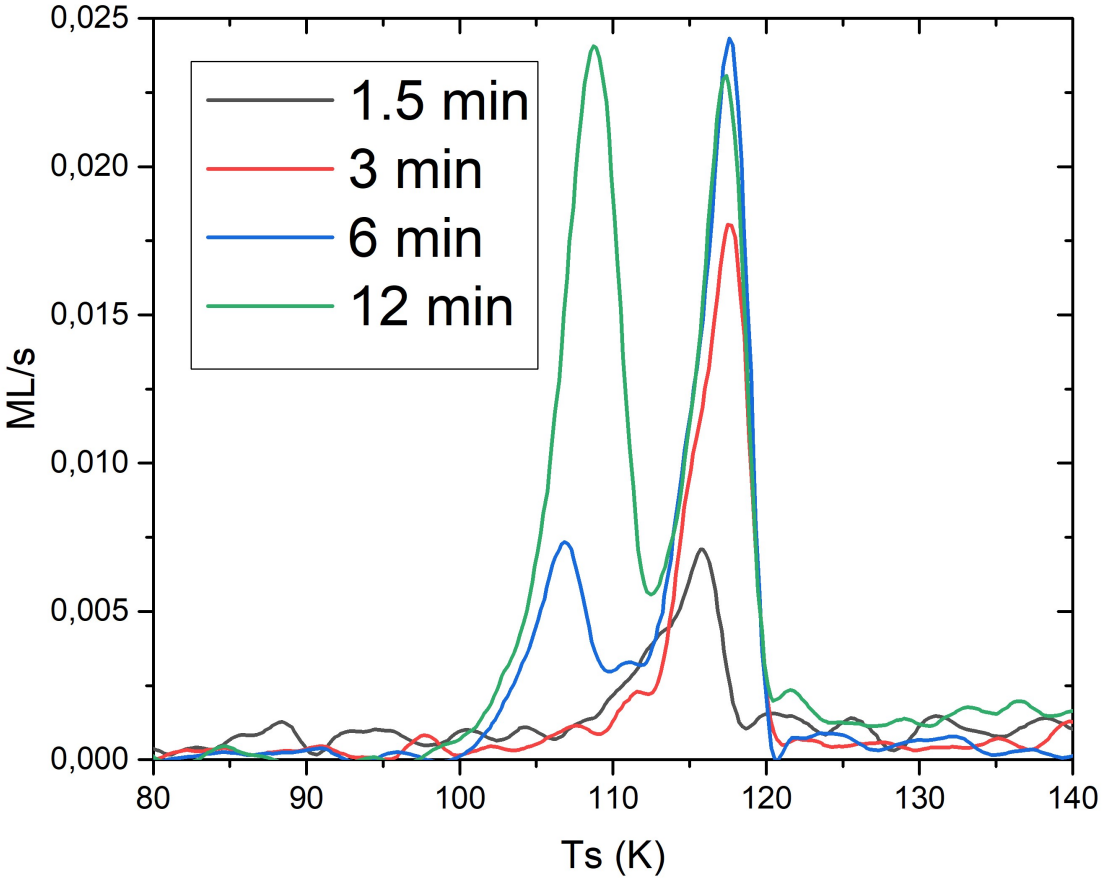

FIGURE 4.1: Set of four smoothed TPDs (m/z=44) for different time depositions of acetaldehyde on HOPG: 1.5 min (0.4 ML), 3 min (0.8 ML), 6 min (1.7 ML), 12 min (3.3 ML).

the two different ices, the three TPDs for the 4 min depositions on HOPG, ASW-c and PCI have been selected. By proceeding this way, the interaction between a monolayer of deposited CH_3CHO and each substrate can be studied. Figure 4.2 shows the results for one of them, i.e., the experiment of 4 min deposition of CH_3CHO on PCI, and the simulation obtained by fitting the data. The procedure is detailed in Chaabouni et al. [2018]. The calculation uses eleven independent TPDs, starting from 4500 K, with an energy gap between each TPD of 150 K (i.e. 4500, 4650, 4800 K...). Each individual TPD is calculated using simple Arrhenius kinetics, named the Polanyi-Wigner equation:

$$r(T) = -\frac{dN}{dT} = AN^n \exp\left(-\frac{E_{des}}{T}\right) \tag{4.1}$$

where $r(T)$ is the desorption rate (in ML s^{-1}), N is the number density of molecules adsorbed on the surface (ML), and n is the order of the desorption equal to 1 in our case. A is the pre-exponential factor (s^{-1}), T is the temperature of the surface (in K), and E_{des} is the activation energy for desorption (in K). If there is no reorganisation of

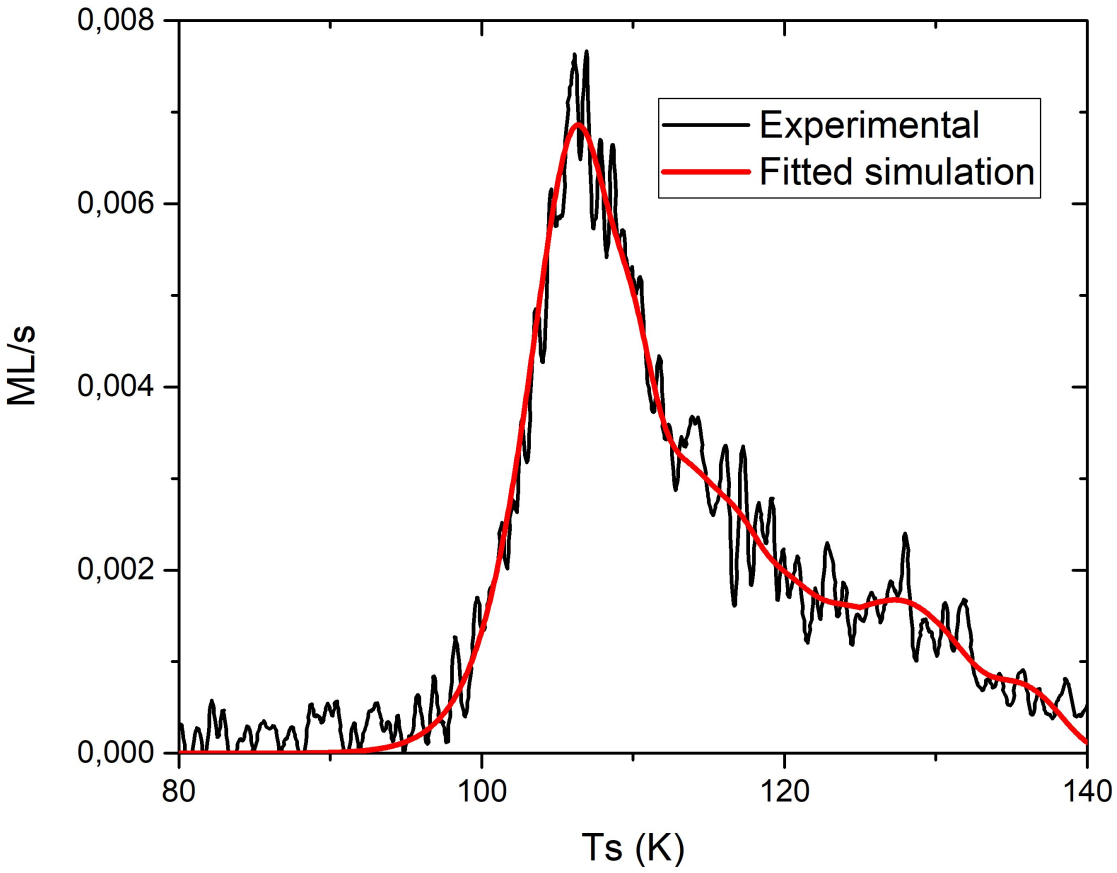

FIGURE 4.2: Simulation of eleven TPDs (red line) used to fit the experimental TPD (black line, raw data not smoothed) obtained from 4 min (1 ML) of CH_3CHO deposition on PCI (pre-exponential factor=1.1×10^{18} s^{-1}, E_{min}=4500 K, E_{max}=6000 K by steps of 150 K).

the surface[1], E_{des} is equal to BE. First order desorption TPD profiles are independent of the surface population, so that each independent BE can be weighted, and finally a distribution of BEs can be found. We have set the pre-exponential factor at 1.1×10^{18} s^{-1} (see the Section 4.5.1). The arbitrary choice of binning the energy distribution (basis of eleven BEs) has been optimized with the aim to have a good fitting of all the three experiments under analysis. Figure 4.2 gives a qualitative idea of the simulation for the case of the PCI substrate. The best values found for the eleven TPDs, also known as energy distribution set for each substrate, are reported in Table 4.1. The values are here expressed as a function of the population, in percentage, having that specific BE. We estimate the accuracy of the method to be around a few percents, mostly due to the noise-to-signal ratio and the presence of a small background noise.

The three energy distributions are displayed in Fig. 4.3. We omit the populations below 4 percents. One can observe the main differences because of the different substrate. For HOPG, there is not an actual distribution, but it rather shows almost only two main

[1]This is 100% true on graphite, but this is an assumption/approximation in case of acetaldehyde on water.

TABLE 4.1: Desorption energy values of the eleven simulated TPDs obtained for three sets of 4 min CH_3CHO depositions: on HOPG, ASW-c and PCI (pre-exponential factor:1.1×10^{18} s^{-1}).

	HOPG	c-ASW	PCI
E_{des} (K)	Population (%)	Population (%)	Population (%)
4500	0	0	< 4
4650	10	16	28
4800	0	32	27
4950	0	10	12
5100	34	12	12
5250	66	7	9
5400	0	8	6
5550	0	9	6
5700	< 4	6	8
5850	< 4	7	< 4
6000	< 4	< 4	< 4

energy values, which are associated with the sub-monolayer regime (at 5100–5250 K). As can be noticed by the 10% population at 4650 K, for the 4 min depositions the multilayer regime slightly started already. This is in agreement with the accuracy of the determination of the flux, which is usually estimated around 15%. The distributions of BEs of CH_3CHO on ices present different characteristics, signature of the more disordered nature of water ice (even for the PCI case). There is a larger distribution of population covering almost all the possible energy values proposed by the simulation. The ASW-c substrate presents the largest distribution of BEs. The energy distribution histogram associated with the desorption of CH_3CHO on PCI presents, instead, a more peaked distribution towards lower values of energy (mainly below 4900 K). This is due to the reduced number of combination of water molecules on the surface. The disorder here is provoked by the possibility of having an O or an H in the vicinity of the adsorption sites, even if the collective structure is cubic. On the contrary, ASW-c have a more disordered nature and, accordingly, the adsorption sites may have a more variable number of water molecules strongly interacting with CH_3CHO (see below). Finally, we calculate the weighted average for each case to estimate the difference in BEs for the different substrates. We obtain the following result: 5150 K for HOPG (range: 4650–5250 K), 5080 K for ASW-c (range: 4650–5850 K) and 4990 K for PCI (range: 4650–5700K). This corresponds to what one can expect by looking at the trend in the desorption profiles.

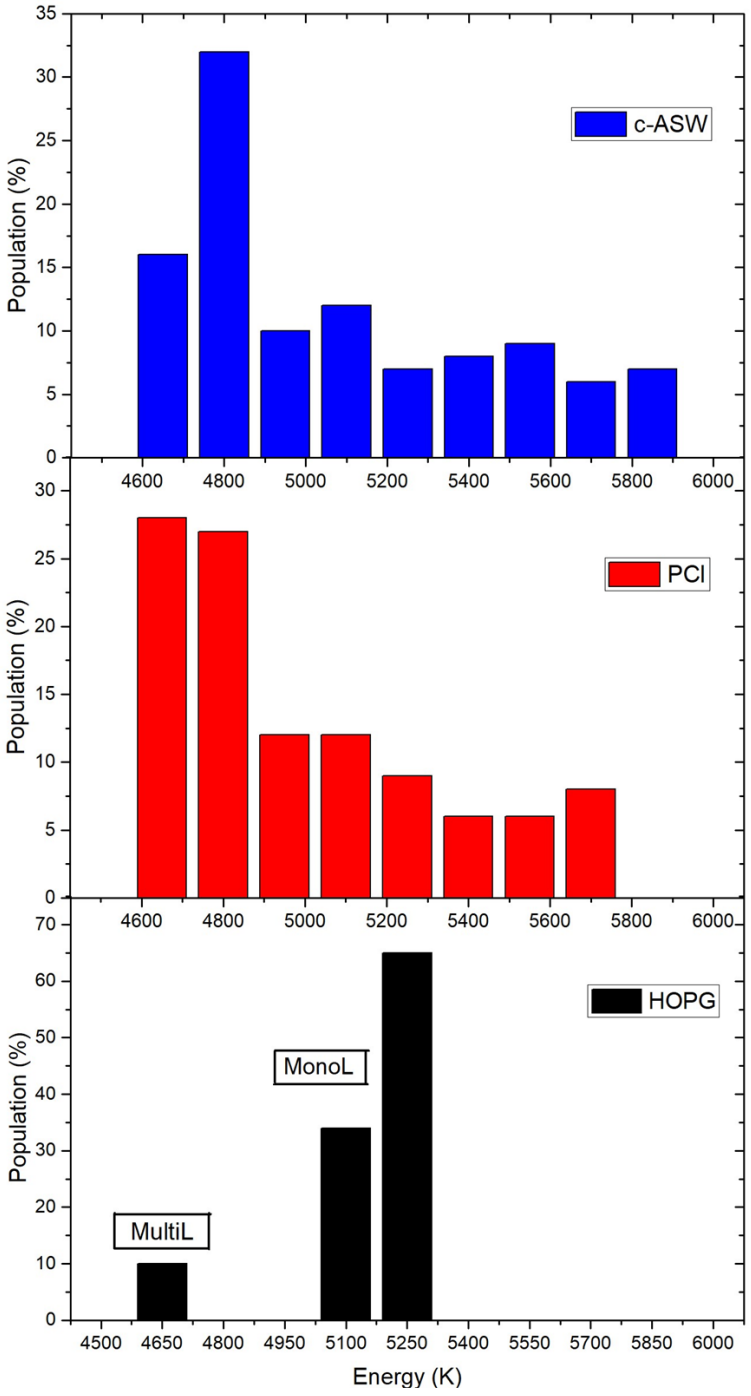

FIGURE 4.3: Energy distributions of eleven simulated TPDs for the 4 min CH_3CHO depositions on HOPG, ASW-c and PCI taken from Table 4.1.

4.5 Discussion

4.5.1 The importance of the pre-exponential factor

Experiments do not directly measure a desorption energy, but a desorbing flux, and, by applying the Polanyi-Wigner equation, a BE is derived (which is supposed to be equal to the desorption energy in most of the cases). However, to do so, one needs to set a value for the pre-exponential factor, since the equation has two parameters: the pre-exponential factor A and the binding energy BE (if the desorption order is set to n=1). Here, following the recommendation by Minissale et al. [2022], we adopt the derivation of the pre-exponential factor based on the Transition State Theory (TST). This theory takes into account both the rotational and translation partition functions of the desorbing molecules and, therefore, allows including in the calculation of the pre-exponential factor, A_{TST}, the entropic effect associated with the kinetic desorption rate. We briefly describe the salient points of the calculation of A_{TST} [more details can be found in Tait et al., 2005]. We used the following formula:

$$A_{TST} = \frac{k_b T}{h}\frac{q^{\ddagger}}{q_{ads}} = \frac{k_b T}{h}\frac{A}{\Lambda^2}\frac{\sqrt{\pi}}{\sigma\, h^3}(8\,\pi^2\,k_b\,T_{peak})^{3/2}\,\sqrt{I_x\,I_y\,I_z} \tag{4.2}$$

where q_{ads} and $q^{\ddagger}$ are single-particle partition functions for the adsorbed (initial) state and the transition state, respectively, calculated at the temperature T_{peak}. A is the surface area per adsorbed molecule. Here, like in other experiments or computational studies, it is fixed to $10^{-19}m^{-2}$ (the inverse of the number of surface sites per unit area). I_x, I_y, and I_z are the principal moments of inertia for the rotation of the particle, obtained by diagonalizing the inertia tensor of the free acetaldehyde. They are fixed to I_x = 52.46, I_y = 46.86, I_z = 8.78 amu Å^2. The symmetry factor, σ, is the number of different but indistinguishable rotational configurations of the particle and it is fixed to 1 in the case of acetaldehyde (as it belongs to the C_s symmetry point group). The thermal wavelength of the molecule, Λ, depends on its atomic mass (44 amu) and on the peak of the desorption energy (T_{peak}=115 K), and it is 24.5 pm. By using these parameters, A_{TST}=1.07 $\times$ 10^{18} s^{-1}. it is important to emphasize, however, that A_{TST} is a function of T_{peak}. As shown in Figure 4.1, the temperature of the peak depends on the surface coverage. For example, when using T_{peak}=108 K, A_{TST} is equal to 8.58 $\times$ 10^{17} s^{-1}, while fixing T_{peak}=117 K then A_{TST}=1.13 $\times$ 10^{18} s^{-1}. In this study, we choose A_{TST}=1.1 $\times$ 10^{18} s^{-1}, which is the average value.

Often, the pre-exponential factor is calculated using the harmonic oscillator approximation introduced by Hasegawa et al. [1992] and here called A_{HH}:

$$A_{HH} = \left(\frac{2\ n_s\ BE}{\pi^2\ m} \right)^{1/2} \tag{4.3}$$

where n_s is the surface density of sites and m is the mass of the adsorbed species. Using this approximation, which does not take into account the fact that the molecule adsorbed does not rotate whereas the desorbed one does, we find $A_{HH} = 1.3 \times 10^{12}$ s^{-1} if we choose an arbitrary value of BE=4500 K. In addition, in the Hasegawa et al. [1992] formulae, the value of A_{HH} depends exclusively on the BE of the adsorbate and is calculated directly from it, so that, in the models, there is a unique parameter, BE, and not the A and BE pair, as determined in experiments. We stress that the chosen pre-exponential factor A can strongly affect the BE value determined using the TPD technique, since they are actually coupled and are somewhat degenerated (monotonic). To compare the values obtained with different pre-exponential factors A, we can re-scale the BE values using A_{HH} and the following formula:

$$BE_{HH} = BE_{TST} - T_{peak}\ ln(A_{TST}/A_{HH}) \tag{4.4}$$

where BE_{HH} and A_{HH} (BE_{TST} and A_{TST}) are the pair BE and pre-exponential factor calculated with the harmonic oscillator approximation of Hasegawa et al. [1992] or the TST proposed by Tait et al. [2005]. One has to consider that a full quantum mechanical (QM) evaluation of the pre-exponential factor can be derived by the statistical mechanical treatment as in the transition state theory, considering the availability of the harmonic frequencies for all involved systems.

4.5.2 Comparison with previous experimental estimates

Now we have a tool to compare BE provided by different values of pre-exponential factors. Corazzi et al. [2021] recently reported an experimental value of BE=3100 K of acetaldehyde co-deposited with water on a substrate made of micrometer-sized olivine grains. It obviously differs from the measured values here and it is less than any calculated value. However, these authors used a fixed value of A=10^{12} s^{-1}. To be able to compare with our results, we use the BE_{HH} equation (4.4) and find that the couple BE=3079 K and A=$10^{12} s^{-1}$ corresponds to the couple BE=4680 K and A=1.1×10^{18} s^{-1}, that is exactly what has been found here for the multilayer energy of acetaldehyde. This example shows us how important is to take into account not only the BEs, but also the pre-exponential factor that allows us to calculate a desorption flux, to reproduce experiments or to simulate the desorption in ISM conditions.

4.5.3 Comparison of experimental and theoretical results

The aim of this section is to compare the experimental and theoretical approaches in order to give an idea on how the experimental results obtained through this study relate to the theoretical calculations run by Ferrero, S. (see Ferrero et al. [2022]). This will be done for the pure acetaldehyde, crystalline and amorphous water ices, separately. Before going into the comparison itself, it is important to give an overview of the computational methods.

Simulations of the adsorption of an acetaldehyde molecule on crystalline and amorphous ice models, as well as a component of a pure acetaldehyde surface have been carried out in order to i) gain insights of the adsorption process at an atomic level, and ii) calculate BEs of the species on ices with the purpose to make comparisons with TPD experiments. All the calculations were performed by Ferrero, S. with the ab initio CRYSTAL17 code [Dovesi et al., 2018]. The code can simulate any kind of system, from non periodic molecules to full periodic 3D crystalline systems, employing atom centered Gaussian basis sets for the description of the electronic structure. In this work, they carried out DFT-based static optimizations using the BFGS optimization algorithm, relaxing both the cell parameters and the atomic positions. These calculations were performed with the PBEsol0-3c functional [Doná et al., 2019], which makes use of an Ahlrichs' polarised valence-single zeta basis set in order to reduce the computational cost. Then, on the PBEsol-3c optimized geometries, single point energy calculations were carried out with the B3LYP functional [Becke, 1993, Lee et al., 1988] added with the Grimme's D3(BJ) correction (to account for dispersive forces [Grimme et al., 2010, 2011]) with the aim to refine the BEs at a higher level of theory. These refinement calculations have been performed using an Ahlrichs' VTZ basis set added with a double set of polarization functions. For the sake of accuracy, the calculations carried out with the B3LYP-D3(BJ) method have been corrected for the basis set superposition error (BSSE), adopting the *a posteriori* counterpoise correction.

Vibrational harmonic frequencies were calculated at the PBEsol0-3c level using a finite differences method. A partial Hessian approach was used to reduce the computational cost of the calculations. Thus, the vibrational frequencies were calculated on the optimized geometries only for a fragment of the entire system, which included the acetaldehyde molecule and the closest water molecules interacting with it. From this vibrational frequency calculations, the zero point energy (ZPE) correction terms were included in the calculations of the BEs.

The crystalline and amorphous water ice surface models used in this study have already been described in Ferrero et al. [2020].

Since the crystalline structure of pure acetaldehyde is not available yet, in order to simulate a pure acetaldehyde slab they resorted to the crystal structure prediction algorithm.

First, the acetaldehyde molecule was optimized in gas phase with the B3LYP-D3(BJ) method combined with the optimized def2-SVP basis set with the Gaussian 09 [Gaussian09, 2009] program. This gas-phase optimized structure was used as input parameter to derive the pure acetaldehyde periodic solid state structures, which was achieved by using the programs of DFTB+ (version 20.2.1) [Hourahine et al., 2020] including Self Consistent Charge [Elstner et al., 1998] and the D4 dispersion model by Grimme [Caldeweyher et al., 2019, 2017], and VASP 5.4.4 [Kresse and Hafner, 1993, 1994, Kresse and Furthmüller, 1996,] using PAW PBE pseudopotentials [Kresse and Joubert, 1999]. Solid-state structure prediction was performed using the USPEX (version 10.4.1) evolutionary algorithm [Lyakhov et al., 2013, Oganov and Glass, 2006, Oganov et al., 2011], with embedded the topology crystal structure generator [Bushlanov et al., 2019], employing the DFTB+ code for geometry optimizations. The first generation of crystal structures were randomly generated, while subsequent generations were obtained by applying the genetic algorithm embedded in USPEX coupled with different variation operators, in particular rot-mutation and lattice mutation. The search space was limited from 1 to 4 molecules per cell. Calculations proceeded for 23 generations and 570 structures, in which USPEX identified the best structure, which contains 2 molecules per cell and a final volume of 118.77 $Å^3$. Since periodic DFTB+ calculations tend to excessively shrink the unit cell, subsequent calculations with USPEX but this time employing VASP calculations were performed using as initial seeds the best structures found by DFTB+. This proceeded for 28 generations and 723 structures, resulting in the final optimized structure characterized by a = 4.960 Å, b = 5.655 Å, c = 4.536 Å, and α = 89.55°, β = 89.70°, γ = 127.17° (with a final volume of 127.17 $Å^3$) The resulting bulk structure has been optimized at the PBEsol0-3c level. Once we obtained the bulk, we cut it along the (010) direction to obtain a 2D periodic slab model, which does not posses a large dipole along the non periodic direction.

4.5.3.1 Pure acetaldehyde ice

By comparing theory with experiments, in general, we compare a static and "unimolecular" calculation with a measurement that is both dynamic and averaged over a large population and a large number of situations. For the pure acetaldehyde ice, experiments provide a BE of 4650 K (MultiL value visible in Fig. 4.3), while calculations dealing with the ideal model of a molecule above the acetaldehyde surface gives a BE of 2650 K. Given the robustness of the measurement [confirmed by Corazzi et al., 2021], one would conclude that what is measured does not correspond to what is calculated. In reality, when a molecular film is heated, it will constantly reorganise itself, and the situation of a molecule on top of the surface is not the most energetically stable configuration.

The other extreme case corresponds to the calculation of the BE of one acetaldehyde molecule extracted from the surface slab, which is 5692 K. We thought that this last computed value is probably overestimated with respect to the experimental BE, as we only focused on the process occurring at the rather stable surface without considering more defective surfaces, from which the desorption can occur from kink and edges leaving the molecule less engaged with the underneath layers. As a first conclusion, therefore, it can be said that the calculations presented in Ferrero et al. [2022] provide good high and low boundary values to the experimental results, but that the dynamic (in the case of experiments) versus the static (in the case of calculations) nature can make any direct comparison somewhat misleading.

4.5.3.2 CH_3CHO desorbing from crystalline water ice

Although in Ferrero et al. [2022] we provide two BE values because of the use of two different unit cell sizes (i.e., 1x1 and 2x1 supercell), here, for the sake of comparison with experiments, we took the value of BE=5194 K obtained using the 2x1 supercell, as it is more realistic. In experiments, we find a distribution of BEs. It is not a bias of the method, as it was possible to derive a unique value of the BE for the HOPG surface. Actually, in experiments, even for a PCI, the surface is disordered. Indeed, the water molecules at the outermost positions of the surface almost randomly alternate dangling hydrogens pointing outside or inside the solid. Therefore, even for crystalline water ice, distributions of BE are usually measured whatever is the adsorbate [Amiaud et al., 2007, Noble et al., 2012, Nguyen et al., 2018]. The calculations, made on a perfectly regular or periodic crystal, are not able to reproduce this disorder. In experiments, the largest population is found for BE=4650 K and it corresponds to the BE of an acetaldehyde multilayer. This means that CH_3CHO molecules prefer to rearrange themselves, probably creating some sort of small clusters, rather than spreading over the surface. In other words, acetaldehyde does not "wet" properly the water ice surface. The low coverage values, which correspond more to the calculations made for a unique molecule, lay between 4950 and 5700 K. This is in excellent agreement with the calculated value of BE=5194 K. We note that the population at 5700 K could also correspond to defaults or steps in the poly-crystalline assembly.

4.5.3.3 CH_3CHO desorbing from amorphous water ice

Both experiments and calculations show a broad distribution of BEs. Calculations demonstrates that, compared to the crystalline case, some sites are more energetically favorable (two over nine), one is about equal, and the other six are less favorable sites

for adsorption. There is no doubt that such less bounded sites exist, but in experiments they will not be populated, as molecules reorganise during the heating phase and tend to occupy the available most favourable adsorption sites. This has been well experimented and documented as the "filling behaviour", for relatively volatile substances [Kimmel et al., 2001, Dulieu et al., 2005]. In the experiments, for all adsorbates, the minimum BE measurable is set by the limit of the BE of the multilayer. This is why we observe that half of the population of acetaldehyde desorbs from sites with a BE very close to that of pure CH_3CHO films. Indeed, this accumulation at the lower part of the BE distribution corresponds, in the calculations, to the six (out of nine) sites that have a BE lower than 4650 K (the multilayer limit). Once again, we find here that the theoretical calculations are in very good agreement with what is obtained experimentally. They show perfectly the extent of the distribution (up to 6000 K), and propose a good sampling of sites. Finally, we point out here that we do not observe any co-desorption of acetaldehyde with water. All the acetaldehyde desorbs prior to the water. This is consistent with the rather low values of BE calculated for the interaction with water, lower than the multilayer BE measurements of the acetaldehyde film alone. This molecule would somehow have a low hydrophilic character.

4.5.4 Comparison of the acetaldehyde BE with those of other important interstellar molecules

The detailed calculations and measurements of the acetaldehyde BEs on water ices show a consistent but complex picture. First, as already reported in other works [e.g. Dulieu et al., 2005, Ferrero et al., 2020], BE on an icy surface is not a single value, but there is rather a distribution of BEs caused by the different sites to which acetaldehyde can be adsorbed. Second, using the BE values without paying attention to its associated pre-exponential factor can lead to inconsistencies, if not mistakes. That being said, most of the astrochemical models use a single value of BE and the A_{HH} pre-exponential factor, which is not a guarantee of correctness. Another question is: which single value of BE to choose from the observed distribution? To choose a single value in the distribution, one needs to know the nature of the ice, for instance, if the surface will be fully or partly covered. Acetaldehyde is a frequently observed molecule in the gas phase, but it has not been detected yet in the ice mantles because its concentration is probably low (but see also the discussion in the Introduction (4.2)). Therefore, the coverage of this molecule on the surface of icy grains should remain low and the low coverage side of the distribution shall be preferred. Moreover, the interval of values that we propose overlaps the BE extrapolated by Wakelam et al. [2017] (5400 K), which turns out to be correct if one adopts the pre-exponential factor of $A=1.1 \times 10^{18}$ s^{-1}. However, if the astrochemical

model uses the harmonic oscillator approximation and a value of $A_{HH} \sim 10^{12}$ s^{-1}, a value around 3800 K shall be preferred. The advantage to use the couple BE=5400 K and A=1.1 $\times$ 10^{18} s^{-1} is that one can then compare this BE with that derived by the theoretical calculations and to the already published BE values of other molecules [Minissale et al., 2022].

4.5.5 Astrochemical implications

From an astrochemical point of view, two points are particularly relevant. The first point regards the presence of acetaldehyde in cold ($\sim$ 10 K) objects [e.g. Bacmann et al., 2012, Vastel et al., 2014, Scibelli and Shirley, 2020, Zhou et al., 2022]. The relatively large BE (4800–6000 K) makes it difficult to explain the presence of gaseous acetaldehyde if formed on the grain-surfaces, and would rather favor a gas-phase formation. Of course, this may just move the problem of the presence of the reactants needed to synthesize acetaldehyde from them, namely ethyl radical and/or ethanol. Non-thermal mechanisms could be at play such as cosmic ray bombardment that would not be chemically selective (Dartois et al. [2019]), whereas the chemical desorption initiated by hydrogenation on the grain surface may have different efficiencies depending on the molecule [Minissale et al., 2016]. As written in the Introduction, the BE of a given species determines at what temperature the species remains adsorbed or goes to the gas-phase. In hot cores/-corinos, several species, including acetaldehyde, have a jump in the abundance in the region where the dust temperature reaches about 100 K. This is believed to be caused by the sublimation of the frozen water [e.g. Charnley et al., 1992, Ceccarelli et al., 2000, Jaber et al., 2014], which is the major constituent of the icy grain mantles [e.g. Boogert et al., 2015]. However, the analysis of the emission lines of different species and their spatial distributions sometimes suggest that there is a differentiation in the sublimation of different species [e.g. Manigand et al., 2020, Bianchi et al., 2022]. The recent study by Bianchi et al. [2022] definitively shows a chemical differentiation between the two hot corinos of the SVS13 protobinary system. Specifically, the analysis of the high spatial resolution ALMA observations leads to the conclusion that gaseous acetaldehyde and formamide (NH_2CHO) are distributed in an onion-like structure of the hot corino, with formamide becoming abundant in a warmer region with respect to the acetaldehyde region. A natural explanation of this behavior is that species with larger BE emit lines (mostly) in more compact regions, i.e., the region corresponding to their sublimation temperature, rather than the water sublimation front, because the large densities ($\geq 10^8$ cm^{-3}) make those species freeze-out back very quickly. Therefore, given their respective BEs, acetaldehyde is emitted in a region more extended and colder than that of formamide.

More in general, by considering their respective BEs, formaldehyde and acetaldehyde would desorb before water, ethanol and methanol with water, but formamide has to wait for higher average temperatures, given its much higher BE. Our new estimates of the acetaldehyde BE, slightly lower than water, would suggest that acetaldehyde should be found approximately in the regions where water and methanol are present too, which is what has been so far found [Bianchi et al., 2022]. On the contrary, formamide has definitively a larger BE range, so that we predict formamide to originate in a hotter region than that of acetaldehyde, which is indeed what is observed in the few cases where a similar analysis has been carried out [e.g. Csengeri et al., 2019, Okoda et al., 2021, Bianchi et al., 2022].
In summary, with the high sensitivity of the new present facilities, such as ALMA and NOEMA, very likely studies revealing a differentiation in the chemical species in hot cores/corinos will become more an more available. We need to be prepared with studies similar to the one reported here, where the BEs of more complex organic molecules are estimated, so that we can appropriately interpret the astronomical observations. In turn, those observations can help to validate our methods, for which so much uncertainty still persists.

4.6 Conclusions

In this Chapter the TPD experiments of the acetaldehyde BEs are presented on a pure acetaldehyde ice, and on crystalline and amorphous water ices. The main conclusions of this work are the following:

- The experiments indicate that the acetaldehyde BE has a distribution of values. In the acetaldehyde ice, the BE has two main energy values, at about 4650 and 5250 K, with the peak around 5250 K being about ten times more frequent. In crystalline water ice, the BE ranges between about 4600 and 5700 K, with a peak around 4600–4800 K. In amorphous water ice, the BE ranges between about 4600 and 5900 K, with a peak around 4800 K. The weighted average in the three cases are 5150, 5080 and 4990 K, respectively.

- The theoretical calculations give BE values on the different sites of the used ice model. BEs spread over 5194 and 7253 K in the case of crystalline ice, and 2809 to 6038 K in the case of amorphous ice. In the pure acetaldehyde ice, two extreme values of 2650 and 5692 K are obtained.

- We discussed and showed the importance of the pre-exponential factor when deriving, comparing and using BE derived from experiments and theoretical calculations. Remarkably, when the correct pre-exponential factor is used with the derived BE, experiments and theory are in fair good agreement.
- A comparison of the derived acetaldehyde BEs with those of other important species shows that acetaldehyde would desorb at temperatures lower than those at which water desorbs and even lower temperatures with respect to formamide.
- The large acetaldehyde BE challenges the explanation for its gas-phase presence in cold ($\sim$ 10 K) astronomical objects, especially if it is formed on the grain surfaces. The problem may be alleviated if it is formed by gas-phase reactions.
- In hot cores/corinos, the measured and computed BEs are in agreement with the observations of acetaldehyde originating in regions colder than formamide, whose BE is larger.

Finally, our study shows the importance to extend the methodology adopted here to other molecules of astrochemical interest that show a spatial segregation probably due to their different BE.

Chapter 5

Experimental high-temperature formation of H_2 on carbonaceous dust grains

This Chapter is a re-organisation of the second publication of this PhD Thesis [Grieco et al., 2023]. This experimental work provides evidence of highly efficient formation of H_2 on carbonaceous dust grains through TPD and DED experiments at LERMA-CYU. The main motivation for this project was to check whether molecular hydrogen could form efficiently at temperatures above 20 K, that had been reported to be the highest temperature for an efficient H_2 formation on dust grains. While exploring several temperature and starting having positive results, we finally were able to confirm the maximum efficiency for such processes around 20 K, but we have actually extended the efficient formation of molecular hydrogen on such surfaces for temperatures up to 250 K.

The undersigned PhD student has been the one in charge of the entire experimental procedure: experiments, protocols (designed together with Prof. François Dulieu), data analysis (with the help of Prof. François Dulieu), discussion of the results for their astrophysical importance (together with all the co-authors of the published paper [Grieco et al., 2023]).

5.1 Abstract

The microphysics of molecular hydrogen formation has implications on galactic-scale star formation rates over cosmic times. It is the cooling agent needed to initiate the

cloud collapse regulating the star formation efficiency. H_2 formation is inefficient in the gas phase under typical interstellar conditions, needing dust grains as catalysts. Small carbonaceous grains with sizes from ≈ 4 to $\approx 100 - 200$ Angstrom, including Polycyclic Aromatic Hydrocarbons (PAHs), have been shown to increase the H_2 formation rates due to their large surface-to-volume ratios. H_2 formation on PAHs was previously thought to reduce above temperatures of 50 K and H atom recombination was believed to be highly efficient only below 20 K. Until now, both laboratory experiments and theoretical modeling have suggested that H_2 cannot form on grains with temperatures above 100 K. Here we report evidence, through direct laboratory measurements, of the high efficiency formation of H_2 at temperatures up to 250 K on a carbonaceous surface mimicking interstellar dust. By pushing their formation towards warmer temperatures, the H_2 molecules could start contributing significantly to the cooling of warmer gas (T $\approx$ 50−250 K). This will have a huge impact on our understanding of H_2 formation in nearby galaxies and its efficiency in high redshift galaxies where the CMB (Cosmic Microwave Background) already pushes dust temperatures to $>$ 20 K.

5.2 Introduction

5.2.1 The efficiency of H_2 formation on dust grains

Molecular hydrogen H_2 is the smallest, simplest but most abundant of the molecules in the Universe, its abundance (i.) shapes the molecular phases of the interstellar medium (ISM) where stars are formed because its self-shielding from the interstellar radiation [Hartwig et al., 2015] controls the extent of the photodissociation regions H_2 [Tielens and Hollenbach, 1985], and (ii.) regulates the star formation efficiency via the effect of H_2, and the subsequent molecules formed, cooling lines on the ISM cooling function for gas temperature T $\leq 10^4$ K [Bigiel et al., 2008, Glover and Clark, 2014]. Molecular hydrogen has three major routes of formation: (i.) the H^+ route ($H + H^+ \rightarrow H_2+ + h\nu$, $H_2+ + H \rightarrow H_2 + H^+$), which dominates for redshifts $z \approx 400$, (ii.) the H^- route ($H + e^- \rightarrow H^- + h\nu$, $H^- + H \rightarrow H_2 + e^-$), which dominates for $z \approx 100$ and (iii.) the grain surface catalytic route (H + H + surface$\rightarrow$ H_2 + surface), which dominates in the local Universe (z = 0). The two gas phase routes dominate in the primordial gas of the Early Universe, and, although inefficient, they play a major role in the formation of the first stars (population III stars). The dominant H_2 formation route depends on the presence of dust grains, hence on the metallicity and the dust temperature. H_2 formation on dust grains can also dominate at redshift 6 - 7, after the formation of the first stars and the enrichment of the ISM with metals and dust grains [Cazaux and Spaans, 2004, Algera et al., 2023]. Our present study focuses on this third and major route. The process of

H_2 formation on interstellar grains can be summarized in three steps. The first consists of the sticking of atoms from the gas phase on the grain surfaces, the second relates to the diffusion and reactivity of the atoms on the surface and the third to the return of the molecule to the gas phase. The most critical step is the second one, since, depending on the temperature of the grain, the atoms already adsorbed can desorb before a new atom arrives, making the recombination impossible. This is why on a water ice surface, for example, as the binding energy of physisorbed H is low (residence time of H short for rising temperature), the recombination efficiency decreases abruptly beyond 12 - 15 K [Amiaud et al., 2007]. The same has been observed for silicate surfaces [Pirronello et al., 1997]. The range is wider for graphite or amorphous carbon surfaces [Vidali, 2013], but overall, if the atoms cannot chemisorb, (i.e. make a covalent bond with the surface), the formation efficiency can no longer be significant beyond 20 K, due to the fast desorption of H. On an aliphatic carbon surface, HD recombination has been reported, at higher temperatures, but with low cross sections [Mennella, 2008]. If the atoms can chemisorb, then Cazaux et al. [2016] estimated that H_2 formation ought to reduce above 50 K and slowly decrease to zero at 150 K. Many studies on H sticking, diffusion and recombination on different surfaces have been performed and are collected in the review article by Wakelam et al. [2017]. But none had performed a direct measurement of the recombination efficiency at temperatures above 20 K.

5.2.2 Astrophysical importance

Dust grains at high redshift are likely partly in the form of very small graphitic grains (PAHs). In fact, both in the nearby and high-redshift Universe, one can see evidence for the PAH mass fraction correlates with metallicity [Galliano et al., 2021, Shivaei et al., 2017] due to harder and more intense radiation fields in low-metallicity galaxies. Given the high dust masses in several high-redshift galaxies, rather high metallicities are expected. Indeed, both observations and models suggest that the metallicity can already be around 20% of the solar value [Jones et al., 2020, Dayal et al., 2022], which would still allow for sufficient PAHs to be present in these high-z galaxies. Recent ALMA observations have demonstrated the presence of large quantities of dust already at redshifts of $z \approx 6$ - 9 [Watson et al., 2015, Pozzi et al., 2021, Riechers et al., 2014, Spilker et al., 2023], it is likely that H_2 formation on dust grains is already the dominant mechanism in those galaxies. Theoretical models predict dust temperatures in high-redshift giant molecular clouds above 60 K [Sommovigo et al., 2020], while estimates from observational studies range between 40 - 80 K [Sommovigo et al., 2022, Faisst et al., 2020, Bakx et al., 2020]. The fact that star formation is efficient in these galaxies suggests that H_2 formation must be efficient as well at those temperatures, to enable high

levels of star formation activity. The experimental results reported in this paper have the potential to revolutionize our understanding of the formation of the first generations of stars at high-redshift. The high H_2 formation rate estimated from the observation of PDR has been proposed to be due to the catalytic effect of PAH [Habart et al., 2004] and its propensity to do chemisorption has been calculated [Rauls and Hornekær, 2008]. There are several studies in literature highlighting that the presence of small carbonaceous grains, with large surface-to-volume ratios in comparison to large grains, increases the H_2 formation rates [Habart et al., 2004, Rauls and Hornekær, 2008, Lipshtat and Biham, 2005]. Direct experimental results supporting the hypothesis of PAHs as active catalysts for H_2 formation under interstellar conditions have so far been lacking. This study provides a breakthrough in experimental insights and will finally enable an estimation of the contribution of PAHs to interstellar H_2 formation at higher temperature until now not considered.

5.3 Methods: FORMOLISM configurations and experimental protocols

To create the right surface to reproduce PAH-like structures for the purpose of this work, few layers of coronene ($C_{24}H_{12}$) are deposited on the sample holder held at 280 K, from a movable crucible, that works like an oven, placed at 3 cm from it. The layers of coronene are obtained by a gentle sublimation of the powder contained in the PAH oven heated up at 420 K. The coronene film is a corrugated surface, probably made of disordered stack or small clusters of coronene, mimicking dust particles with surface defects. A beam of D atoms is aimed at the surface through a triple stage of differential pumping. D isotope is used instead of H, because H_2 is the major contaminant of any UHV system, and will give a better signal to noise ratio. When the beam is aimed at the surface, the overall pressure in the main chamber only rises by 1^{10-11} hPa, and the partial pressure directly in the beam at the surface is estimated to be $\approx 1^{8-10}$ hPa. In such conditions, D atoms land on a surface adsorption site every $\approx$ 100 s. The atoms are produced from a plasma discharge, but the D_2 dissociation efficiency is not perfect. The atoms are at a temperature slightly above the room temperature ($<$ 350 K), and approach from the surface at an angle of 40°, reducing their kinetic energy perpendicular to the surface. The detection tool of this set-up is a Quadrupole Mass Spectrometer (QMS) that can be rotated to be placed in front of the beams or the surface depending on the type of the experiments. In our experimental methodology there are a few important points to stress before going into their technical details. In order to infer the efficiency for the atoms to scan the surface and recombine to form molecules, it is indeed extremely crucial to calculate the amount of them produced by our system

when the plasma is switched on (when off, only D_2 reaches the surface) and the level of the background partial pressure present in the chamber. Those determinations help in knowing the amount of D_2 molecules due to the recombination of the atoms reaching the surface and to exclude any effect coming from a change of the background signal during experiments. Figure 5.1 describes the protocol followed to estimate the ratio of D_2 and D in a given experiment. The set up configuration, together with the corresponding signals measured by the quadrupole mass spectrometer (QMS) are displayed. Here the QMS directly intercepts the beam, and the surface does not contribute to the signal. The discharge can be switched ON (configuration 3, 4), or switched OFF (1, 2). The beam can be intercepted by a metallic flag in the main chamber (1, 4). On the left part of the Figure we represent the signal of m/z=4 noted M4 (corresponding to D_2), and M2 i.e. m/z=2 (composed of residual H_2 from the background (noted BKG), cracking pattern of D_2 (a few % of M4) and D atoms produced by the plasma). The M2 has been subtracted from the constant H_2 BKG. One can see the decrease of M4 when the discharge is switched ON, as well as the increase of M2 corresponding to the appearance of D atoms. To evaluate the dissociation efficiency only the drop in signal of M4 is considered and it can be calculated using the following formula:

$$\tau = \frac{(M4_{\text{plasma off}} - BKG_{\text{plasma on}}) - (M4_{\text{plasma on}} - BKG_{\text{plasma on}})}{M4_{\text{plasma off}} - BKG_{\text{plasma off}}}. \tag{5.1}$$

The dissociation efficiency $\tau(\%)$ is measured before and after each experiment and is stable over a day, but has some day to day variation of a few %, for a typical value of 60%.

Figure 5.2 displays the protocol we use to measure the recombination efficiency of D into D_2, for a given surface and temperature. The beamline containing D_2 aims towards the surface where the temperature-dependent results reported in this paper are measured. For the recombination efficiency experiments the QMS is placed in front of the surface, and it is mostly measuring what is coming off the surface (plus some unavoidable background contribution from the wall of the chamber). The beam, dissociated (1,2) or not (3,4), can be intercepted by the flag (1,4). This way we can subtract the contribution of the chamber. The black curve on the left panel is the measurement of the M4 (m/z=4 corresponding to D_2) using as surface a coronene film held at 250 K, whereas the blue curve is for an amorphous compact solid water ice film (c-ASW) of 30 layers of thickness deposited on the sample holder at 100 K. The ice film has been deposited to validate our protocol and to prove the difference in results with respect to when the coronene is used as surface. For the blue curve, we observe no increase of the M4 when the dissociated beam is aimed at the surface. The increase between step 1 and 2 is only due to the undissociated part of the beam. On the contrary, we observe a clear increase of the signal when the coronene film is used (black curve). This is the direct evidence that in

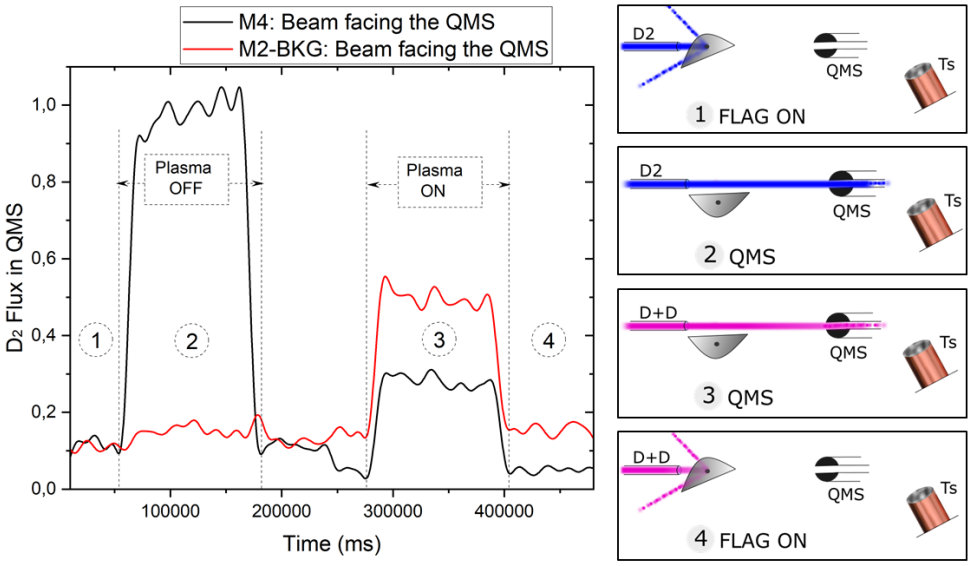

FIGURE 5.1: Schematic configuration of FORMOLISM setup including position and role of the flag, position of the QMS (right). M4 (D_2, m/z=4, black line) and M2 (H_2 or D, m/z=2, red line) signals measured to calculate the dissociation efficiency (left).

the case of coronene films D_2 molecules are formed and readily desorb to be detected by the QMS. In the case of water ice, as expected, the contribution of D_2 formation is measured as negligible, which demonstrates the robustness of the protocol. From this graph, and by taking into account the dissociation efficiency, one is able to calculate the efficiency of D+D recombination mediated by the surface at a given temperature. Since the total signal of M4 detected when the plasma is on equals the background signal plus the undissociated part of the beam and the signal from recombination, the efficiency (ϵ) is therefore expressed as follow:

$$\epsilon = (M4_{\text{ plasma on}} - BKG_{\text{plasma on}}) - (M4_{\text{ plasma off}} - BKG_{\text{plasma off}}) \cdot (1 - \tau). \quad (5.2)$$

Where "$M4_{\text{plasma on}} - BKG_{\text{plasma on}}$" is the total signal detected with the QMS when the plasma is ON after background subtraction; "$M4_{\text{ plasma off}} - BKG_{\text{plasma off}} \times ((1-\tau)$" is the part of the signal coming from the undissociated molecules and where τ represents the dissociation efficiency (%) measured before and after each experiment (see Figure 5.1). ϵ is normalized to the signal of m/z=4 detected when the plasma was off subtracted from its background ($M4_{\text{ plasma off}} - BKG_{\text{plasma off}}$). ϵ corresponds to the probability for an atom impinging the surface to recombine and be detected as a molecule, it includes all steps of accretion, diffusion and reaction. The definition of recombination efficiency can therefore differ depending on the inclusion of those steps. In Cazaux and Spaans [2004], the quantity displayed does not include the accretion (i.e. sticking) phase.

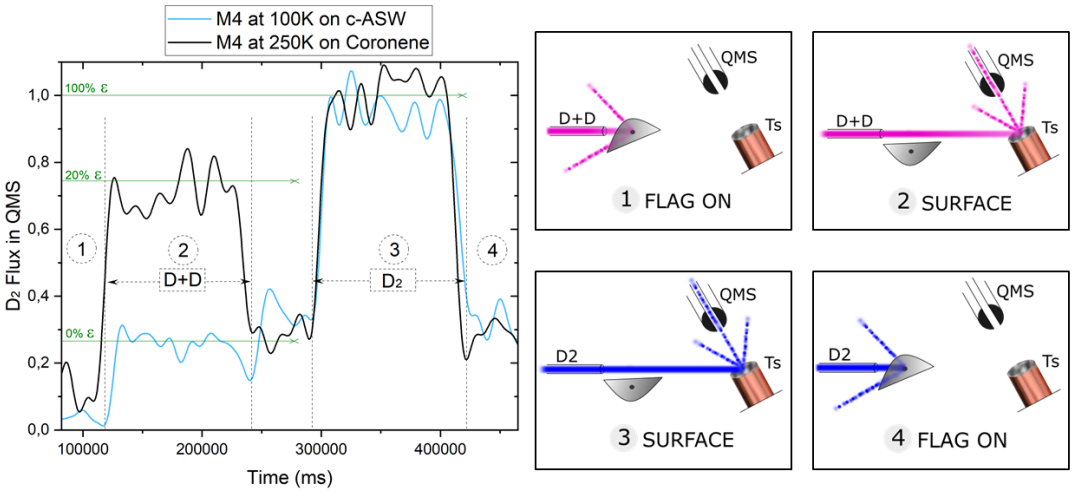

FIGURE 5.2: Comparison between M4 (D_2, m/z 4) signals by using Coronene (black line, Ts=250 K) and c-ASW (light blue line, Ts=100 K) as surfaces (left); 4 schematic configurations of FORMOLISM including position and role of the flag, position of the QMS associated to the 4 divisions of the signal shown on the left (right). The green lines show the values of the recombination efficiencies ϵ.

5.4 Experimental Results

Figure 5.3 displays the variation of ϵ with the surface temperature. The points at temperature above 100 K have been performed at fixed temperature, whereas the points below have been measured on the fly, using the TPDED technique with a 1 K/min ramp [Minissale et al., 2016]. The error bars have been estimated by adding all sources of uncertainties, including the most extreme fluctuations of the dissociation efficiency which gives the major contribution in the uncertainty. We observe a plateau above 100 K, at around 20%, a higher value at around 30% between 30 K and 80 K, two extreme values around 20 K, and a sharp decrease at 10 K. The reduction of efficiency at 10 K is due to the presence of adsorbed molecules. The presence of pre-adsorbed molecules reduces the direct contribution of formed molecules, as similarly observed on water ice films [Congiu et al., 2009]. The overall efficiency of the recombination depends on different competing mechanisms. The sticking or accretion, is not supposed to be very dependent on the surface temperature in this range [Cazaux et al., 2011] and it should be around 0.5, which is in line with our upper value of ϵ. This is due to the corrugated nature of our Coronene, contrarily to when graphite is used as substrate, where coronene forms an uniform and flat film. The desorption of atoms is increasing exponentially with the temperature, and should become a dominant loss channel. For a typical binding energy of 45 meV, the residence time is hundred picoseconds at 60 K, therefore, the only chance for an atom to recombine is to be incorporated in a chemisorption site. Fortunately, C-H termination of PAH can procure such chemisorption sites. This has been first proposed and calculated by Rauls and Hornekær [2008], and the inclusion of D atoms to

coronene has been experimentally demonstrated later [Thrower et al., 2011]. Mennella [2008] has also shown that the aliphatic group could also have a similar catalytic role, despite its lower cross section. The plateau at around 20% for temperatures $> 80 - 100$ K is therefore the probability of a D atom to react with an extra D atom already chemisorbed on the surface or to find a default site in the coronene film. We note here that there should be a barrier for the first hydrogenation, but that has no real importance in steady state conditions such as in our experimental protocol. The results were found constant after an exposition of a few 10^{15} atoms/cm^2, which correspond to a film of coronene just slightly superhydrogenated [Thrower et al., 2011]. When the surface temperature is reduced, the D residence time on the surface increases exponentially, and the physisorption-chemisorption transfer is probably favored. The maximum is obtained for a surface slightly higher than 20 K where the surface is still free of D_2 molecules that could have adsorbed. Below this temperature, D_2 molecule coverage increases and may prevent D atoms from accessing reactive sites/partners, simply by reducing their accretion rate on the surface. This has to be studied in better detail in forthcoming experiments. Considering the fact that small carbonaceous grains make a dominant contribution to the total grain surface and have numerous chemically bonded hydrogen atoms, we demonstrate for the first time that they play a key role in H_2 formation by chemisorption. Our study shows that the H_2 formation pathway on surfaces can be much more efficient than previously estimated, and over an extended range of temperatures.
One has to keep in mind that chemisorption is specific for PAHs, because the same results would not be possible on graphite, for example. The research group led by L. Hornekaer [Hornekær et al., 2006] studied, through experiments and calculations, the possibility for H atoms to chemisorb on graphitic planes. The activation barrier to make a carbon accessible is too high and it would require very high temperatures ($\approx$ 2000 K) to obtain the hydrogenation of such surfaces. In fact, in our previous experiments we have not been able to hydrogenate the HOPG surface either. The same group has instead demonstrated that the hydrogenation of PAHs is possible at every temperature and they even report experiments on the interaction of H atoms with low-T coronene [Thrower et al., 2012, Simonsen et al., 2020].
The incredible catalytic nature of coronene and the possibility to provide chemisorption and stabilization of H atoms to further recombine, found with our results, is therefore perfectly in line with previous works in this field.

5.5 Discussion & Conclusion

As soon as carbonaceous dust appears, the cooling capacity of the interstellar medium increases sharply, and thus its condensation in pre-stellar cores. Our work on molecular

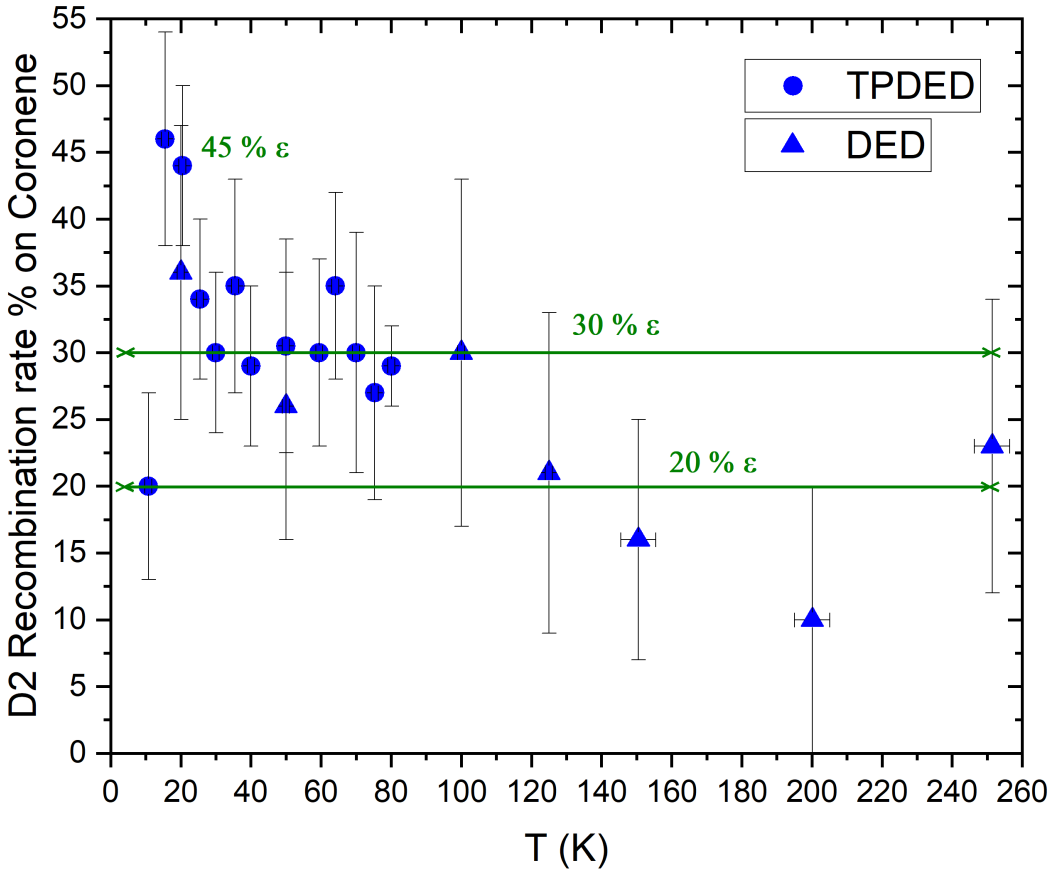

FIGURE 5.3: Temperature-dependent percentage recombination efficiency (ϵ) of D_2 on Coronene. Circles: TPDED experiments; triangles: DED isothermal experiments. Data are presented as mean values +/- SEM (1-sigma error), in which the error bars are derived from each component of the equation of ϵ. Those components are each the average of the signal recorded at a specific temperature for that setup configuration (flag on (BKG) or off, plasma on or off), each providing a different sample size (n number) depending on its detection time.

hydrogen surface formation involving chemisorption on carbon surface at temperatures around 100 - 200 K is of prime importance in astrophysics. It will change the location of the H/H_2 photodissociation front and the respective size of HII regions, PDR and molecular regions in a classical PDR picture [Tielens and Hollenbach, 1985]. Our results may furthermore explain the under-prediction of observed H_2 column densities by models [Habart et al., 2011] and the shift of the H/H_2 transition closer to the ionization front in resolved PDRs [Habart et al., 2023]. Additionally, our work brings one possibility to solve the contradiction between on one hand the possible discovery of James Webb telescope ultra-high redshift galaxies [Finkelstein et al., 2022] and on the other hand the redshift limit above which stars could not have formed, obtained by crossing the efficiency of H_2 formation against dust temperature and the dust temperature dependence against the redshift [Sommovigo et al., 2022, Bakx et al., 2021, Liang et al., 2019, Viero et al., 2022], with a minimum temperature ultimately defined by the CMB. The warmer

CMB of high-redshift galaxies is observed in the (sub-)millimeter dust continuum and the line emission as it provides an additional source of heating [da Cunha et al., 2013, Lagache et al., 2018].

Another implication of our experimental results could be the impact that the high temperature formation of H_2 might have on the star formation rate (SFR) and on the cloud collapse timescales. The formation of new stars per unit time strongly depends on the environment, since the latter affects the gas density of the pre-existing cloud and the final SFR [Longmore et al., 2013]. In general, observations underline how the gas density has a crucial role in assessing the SFR per unit dense gas [Schinnerer and Leroy, 2024]. This molecular gas mass is traced through CO emission and it depends on the conversion factor αCO, which translates the observed CO emission into a H_2 mass. It has been demonstrated that the CO-to-H_2 conversion depends on the metallicity and for low values the star formation unit per molecular hydrogen mass increases [Glover and Clark, 2012]. Regions where star formation is happening are dust-rich, underlying their role in the formation of H_2 gas [Schinnerer and Leroy, 2024]. Focusing specifically on PAHs, their relative abundance to dust grains exhibits a strong metallicity dependence as well [Li, 2020]. New studies report on the coexistence of PAH emission with H_2 lines [Van De Putte et al., 2024], the possibility to use PAHs to trace molecular gas [Shivaei and Boogaard, 2024] and the fact that they can be used as tracers of star formation rate [Sandstrom et al., 2010]. These reported connections between PAH and H_2 seem to support a scenario in which H_2 molecules can efficiently form on the surfaces of PAH molecules, in line with our experimental results.

The time needed for a molecular cloud to collapse to form stars ("free-fall" timescale) has been estimated to be 4–20 Myr, up to $\approx$ 80 % of the total cloud lifetime [Corbelli et al., 2017, Kim et al., 2023]. The fact the H_2 can be efficiently formed on PAHs at higher T_{dust} might have an effect in providing higher gas densities in regions where dust is warmer, so molecular hydrogen could already be a cooling agent for a more efficient cloud collapse. Moreover, the free-fall timescale is inversely proportional to n_{H}, so if higher gas densities are possible in warmer T_{grains} regions, then the free-fall time could be shorter than the typical 4–20 Myr reported above. It is also possible to foresee that with high T H_2 formation, the cloud will be efficiently enriched with molecular hydrogen, contributing to reach a cloud of high mass that would collapse earlier (due to increased mass), or faster, because of the cooling provided by H_2 to form stars.

To conclude, correctly accounting for molecular hydrogen formation over cosmic time is a key ingredient for several reasons, from the interpretation of the James Webb telescope observations in the local Universe to the atomic and molecular emission lines of high-redshift galaxies in general.

Chapter 6

Experimental H_2O formation on carbonaceous dust grains at temperatures up to 85 K

This is the last Chapter reporting experimental results of this Thesis and it corresponds to the third publication of this PhD [Grieco et al., 2024]. By adding atomic oxygen to the "equation" of Chapter 5, we explored if, by exposing coronene to H and O atomic beams, we would efficiently form ice layers and until what temperature this would be efficient. In the work we therefore report evidence of experimental ice formation on carbonaceous dust grains for temperatures up to 85 K and we discuss the astrophysical implications of such findings: the effect on oxygen depletion and other consequences involving grain growth and ice mantle formation.

The undersigned PhD student has run and designed the whole experimental procedure (with the help of Prof. François Dulieu), while the astrophysical implications of the obtained results have been discussed together with Prof. Ilse De Looze and Prof. François Dulieu.

6.1 Abstract

Water represents the main component of the icy mantles on dust grains, it is of extreme importance for the formation of new species and it represents the main component for life. Water is observed both in the gas-phase and frozen in the ISM, where the solid-phase formation route has been proven essential to explain abundances in molecular clouds. So far, experiments have focused on very low temperatures (around 10 K).

We present the experimental evidence of solid water formation on coronene, PAH-like surface, for a higher range of temperatures. Water is efficiently formed up to 85 K through the interaction of oxygen and hydrogen atomic beams with a carbonaceous grain analogue. The beams are aimed towards the surface connected to a cryostat exploring temperatures from 10 K to 100 K. The results are obtained with a QMS and analyzed through a temperature-programmed desorption technique. We observe an efficient water formation on coronene from 10 K up to 85 K mimicking the temperature conditions from the dense ISM to translucent regions, where the ice mantle onset is supposed to start. The results show the catalytic nature of coronene and the role of chemisorption processes. The formation of the icy mantles could be happening in less dense and warmer environments, helping explaining oxygen depletion in the ISM. The findings have several applications such as the disappearance of PAHs in translucent regions and the snowlines of protoplanetary disks. We stress on how JWST projects characterizing PAHs can be combined with H_2O observations to study water formation at warm temperatures.

6.2 Introduction

6.2.1 Experiments and theoretical studies on water formation routes

The study of water formation in the interstellar medium (ISM) is very important as the main molecule constituting icy mantles, storing and catalyzing the formation of potential biologically relevant structures. Water is observed as vapor in the gas-phase in cold regions with temperatures below 50 K, such as molecular clouds [Caselli et al., 2010], but also frozen, up to about 2×10^{-4} in abundance, with respect to H_2, in colder objects. The frozen water is believed to consist mostly of icy mantles on dust grains [Boogert et al., 2015]. In both the solid and gas phases, water is considered to lock most of the elemental oxygen into the molecular form [van Dishoeck et al., 2013]. Also, interstellar water has a very strong implication in planets' habitability research. Apart from its important role as a major factor for life, it can give indications on eventually detectable biospheres. Having more details about the abundance of solid water, its freezing and melting temperatures can help constraining the so-called habitability index [Silva et al., 2017]. Understanding the origins of water is also key in several other fields and there are still many questions regarding when and where ices are formed in both planet-forming disks and stellar systems, for example. They are thought to possibly form through two main processes: I) in the dense ISM, ices could form in cold molecular cloud cores prior to star formation. Here interstellar ices would be incorporated into all planet-forming disks. II) They could also be products of reprocessing within the central star nebula. In

this case we would have large water abundance variations for different stellar systems [Cleeves et al., 2014]. The link between the formation and the observation of water on planetary systems remains of fundamental importance in astrochemistry. The study of its chemical and physical evolution can therefore give more info about the origin of water in Solar System bodies [Jensen et al., 2019]. For example, terrestrial and sub-Neptune planets should be forming water in the inner regions of proto-planetary disks where water plays a crucial role. Besides eventually needing a water reservoir for their formation, this rises the question about the birthplace of the available water, if in situ or from the outer disk. Understanding the position of the snowline as well as the role of dust/ices and temperatures are interesting points since the replenishment of both gas and dust from the outer disk could be one of the main water reservoir contributors [Perotti et al., 2023]. Finally, the icy mantle-covered dust grains in the rotating disks around stars come from the accretion of gas onto dust in molecular clouds, from where the planets will be afterwards formed [van Dishoeck, 2004]. Assessing how the ice mantles form, in which regions and under which physical conditions and range of temperatures could therefore be linked to many other aspects at bigger scales. However, independently from specific applications, studying water formation requires an understanding of how water interacts with a dust grain surface, how the latter contributes to its formation and which ranges of temperatures are involved in those processes. In the last decades, there have been different laboratory studies and models trying to unveil the water formation routes on dust grains, focusing on three main possible chemical routes initiated with different reaction [Tielens and Hagen, 1982]: 1) O+H reactions [Dulieu et al., 2010, Vidali, 2013]; 2) hydrogenation of O_2 [Oba et al., 2009, Ioppolo et al., 2008, Matar et al., 2008]; 3) hydrogenation of O_3 [Mokrane et al., 2009, Romanzin et al., 2011].

All the models and experiments that have helped us understanding water formation processes are often carried out in different conditions. This makes it challenging to directly apply and interpret those findings for several ISM regions. Thus, there are still many open questions that need to be answered in this field. Nevertheless it is now clear that the formation of water molecules in the gas phase is incapable of explaining the observed abundances in molecular clouds, especially for the solid form [Ceccarelli et al., 2007, Parise et al., 2005]. In general, water molecules are mainly believed to be synthesized by atomic reactions involving H and O atoms on pre-existing silicate or carbonaceous grains at around 10 K. However, OH+H_2 may probably be another important alternative, as explained by the difference in deuteration efficiency for the D and HD routes [Kristensen et al., 2011, Oba et al., 2012].

The first formation route (O+H reactions) has been studied intensively by Cuppen and Herbst [2007] who found it to be the main one for O atoms on grains in cool diffuse clouds with no activation barrier (in the gas phase), where H and O atoms are the major gas-phase species: O + H $\rightarrow$ OH (reaction 1); OH + H $\rightarrow$ H_2O.

From reaction 1, OH can also follow a different path, encountering molecular hydrogen already adsorbed on the grain, as shown below (activation energy of 5.16 kcal/mol in the gas phase [McCormac, 1973]): $OH + H_2 \rightarrow H_2O + H$.
The second route relates to the hydrogenation of O_2. Tielens and Hagen [1982] proposed:
$O + O \rightarrow O_2$;
$O_2 + H \rightarrow HO_2$ (no barrier); $HO_2 + H \rightarrow H_2O_2$;
$H_2O_2 + H \rightarrow H_2O + OH$.
Those are the main routes in cold molecular clouds where H_2 molecules are the major gas-phase species. There are laboratory experiments studying this second water formation network reporting the formation of water molecules under conditions mimicking cold interstellar molecular clouds. By starting from reactions of cold H atoms with solid O_2 molecules at 10 K, they found the following reaction steps to be the most efficient:
$O_2 + 2H \rightarrow H_2O_2$; $H_2O_2 + H \rightarrow H_2O + OH$; [Miyauchi et al., 2008, Kristensen et al., 2011].
For the third route, since the chemical models by Tielens and Hagen [1982], there have been many others confirming the hydrogenation of O_3 leading to water formation on grains. Parise [2004] proposed a water formation scheme where O_3 molecules react with H or D atoms to form OH or OD, and subsequently the reaction H_2 + OH/OD would lead to H_2O/HDO. This has been confirmed experimentally by Oba et al. [2012]. The Monte Carlo simulations of Cuppen and Herbst [2007] emphasize the non-negligible contribution from the $H + H_2O_2$ reaction (H_2O_2 being a product of the $H + O_2$ pathway) and the unusual high abundance of reactants such as OH and O_3.
It is also relevant to mention experiments on water formation via OH radicals. Oba et al. [2011] produced them in a H_2O microwave-discharge plasma, where water was formed at 40 K and 50 K, but not at 60 K, together with H_2O_2. The study shows the importance of OH radicals as well as the possibility to investigate water formation at higher dust grain temperatures and the role of the surface. Lastly, there have been several experimental studies reporting water formation on dust grains or in astrophysically relevant conditions. The reality is that, under dark cloud conditions, only the very first monolayer grows on bare silicate or carbonaceous grains [Papoular, 2005], most water molecules should be subsequently synthesized on a surface mainly composed of ices. Dulieu et al. [2010] ran an investigation on how water formation continues on the icy surfaces of cosmic grains. At 10 K, deuterated water molecules were formed with a high efficiency (about 50%) by exposing amorphous water ice substrate to O and D atoms. Furthermore, the details about all the possible different networks have been deeply investigated by Kristensen et al. [2011] and Kristensen et al. [2011]. Later on, it has been also shown that, if water forms in excess of energy, the newly formed molecules can undergo chemical desorption mechanisms. This process is more efficient for harder surfaces [Dulieu et al., 2014]. Until now, all the studies have only considered water formation through physisorption

mechanisms. However, we have already demonstrated the importance of chemisorption processes for H_2 formation on carbonaceous dust grains at temperatures up to 250 K [Grieco et al., 2023]. Therefore we want to keep investigating the role of those surfaces for the formation of small and important molecules in the ISM, such as H_2O in this paper. Reporting the main H_2O formation pathways and the state of the art of several studies on dust grains gives us the right context to address the main goal of this work: the experimental study of H_2O through its formation and interaction with a carbonaceous surface for a higher range of temperatures. An overview of different studies of PAHs and ice interactions are given in the following Section (6.2.2).

6.2.2 PAHs in ISM, O and H atoms interactions and interstellar ices

Already in the 1970s, broad mid-infrared (mid-IR) emission features present in almost all objects (bright HII regions, surfaces of dark clouds and the general ISM) were attributed to polycyclic aromatic hydrocarbons (PAH), molecules of about 50 carbon atoms [Allamandola et al., 1989, Puget and Leger, 1989].
PAHs are ubiquitous ($10^{-7}/n_{\mathrm{H}}$) in the ISM. These species play an important role in the heating of neutral gas, in the ionization balance in molecular clouds as well as in the phase structure of the ISM and its ion-molecule chemistry. Since then, models have provided much insight into the formation and evolution of interstellar PAHs. PAHs represent an important reservoir of interstellar elemental carbon (fc of about 3.5×10^{-2}) and they can be found in both gas and solid phases in the ISM [Tielens, 2008, Salama, 2008]. They are supposed to either form in the envelopes around carbon stars by a series of reactions building up large PAHs from small carbon chains, or by top-down routes through fragmentation of large grains in the ISM [Chastenet et al., 2019]. The main part of the PAH population is bigger than C_{40} [Jochims et al., 1999] and PAHs smaller than this will be destroyed by UV irradiation in regions of high photon flux, coagulate in dense regions or they can survive in icy grain mantles in molecular clouds. Also, many new small cyclic N-bearing carbon molecules have been detected in the molecular cloud TMC-1. McGuire et al. [2021] analyze and discuss in situ gas-phase formation from smaller organic molecules, but they are not able to explain and match the observed abundances with neither top-down or bottom-up pathways. The formation of those molecules in molecular clouds and their survival in those conditions in order to be observed could be an indication of the strong stabilization that small aromatic structures can provide. This open the doors to other possible formation routes that should be considered for those heteroatoms-bearing structures, as for example chemisorption processes involving C and N atoms from the gas-phase landing on the surface and further form new functional groups on the ring.

In the present experimental study, the PAH used as interacting surface is coronene, a molecule of 24 carbon atoms ($C_{24}H_{12}$). Coronene is often used in the laboratory to model more interstellar-relevant PAHs. In fact, it is often considered as an archetypal interstellar PAH. It is believed to represent a favoured structure during PAH growth and formation [Oomens et al., 2001]. $C_{24}H_{12}$ is indeed one of the largest PAHs that can be easily manipulated in the laboratory and using this type of surfaces is a standard experimental approach. Coronene is also found to be relatively resistant to UV photodecomposition [Noble et al., 2017]. During their lifetime in the ISM, PAHs can be both functionalised with chemical side groups, or be substituted with heteroatoms (observations: Peeters et al. [2002]; calculations: Sadjadi et al. [2015]; experiments: Bernstein et al. [1999], Gudipati and Yang [2012], Guennoun et al. [2011], Bouwman et al. [2011], Noble et al. [2020], Cook et al. [2015]).

In cold regions of the ISM, PAHs are expected to be frozen out on dust grains. There are laboratory experiments investigating water-ice and PAH mixtures and they show that superhydrogenated PAHs are produced together with PAHs with alcohol and ketone functional groups. These studies suggest that oxygen-bearing PAH species could be formed in the ISM on icy grains [Jaganathan et al., 2022]. In fact, laboratory studies on the reactivity of PAHs and water molecules show an efficient formation of oxygenated PAHs, higher than the actual abundance observed in denser regions. Destruction routes of such species should therefore be efficient [Noble et al., 2017, Thrower et al., 2014]. Specifically, in regions with higher extinction (A_V higher than 2) it is not clear whether PAHs exist and under what form. PAHs can condense on small grains or be incorporated in icy mantles. Indeed A_V around 2 correspond to the onset of detection of solid water ice in the ISM [Boogert et al., 2015]. In these edge zones, PAHs in water ice can become oxygenated or be chemically transformed in the gas phase. O atoms are responsible for these changes. In particular they can be the main actors since they can remain in the gas phase or they are kept in the form of water. Actually, O atoms can easily be inserted on the edges of small PAHs, and thus coronene, but they can also push the chemical destruction of these molecules into smaller ones, such as ketene, and enhance their entrance in the interstellar medium [Dulieu et al., 2019]. Finally, another important point is the role of dust grains as catalysts, and specifically PAHs, for the formation and thus abundance of molecules in the cold interstellar medium (ISM), such as H_2, H_2O, H_2CO and CH_3OH, that cannot be synthesized solely by gas phase reactions. One of the simplest water formation routes ever proposed is the sequential hydrogenation of O atoms, producing OH and then water, as shown experimentally [Dulieu et al., 2010]. The interaction of the incoming species (H, OH and CO) with PAHs has been recently modeled. They can react with axial H atoms of hydrogenated PAHs following the Eley–Rideal mechanism and H_2O is produced with no activation barrier [Ferullo

et al., 2019]. As introduced in the previous Section (6.2.1), there are several water formation routes involving dust grains. The study of the role of PAHs on icy mantles, their reactivity with water, the interaction with H and O atoms to eventually form water is therefore of fundamental importance in this field. In our laboratory we studied the behavior of hydrogen and oxygen atoms sent onto coronene and the eventual formation of water on the surface at several temperatures up to 85 K. This work has the aim of verifying if the main H_2O routes, when a typical PAH-like surface is used, can compete with the incorporation of O and H atoms into the grain and how the efficiencies vary with the temperature.

6.3 Methods: FORMOLISM configurations and experimental protocols

6.3.1 Set-up and detection methods

In the current set-up, we study the interaction and reactivity of oxygen and hydrogen atomic beams with a PAH-like surface, coronene, mimicking interstellar carbonaceous dust grains. Exactly like it has been discussed for the experiments of Chapter 5, a few layers of coronene ($C_{24}H_{12}$), contained in a movable crucible, are deposited on the sample holder held at 280 K. The movable crucible is placed at 3 cm in front of the sample holder and it works like an oven that heats up the solid powder. In our case, coronene (higher than 99% purity, Sigma-Aldrich) is deposited on the surface by bringing the crucible up to 420 K to obtain a gentle sublimation. After the deposition the crucible is retracted into its own vacuum chamber. The obtained coronene film is a corrugated surface of disordered molecular clusters that mimicks typical dust particles with surface defects. Since the coronene powder is hygroscopic, the eventual water trapped inside the coronene layers upon deposition has been checked after each set of experiments. No visible water peaks have been observed together with the desorption of the coronene film.

Two beams containing oxygen and hydrogen are aimed at the surface through a triple stage of differential pumping (three vacuum chambers connected together by tight diaphragms of 3 mm diameters). When the beams are sent to the surface, the overall pressure in the main chamber only rises by 1×10^{-11} hPa, and the partial pressure directly in the beam at the surface is estimated to be 2×10^{-8} hPa. Molecular pressures injected in the gas lines are about 1.5 mbar for the oxygen beam and 3 mbar for the hydrogen beam, and the atomic form of the beams is obtained by a microwave plasma discharge. However, after expansion in the source chambers, the pressure is immediately reduced to a few 10^{-5} mbar and so the atoms finally mostly interact only with

the surface, after a free flight. The atoms are at a temperature slightly above the room temperature (<350 K), and they reach the surface at an angle of 40° for the hydrogen beam and 57° for oxygen, resulting in a reduced kinetic energy perpendicular to the surface.

As already mentioned, FORMOLISM is equipped with a quadrupole mass spectrometer (QMS). It allows both the detection of species desorbing from the sample during a TPD (temperature programmed desorption) and, when placed in front of the beam-line, the characterization and calibration of molecular beams, as well as the evaluation of the dissociation efficiency. TPDs represent the most common experiments to determine the interaction energies and behavior between chemical species and involved surfaces. These types of studies consist in selecting a system made up of a surface, coronene, on which a gas-phase species is sent, oxygen and hydrogen in our case. The latter would land, stick, react with incoming or already present species and further desorb, depending on the conditions. The temperature at which the surface is kept plays a crucial role. Every species (hydrogen, oxygen or newly formed molecules like water), have indeed a certain propensity to interact with the surface and to reside on it based on the surface temperature and binding energies. Once a specific temperature is reached, a given species can desorb, while at very low temperatures a species has enough residence time to stay on the surface, eventually diffuse and react with others forming new ones (in this work: water, O_2, O_3). In our TPD experiments, coronene is cooled to temperatures ranging from 11 K to 100 K and is exposed to oxygen and hydrogen beams. The interaction between the species and the surface can go from a simple, and lower in energy, physisorption to the formation of actual chemical bonds (chemisorption). Chemisorption is the only interaction mechanism that makes oxygen and hydrogen atoms stay on the surface at temperature above 40 K for a longer residence time, this enables further processes on the surface instead of sudden desorption. The eventual newly formed species, mainly water and O_3 in our study, will have a new binding energy with the surface and a new temperature of desorption. During our temperature-programmed desorption, coronene is heated over time with a linear ramp (β = 12 K/min) from an initial temperature (experiments from 11 K to 100 K) to a higher one, 180 K, sufficient for the desorption of all the species in our system. Water molecules are the last ones to desorb at temperatures around 150 K. The signal of the desorbing species is detected by the quadrupole QMS in counts per second through the mass to charge ratio (m/z). The temperature at which each species desorbs, the shape and intensity of the peak, indicates the strength of the interaction (binding E), the type (order) of desorption and the amount of species undergoing that process.

Thus, TPDs are powerful tools to study the mechanisms of chemical reactions that occur on a specific surface and to infer the nature of the interaction between the surface and the adsorbing species.

The dissociation efficiency is instead measured by placing the QMS in front of the oxygen and hydrogen beams. The two beams do not interact with the surface in this case and this is just a measure of the amount of atoms that we are able to produce by dissociating the oxygen and hydrogen molecular beams. To evaluate the dissociation efficiency, we measure the drop in signal of the molecular mass, m/z=32 for O_2 and m/z=2 for H_2, and we observe a proportional increase of the signal of the atomic one, m/z=16 for O and m/z=1 for H. The dissociation efficiency (%) for both the hydrogen and oxygen beams is usually stable over a day and we measure a typical value of 60% for both beams.

6.3.2 Experimental protocol

This study focuses on exposing coronene to hydrogen and oxygen atomic beams in order to verify their respective and conjugated effect when they are sent onto the surface. In particular, we investigate the probability of the atoms being locked on the surface, how they physi- or chemi-sorb and/or if they promptly react with each other forming water molecules, or O_2 and H_2. The protocol is therefore divided into two main parts: preparation of the surface, with the collection of a reference, followed by an interaction of the surface with atomic oxygen and hydrogen beams. Firstly the coronene surface is formed by depositing it as described in Section 3.1 and afterwards cooled down to reach 10 K. At this point, to quantify the structure of the surface, its role as catalyst and the eventual changes due to the atomic irradiation, we use the molecular oxygen desorption peak as reference. This O_2 peak (after deposition of about 1 monolayer on the surface at 11 - 12 K) is taken everyday by detecting its desorption through the QMS with TPDs up to 50 K. The position (at a temperature of about 35 K) and shape of the O_2 desorption peak are well studied in the literature and eventual changes can thus be an indication of surface alteration and evolution [Mohamed Ibrahim et al., 2022]. This reference O_2 desorption peak is the black curve visible in Figure 6.1 and it shows very little differences due to day-by-day changes on the coronene surface that, even if deposited by carefully controlling all the parameters, carries an experimental error. Once we are sure to have deposited the coronene and to have the reference for the day, we start with the second part of the protocol. Now, the following phase represents the actual investigation of the paper. Coronene, kept at a fixed temperature, is exposed to hydrogen and oxygen atomic beams for a certain time/dose. Right after the irradiation, the surface is cooled down to 10 K and at this point, we deposit molecular oxygen again to compare its desorption peak to the daily reference and to detect any changes to the surface due to the prior atomic irradiation. Therefore, after depositing about 1 monolayer of molecular oxygen, we perform the very final and most important TPD up to 180 K to detect the

desorption peaks of O_2 just sent on the surface (green and magenta curves in Figure 6.1, desorption T around 35 K), O_3 (green and magenta curves in Figure 6.1, desorption T around 65 K) and water (blue and red curves in Figure 6.1, desorption T around 150 K). The surface is subsequently cooled down to a given surface temperature, T_s, and a new protocol cycle can start.

At the beginning of the study, we have mainly focused on determining the effects for surface temperatures of 11 K and 45 K, Figure 6.1. Afterwards we have examined different times/doses (see Figure 6.2) for these same two temperatures in order to define the best one suitable for comparing different temperatures. Finally, we have evaluated the amount of water formed through the O and H atomic irradiation of coronene kept at fixed temperatures ranging from 10 K to 100 K for the chosen time/dose (30 minutes), Figure 6.3. The last but very important detail regards the two different approaches used right after the irradiation, and before the O_2 deposition to check the surface changes, for temperatures below and above 35 K. Since the molecular oxygen coming from the undissociated part of the beam sticks on the surface during the irradiation for temperatures below 30 K, this one is removed after the irradiation and before any further analysis by heating the surface up to 50 K. This allows us to verify only the effect from the atomic beam and to have the same conditions for experiments at all temperatures. Once the irradiation is finished and we have eventually removed the O_2 stuck on coronene for temperatures below 35 K, the surface is cooled down to 10 K to deposit 1 ML of O_2 for the daily reference comparison and the protocol follows the general description given above.

To sum up, all the experiments presented here consist in depositing the coronene surface every day before any set of experiments (typically 1-3 cycles of water formation, without substantial changes to the coronene), collecting a O_2 reference, atomically irradiating the surface and checking its changes through the molecular oxygen peak, lastly recording the molecules formed though TPDs up to 180 K. With the QMS, the same molecule can be detected with different m/z ratios corresponding to the fragmentation of the parent molecules after the electron impact (here at 30 eV). The main fragments under study here are m/z=2 (molecular mass of H_2), m/z=18 (molecular mass of H_2O), m/z=32 (molecular mass of O_2 and main fragment of O_3) and m/z=48 (molecular mass of O_3).

6.4 Experimental results

All the results shown in the following paragraph come from the temperature programmed desorption experimental method (TPD), as described in the protocol. The idea is to

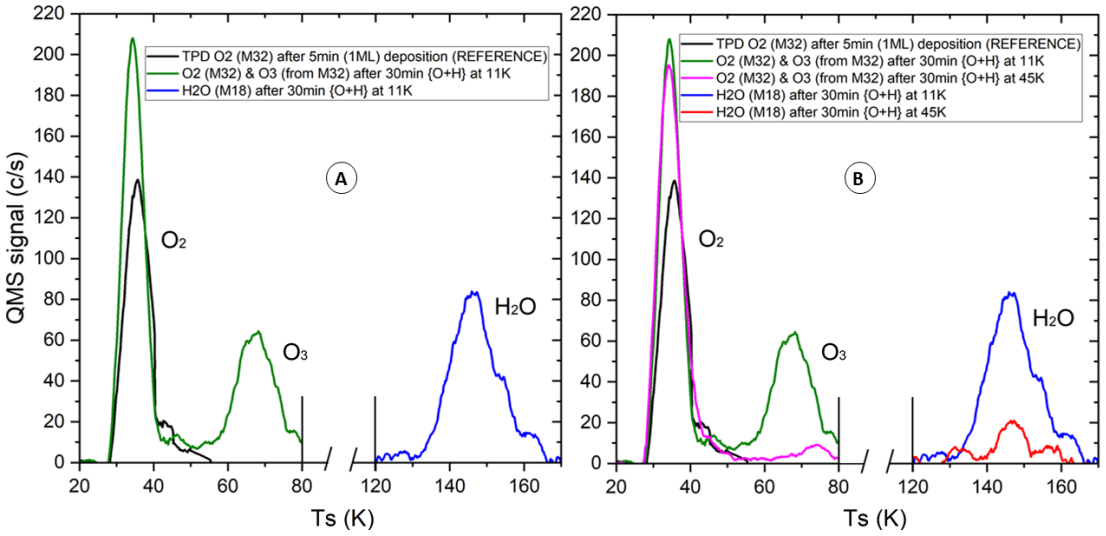

FIGURE 6.1: A. Black curve: O_2 reference peak; green curve: O_2, of about 1 ML deposition added after irradiation, and O_3 from 30 minutes {O+H} exposure at 11 K; blue curve: H_2O from 30 minutes {O+H} exposure at 11 K. B. Black curve: O_2 reference peak; green curve: O_2, of about 1 ML deposition added after irradiation, and O_3 from 30 minutes {O+H} exposure at 11 K; blue curve: H_2O from 30 minutes {O+H} exposure at 11 K; magenta curve: O_2, of about 1 ML deposition added after irradiation, and O_3 from 30 minutes {O+H} exposure at 45 K; red curve: H_2O from 30 minutes {O+H} exposure at 45 K.

check both the changes produced on the surface when the atoms are sent and, most importantly, the amount and type of molecules (namely O_2, O_3, H_2O) formed.

6.4.1 Experiments at 11 K

In Figure 6.1A we show the TPD peaks recorded by using the QMS for the first part of this study. The surface is kept at 11 K and two types of analyses are performed here. Firstly we collect the reference peak of about 1 ML (monolayer) of O_2 (referred to as mass 32 (M32), see black curve) to have the position (desorption temperature/binding E) and the shape of O_2 interacting with coronene. Secondly, and separately, the surface is exposed simultaneously to hydrogen and oxygen atomic beams for 30 minutes, before detecting the desorbing species with the TPD method. The main molecules under analysis here are molecular oxygen, O_3 and water molecules. As shown in Figure 6.1A, O_2 is characterized by a desorption peak at around 35 K (m/z=32 reference peak, black curve). In Figure 6.1A we also observe the other two main products of the {O+H} exposure: ozone, O_3, (from the m/z=32 fragment signal, green curve) with a TPD peak around 70 K and water molecules (m/z=18, blue curve). H_2O is the one desorbing at the highest temperatures in our system, as shown by its peak centered at 150 K. By checking the behavior of M18 (m/z=18) during the TPDs, we observe a peak at higher temperatures only for the experiments at 11 K. The water peak also represents the main

fragment of the H_2O_2 molecule and we do see a sign of its desorption around 177 K only when O and H atoms are sent onto the coronene at 11 K. This is in agreement with previous works studying water formation at very low temperatures [Chaabouni et al., 2012, Ioppolo et al., 2008]. In fact, at temperatures around 10 K, O_2 represents a stable and largely available reactant whose chemistry also leads to the formation of H_2O_2, as reported in the introduction. The reactivity of O_2 towards the formation of H_2O_2 becomes less relevant at higher temperature due to its mobility on the surface, by approaching its desorption temperature, and the appearance of a more relevant O_3 chemistry with an overall water formation being favoured instead.

In Figure 6.1, one can notice how the amount of molecular oxygen desorbing from the 1 ML deposition realized after irradiation (green and magenta curves) is consistently higher than the reference peak (black curve). The most simple explanation relates to the actual higher quantity of O_2 deposited in the same 5 minutes, that are usually used as reference. Since this deposition is realized after the atomic irradiation, during which the plasma is turned on, the molecular flux tends to be higher when compared to the conditions prior to the {O+H} exposure. Even after waiting a certain time for all the parameters and pressure to be back to the initial conditions, there is a trend in all experiments that shows an average of about 30% of more molecular oxygen coming from the surface with respect to the reference peak. The actual flux after atomic irradiation is therefore depositing more O_2 than expected. Since we are controlling, with the time/dose and pressure we are using, the deposition of about 1 ML of O_2 only, even if we observe the desorption of a higher quantity, we keep referring to these reference peaks as the desorption peak of the deposition of about 1 ML of O_2. This does not have an impact on the analyses and on the interpretation of the results. To this main factor, one has to add the possible change in sticking coefficient because the surface is now hosting the newly formed species, namely ozone and water. In Figure 6.1A, as expected at 11 K, the molecular part of the oxygen beam is sticking on the surface during irradiation, allowing all the 3 mechanisms for water formation described in the introduction. The first formation route (O+H path) is the most obvious, but also the presence of O_2 during the plasma exposure allows, given a certain degree of dissociation, the formation of O_3 and its further hydrogenation, as well as the reaction of O_2 with the incoming H atoms. Also, one would expect that at these low temperatures the direct interaction of atomic oxygen and hydrogen mediated by coronene would result in a reaction that forms water with a 100% efficiency, while only a part of our system goes in this direction. The explanation is due to the hydrogen being the limiting reactant, allowing the rest of O to recombine as O_2 or to form O_3.

The black curve, reference O_2 peak, is mostly used to compare the effect of the {O+H} exposure on the coronene surface. The goal is to check if there is evidence of a relevant position shift (different desorption temperature and therefore different binding E) and

shape of the molecular oxygen peak after the {O+H} irradiation (green curve). No relevant variation from the reference of the O_2 peak is observed here.

6.4.2 Experiments at 45 K

So far we have presented and introduced the topic by using the results obtained at widely studied low temperatures, 11 K in our case, where the expected reaction pathways are very efficient. Figure 6.1B shows, by following the same protocol of Figure 6.1A, also the results when the coronene surface is kept at 45 K during the {O+H} exposure. The main point here is to check the surface temperature effect on the quantity of O_3, magenta curve, and H_2O, red curve, formed. At temperatures higher than 35 K, molecular oxygen does not accumulate on the surface anymore, since it instantaneously desorbs upon sticking, limiting its contribution in forming O_3 and further water formation pathways during the atomic exposure. The O+H reaction route is happening in both cases (at 11 K and at 45 K), with an evident and obvious higher efficiency at 11 K. All those effects result in a noticeable higher quantity of water synthesized on the grain during {O+H} irradiation at 11 K. The predictable and almost negligible amount of O_3 at 45 K is not surprising, but the presence of formed water represents here the novelty of this study. Thus, the fact that there is still a quantifiable amount of H_2O formed at 45 K stimulated us in this study to search for higher temperatures at which the system {O+H}-coronene would still produce a reasonable amount of water.

6.4.3 Temperature effect

Figure 6.2 displays the effect of different {O+H} doses and the comparison for temperatures below and above the O_2 desorption (around 35 K). Every point on the graph represents the integrated areas under each respective peak. The first thing to notice is a good proportionality found for the area of the H_2O peaks with increasing doses of {O+H} at both 11 K and 45 K. The most efficient water formation pathway, in terms of quantity recovered, is as expected happening at 11 K, with twice the efficiency with respect to the same atomic irradiation method at 45 K. Again, at 11 K all the water formation routes are open. The other remarkable point is the proportionality of O_3 formation at 11 K and the absence of variation detected at 45 K, underlining the important role of the sticking of O_2 molecules on coronene for its formation and their eventual hydrogenation to form water. Last but not least, this plot allows to choose the best dose to use to further compare the behavior at different temperatures. The 30 minutes time-dose is found to be a reasonable reference in order to maximise the amount

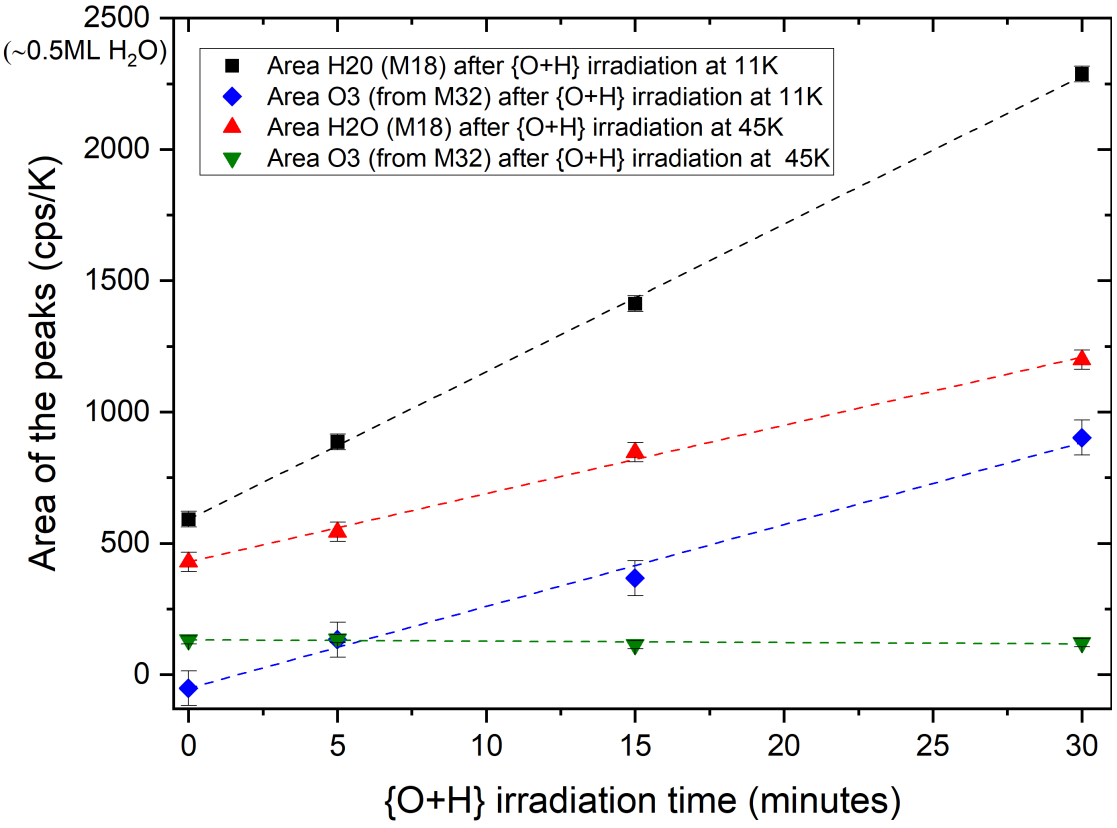

FIGURE 6.2: Area of O_3 and H_2O peaks after several irradiation times (0, 5, 15, 30 minutes) at 11 K and 45 K. The error bars are obtained from the linear regression.

of water recovered from the surface before having too many molecules covering it and therefore reducing the effect from the coronene surface itself. The max amount of water formed on coronene is in fact obtained for the 30 minutes deposition at 11 K, but it stays right below 1/2 ML, ensuring the exposure of the surface to the incoming beams. To determine the area of 1 ML of water on coronene, we have deposited 30 ML of ice film on the coronene surface by using a separate channel and a micro-capillary array doser, keeping the pressure of the main chamber always below 10^{-8} mbar, as reported in previous work [Ferrero et al., 2022]. The value has been confirmed by comparing it to the area of about 1 ML of water deposited on coronene, which differs only 13%. The 30 minutes dose is afterwards also used to compare the effect and the results from exposing the surface with the O and H beams together, up to 100 K, alone or in sequence at T_s = 25 K.

Figure 6.3 shows the integrated values of the water peaks detected after irradiating the surface with the {O+H} beams during 30 minutes at temperatures up to 100 K. The reported values are normalized with respect to the area of about 1 ML of water on coronene. A stable and maximum situation is obtained for temperatures up to 25 K, while the first decrease of the plot is observed between 30 - 35 K. After 35 K the amount of water formed with {O+H} irradiation already reaches a lower value that extends

up to 85 K, with a non-negligible area still at 100 K, even if the calculated error bar already falls in the noise level. The molecular oxygen from the undissociated beam, and the newly formed one through recombination, can stick and remain on the surface upon irradiation at temperatures lower than 35 K, as shown by the first dashed vertical line in Figure 6.3. During the {O+H} exposure, the presence of O_2 therefore helps in forming O_3 and water, with the advantage of a longer residence time for the atoms at those temperatures. This results in an overall more efficient water formation pathway when the coronene is kept at temperatures up to 35 K: all the main 3 formation routes are possible. Between 35 - 70 K there is no O_2 staying on the surface anymore, but the formed O_3 and the incoming oxygen and hydrogen atoms still provide an efficient water formation on coronene. After 70 K, second dashed vertical line, O_3 desorbs and does not contribute anymore to form water through its hydrogenation. This is when only the O+H route is available and we observe the lowest water formation efficiency. The bottom magenta line displayed in Figure 6.3 represents the integrated area of the water peak when only H atoms are sent onto the surface, at 25 K. In this conditions the water could only come from the beam, as a pollutant, or from the chamber and it is not due to the {O+H} interaction. Its level is thus taken here as a minimum noise level. However, Figure 6.3 confirms the important role played by coronene and the temperature dependence of the system under study in this paper, as well as the important role of the O_2 and O_3 molecules. The fact that water is formed at temperatures higher than 40 K proves the chemisorption of O atoms on coronene, since they would otherwise never be present on the surface for further reactions at those temperatures. The chemically adsorbed oxygen atoms therefore represent available reactants for the incoming O, O_2 and H to undergo all the possible reactions.

6.4.4 Catalytic role of coronene

Our experimental results provide further evidence to the catalytic role of coronene in these types of systems, already observed in previous work from our group for H_2 recombination [Grieco et al., 2023]. As already discussed above, coronene represents an efficient catalytic surface for water formation up to 85 K when O and H atoms are sent together. In this Section we study the role of the surface when the atomic beams are sent separately or in sequence and we compare the different results in order to understand the mechanisms involved.

Figure 6.4 reports the amount of O_2, O_3, and H_2O recovered after each irradiation. All of them were obtained by exposing the surface to the hydrogen and oxygen beams together ({O+H}), separately ({O} and {H}) or in sequence ({O}+{H} and {H}+{O}), at 25 K. Since the experiments displayed in Figure 6.4 are carried out at a temperature below

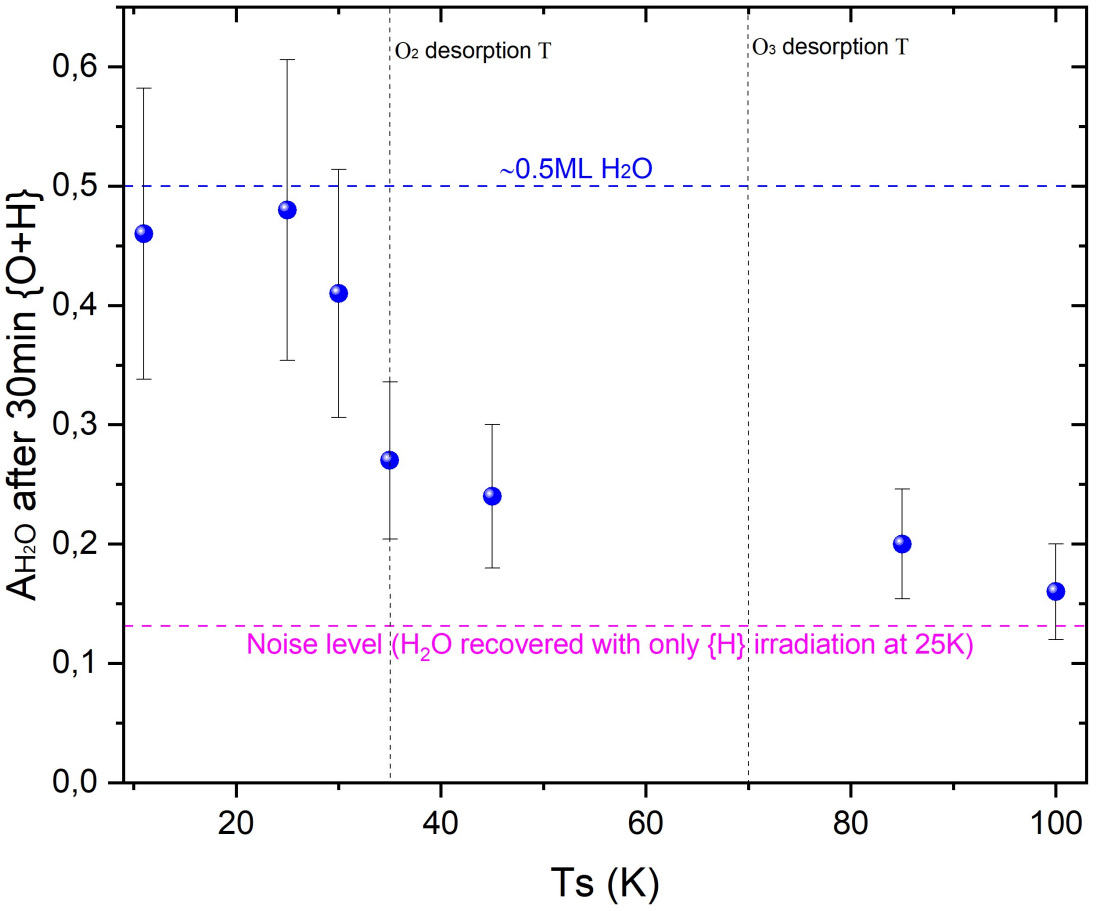

FIGURE 6.3: Area of H_2O after 30' irradiation dose at 11, 25, 30, 35, 45, 85, 100 K normalized to 1ML H_2O Area on Coronene. The error bars represent the standard error from standard deviation.

the desorption one of O_2, the integrated area of the oxygen peak shown here represents the actual molecules stuck on the surface, coming from the undissociated part of the oxygen beam as well as the ones eventually formed by atomic recombination, that have not resulted in water formation. The most H_2O is detected for the {O+H} exposure (black histogram) since, as expected, when hydrogen and oxygen atoms are sent together towards coronene, they can promptly react and undergo all the possible pathways. In this case hydrogen represents the limiting factor for a full water transformation, this is why we still observe a certain amount of O_2 and O_3. One has also to consider that a part of the newly formed water could have been returned to the gas-phase through chemical desorption. In fact, by comparing the total oxygen recovered when only oxygen atoms are sent to coronene ({O}, blue histogram) with the black histogram ({O+H} exposure), one can indeed conclude that more or less 1/3 of the overall oxygen is recovered when O and H atoms are sent together and only 1/6 of it is observed in the form of water desorbing from the surface.

The most O_2 is instead detected when coronene is exposed to only oxygen atoms ({O},

blue histogram). In this case in fact, except for the hydrogen that can be found on the surface or abstracted from it, oxygen atoms act alone in order to recombine (highest O_2 value in Figure 6.4) or to form O_3 with the available molecular one. As expected, this is when the smallest amount of water is formed.
On the other hand, the experiment with only hydrogen atoms ({H}, magenta histogram) irradiating the surface allows us to have an idea of the role of the surface in water formation and to be sure that the oxygen beam is the only source of O atoms in our system. No O_2 or O_3 are indeed recovered from the surface in these conditions, while there is a certain amount of water desorbing even after this experiment. It has to be considered that water could come from the beams as a pollutant or was already be present as a low background in the chamber. For this reason, the amount of water desorbed when only H atoms are sent onto the surface for 30 minutes at 25 K are taken in this study as the noise level (see Figure 6.3). Finally, we have investigated the effect of exposing coronene to the hydrogen and oxygen beams in sequence, therefore separately, and not together. In Figure 6.4 we show the two possible cases: when the 30 minutes exposure of oxygen atoms happens before the hydrogen one ({O} + {H}, red histogram) and the reverse situation ({H}+{O}, green histogram). In the first case, red histogram, we observe the second highest amount of water detected out of all the experiments, after {O+H}. A temperature of 25 K ensure in fact a residence time long enough to stabilize an interaction oxygen-coronene that will make the atoms available on the surface for the H atoms that are only going to be sent afterwards. However, since the amount of water is lower than the {O+H} experiment, we observe a larger amount of oxygen transformed into O_2. The max amount of O_3 is instead detected for the reverse experiment: {H}+{O}, green histogram. Contrary to what happens when oxygen atoms are sent before the H ones, in this case 25 K is a temperature already too high for the hydrogen atoms to reside on the surface long enough for the afterwards incoming O. For this experiment, the amount of water observed can be explained similarly to the {O} case.
All the results shown in this paper are therefore of extreme importance for a better understanding of water formation on carbonaceous dust grains at temperature up to 85 K, the role of a PAH-like surface at different temperatures and the effect of the interaction of oxygen and hydrogen atoms with coronene.

6.5 Discussion & astrophysical implications

The main results from this paper are 1) the formation of water on PAH-like carbonaceous surfaces for temperatures up to 85 K and 2) the catalytic role of coronene. To understand the astrophysical importance of these findings we have to focus on the ISM

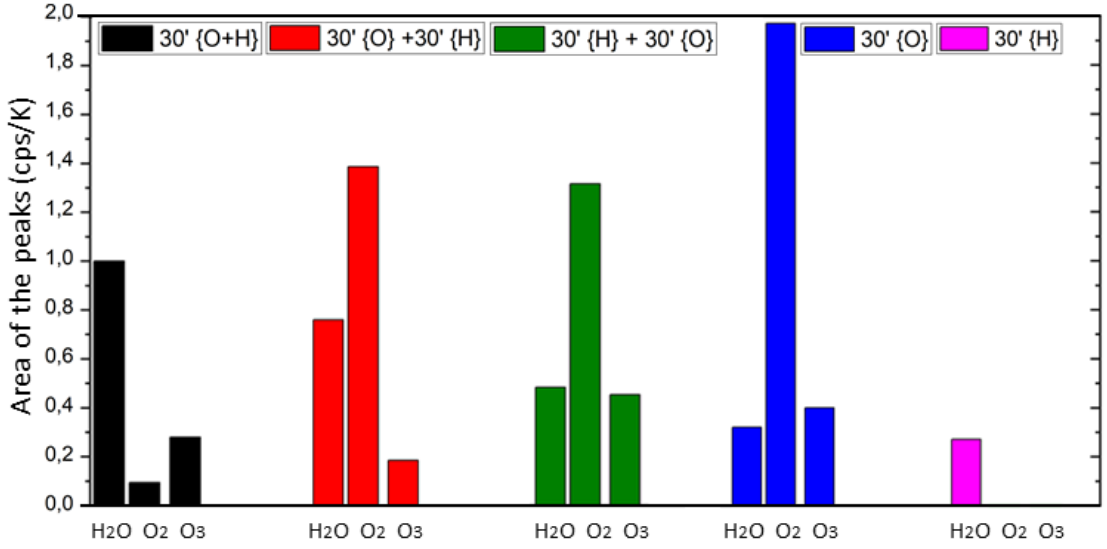

FIGURE 6.4: O_2 (from the irradiation, M32), O_3 (M48), H_2O peaks Area after {O+H} 30' irradiation at 25 K normalized to Area of H_2O recovered from the 30' {O+H} exposure.

phases where this could be relevant: the presence of PAHs, the physical conditions, such as the grains temperature, and the availability of O and H atoms.

6.5.1 Water formation at high temperatures

Talking about the high temperature formation of water on dust grains, one should zoom into the ISM regions right before the onset of the ice mantle (A_V = 0 - 3). In these regions there are wide temperature ranges, with values higher than the ones so far believed to be important to form water on grains and for ice mantle formation [Corby et al., 2018]. The temperature drops going towards denser regions reaching conditions widely studied and accepted. At lower T, around 10 K, the catalytic effect of the PAH surface no longer plays an important role, since the grains start to be covered in layers of ice. In these conditions new ice layers will form on top of the pre-existing ones and we only observe a thickening of the ice mantle. The observed ice abundances are in fact generally in agreement with considering water formed by atomic accretion from the gas phase followed by grain surface chemistry. From observations, the ice mantle formation threshold is believed to be around $A_V = 1.6$, near local cloud edges, and this is actually taken as the onset of rapid ice mantle growth after a first monolayer has formed [Hollenbach et al., 2009]. In fact, as stated in the introduction, in regions with A_V higher than 2, therefore in the so-called transition zones, it is more difficult to assess whether PAHs exist, as small grains or incorporated in the already existing icy mantles [Boogert et al., 2015]. The actual reasons behind the disappearence of typical PAHs features

from detection represent the many question marks about this phenomenon. JWST will for sure help in studying PAH abundances and give more details about different environments. As said before, coronene is one of the most stable and least reactive PAH species and, from the results obtained in this study, there is not enough evidence and experimental accuracy to exactly asses the eventual O or H lockup in the grain, while a prompt reaction to form H_2O is surely favoured instead. Water could start covering the surface at higher temperatures than considered before.
This process could have a relevant impact on the formation of other molecules whose formation depends on icy grains and their surface temperature. Many molecular reactions happening on dust grain icy mantles are indeed strongly temperature dependent, even if the ice does not exactly participate as a reactant itself. The most interesting ice-dependent species are complex organic molecules (COMs). They can form as by-products from the ices or by combination of photo-processing with UV photons penetration. In fact, some COMs are thought to be formed in translucent conditions where the built of ice mantles combines with an external UV field. In particular, some studies have focused on how these reactions and conditions could be relevant for new surface/ice reactions involving CH and CH_2. Other two COMs involved in energetic ice formation pathways are formamide and acetaldehyde [Martín-Doménech et al., 2020, Whittet, 2010]. The earlier set of ices on dust grains discussed in this paper would involve regions where higher temperatures and the presence of UV photons could have an effect on the formation of those molecules. Many aspects discussed in this section are summarized in Figure 6.5, that is here used to give a better idea of the regions in which the formation of water up to 85 K can be relevant: T_{grain} = 10 - 100 K, $0 < A_V < 3$ and a certain availability of oxygen and hydrogen atoms. Given the efficiency by which O atoms are transformed into water as soon as H atoms appear, and in the presence of catalytic surfaces such as PAHs, these regions could represent a perfect candidate for such reaction. For A_V lower than 1, where we actually have T_{grain} around 85 K, the eventually formed water is immediately injected into the gas-phase, where it can undergo photodestruction ($K_{H_2O^*}$ in Figure 6.5 represents indeed the ratio between its formation and photodestruction). After the H/H_2 front, water molecules remaining on the surface could start covering the grains by forming the very first sub-layers before the ice mantle regime ($A_V = 3$).

6.5.2 Hydrogenation and functionalisation of PAHs

In UV dominated zones (diffuse to translucent clouds, up to boundaries of dark clouds) proof has been found of hydrogenated PAH [Le Page et al., 2003, 2009] and it would be very useful to also assess the presence of functionalised PAH that would eventually

lead to water formation. In interstellar regions with number density $> 10^4/cm^3$, the O+H route seems to be crucial, it is thus reasonable to consider these reactions as relevant in environments where UV photons and atomic species dominate. In diffuse clouds and boundaries of the dense ones, $A_V < 3$, the O+H reaction route may be the only process for the efficient formation of the first monolayer of water ice on bare interstellar grains. Specifically, in regions with low UV flux PAHs are expected to be mainly neutral and possibly superhydrogenated [Allamandola et al., 1989, Le Page et al., 2003]. Even hydrogen already adsorbed or present on the surface could contribute in further hydrogenation of the newly formed OH. Rauls and Hornekær [2008] and Jaganathan et al. [2022] report the possible oxygen-functionalisation of PAHs where a subsequent H addition leads to the loss of the oxygen-functional groups via the formation of small oxygen-containing species such as water. There is experimental evidence for the enhanced reactivity of oxygen-functionalised PAHs as compared to their pristine analogues. The fast reaction with incoming H atoms could represent an explanation for why oxygen-functionalised PAHs are more elusive in the ISM gas-phase [Dulieu et al., 2019]. If the temperature of the system is below the desorbing temperature of water molecules in fact, the newly formed OH may remain on the grain forming ices.
PAHs are assumed to have an important role in providing a catalytic surface for reactions in the ISM, but they can also play a role in water formation and therefore ice formation extending the range of temperatures than previously thought. If we take into account the results of our work, for temperatures below 100 K this could already be happening. Regions characterized by $A_V < 3$, presence of atomic oxygen and hydrogen as well as neutral or superhydrogenated PAHs with temperatures higher than few tens of K, could therefore be the perfect conditions for the results presented in this paper, as summarized in Figure 6.5. So far, the formation of water on a grain has been mainly considered at temperatures around 10 K in cool or dense clouds, and there are studies about its formation at max 40 K and 50 K. The results reported here extend the temperatures of interest and could give new answers on why PAHs seem to disappear in transition zones by considering higher temperatures for the formation of ice in the ISM. Also, this study confirms and underlines the catalytic role of PAHs for the formation of small molecules such as H_2 and H_2O. If water can be formed by hydrogen and oxygen addition on PAHs, eventual water-PAH complexes could also lead to CO_2 formation driven by UV photons, as reported by the study of Potapov et al. [2019].

6.5.3 Evidence of grain growth

Another question of this project has been the possible lock up of oxygen into the carbonaceous grain, contributing to its growth and being a possible explanation for O

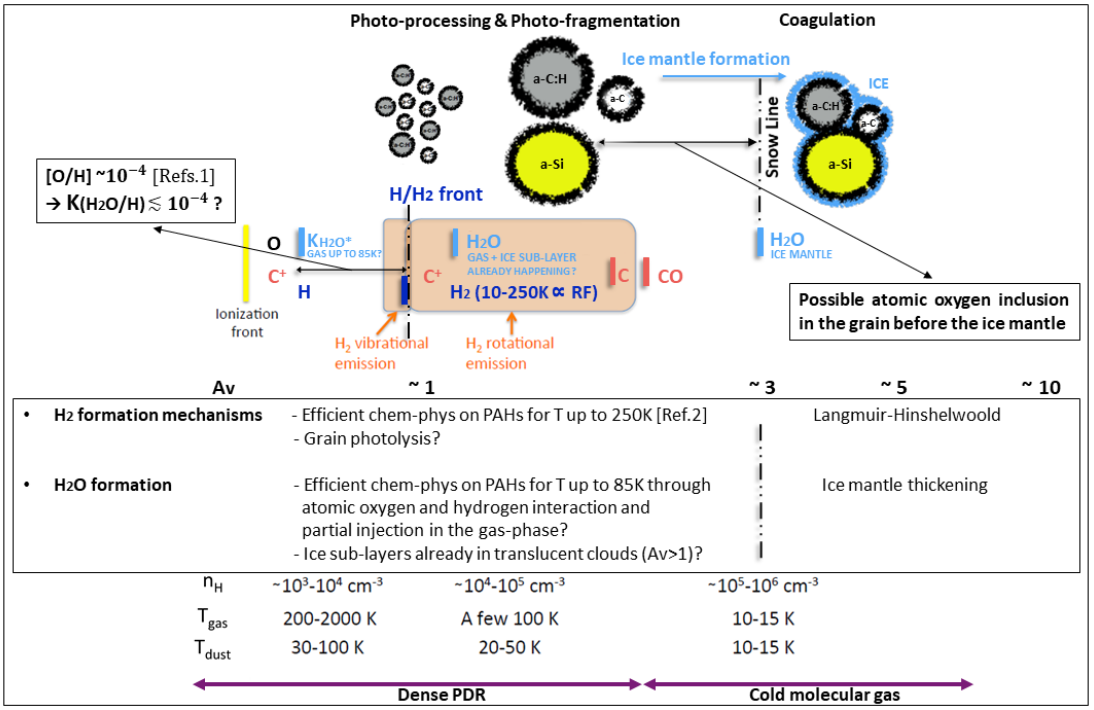

FIGURE 6.5: Summary schematic illustration of the main H_2 and H_2O formation processes in PDRs including the results of this study. Updated version of the scheme taken from Wakelam et al. [2017]. Refs.1: Fuente et al. [2019], Laas and Caselli [2019]. Ref.2: Grieco et al. [2023].

depletion. In our conditions, by using coronene and at a given experimental accuracy, it is not possible to easily assess whether oxygen is locked up in the surface. In order to verify the eventual inclusion of oxygen atoms in the grain we checked the surface with O_2 peaks after the irradiation, see green and magenta curves in Figure 6.1, and compared them to a reference taken before any modification. In order to study a possible evolution or morphological changes in the surface structure, we were aiming to see a certain change in the shape and/or position of the peak, in addition to recovering M16 or M32 (respectively m/z=16 for O and m/z=32 O_2) together with the desorption of coronene from the sample holder (at around 300 K, m/z=300). We have not observed a release of atomic or molecular oxygen upon surface desorption. The O_2 peak method has been used also to check the surface after irraditions up to 100 K, not only for 11 K and 45 K as shown in Figure 6.1. In all cases, we only observe a trend for the peaks to shift towards slightly higher temperature when less water is formed (higher temperature for the {O+H} exposure). In addition, our experiments are hampered by an uncertain input flux as suggested by the higher depositing flux for the O_2 peaks after irradiation. Due to additional possible changes in the sticking coefficient and the complex surface chemistry involved, it is not trivial to assess whether oxygen is locked up in the grain. Given the strong catalytic role of PAHs and the fact that we do not see any M16 or M32 desorbing with coronene, it is possible that oxygen has not been locked up in our surface,

therefore there is no direct sign of grain growth. Coronene-like structures could not be adequate surfaces, but also the experimental study of the oxygen depletion problem and grain growth seem to carry a very high complexity. Coronene corresponds in fact to a very small and stable structure that does not easily accumulate atoms or molecules inside. In our case, we observe how oxygen atoms suddenly react with the always available H atoms forming ices. There have been theoretical studies [Jones and Ysard, 2019] about the role of atomic O interacting with a-CH mantles of grains aiming to explain the disappearance of oxygen in the denser interstellar medium, or what they would define an "anomalous incorporation of oxygen into dense ISM". These doubts arise since the depletion of O, 40% of the overall abundance (170 - 255 ppm) [Whittet, 2010], is faster than incorporation into dust. They suggest incorporation of O into a-CH mantles to form epoxides and carbonyls. The latters functional groups can further react with CO_2 and O to finally give cyclic organic carbonates. Organic carbonates would thus solve the problem and explain the elemental abundances/depletions and ratios involved; they should form in the translucent ISM before ice mantles [Jones and Ysard, 2019].
There are other relevant works trying to address the oxygen depletion problem. Poteet et al. [2015] investigate if in the diffuse to dense cloud transition zone there is a chance for the missing, or not easily observable, oxygen to be locked up in big O-bearing grains opaque to IR radiation. Another option that they consider is the possibility of thick H_2O ice mantles being an important reservoir of oxygen as well. Those two solutions could both lead to an explanation for the missing oxygen, but only future observation can shed light on these hypotheses. Wang et al. [2015] consider instead the possibility of having µm-sized H_2O ice grains formed in dense clouds, but still present in more diffuse environments before being photo-sputtered. For both cases, the results of this paper could support the hypothesis that forming water ice at warmer temperature could either contribute to the formation of an eventual thicker ice mantle or to the existence of µm-sized ice grains before very dense environments. In Figure 6.5, apart from stressing on how the results of this paper could be crucial to understand the catalytic formation of water on PAHs up to 85 K, we also point out that a possible inclusion of oxygen atoms in the surface could happen only before the onset of the ice mantle. However, the formation of ices at higher temperatures than previously thought can still be considered to contribute to the explanation of O depletion. Also, in conditions where H atoms are so abundant, their interaction with oxygen through a PAH surface would most probably lead to water molecules formation rather than O atoms inclusion in the structure. Finally, we want also to acknowledge how the results provided in this paper could be used to help answering new questions in other fields. The formation of water on carbonaceous grains at temperature higher than so far demonstrated could help understanding why H_2O would remain frozen in relatively warm environments. This could give new insights in the study of snowlines in protoplanetary disks [Tinacci et al., 2023].

This study, even if it is not providing answers or supporting the organic carbonate route in the case of coronene and possible grain growth, confirms the role of small and stable PAH-like structures as catalysts. It opens the door to further experiments that should focus on surfaces that could more easily incorporate atoms into their structures and be more easly functionalised in order to assess grain growth and interstellar elemental depletions.

6.6 Conclusions

In this paper we provide experimental evidence of water molecules forming on a PAH-like surface by oxygen and hydrogen accretion from the gas-phase at temperatures up to 85 K. This study represents another crucial experimental proof of carbonaceous surfaces being efficient catalysts.

In a previous study from our group we have reported new results that extend the H_2 formation temperatures up to 250 K, when coronene is used as surface. We demonstrated the possibility of chemisorption as an explanation for the H atom recombination on coronene at high temperatures [Grieco et al., 2023]. The same happens in this set of experiments when O and H atoms are sent to the surface. All three mechanisms leading to water formation can happen in our conditions, with different probabilities and efficiencies depending on the temperature at which the surface is kept. About 1/2 ML of water is formed and detected for temperatures around 20 K with 30 minutes {O+H} coronene exposure, and a non-negligible amount above the noise level is still recovered at 85 K. Thus, also in this case, as for H_2, coronene plays a very important catalytic role.

Chemisorption is the phenomenon that would explain why O and H are still on the surface and react at temperatures above 40 K. Temperatures at which atoms start to desorb are usually very low if only physical bonds are involved while here we observe the resilience of the atoms staying on the surface at higher temperature to further react or recombine. This is a typical example of chemisorption where the stabilization happens through actual chemical bonds that need higher energies/temperatures to be broken and result in the desorption of the species. This naturally has a direct effect on the residence time and it gives more chances to go through other processes while being on the surface. In our system O atoms can chemisorb on the surface forming O_2 and O_3, as well as OH and finally H_2O as soon as H atoms appear.

In our conditions we indeed observe how water formation is extremely favoured, but we are not able to precisely asses an eventual atomic lockup in the surface resulting in grain growth, functionalization or morphological change by only using a reference O_2 peak as

a probe.

Here we also want to mention the importance for these results to be taken into account for future and/or ongoing JWST projects in characterizing PAHs to be eventually combined with H_2O observations in order to study their potential impact on its formation at warm temperatures. There are already some first JWST results by the PHANGS group studying the changes, over three nearby galaxies, of the average PAH sizes as well as their ionization state. They report regions with hotter PAHs and a more important heating/change in PAH size correlation with higher molecular gas content [Chastenet et al., 2023]. Future studies on PAH characterization by mapping their sizes, temperature and ionization state in different regions could help to further understand their role for physical-chemical processes happening on dust grains and eventually support the warm temperature formation of H_2O on those catalytic surfaces.

Considering the stability of coronene and the ability to stabilize species to further making them react, we can conclude on its incredible catalytic role and extend the range of temperatures for the formation of water. We stress that also the potential formation of other molecules on carbonaceous grain surfaces at high temperatures should be considered in the future.

Chapter 7

Introduction to codes in astrochemistry

Several methods are nowadays used to study astrochemistry in terms of dust grains interacting with gas-phase elements. At the very beginning, in the development of gas-grain models, gas-phase models were implemented to interpret surface reactions and the grain surface chemistry was treated almost as gas-phase chemistry. The main problems with this approach were found in the regime where the surface abundance is low, the so-called "accretion limit". The importance of dust grains for the formation of relevant molecules such as H_2 and H_2O had been understood already in 1949 [van de Hulst, 1949], when also the role of grain surface chemistry, to study the processes happening in the ISM, became more popular. Since then, several methods have been developed to reproduce at best all the astrochemical conditions. Different techniques have been applied to surface astrochemistry, for instance by trying to start from new experimental information. Experiments are, in fact, crucial to test the physical and chemical processes happening in the ISM, but models are needed to actually understand the relevant astrochemical timescales. Codes represent the bridge between experiments and observations and they are very important to understand how experimental results can be applied to the observed processes in a MC. The main differences between the several available gas-grain models relate to the computational cost/time needed to have enough details to be able to study the physical and the chemical evolution of the systems in real time. In fact, all these numerical models seem to be able to answer and solve important aspects, but also to have several limitations [Cuppen et al., 2013].

Gas-grain codes can use several approaches to model the chemistry and the physics involved in the interaction of dust surfaces with gas-phase species in different ISM regions. There are some codes that focus on the chemistry by using binding energies and reaction rates (rate equations and molecular dynamics methods, with different timescales), while

others provide a more detailed description of the gain surface, being able to account for its inhomogeneities as well. For example, Monte Carlo simulations represent stochastic methods to either study the single interaction of a species with each surface binding site, even at long timescales (i.e. random-walk microscopic MC, see Cuppen et al. [2009]), or they can provide results to describe an averaged overall behavior of the system (macroscopic MC) [Cuppen and Herbst, 2007].
Lastly, we introduce photo-ionisation and dissociation models that are capable of modeling the observed emission (continuum and lines) from the ionised gas all the way to the PDRs and dense gas. Given the relevance that PDRs assume in this Thesis, it is important to mention the field of PDR-modelling and the main codes available. PDR modelling started in the 70s [Hollenbach et al., 1971], when the first codes implemented the study of the H to H_2 transition and the molecularization of C^+ into CO. In general, PDR models try to address the chemical, physical and thermal structure of a cloud close to a radiation field, source of FUV ionizing photons with a variety of assumptions and simplifications [Röllig et al., 2007].
An overview of the main characteristics of the available codes and a more detailed description of the ones chosen for the projects reported in Chapter 8 and 9 are given below.

7.1 PDR codes

PDRs codes are characterized by a close interaction between chemical-thermal balance and radiative transfer. Typical PDR codes solve the local chemistry to determine local densities, energies and physical properties like temperatures, pressures, level populations. Every code includes different assumptions and approximations, but in general the main aspects are the geometry of the cloud interacting with the RF, the description of the chemistry involved, the type of RF, the treatment of dust grains and the possibility to study the gas-phase through its cooling and/or heating functions. Every model also shows limitations in terms of ranges of input parameters that can be used, affecting the different possible model outputs and numerical treatments.
The individual strengths and weaknesses of each available PDR code are summarized on the website: https://lecture.ph1.uni-koeln.de/pdr-comparison [Röllig et al., 2007].
In this Thesis, and specifically in Chapter 8, we have used the `Cloudy` code, version c23, to tackle the theoretical follow-up of Chapter 5 and to study the possible implications of the high temperature formation of H_2 on PAHs for typical PDR pictures.
Cloudy is an ab initio spectral synthesis code for astrophysical plasmas ranging from far to to Local Thermodynamic Equilibrium (LTE) and Strict Thermodynamic Equilibrium

(STE) [Chatzikos et al., 2023]. A more detailed description of `Cloudy`, to understand the methods reported in Chapter 8, is given in the following section.

7.1.1 `Cloudy` code brief description

`Cloudy` is a numerical photoionisation code written in Fortran and first released in 1978 to simulate plasmas and their spectra. `Cloudy` provides an accurate description of chemical and physical processes at atomic and molecular levels. By assuming that the energy is conserved and all the atomic processes have reached steady state, it calculates the ionization state of the gas-phase species, the related chemistry (based on UMIST network database [McElroy et al., 2013]), and gas kinetic temperatures. In our case, we were interested in the emission level populations of the studied systems therefore they have been modelled through the `Cloudy` cooling functions. The code also solves grain physics and it calculates the observed dust emission spectrum. `Cloudy` divides a cloud into concentric zones of almost constant physical conditions. Usually, the code computes 100 to 200 zones in an optically thick model of an HII region. Thus, this code predicts the thermal, ionization, and chemical structure of a cloud within certain limits, and predicts its observed spectrum in a self-consistent way. This is done by simultaneously solving the statistical and thermal equilibrium equations. The main code boundaries concern the kinetic gas temperatures (between 2.7 and 10^{10} K), low density limits and the radiation field (30 meV to 200 MeV). In order to obtain those results, one needs to specify the shape and intensity of the external radiation field reaching a cloud, the chemical composition and grain content of the gas, and the geometry of the interacting gas. [Ferland et al., 1998, 2017]

- Radiation Fields

  A defined central object emits radiation that defines the incident RF illuminating the cloud. The incident RF therefore describes the very energy source of the system. While the radiation travels through the cloud, dust extinction diminishes the incident RF defining the net emission that emerges from the shielded side of the cloud. The Transmitted Field thus is the sum of the attenuated RF and the Diffuse one. The Diffuse Radiation Field represents the emission of gas and grains within the interacting cloud. Finally, there is a Reflected Radiation Field which is the emission by the illuminated side of the cloud facing the RF source. It is the sum of the emission from the interacting cloud (Diffuse) and the backscattering of the incident RF. A visual scheme is given in Figure 7.1.

- Shape and Intensity of the RF

  Both the shape and intensity of the external Radiation Field ionizing the cloud

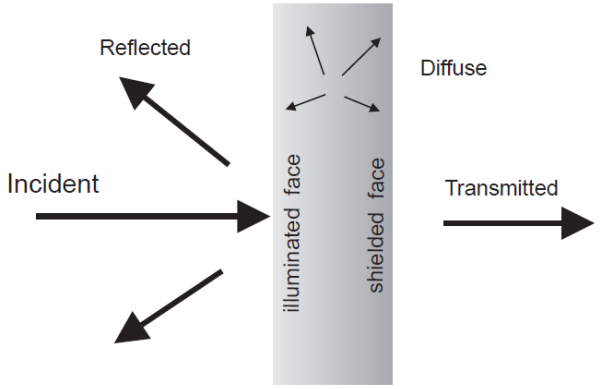

FIGURE 7.1: The different Radiation Fields considered in `Cloudy`.

need to be specified. The shape of the RF is defined in terms of spectral energy distribution (SED), but it has to be within the limits reported above. A fundamental form to specify the RF is for example the blackbody emission. The intensity or luminosity of the external Radiation Field can be given either as the flux striking a unit surface area of cloud or as luminosity radiated by the central object. The intensity and luminosity define the strength of the radiation field.

- Chemical and grain composition
  `Cloudy` considers the lightest 30 elements of the ISM. Grains are included if specified and they can be described in different ways (e.g. PAHs and their sizes in terms of number of C atoms). The code treats all the photo-ionization states that are included as ionization mechanisms, from valence to inner molecular and atomic shells. The chemistry includes many molecules and it goes to fully molecular limits (H in H_2 and C or O in CO). The default composition is solar but several other standard mixtures can be specified.

- Geometry
  In the simplest case the geometry is spherical, or plane parallel if the inner radius is much larger than the thickness of the cloud. The output at the end of the calculation underlines whether the geometry was plane parallel (the ratio of the thickness to the inner radius, ($\Delta r/r_0 < 0.1$), a thick shell ($\Delta r/r_0 < 3$), or spherical ($\Delta r/r_0 > 3$). A schematic picture is presented in Figure 7.2.

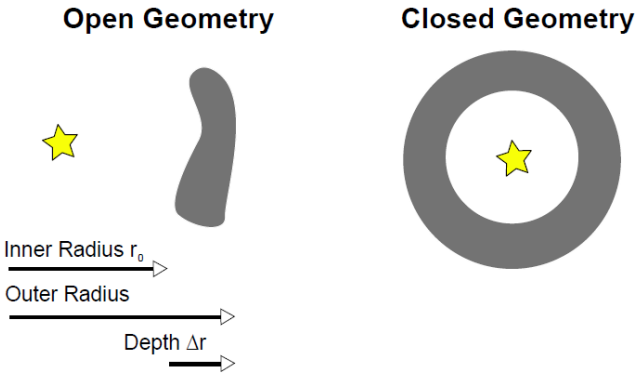

FIGURE 7.2: Two limiting cases of geometries can be assumed. The star is the source of ionizing radiation and the shaded area represents the cloud. An open geometry is the default, and a closed geometry will be computed if the sphere command is entered. The radius is the distance from the center of symmetry, usually the center of the central object, to a given point. The depth is the distance between the illuminated face of the cloud and a point within the cloud. The inner radius is referred to as r_0, the depth is Δr, and the current radius is r. The depth or radius for a zone is the distance to the center of the zone.

7.2 Gas-grain chemistry codes

Given the importance of dust grains in astrochemistry for observed extinction of the starlight, shielding and being responsible for molecular complexity, it has been important to develop models accounting for both gas and grain chemistry and for the description of their interface. The usual approaches to combine these two phases involve various numerical methods with different degrees of complexity: molecular dynamics, rate equations, the master equation approach, macroscopic KMC (Kinetic Monte Carlo) method and the microscopic one. [Ruaud et al., 2016]

As already mentioned, each comes with a different level of chemical and physical accuracy, limitations, computational cost.

In particular, molecular dynamics helps in a good description of the system and molecules involved in terms of orientation and location of the species, but the simulated time is so small that it stays within the picosecond and the nanosecond frame.

Rate equations can cover the lifetime of a molecular cloud, with a moderate computational cost, but with weak description of the molecules. The species are only treated in terms of numbers and their exact position is not accessible. Solving these equations for a system is of extreme importance though, because they can give constants and insights about all the processes happening on the surface (adsorption, desorption, diffusion, reaction rates). Finally, KMC seems to lie in between, even if several versions of these models can be found, all with different levels of difficulties in terms of computations and applications. In particular, the KMC methods had been introduced to solve the problem of the accretion limit, by solving the master equations they can simulate long

timescales. Master equations provide a stochastic description of the system, with the probability of having a number species in certain positions on the surface. If the number of particles expands, either by a change in physical conditions or by increasing the number of considered species in the model, the number of equations becomes exponentially higher. Already this can be seen as a limitation, since atomic coordinates restrictions have to be put, and the physical interactions become not so realistic anymore. Moreover, traditional KMC models work by defining a table of events that, even if it is difficult but possible to be defined in for crystalline grains, it becomes impossible for amorphous ones, that is most of the time the case for ISM grains and ices. To overcome these problems, new directions have been undertaken, all of them requiring the use of other methods, together with KMC, or a combination of them, resulting in a more complicated method and more computational costs [Cuppen and Herbst, 2007]. The model that has been taken into account for the development of Chapter 9 is the `Nautilus` code, developed at Laboratoire d'Astrophysique de Bordeaux. In particular, its new 3-phase version is able to account for gas, grain surface and grain mantle in separate ways in order to better describe the dynamics of a system by using differential equations. A more detailed description is given in the following section.

7.2.1 `Nautilus` code brief description

The model here described is `Nautilus` and takes the name from the one developed by Hasegawa et al. [1992], a 2-phase model one (gas and overall grain description). A 3-phase code that distinguishes between grain surface and mantle has been introduced a year after by Hasegawa and Herbst [1993]. A limitation still present in that version was the inert mantle description, that has been improved in the current version in a chemically active participation of the under-surface mantle since photodissociation, diffusion and recombination should be at work in interstellar grain mantles. Bulk diffusion is driven by the diffusion of water molecules in the ice, both accretion and desorption only occur between the gas and the outer layers and chemical reactions can occur in the mantle, with a smaller diffusion rate of the species compared to the surface [Ruaud et al., 2016].

The 3-phase `Nautilus` code has been developed at the Laboratoire d'astrophysique de Bordeaux by a group of researchers led by Valentine Wakelam, from the original code of Hasegawa et al. [1992]. The code uses differential equations to describe the gas, the surface and the mantle of the grains. The equations contain reaction rate coefficients, accretion, ionisation and dissociation (cosmic rays, UV) rates. The model describes the mantle-surface species swap (it depends on the thermal hopping), diffusion and desorption (thermal or not). More details can be found in Ruaud et al. [2016]. The surface

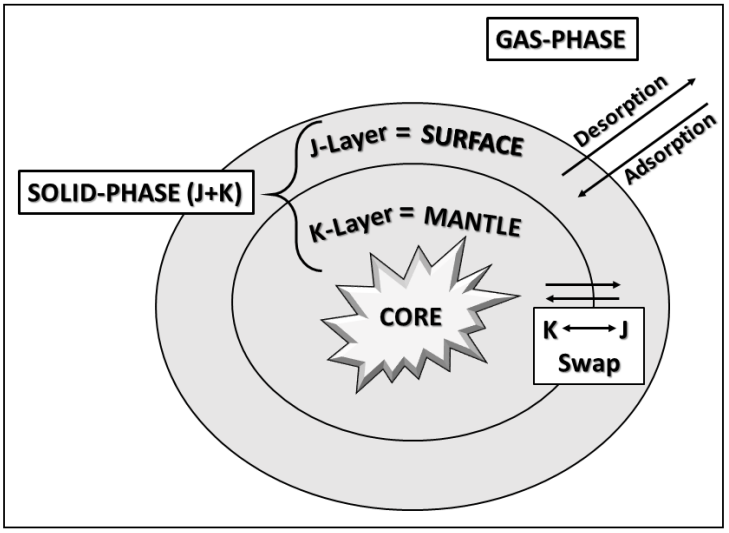

FIGURE 7.3: Schematic picture of the 3-phase (gas, J, K) `Nautilus` system with the main processes involving dust grains and their interaction with the gas-phase.

reactions are considered mainly through a Langmuir-Hinshelwood mechanism so that two gas-phase species adsorb on the surface to further meet and eventually react, diffuse and desorb. This mechanism is the most effective for the low diffusion energy to binding energy ratio used in the code (0.4), except for H for which a specific value is used instead. One has to take into account also the limitations, since the comparison of the computed abundances in dark clouds with some observations has shown less good agreement when compared to the 2-phase model because of large accretion on the grain. This strongly constrains the chemical-age of these clouds to be of the order of a few 10^5 years and strongly rejects the largest ages of few 10^6 years for dark cloud applications [Ruaud et al., 2016]. The limitations and comparisons between the 2- and 3-phase model in the case of translucent clouds has not yet been reported in literature.

A simple study trying to reproduce a typical TC environment is given in the Result and Discussion Section (9.3) of this Chapter. The documentation given by the `Nautilus` developers helps using the code and easily tuning some parameters in order to better describe the purposes of the research as well as to familiarize with the very useful tools provided. Figure 7.3 shows a scheme of the 3-phase `Nautilus` described in this Section, to give a visual idea of the different structures, layers and processes used in the code.

Chapter 8

Modelling the effect of high temperature H_2 formation on the location of the DF in a classical PDR picture with `Cloudy`

This Chapter discusses the results of a collaboration started right after the publication of the paper reported in Chapter 5 [Grieco et al., 2023] with the second author of that paper. After obtaining such novel results, the first idea was to rapidly check if the efficient high temperature formation of H_2 on coronene could have a direct effect on the typical PDR picture, specifically on the location of its DF. Thus, the aim of this study is to find a way to implement the experimental data into a photo-ionisation and -dissociation code, `Cloudy` in our case, to investigate this question.

The undersigned PhD student has performed the fitting of the experimental results of Chapter 5 and their implementation in `Cloudy`, the data analysis and interpretation. The idea behind studying the effect of the high T H_2 formation on the location of the dissociation front (DF) in PDRs has been firstly proposed by Dr. Patrice Theulé (collaborator of the project and second author of the published paper presented in Chapter 5). The discussion and the astrophysical implications of the obtained results have been discussed together with Prof. Ilse De Looze, Prof. François Dulieu and Dr. Patrice Theulé.

8.1 Introduction

A general description of PDRs and their physical-chemical structure has been given in Section 1.2.4, but here the focus will be on the molecular hydrogen formation in PDRs and how the experimental results presented in Chapter 5 might have an effect on the location of the Dissociation Fronts. PDRs are mainly neutral regions of the ISM and their conditions in terms of physics and chemistry depend on the radiation fields that illuminate the PDR. In the PDR, we observe the transition of gas from atomic to molecular. Since H_2 is the main and most abundant molecule of the Universe, it is of particular importance trying to understand its formation and distribution in PDRs. The main formation mechanism of molecular hydrogen is considered to take place on grain surfaces. Depending on the surface temperature, H_2 can form through two different reactions. The Langmuir-Hinshelwood mechanism describes two physisorbed H atoms migrating on a dust grain surface that react and desorb as H_2; the Eley-Rideal mechanism concerns a gas phase hydrogen atom reacting with a chemisorbed one forming a molecule. Based on the results of high temperature formation of H_2 on coronene presented in Chapter 5, Eley-Rideal is the most interesting mechanism, being effective at high dust temperatures at stake in PDRs. As already discussed in Chapter 5, H_2 formation rates on PAHs were previously thought to reduce for grain temperatures above 50 K with H atom recombination being highly efficient only below 20 K and the impossibility for molecular hydrogen to form above 100 K. In particular, Habart et al. [2004] had set upper limits for the gas and grain temperatures that would still allow a certain and efficient H_2 formation rate, with T_{gas} around 300 K and T_{grain} of about 30 K (considering the grain at thermal equilibrium with the radiation field). The PDR conditions are totally controlled by the local gas density and the intensity of the RF. The dust grains, heated by the UV and optical photons of the RF, always have a temperature lower than the gas T and T_{dust} decreases going towards the inner parts of the cloud. Since the formation of molecular hydrogen strongly depends on the grain temperature which depends on the RF, one has to consider that the physical and the chemical processes vary with the depth of the cloud, A_V. The UV field is indeed progressively attenuated by dust. As already presented in Section 1.2.4, the resulting PDR structure is composed of different layers: a hot atoms region before the H/H_2 transition (DF front), a molecular layer still warm between the H/H_2 transition and the $C^+/C/CO$ transition, and the typical cold and dark molecular cloud afterwards. Even if the behavior and the general description of the gas temperature inside a PDR is well understood, it is not the same for the surface temperature of dust grains, especially for small grains and PAHs. They are thought to have temperature fluctuations showing spikes of a few 100 K, due to the presence of UV photons in certain regions [Desert et al., 1986, Draine and Li, 2001]. The temperatures of the grains can determine and

change the formation rate of H_2 in the PDR and, therefore, shift the typical depth at which we observe the DF. The position of the DF will have important implications in terms of chemical diversity and physical conditions at a given cloud depth A_V. In this Chapter, we aim to implement our experimental results on highly efficient H_2 formation on PAHs at high T in a PDR model to study the implications. Also, H_2 formation on PAHs is an important contributor to the total H_2 formation rate and one has to consider that the emission of PAHs coincides with the presence of H_2 molecules [Van De Putte et al., 2024]. As already mentioned in Section 1.3.2.1, JWST is providing new insights with regards to the transitions between the ionization and dissociation H fronts of PDRs and the community is now able to spatially resolve the high T rotationally and vibrationally excited H_2 lines. Since the H_2 detections in the NIR/MIR with Webb trace warm H_2 gas, these new data provide an ideal test ground for our experimental model of high T H_2 formation of dust grain surfaces. So far, PDR models have used the typical temperatures for H_2 formation on grains. Here we present the attempt to implement a new formation rate for molecular hydrogen resulting from the fitting of the experimental results of Chapter 5. We used `Cloudy` to predict PDR structures, namely the location of DF and IF, the emission of the main species involved (H, C, O), and the main H_2 emission lines, exploring several gas densities and ionization parameters. [Wakelam et al., 2017, Castellanos et al., 2018, Hollenbach and Tielens, 1999, Habart et al., 2003, Cazaux et al., 2016]

8.2 Methods

In this study, we have used the c23.00 version of the `Cloudy` code described in section 7.1.1. The first way to approach the goal of this study has been to obtain a reference and classical PDR picture by using `Cloudy` with a set of standard inputs. To have an overall description and for the aim of this work, it was important to focus on the hydrogen IF and DF together with the transitions associated to carbon (C^+/C/CO). Table 8.1 displays the very first important parameters chosen to run `Cloudy`. The input parameters have been selected from standard sets provided by `Cloudy` in order to obtain a result that has physical meaning when compared to literature [Wolfire et al., 2022], mostly in terms of positions of the IF and the DF. The main scope is to provide a side-by-side parallelism between the standard results and the outcomes from forcing the H_2 formation on grain with the coefficients obtained from the experimental data of Chapter 5.

The ionization parameter is the dimensionless ratio of hydrogen-ionizing photon to total-hydrogen densities and it is taken in its log value. Its precise physical expression is

TABLE 8.1: First inputs used in `Cloudy` to test the methodology and obtain the reference PDR structure of Figure 8.1.

INPUTS NAME	VALUE/DEFINITION
Shape and Intensity of the RF	Table star BC03
Abundances of the interacting gas/cloud	Table 8.2
Ionization parameter (U)	-1
$n_{\rm H}$ (gas density)	1000 $\rm cm^{-3}$
Geometry of the interacting gas/cloud	Spherical
Grains type	ISM grains + PAHs (size distribution from Abel et al. [2008])
Chemistry	Full H_2 chemistry database
$A_{\rm V}$ (stopping parameter)	10

TABLE 8.2: Input fractional abundances wrt H for all the species included in the gas/cloud interacting with the RF in `Cloudy`.

Hydrogen	1.00	**Sodium**	1.62E-06	**Scandium**	1.45E-09
Helium	9.77E-02	**Magnesium**	3.63E-05	**Titanium**	8.51E-08
Lithium	1.90E-09	**Aluminium**	2.69E-06	**Vanadium**	7.76E-09
Berylium	2.09E-11	**Silicon**	3.16E-05	**Chromium**	4.17E-07
Boron	6.41E-10	**Phosphorus**	2.57E-07	**Manganese**	2.63E-07
Carbon	2.65E-04	**Sulphur**	1.32E-05	**Iron**	3.31E-05
Nitrogen	6.17E-05	**Chlorine**	1.78E-07	**Cobalt**	8.51E-08
Oxygen	5.75E-04	**Argon**	2.51E-06	**Nickel**	1.58E-06
Fluor	2.75E-08	**Potassium**	1.10E-07	**Copper**	1.51E-08
Neon	1.23E-04	**Calcium**	2.09E-06	**Zinc**	3.63E-08

reported below:

$$U = \frac{Q(H)}{4\pi r_0 n(H) c} \equiv \frac{\Phi(H)}{n(H)c}; \tag{8.1}$$

where r_0 is the separation [cm] between the center of the source of ionizing radiation and the illuminated face of the cloud, n(H) [$\rm cm^{-3}$] is the total hydrogen density (ionized, neutral, and molecular), c is the speed of light, Q(H) [$\rm s^{-1}$] is the number of hydrogen-ionizing photons emitted by the central object, and $\Phi(H)$ [$\rm cm^{-2}\ s^{-1}$] is the surface flux of ionizing photons.

With these first parameters, we obtained a full description of the species for visual extinction up to 10 and we were therefore able to have a first idea of the hydrogen and carbon atomic to molecular transitions. In Figure 8.1 the PDR structure of this first standard model is shown with the Ionization and Dissociation Fronts, where the abundances of the main species such as H^+, H, H_2, C^+ and CO are plotted versus the visual extinction. We obtain a typical PDR picture comparable to a general description, as shown in Figures 1.2 and 1.4 (Chapter 1). Once we had a reference PDR scheme from our inputs, it was time to start studying the implementation of the experimental findings of Chapter 5 in the code. `Cloudy` treats the molecular hydrogen formation on grains by using a general modified Arrhenius equation, usually used in all astrochemistry

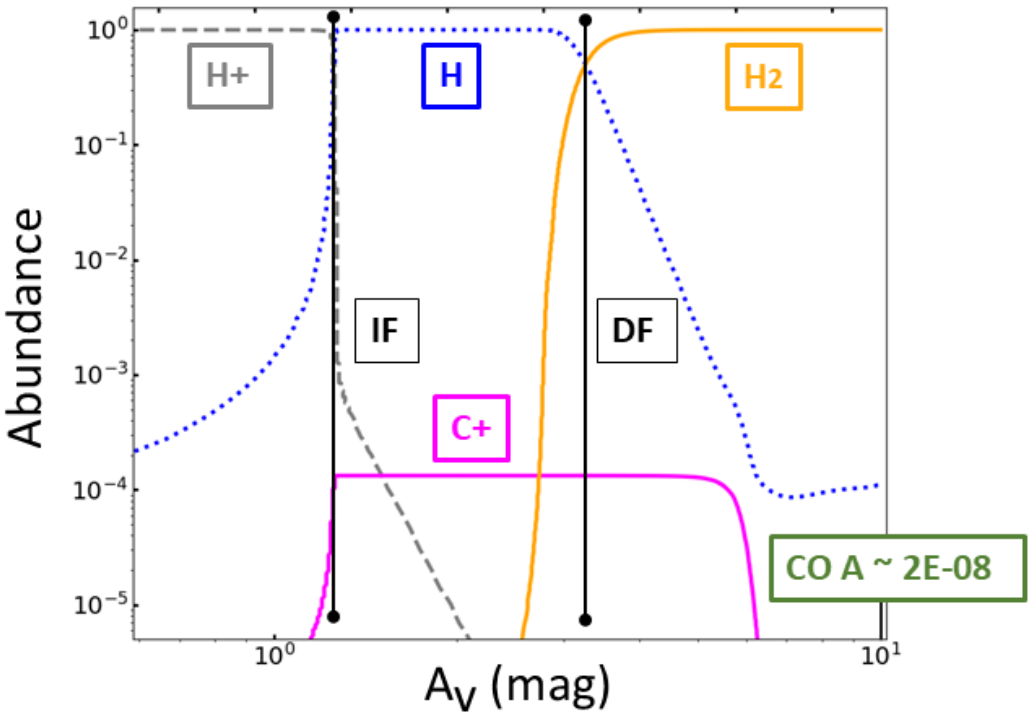

FIGURE 8.1: Reference PDR picture with IF and DF, including H^+, H, H_2, C^+ and CO, from the inputs of Table 8.1.

codes. As reported by Meisner et al. [2019], the equation is the following:

$$k(T) = \alpha \left(\frac{T}{300\,\mathrm{K}} \right)^{\beta} \exp\left(-\frac{\gamma}{T} \right) \tag{8.2}$$

Here, the parameters α, β and γ are obtained by fitting to either experimental measurements or from accurate computations, thus α, β and γ are purely fitting parameters. In `Cloudy`, the line regarding the H_2 formation on grains is described as only dependent on the α parameter, thus this coefficient had been selected as the main character of this study. Before going to the main core of the methodology, it was very relevant to have a first idea of the degree of dependence that the DF has on α. In Figure 8.2, we show an example for increasing α values, from the reference one of 1 up to 1000. One can notice that the DF, i.e. the transition from atomic to molecular hydrogen, shifts towards lower values of A_V. This suggested that the efficiency of H_2 formation can have an impact on the location of the DF.

In order to express the experimental results reported in Figure 5.3 (Chapter 5) for the D_2 recombination rate on coronene in terms of the modified Arrhenius equation presented above, we proceeded with an analytical fitting of the data. Figure 8.3 shows the outcome of a regression that approximates the experimental data to a modified Arrhenius equation. The resulting equation is the following:

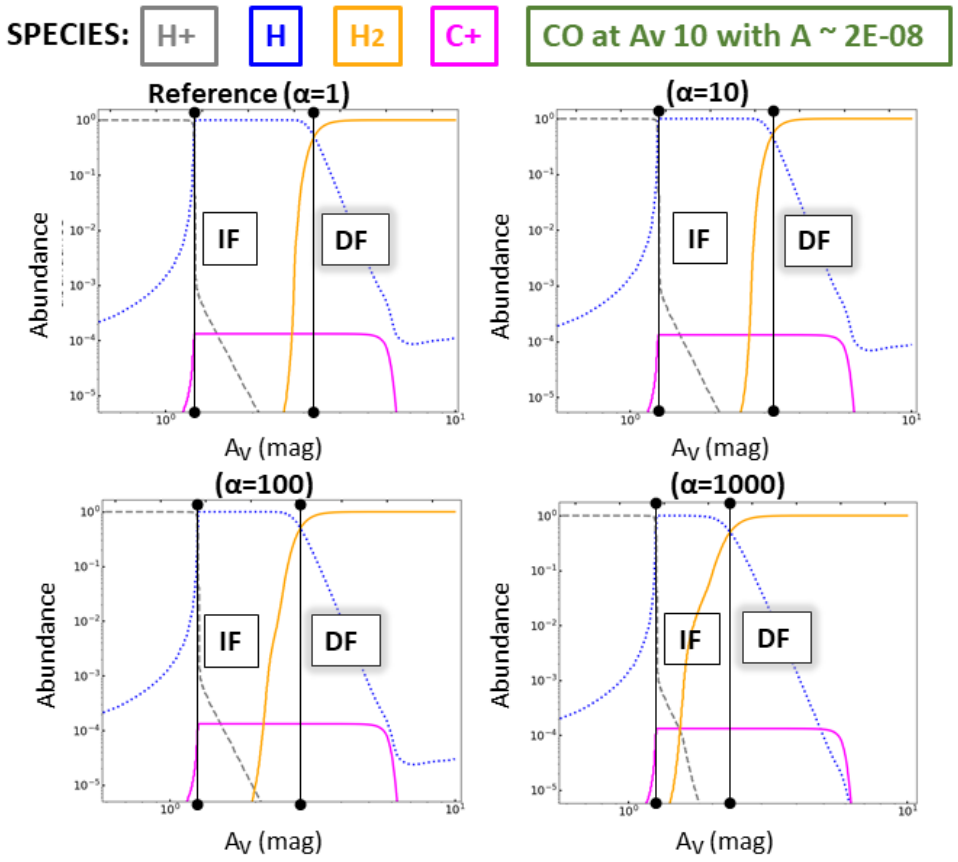

FIGURE 8.2: PDR pictures with IF and DF, including H^+, H, H_2, C^+ and CO, from the inputs of Table 8.1 for different values of α.

$$k(T) = 15 \left(\frac{T}{300\,\mathrm{K}}\right)^{-0.5} \exp\left(-\frac{5}{T}\right); \tag{8.3}$$

with errors on $\alpha = \pm 2$, on $\beta = \pm 0.1$ and on $\gamma = \pm 3$.

8.3 Results & Discussion

Once the PDR reference picture with IF and DF and the methodology to implement the experimental data from Chapter 5 were found, we proceeded with trying to obtain a PDR scheme that took into account the formation of H_2 on coronene up to 250 K. Comparing this experimental $\alpha = 15$ value to the values used to explore the H_2 formation on grains in `Cloudy` in Figure 8.2, we do not expect to have such a big shift of the atomic to molecular hydrogen transition location by only checking the ionization and dissociation fronts in this very qualitative way. This is in fact visible in Figure 8.4, where we show the PDR picture obtained with `Cloudy` when the α coefficient found by fitting the experimental data is used. After obtaining this result, we decided to add a prediction of the main H_2 emission lines in order to verify if in this way an eventual

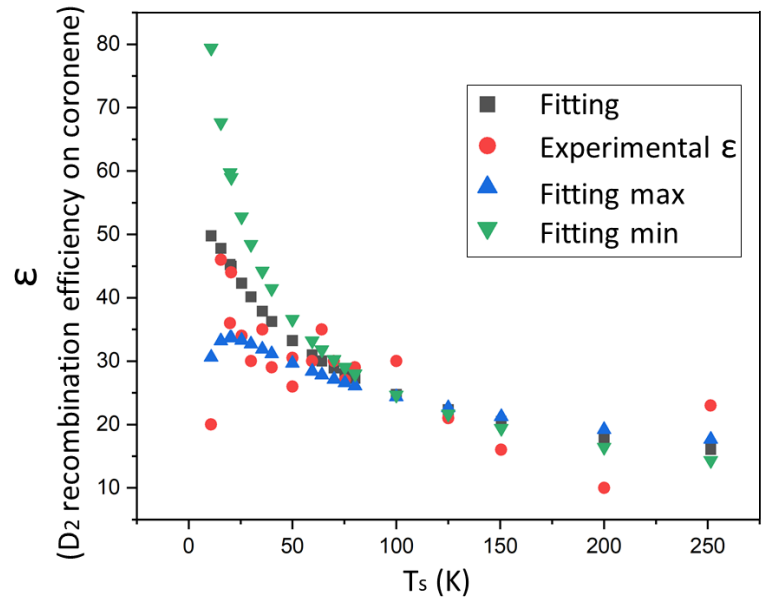

FIGURE 8.3: Fitting of the experimental data displayed in Figure 5.3 with the modified Arrhenius equation (eq. 8.2). The fitting is a non-linear regression using the least squares method without including the ϵ error bars. The min and max fitting curves represent the extremes of the model within the uncertainty of the parameters.

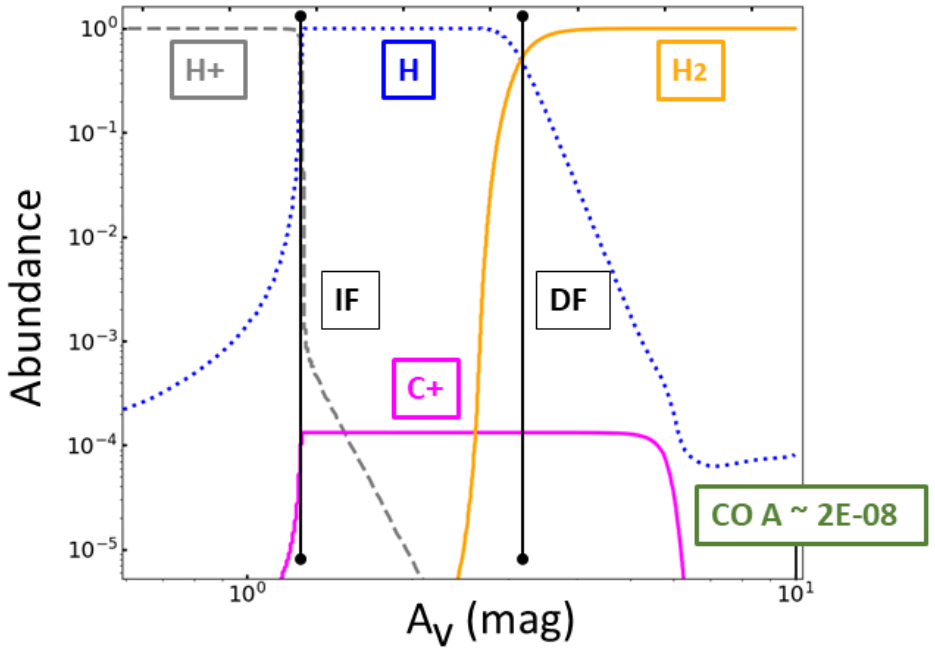

FIGURE 8.4: PDR pictures with IF and DF, including H^+, H, H_2, C^+ and CO, from the inputs of Table 8.1 obtained by using the α coefficient from eq. 8.2

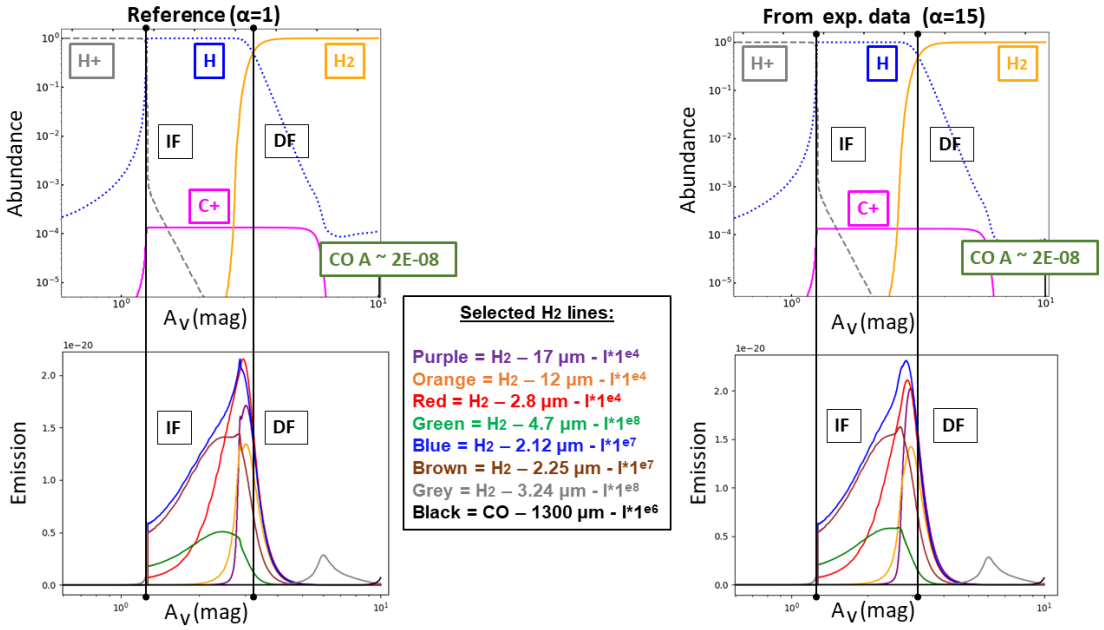

FIGURE 8.5: Comparison between the PDR pictures with IF and DF, including H^+, H, H_2, C^+ and CO, from the inputs of Table 8.1 obtained by using two different α coefficients (the reference one (left), α=1, and the one through the fitting of the experimental data (right), α=15 from eq. 8.2) with the corresponding H_2 emission lines.

change caused by the experimental data could be more visible. As anticipated in Section 1.3.2.1, typical models usually predict lower column densities for rotationally excited H_2 than the observed ones and, since the spectroscopic observations of *Spitzer*, a way to reduce this difference is believed to be an enhancement of the H_2 formation rate. The value of this rate has a strong effect on the line intensities and on the location of the DF in modelled PDRs. [Habart et al., 2004]

The implementation of the experimental high efficiency of H_2 formation at high T on PAHs in `Cloudy` seems to be a way to eventually obtain higher H_2 emission line intensities, closer to the observed ones. A set of H_2 emission lines had been selected from the literature [Peeters et al., 2024, Allers et al., 2005] and included in the input file to predict the intensities and shapes of the chosen H_2 lines. We selected the emission lines typically seen at lower T and visible with *JWST*. In Figure 8.5 we show a side-by-side comparison between the reference PDR picture and the PDR picture with H_2 formation at high T with, most importantly, the outputs of the predicted H_2 emission lines. At first sight, there seems to be a difference in shape and, possibly, in intensity between the outcomes. In order to check whether there was a quantitative effect in forming molecular hydrogen on PAH up to 250 K from this very first and simple approach, we decided to pursue calculations of the ratio between the reference output (left spectrum in Fig. 8.5) and the one obtained from the experimental fitting (right spectrum in Fig.

8.5) for two integrated emission lines (namely the ones at 17 μm and 2.8 μm). No substantial difference has been observed and more doubts were raised on the actual position of such H_2 rotational emission peaks since they are supposed to overlap with the DF, as shown by Peeters et al. [2024]. Nevertheless, when the experimental α is used (right picture in Fig. 8.5), the position of the lines seems to be slightly closer to the DF than the reference one on the left. Before having a final idea on how the simple fitting of the experimental results could have an effect on the DF location of PDRs predicted by `Cloudy`, we decided to vary a few more parameters (ionization parameters of -1.5 and -2 for the initial gas density of 1000 cm^{-3} but also for 100 cm^{-3}). Several input files have been created where all the possible combinations of the three ionization parameters (-1, -1.5, -2) and the two gas densities (1000 cm^{-3} and 100 cm^{-3}) were explored. In this way we obtained several versions similar to Figure 8.5 for the different U and n_{H}. The idea behind this parameter exploration was to see if more diffuse and highly UV exposed conditions than the ones used for the very first results of this study (Table 8.1), would give more promising outputs, since they would describe regions where T_{grain} is supposed to be higher therefore making our experimental results potentially more effective. Also in this case, we were not able to qualitatively and quantitatively see a difference between the PDR structure obtained with reference values and the one with the experimental α. A last check has been done by using different PAH populations as surfaces for H_2 formation on grains, namely PAHs made up of 15 or 120 carbon atoms. We wanted to check if a different available surface for the atomic hydrogen to undergo its molecular transition would have an effect on the location of the DFs, emission line intensities and integrated line ratios. Again, the predictions resulted in a situation similar to the one reported in Figure 8.5. Moreover, after comparing the distances between the IF and DF in the PDR models with the ones reported in the literature (see Peeters et al. [2024]), we realized that we could not reproduce the observations. Since the collaboration behind this study had started as a fast follow-up to simply check if a basic implementation of the freshly published experimental data could have a direct effect on the predictions of a PDR picture in `Cloudy` and we could not obtain something different from a classical scheme, we decided to stop here without having the expected results. A more complex and deeper study to reproduce the IF-DF distance observed in Orion and reported by Peeters et al. [2024], to understand the low emission line intensities predicted by models and to explore more parameters in order to fully include the high T efficient H_2 formation on PAHs in `Cloudy` would have needed way more time, which was beyond the scope of this PhD Thesis.

8.4 Conclusions, doubts & open questions

Besides the fact that this study did not come to a positive end in terms of seeing an effect of the experimental data when implemented in `Cloudy`, it is important to stress on a few take-away messages to keep in mind that this study represents a first step towards understanding the high temperature formation of H_2 on PAH-like surfaces.

First of all, one has to point out that this has been a fast and simple way to check if it would have been possible to produce a shift of the Dissociation Front location towards lower A_V values effecting the classical PDR pictures. This has been studied by only playing with the α coefficient of the modified Arrhenius equation used to describe the formation of molecular hydrogen on grains, therefore the whole work was probably missing a better overall description of the experimental results to be included in `Cloudy`. This would have required more time and possibly a whole project dedicated to it, thus not the goal of this follow-up. The first hypotheses regarding what could have changed the outcome of this study include (I) a more dynamical approach and (II) an eventual update of the chemisorption-dependent sticking coefficient used in `Cloudy`.

In our predictions we have always used a constant density while a possible introduction of a pressure/density law gradient could have helped in better describing the PDR structure (see the work done by Cormier et al. [2019]). Also, Wakelam et al. [2017] reports how, for chemisorption processes, the sticking coefficient/probability (S_{chem}) uses the formalism of Sha et al. [2005] and Kristensen et al. [2011], where it strongly depends on the T_{grain} and on the $E_{\rm chem}$ (the entrance barrier to the chemisorption sites). Given the importance of S_{chem} in our experimental study, this underlines how, even if we tried to extent the temperature dependence of the H_2 formation on PAHs, a whole new description should also include updated values and studies of the chemisorbed-driven H atoms recombination on PAH-like surfaces at higher temperatures than the only ones thought to be at stake so far.

The new data on H_2 emission lines and insights on the PDR structure arriving from *JWST* make such topics very important. In particular, we need future studies that keep investigating the role of grain temperatures in molecular hydrogen formation, the importance of PAHs and the possible new PDR pictures that show different locations or structures of the DFs than classically reported (as seen in Peeters et al. [2024]) to make a crucial next step in this field. There are already several studies focusing on H_2 lines in PDRs through JWST observations (such as Habart et al. [2024] and Appleton et al. [2023]) with many new exciting ones to come in the near future.

On the other hand, typical models keep giving H_2 emission line intensities lower than the observed ones, even after introducing higher H_2 formation rates or considering the possibility of having gas-phase H_2 at a higher temperature, as reported by Habart et al. [2004].

While in our study we did not see any visible difference in the implementation of the experimental results in `Cloudy`, it does not mean that there is no effect at all, but it means that there is still a lot of work to do so that the models currently available can better reproduce the new observations.

Chapter 9

Exploring oxygen depletion in translucent clouds with `Nautilus`

The project behind this Chapter started as a natural theoretical follow-up after the experimental work presented in Chapter 6. The problem of oxygen depletion into dust mantles, its interaction with carbonaceous surfaces and the possibility of an eventual surface oxidation related to grain growth in TC conditions, before the onset of the ice mantle, have proven difficult to study in an experimental setup. In this Chapter, we aim to tackle this problem through a different approach. The `Nautilus` code has been chosen to investigate this important topic. Here we report the description of a translucent cloud (TC) through its chemistry, relative physical parameters and elemental abundances. The main goal is to study and reproduce the observed gas-phase oxygen depletion in TC onto a carbonaceous dust grain following the organic carbonate hypothesis presented by Jones and Ysard [2019] and already introduced in Chapter 6. The project reported and described here is the last one approached in this PhD Thesis and it can be almost considered as an ongoing one. For these reasons it is written as a step-by-step study trying to understand how to tackle such topics by implementing a preliminary and simple yet innovative strategy in the `Nautilus` code.

The undersigned PhD student has performed the optimization of the physical parameters to reproduce a TC in `Nautilus`, the data analysis and interpretation, and the implementation of the "sink molecules" strategy in the code. The idea behind the presented strategy to study oxygen depletion and grain growth and the discussion of the obtained results come from a team work with Prof. Ilse De Looze and Prof. François Dulieu.

9.1 Introduction

Molecular clouds in the ISM are usually defined as a 3-phase system whose bulk mass is contained in the CNM. The main two phases are the diffuse clouds, observed through absorption spectroscopy of stars in the background, and the dense ones observed by CO mm emission. The dense cold clouds host the birthplace of stars. Traditionally, those two main phases are more simply defined by extinction properties ($A_V < 1$ for diffuse, >5 for dark dense clouds). The photodissociation and the UV field are important factors in diffuse environments, where the gas-phase H is ionized or in the atomic form. The dense clouds instead, also defined as molecular, are enough shielded from the UV photons preventing the photodissociation of the available species. As already anticipated in the Introduction of this Thesis (Chapter 1, Section 1.2.2), a transient situation between the just cited cloud environments is defined as a translucent cloud (TC). The transition from diffuse to dense regions is however only one of the ways that explains an A_V between 1 and 5, because these values can also be the result of multiple diffuse ones. A better way to characterize MCs would be a general description of them by, for example, following the change of atomic and ionized elemental abundances through their incorporation into molecules. There have been studies suggesting that the ratios CO/H_2 and CO/C(I) would give a more appropriate description of this transition. The CO/H_2 ratio goes from low to high values with increasing of molecular fraction, since the CO abundance is more sensitive to the physical changes of the clouds and it represents the main molecule for the "molecularization" of ionized carbon [Burgh et al., 2010].
For the scope of our research, it is also important to keep in mind that a translucent cloud represents the ideal physical and chemical conditions for grain growth and for the depletion of gas-phase species that are being incorporated in the grain mantle right before the onset of the icy mantle. The transition from diffuse to dense represents indeed a special condition with a high abundance of elements, low temperature and enough UV shielding. The study of translucent clouds also represents a crucial scientific topic for several open questions in this field regarding elemental depletions. So far, through our experimental work and the first results from the model, we have mainly focused on oxygen and carbon. Nitrogen is not of crucial importance for dust and interstellar depletion since many studies indicate that it exhibits low-level depletion in the diffuse ISM.
Jenkins [2009] reports a study of 17 elemental abundances and underlines how the incorporation of oxygen into the solid-phase should be higher than the amount accounted for in normal dust grain structures. Also, even though carbon is one the main constituents of grains, there is not a full understanding on the actual differential consumption of it yet. More carbon from the gas-phase should be in fact depleted in order to explain some dust optical properties [Jones and Ysard, 2019]. The residual oxygen depletion

should be considered as associated with carbon and hydrogen to be eventually locked up in some molecular or structural forms. Ioppolo et al. [2008] proposed an increment of the amount of oxygen forming amorphous ices, or one could consider other solid-phase species and reactions on the grain leading to its growth through structures difficult to be observed and distinguished in the IR features. Jenkins [2009] found in his study a large loss of oxygen atoms from the gas phase that does not reconcile with current models of interstellar grains. On the same page, Whittet [2010] reports how the depletion of oxygen should be further studied and be explained, and how its incorporation in the grain might affect its persistence in denser clouds. In this study, they also discuss the most plausible form of an oxygen bearing species as one made up of carbon, given the high chemical affinity. It is therefore of scientific interest to study the depletion of oxygen and its solid forms near the interface of translucent and dense clouds. This is why Whittet [2010] assesses the implications of a recent discovery that atomic oxygen is being depleted from diffuse interstellar gas at a rate that cannot be accounted for by its presence in silicate and dust grains in general. If this reservoir of depleted oxygen persists to higher densities it might have implications for the oxygen budget in molecular clouds, where a shortfall of the same order is observed. Out of various potential carriers, the most plausible one appears to be a form of O-bearing carbonaceous matter similar to the organics found in cometary particles returned by the stardust missions. The observed values and limits on the abundances of the main O-bearing species in the gas-phase (CO, H_2O and O_2) appear insufficient to account for the oxygen not tied up in dust and ices in regions dense enough for the atomic O to be converted into molecules. Figure 9.1 displays an overview on the oxygen depletion matter just discussed. It is therefore particularly important to find answers about the oxygen depletion happening in the transition of diffuse-to-dense clouds involving carbon and hydrogen elements, being the most abundant and chemically available elements. While going from diffuse to dense environments, accretion and coagulation play the most important roles. In the "reverse' sense, it is photo-desorption that results in ice mantle loss and volatilisation of aliphatic-rich mantles. In both cases oxygen, carbon and of course hydrogen seem to be the main actors. Also, the high abundance of CO_2 in ices could be related to oxygen depletion and several ways to explain its origin should be re-discussed, ranging from CO reactions on the grain or from photolysis of other species [Boogert et al., 2015].
The paper by Jones and Ysard [2019] has been already widely used in this Thesis as an important reference for the general purposes of the entire project: oxygen depletion, grain growth, ice mantle formation, physical aspects regarding the diffuse to translucent to dense clouds mechanisms. They propose a concrete application for the observational limits as well as for the theoretical studies and hypothesis discussed above. The depletion of about 40% of the available gas-phase oxygen may be happening through its incorporation into organic carbonates, which are molecules that are difficult to observe

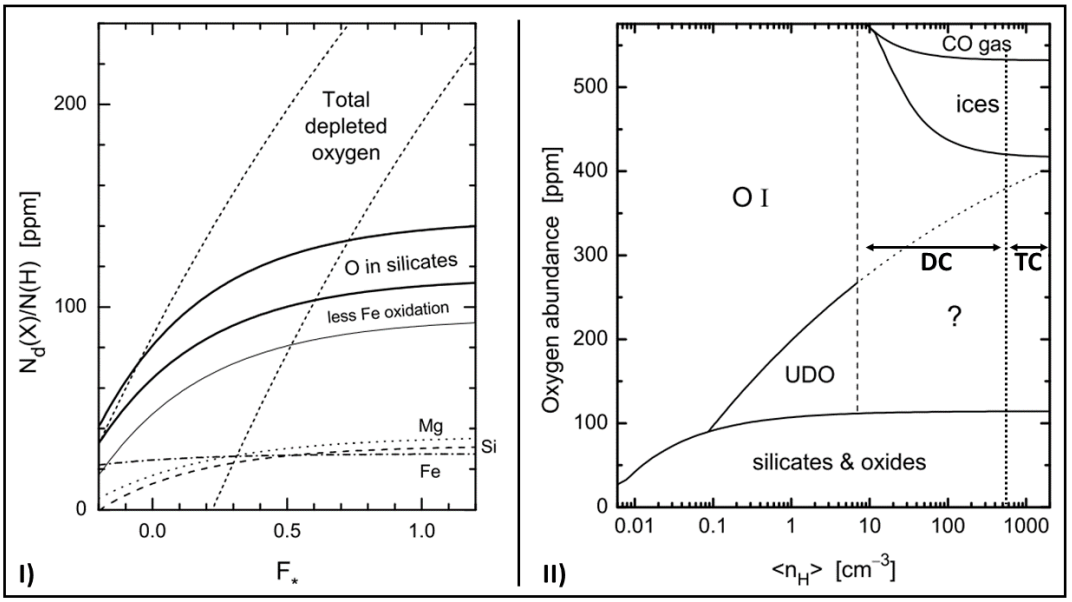

FIGURE 9.1: Figures and caption text reproduced from Whittet [2010]: **I)** Plot of solid-phase abundance $N_d(X)/N(H)$ vs. depletion factor F_* for the principal elements depleted into silicate/oxide dust in the ISM (X = O, Mg, Si, or Fe). Abundances in this and subsequent figures are presented in parts per million (ppm). The dotted, dashed and dotdashed curves toward the bottom of the plot denote Mg, Si and Fe, respectively, constructed from empirical fits to depletion data from Jenkins [2009]. The area labelled 'O in silicates' represents the probable range of O depletion into silicates and oxides, assuming oxidation of all depleted Mg, Si and Fe, with O/M = 1.5 and 1.2 (upper and lower bounds, respectively, thick solid curves). The thin solid line indicates a possible downward revision of the lower bound, assuming that the silicate/oxide dust includes all of the depleted Mg and Si but only 40% of the depleted Fe [Weingartner and Draine, 1999]. Upper and lower limits on the total depleted oxygen (dashed curves) are based on empirical fits from Jenkins [2009]. **II)** A schematic overview of the distribution of oxygen between major reservoirs over a wide range of interstellar environments, combining observations of element depletion in the diffuse ISM with those of ices and gas CO in a prototypical dense cloud. Ticks on the ordinate correspond to increments of 50 ppm, and the total range is set to the adopted reference abundance (575 ppm). The abscissa represents mean line-of-sight number density. The vertical dashed line denotes the effective observational limit on depletion studies imposed by the UV opacity of the ISM at higher densities. The area labelled UDO (unidentified depleted oxygen) is bounded by the median of the upper and lower curves for O in **I)**; a speculative extrapolation to densities higher than those sampled by the relevant observations is also shown (dotted curve). The diffuse cloud (DC, 10 cm^{-3} < n_H < 500 cm^{-3}) and the translucent cloud (TC, 500 cm^{-3} < n_H < 5000 cm^{-3}) regions (values from Snow and McCall [2006]) are indicated on the right panel (**II)**).

and require a reasonable amount of carbon (10 - 20%) known as organic carbonates. This compound would be able to also explain a certain amount of CO sequestration and the CO_2 re-admission by thermal or photolytic decomposition of these organic carbonates.
All these previous works have been for us a reference for both experiments and mainly, as discussed in this Chapter, theoretical studies. In fact, through the experiments we have so far focused on the interaction between carbonaceous surfaces with oxygen and hydrogen trying to understand whether those atoms can adsorb, be locked up or react on the grain. The model is a way for us to understand the behavior, in translucent clouds, of the main O-bearing gas-phase and grain surface species that could be involved in oxygen depletion and grain growth, eventually being able to make a comparison with the observations. The idea of this Chapter is to verify the change in abundances of the most relevant molecules by defining an average translucent cloud environment. A collaboration with the developers of `Nautilus` has started for further modifications of the code that are necessary to assess the growth of grains through oxygen incorporation by forming organic carbonates-like species or a phantom molecule that can incorporate different ratios of carbon and oxygen trying to reproduce observed depletions. This would require a chemically-active grain surface that is achievable by the addition in the code of a non-desorbing surface molecule that is able to react with gas-phase species (C and O in a specific proportion), thus participating in their depletions.

9.2 Methods

The model here used is the 3-phase `Nautilus`, version 1.1, described in section 7.2.1. The first part of our approach has been to study all the input files given in the code and to understand what would have been worth changing to better match our aims. As said, the main point for a first use of `Nautilus` is to describe a typical/average translucent cloud through its main physical parameters and to try understanding how abundances of the main gas and grain species change over time. The first under-study element is oxygen and the main molecules containing it. The idea is to reach a steady state situation after running the code for typical MC timescales and to check the effect of some of the switches inside the code. By switches, we refer to the tools available in the code that allow special conditions such as photodesorption, cosmic rays induced diffusion and constraints on H_2 formation with respect to its atomic availability for other reactions. The main tools used so far are the plot of abundances over time and the main reactions involved in a specific molecular production and destruction. After defining a typical translucent cloud, we have taken a few references (Fuente et al. [2023], Laas and Caselli [2019], Fuente et al. [2019]) to reproduce the translucent region of Taurus MC and to construct a database

TABLE 9.1: First physical parameters used in `Nautilus` to define an average TC.

PHYSICAL PARAMETER	VALUE/DEFINITION/RANGE
Initial gas density ($n_{\rm H}$)	1000-9000 cm^{-3}
Elemental abundances	Table 9.2
Gas temperature	10-45 K
Grain temperature	15K
Initial visual extinction ($A_{\rm V}$)	1.5-3.5 mag
Scale factor of the UV RF (χ)	5-50
Cosmic ray ionization rate	1E-17 s^{-1}
Grain density	2 g/cm^3

TABLE 9.2: Input fractional abundances wrt H for all the species used to describe a TC in `Nautilus`.

H	0.99	**H$_2$**	5E-05	**He**	9.55E-02	**S$^+$**	1.66E-05	F	3.63E-08
O	5.7544E-04	**C$^+$**	2.0893E-04	**N**	5.7544E-05	**P$^+$**	2.57E-07	**Cl$^+$**	2.88E-07
Mg$^+$	3.6308E-05	**Si$^+$**	3.1623E-05	**Fe$^+$**	2.7542E-05	**Na$^+$**	1.74E-06	**e$^-$**	3.233E-04

to have the best parameters in order to compare the observed abundances for the main O-bearing species. The optimization of the parameters also involves a double checking of the ice mantle being formed on the surface at the $A_{\rm V}$ relevant to this study (between 1.5 and 3.5). Since the focus of this project resides on the study of grain growth and O atoms incorporation on a carbonaceous surface before the latter being covered by a full ice layer, it was important to be sure that the set of parameters used to recreate the transient region of Taurus would also take this aspect into account. Finally, the strategy to study oxygen depletion into a non-desorbing surface species that would lock specific ratios of O and C to reproduce observed depletions is reported. In Table 9.1 we display the main initial physical parameters we used for the first runs of the code in order to describe an average translucent region on the border of a MC.

9.3 Results and Discussion

In order to select the best parameters to describe a TC in `Nautilus` before going into the details of Taurus, it is important to choose the best values of $n_{\rm H}$, gas temperature, $A_{\rm V}$ and the scale factor of the UV radiation field(χ)[1] that can reproduce at best the observed abundances and conditions. Regarding the UV flux parameter, a pre-selection has been arbitrarily made because Fuente et al. [2023] already reports the main value

[1] χ is the scale factor of the UV RF that corresponds to the average far-ultraviolet interstellar radiation normalized to the Draine [1978] field (indicated as χ_0). It can be related to the one normalized to the units of the Habing [1968] field (G_0) with the expression $G_0 = 1.7\ \chi_0$. G_0 = 1.6E-3 erg s^{-1} cm^{-2} (Tielens [2010]) and it is the radiation integrated between 6 and 13.6 eV in the UV.

TABLE 9.3: Set of final physical parameters used in `Nautilus` to define an average TC and the translucent region of Taurus MC reproducing at best the abundances reported in literature.

PHYSICAL PARAMETER	VALUE/DEFINITION/RANGE
Initial gas density ($n_{\rm H}$)	3000 cm^{-3}
Elemental abundances	Table 9.2
Gas temperature	25 K
Grain temperature	15K
Initial visual extinction ($A_{\rm V}$)	1.5 & 3.5 mag
Scale factor of the UV RF (χ)	5
Cosmic ray ionization rate	1E-17 s^{-1}
Grain density	2 g/cm^3

needed to simulate TC conditions in the case of Taurus. Thus, a scale factor of the UV radiation field of 5 has been used in the following calculations. The main molecules of interest for which abundances in TC regimes are reported in the literature (from Fuente et al. [2019] and Laas and Caselli [2019]) are: CO, HCO^+, OCS, SO, SO_2, H_2S, CS. Firstly, it was important to obtain a set of reference abundances to be used later on, by optimizing the initial physical parameters displayed in Table 9.1. In particular, we have explored 4 $n_{\rm H}$ steps (1000, 3000, 6000, 9000 cm^{-3}), 8 different gas temperatures (from 10 K to 45 K with a 5 K step), $A_{\rm V}$ of 1.5 and 3.5. We only show the results for the best set of selected physical parameters (see Table 9.3) chosen to reproduce the abundances of the molecules reported above. For the initial visual extinction, the following analyses will be run for both values visible in Table 9.3 since they define the boundaries of a typical TC. Figure 9.2 shows the abundance evolution of those molecules over time (up to 10^7 years) for $A_{\rm V}$ of 3.5 and Figure 9.3 for 1.5. In general, previous theoretical works on molecular clouds have shown better agreement with observations for chemical ages between 0.1 and 1.0 Myr (see Fuente et al. [2023]). Since we are exploring low densities and low $A_{\rm V}$ values, we decided to keep this timescale for the first consistence check of the parameters.

To have a more quantitative idea of the actual results obtained by trying to reproduce a translucent cloud, Table 9.4 shows a comparison between the abundances inferred with `Nautilus` and the observed abundances found in the literature. Overall, the ranges are in good agreement with the observed values reported in previous works, except for HCO^+, probably due the fact that the abundances are taken at 10^7 years. The latter always showed a low abundance for all the attempts that have been made to optimize the physical parameters to reproduce at best the conditions of a translucent MC. The abundances here shown are only considered as references for the next calculations in order to be sure to define a general TC condition before introducing new species, playing with the chemistry of the code and developing a strategy to study grain growth

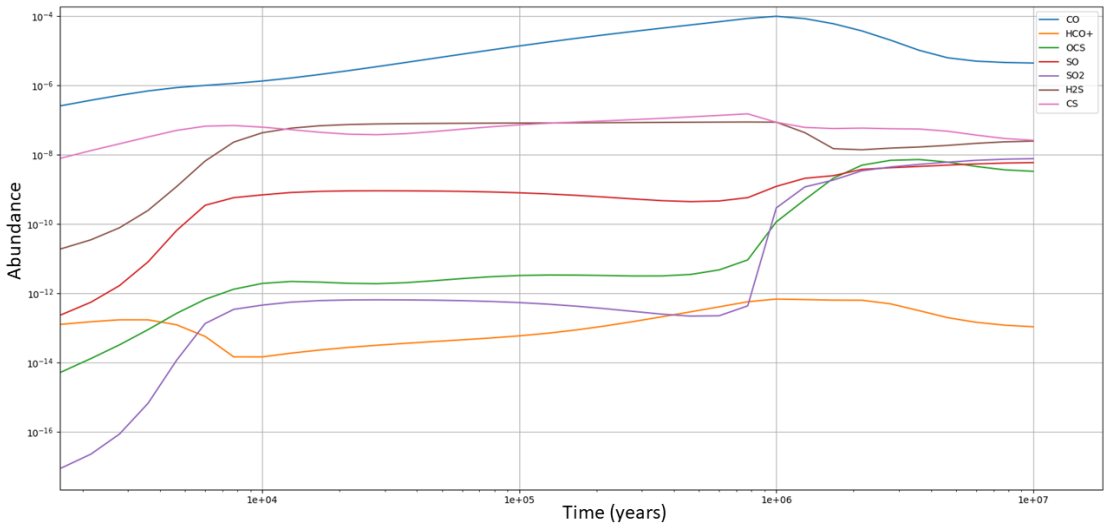

FIGURE 9.2: Abundances over time (up to 10^7 years) by using the physical parameters reported in Table 9.3 and A_V of 3.5 as initial inputs in the `Nautilus` code for the following species: CO, HCO^+, OCS, SO, SO_2, H_2S, CS.

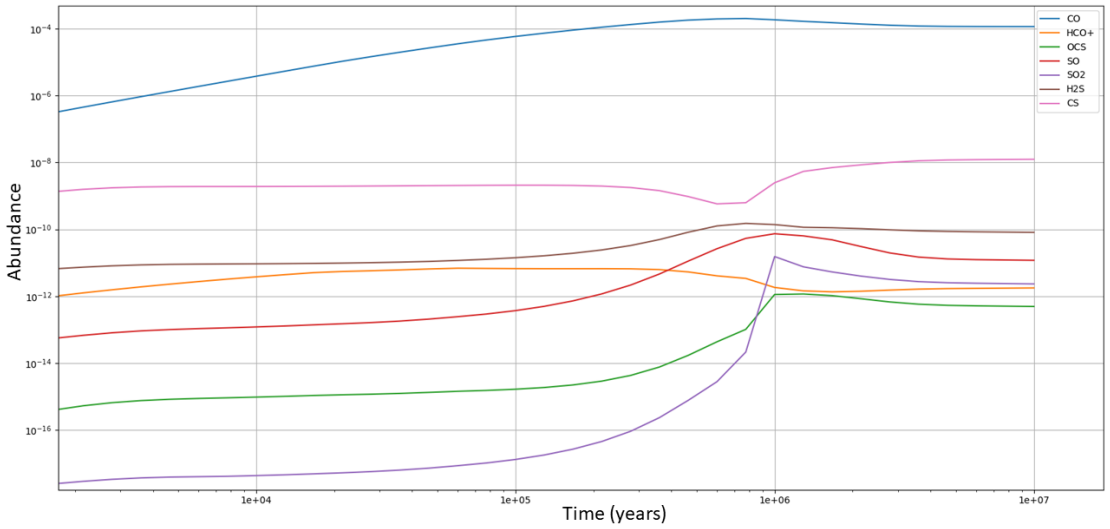

FIGURE 9.3: Abundances over time (up to 10^7 years) by using the physical parameters reported in Table 9.3 and A_V of 1.5 as initial inputs in the `Nautilus` code for the following species: CO, HCO^+, OCS, SO, SO_2, H_2S, CS.

and oxygen depletion. By adopting a scale factor of the UV radiation field of 5, the idea is to specifically reproduce and study Taurus conditions as our target TC with `Nautilus`. The reason behind this choice can be explained in a few points. There is already some literature on TMC, so there is the advantage of having some available and ready-to-compare data, but also Taurus has been included in many previous works on elemental depletions (see Fuente et al. [2019, 2023]). Last but not least, the TMC has been widely studied and it presents specific conditions that make it easier to study. New radio observations of TMC have even reported the specific detection of two isomers of small PAHs and they discuss all the possible in-situ formation pathways [McGuire et al.,

TABLE 9.4: Comparison between the final abundances (from Figure 9.2 and 9.3, taken at 10^7 years) obtained with the `Nautilus` code by using the parameters of Table 9.3 for the selected molecules (CO, HCO^+, OCS, SO, SO_2, H_2S, C) and the literature values.

MOLECULE	Nautilus From Figure 9.3	Nautilus From Figure 9.2	From Laas and Caselli [2019]	From Fuente et al. [2019]
CO	1.2E-04	4.4E-06	X	1.4E-04 - 9.7E-05
HCO^+	1.8E-12	1.1E-13	X	1E-08 - 6.7E-09
OCS	5E-13	3.3E-09	1E-09	X
SO	1.2E-11	5.9E-09	4E-08	2.9E-09 - 8.8E-10
SO_2	2.3E-12	7.7E-09	<1E-09	X
H_2S	8.1E-11	2.5E-08	6E-09	X
CS	1.2E-08	2.6E-08	4E-09	1.3E-08 - 4.8E-08

2021].

Whittet et al. [1988, 1989] report how the column densities of H_2O and CO in ices are in good correlation with the visual extinction and they underline how in TMC water ice is the main component until an A_V of 5.3, with a monolayer threshold around 3.3. For the purpose of this study and the parameters already selected, those conditions represent the best way for a first study on O depletion with `Nautilus` in TC conditions.

As said in the Methodology section, this study focuses on the interaction of atomic oxygen and carbon with the dust surface trying to assess the amount of their possible depletion into a specific form that could eventually be linked to grain growth. For this reason, it is therefore of primary importance to establish the degree of ice coverage for the grain at the specific MC evolution time taken into account for our analyses. For this purpose, Figure 9.4 shows the evolution of solid water forming a mantle around the grain. The J-species represent the most external layer (surface) that, when saturated, starts to exchange species with the mantle (K-species) that will keep growing underneath. The abundance crossing point between the mantle and the surface solid water has been taken as the time at which a full monolayer is formed for sure. The following runs of the `Nautilus` will be made up to 10^5 years and the values will be taken at 10^4 years, to be sure that the conditions reproduce a sub-monolayer regime and there is still direct interaction between the surface and the gas-phase species landing on the grain, similar to what should be the environment of a TC before an A_V of 3.3 - 3.5. In Figure 9.4 only the water component of ice is taken into account since at those values of visual extinction it is believed to be the main and almost only molecule building ice layers on dust grains [Boogert et al., 2015, Smith et al., 1993]. A last check to be certain to have the correct amount of solid water in our conditions in order to be right before the ice monolayer threshold is displayed in Figure 9.5. By using equation 9.1, one can translate the total solid water (KH_2O + JH_2O) abundance at 10^4 years from Figure 9.4 into a column density value. We obtained solid water ice column densities of 1.7E+16 cm^{-2} and 5.4E+16 cm^{-2}, respectively for A_V of 1.5 and 3.5. The comparison with the expected values found in literature is shown in Figure 9.5, where the column densities resulted from `Nautilus` are overlaid as two yellow dots on the plot reported by Nguyen

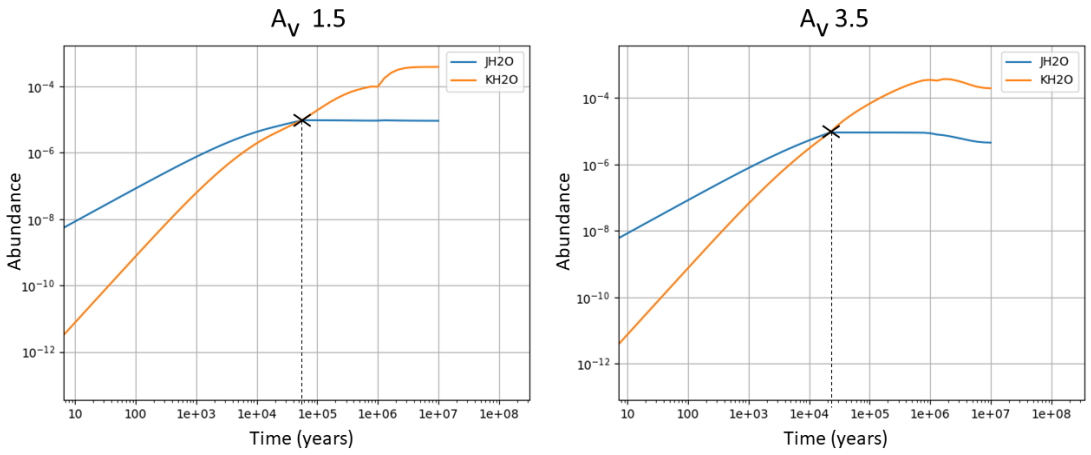

FIGURE 9.4: Solid water abundance evolution over time (up to 10^7 years) by using the physical parameters reported in Table 9.3 in the `Nautilus` code for the species JH_2O (surface) and KH_2O (mantle).

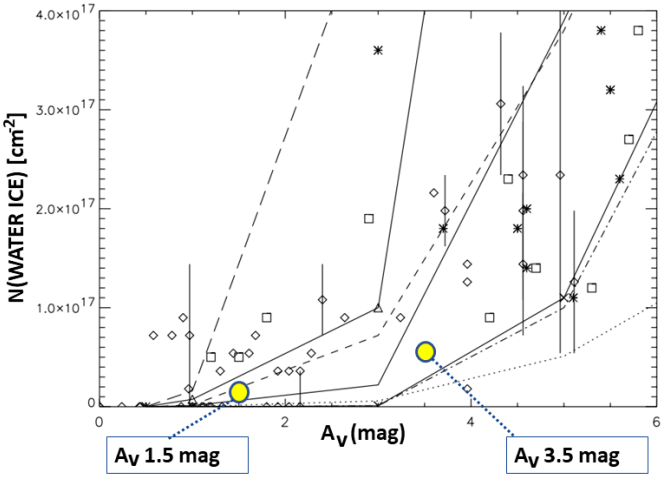

FIGURE 9.5: From Nguyen et al. [2002]: calculated and observed column densities of water ice as a function of A_V over the limited range $0 < A_V < 6$ in TMC. The solid water ice component column densities found with our calculations at time 10^4 years are superposed at the bottom of the plot (yellow dots).

et al. [2002].

$$N_i = \frac{A_V}{5.34x10^{-22}} X_i; \tag{9.1}$$

where X_i is the fractional abundance of the selected species. Before adding the formation of an O-bearing species to `Nautilus`, it is of extreme importance to report the abundances of the species that are going to be the main ones for the study of grain growth and oxygen depletion in a TC. Figure 9.6 shows the evolution of the abundances of some gas-phase and solid-phase species that are selected to be the ones important to assess the depletion of elements such as C and O together with main molecules involved in the ice mantle formation. The reference abundances are taken at 10^4 years and they are

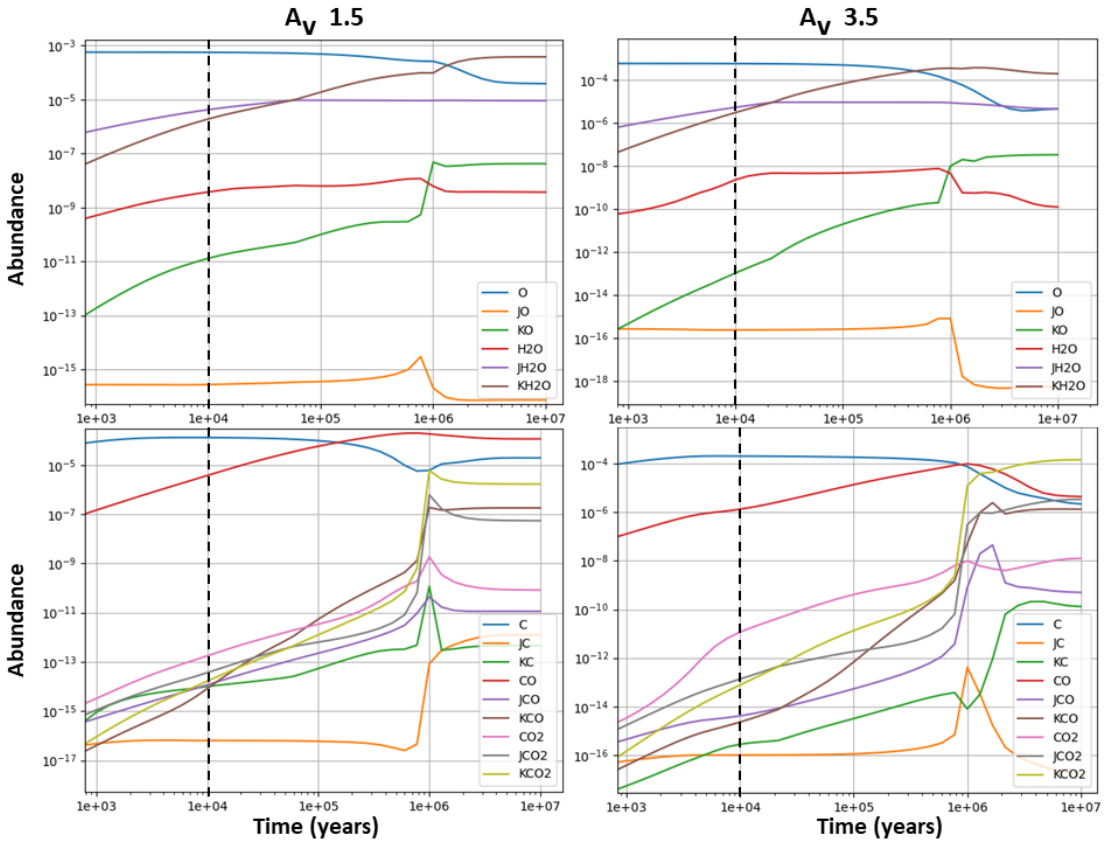

FIGURE 9.6: Abundances for the main ice constituents (O-bearing species on the top plots and C- bearing species on the bottom plots) together with atomic O and C for both gas-phase and solid-phase (J and K species, respectively surface and mantle species) obtained with `Nautilus` by using the physical parameters of Table 9.3. The results for visual extinction of 1.5 are displayed on the left, the ones for 3.5 are on the right.

reported in Table 9.5. They will be used for the calculation of the depletion percentages and act as references for the "sink molecules" strategy presented in the following section to be sure to still reproduce the observed abundances of the main molecules.

9.3.1 Grain growth and oxygen depletion: the strategy

So far, the purposes have been the chemical and physical description of a translucent cloud, representing an ideal case right before the onset of the icy mantle. These dense and UV-shielded environments could give some insights into oxygen depletion and the role of carbonaceous surfaces to host new species by locking oxygen arriving from the gas-phase, eventually participating to the growth of the grain. Here we present a strategy to study this scientific question by following the approach presented by Jones and Ysard [2019]. To our current knowledge, in the transition from diffuse to dense clouds, up to 40% of gas-phase oxygen is depleted into an unknown surface species because the speed of its disappearance and the amount found in ices and silicates does not explain the

TABLE 9.5: Abundances (from Figure 9.6, taken at 10^4 years) obtained with the `Nautilus` code by using the parameters of Table 9.3 for the main ice components together with atomic O and C. Gas phase species: O, H_2O, C, CO, CO_2. Solid-phase species: JO, KO, JH_2O, KH_2O, JC, KC, JCO, KCO, JCO_2, KCO_2. J indicates the surface species while K refers to the mantle ones.

SPECIES	ABUNDANCE (From Figure 9.6, A_V=1.5, at 10^4 years)	ABUNDANCE (From Figure 9.6, A_V=3.5, at 10^4 years)
O	5.7E-04	5.7E-04
JO	2.7E-16	2.4E-16
KO	1.3E-11	1.0E-13
H_2O	3.7E-09	2.2E-09
JH_2O	4.2E-06	5.2E-06
KH_2O	1.9E-06	3.0E-06
C	1.3E-04	2.0E-04
JC	6.4E-17	1.0E-18
KC	9.9E-15	2.8E-16
CO	3.8E-06	1.3E-06
JCO	1.2E-14	4.1E-15
KCO	8.3E-15	2.3E-15
CO_2	1.8E-13	1.2E-11
JCO_2	3.7E-14	1.4E-14
KCO_2	1.7E-14	7.8E-14

observed changes in abundances. Therefore it should exist in a form of O-rich material being IR inactive or difficult to observe and to distinguish. There is also a certain amount of carbon (up to 10 - 20%) probably depleted onto the grain in those transient regions that needs to be further investigated. Jones and Ysard [2019] therefore proposes a family of molecules, the organic carbonates, as a possible solution for the locking of the observed depleted amounts of oxygen from the gas-phase in translucent clouds together with carbon in a specific ratio, given the chemical structure of those compounds. The incorporation of oxygen into carbonaceous grains was already proposed in 2016 [Jones, 2016]. The formation of organic carbonates should be at stake through the reaction of, firstly, gas-phase oxygen with aliphatic C-H and C=C bonds (surface species), to form expoxides and carbonyls, and secondly the newly formed functional groups would react with incoming gas-phase CO and CO_2 to result in organic carbonates. The ratio between the overall O to C involved in the formation of those species is 3 to 1 and this is in perfect agreement with the observed and unexplained depletions. The underlying theory behind this hypothesis also relies on the fact that the organic carbonates could be difficult to observe since they do not have a strong and well-defined IR signature, and they can be confused with more simple carbonyls or epoxides. Also, organic carbonates are chemically possible in terms of the amount of oxygen and carbon needed for their formation, with respect to the depleted amount and the available species both in the gas- and solid-phases. Finally, photolysis and thermal decomposition of organic carbonates would contribute to a new formation route for CO_2 and CO returning to the gas-phase together with an aromatization of the surface. To follow this hypothesis we have decided to implement a phantom molecule into `Nautilus` that would incorporate the incoming

elemental oxygen from the gas phase, but also stay on the surface without desorbing ideally mimicking the growth of the mantle. To take into account the ratio between oxygen and carbon needed to explain the observed depletions and the chemical structure of organic carbonates, another carbon-based molecule has been added to the code. The new species have been named JXO and JXC, respectively O-based and C-based. We refer to them as "sink molecules" to underline the fact that they have been implemented with an extremely high binding energy that anchors them to the grain. They do not have a precise chemical structure, they have been only inserted in their J (surface) and K (mantle) components where only the J component is responsible for the first interaction with the oxygen and the carbon from the gas-phase. The idea is to check if it is possible to lock O and C into the grain in a ratio that mimics the one of the organic carbonates chemical structure and if it is possible to reproduce the observed depletions without affecting the abundances of the other relevant O- and C- bearing species reported as a reference in Table 9.5.

The last and most important detail in the JXO and JXC addition is the definition of the so-called branching ratio. The branching ratio is the fraction of gas-phase species for a specific molecule that is locked in one or more solid-phase forms upon adsorption. If the interaction of a molecule in the gas-phase with the grain surface is defined by only one adsorption reaction, 100% of it will follow that specific reaction. However, if more reactions are at stake, more branching ratios will compete for different fractions of gas-phase species to follow several pathways upon arrival on the surfaces, resulting in various amounts of different solid-phase molecules. In `Nautilus`, the amount of atomic oxygen and carbon arriving from the gas-phase to the surface are described only with the grain reactions that form JO and JC, respectively. They can afterwards desorb, diffuse and/or react with other species already present on the surface. With the insertion of the sink molecules as competitors to lock O and C atoms on the surface, it has been of extreme importance to deal with the ratios of the amounts of gas-phase oxygen and carbon that would eventually be part of JO and JC or being inserted into JXO and JXC. The branching ratio default value for the O $\rightarrow$ JO reaction is 1, where 100% of the incoming oxygen goes into JO (same for C $\rightarrow$ JC). When the O $\rightarrow$ JXO has been added with a branching ratio of 1, now 50% of the gas-phase oxygen landing on the surface would form JO and the other half JXO (same for C $\rightarrow$ JXC). In this way we were able to assess different branching ratios for the sink molecules reactions changing the amount of oxygen being locked up in JXO and JO, (same for carbon, JC, JXC) by keeping the JO and JC equal to 1. In the case of carbon, the JXC branching ratio is always 1/3 of the one used for JXO in the same run of the code, to better reproduce their ratio in the organic carbonates hypothesis described by Jones and Ysard [2019]. Figure 9.7 shows the very first results obtained with the implementation of the sink molecules starting with the JXO branching ratio of 1. Here only the behavior of gas-

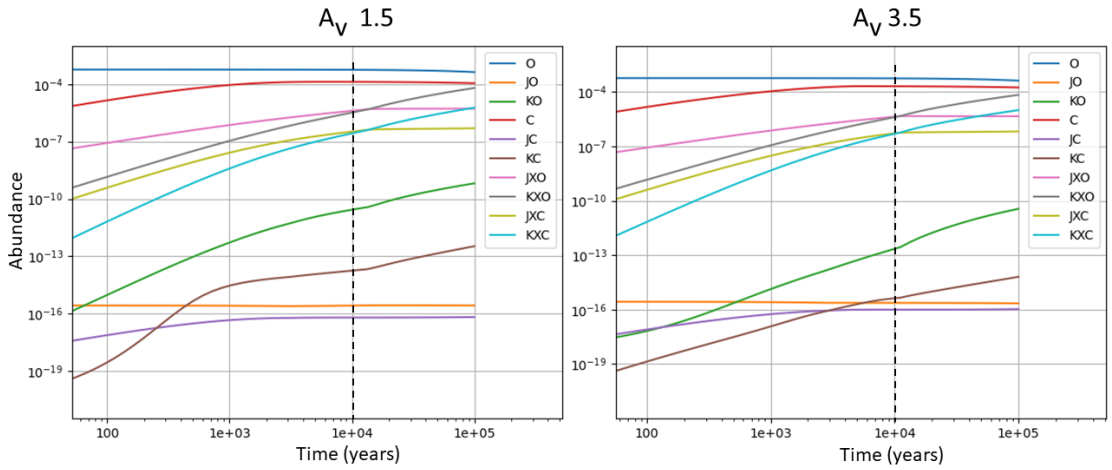

FIGURE 9.7: Abundances up to 10^5 years for the O and C elements and for the sink molecules added to the code (JXO, KXO, JXC, KXC). O and C abundances are shown both in gas and solid phases (J=surface and K=mantle). JXO branching ratio of 1. Plots obtained by using `Nautilus` with the physical parameters of Table 9.3. The results for visual extinction of 1.5 are displayed on the left, the ones for 3.5 are on the right.

and solid-phases O and C with JXO, KXO, JXC, KXC is studied. It is important to notice that the J species always show a higher abundance with respect to the K ones at the beginning, being the ones interacting with the gas-phase elements at first, until reaching the crossing point where the saturation of the surface generates the swapping of the J-species with the mantle (K-layer). Finally, the much higher abundance reached by JXO after the first decades, if ones compares it to JO since they have the same branching ratio, is probably due to the fact that the sink molecule does not desorb and it is not involved in other grain reactions. The very next step focuses on the most important molecules involved in the formation of organic carbonates and the ones relevant for the formation of the icy mantle. Since CO_2 shows a very low abundance in our conditions at 10^4 years (see Figure 9.6), the only species that will be followed in this section are O, H_2, C, CO (gas- and solid-phase) together with JXO, KXO, JXC, KXC. By varying the branching ratios of JXO, and the ones of JXC accordingly, we tried to study the values required in `Nautilus` in order to get the closest match with the observed oxygen depletions discussed above. We explored several JXO branching ratios (0.6, 0.8, 1, 1.2, 1.4, 1.6, 1.8, 2, 10, 20) with the JXC one being 1/3 of it and the JO, JC ones fixed to 1. It is important to stress that, for the highest BR used (20), almost 95 % of the incoming gas-phase O goes into JXO, the rest is locked as JO on the grain. Figure 9.8 displays the most important results of this project. In this plot one can see the abundance variations of the gas-phase species (O, H_2O, C, CO) and the sink molecules for the different branching ratio used to describe the O → JXO and C → JXC reactions in `Nautilus`.

Given the purpose of this study, the main result concerns the depletion of the gas-phase oxygen. Even if a little change of its abundance was already visible with a first introduction of JXO and with branching ratios around 1, the quantitative results come after 10 and mainly at 20. Starting with an abundance of 5.75E-04 (see Table 9.2 for O), in Figure 9.8 the abundance of gas-phase oxygen at 10^4 years in TC conditions, at the highest used branching ratio of 20, is 4.2E-04. Thus, 27% of it has been depleted into the grain. On the other hand, the total XO abundance (mantle + surface) in the same conditions reaches a value of 1.5E-04, the 26% of the initial gas-phase O input into the TC. A similar discussion can be done for JXC, participating to almost 8% of C depletion. The actual abundances for all the species shown in Figure 9.8 are reported in Table 9.6, only for the branching ratio of 20 and compared to the reference values of Table 9.5. The other molecules involved in this study are H_2O and CO. With the addition of the sink molecules and the high branching ratio, they both show a decrease of their gas-phase abundance and a proportional increase of their surface component, however they remain comparable and inside the range of values from Table 9.5. One has also to consider that H_2O and CO are the main components of the icy mantle that starts to set in these conditions thus this behavior, within certain limits, was somehow expected.

Regarding the possibility of addressing the grain growth problem through the study of O depletion by locking some of the O into organic carbonates, we can deduce some preliminary conclusions from our results. By accreting O and C atoms on a carbonaceous spherical grain in the ratio 3/1 with `Nautilus`, we were able to reproduce, in terms of abundances, the formation of ≈ a monolayer of organic carbonates with our "sink molecules" strategy. If we consider the typical length of the bonds involved (two C-O single bonds and one double [Zurich University, 2024]), the grain shows a growth of ≈ 0.4 nm. Even if this study has not reached the depletion levels for O and C reported by Jones and Ysard [2019], one has to consider that this is a first attempt for a simple description of the hypothesis discussed in his work. The aim here was to study the possibility to deplete gas-phase oxygen into a non-desorbing species on a carbonaceous grain together with carbon in a 3 to 1 ratio, without affecting much the abundances for the other relevant species important for the formation of the icy mantles at the A_V values used in this project.

9.4 Conclusions, doubts & open questions

In the transition from the diffuse through translucent into dense clouds, almost one half of the cosmic abundance of oxygen must accrete into an unknown, well-hidden, O-rich material. Jones and Ysard [2019] proposes organic carbonates as possible grain

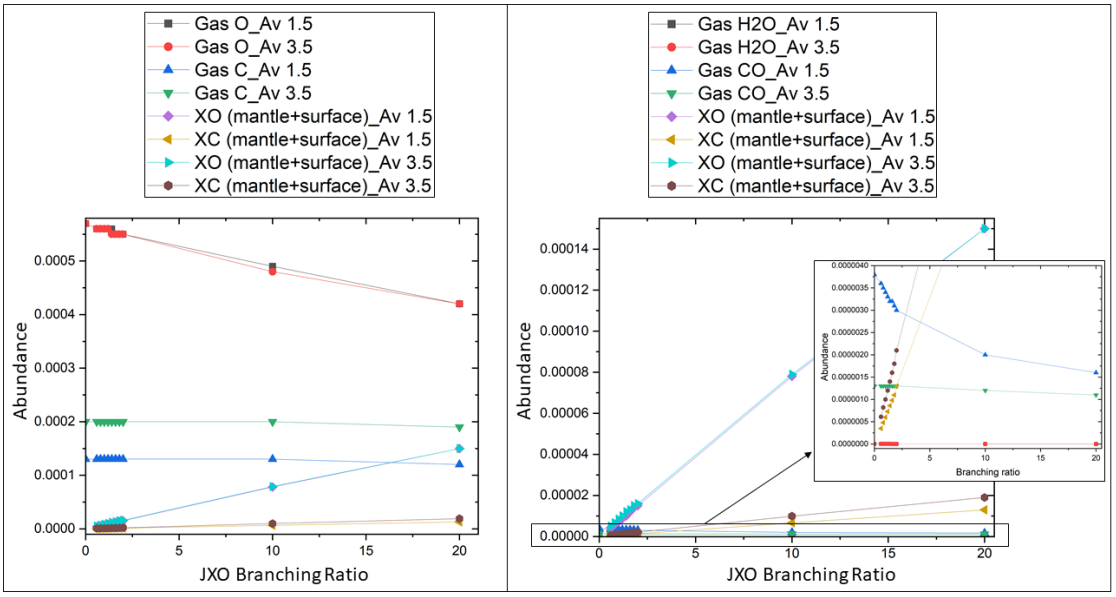

FIGURE 9.8: Abundances for several JXO branching ratios (0.6, 0.8, 1, 1.2, 1.4, 1.6, 1.8, 2,10, 20) for the sink molecules added to the code (XO and XC) and the following gas-phase species: O, C, H_2, CO; for A_V 1.5 and 3.5. A zoom-in panel is overlapped on the right graph to show the behavior of H_2O and CO in gas-phase for A_V 1.5 and 3.5. All the abundances are taken at 10^4 years by using `Nautilus` with the physical parameters of Table 9.3.

TABLE 9.6: Comparison between the abundances from Table 9.5 and the ones resulting from the implementation of the sink molecules (XO and XC) by using a JXO branching ratio of 20, at 10^4 years. Both are obtained with the `Nautilus` code with the parameters of Table 9.3. Reported species: O, H_2O, C, CO, XO, XC. The abundances of the solid-phase species are the sum of the J and K, where J indicates the surface species while K refers to the mantle ones.

	REFERENCE ABUNDANCES FROM TABLE 9.5		ABUNDANCES FROM FIGURE 9.8 FOR JXO BR=20	
SPECIES	**A_V=1.5, at 10^4 years**	**A_V=3.5, at 10^4 years**	**A_V=1.5, at 10^4 years**	**A_V=3.5, at 10^4 years**
GAS-PHASE O	5.7E-04	5.7E-04	4.2E-04	4.2E-04
SOLID-PHASE O (MANTLE+SURFACE)	1.3E-11	1.0E-13	5.3E-10	5.2E-12
GAS-PHASE H_2O	3.7E-09	2.2E-09	2.2E-10	6.7E-10
SOLID-PHASE H_2O (MANTLE+SURFACE)	6.1E-06	8.2E-06	7.0E-06	7.2E-06
GAS-PHASE C	1.3E-04	2.0E-04	1.2E-04	1.9E-04
SOLID-PHASE C (MANTLE+SURFACE)	1.0E-14	2.8E-16	3.8E-13	6.4E-15
GAS-PHASE CO	3.8E-06	1.3E-06	1.6E-06	1.1E-06
SOLID-PHASE CO (MANTLE+SURFACE)	2.0E-14	6.4E-15	6.8E-12	5.5E-14
XO SINK MOLECULE (MANTLE+SURFACE)	X	X	1.5-04	1.5E-04
XC SINK MOLECULE (MANTLE+SURFACE)	X	X	1.3E-05	1.9E-05

species able to lock O and C in the correct ratio to reproduce the observed depletions. This project started as the theoretical follow-up of Chapter 6, where some important questions regarding atomic oxygen interaction with carbonaceous dust grains, O incorporation into the surface and eventual grain growth had been addressed. This Chapter represents a very first approach to address this question by following the work of Jones and Ysard [2019], Jones [2016] and using the `Nautilus` code. We were able to study oxygen depletion into two non-desorbing grain species locking gas-phase O and C in a ratio of 3 to 1, accordingly with the chemical structure of organic carbonates. A high value of oxygen depletion has been reached (almost 30%) without affecting much the abundances of other species relevant to the onset of the mantle in TC conditions and made up of C and O involved in the study. This is a promising result. Also, one has to consider that, by simply varying the scale factor of the UV radiation field, the same analyses and strategies presented in this work can be applied to several TC. Nevertheless this work does not represent a comprehensive and exhaustive study to the topic for the following reason. The strategy used in this Chapter has two main problems that need to be addressed in the future, being the natural steps of this project, but requiring some time to be explored. Firstly, a better description of the chemistry of the sink molecules and a better evaluation of the overall changes made by these additions to the chemistry of the whole system. The XO and XC molecules should be chemically described as organic carbonates and some reactions for their formation need to be implemented. A deeper collaboration with the developer of the code, already started to be sure of the reliability of this strategy, would be essential for this aspect. Secondly, `Nautilus` equations couple diffusion and binding energies. A decoupling and a better definition of both are very important for any further step eventually taken in this project. A last sentence is here reported regarding the overall organic carbonates idea. Since it is seems to be a good way to answer many questions about the physics and the chemistry in TC, some more scientific support would be needed. As reported by the authors of this work, more experiments involving carbonaceous surfaces interacting with atomic O and gas-phase CO and CO_2 would be very relevant to this field. Also, more IR verification and carbonates search in observational data to distinguish between substrate features would be key. Finally, a deeper observational and experimental exploration of this hypothesis would bring significant insights into gas-grain interactions leading to complex organic interstellar chemistry in the translucent ISM before ice mantle onset.

Chapter 10

Conclusions and future perspectives

In this Thesis we present an experimental and theoretical study of the interaction between astrochemically-relevant carbonaceous surfaces with a diverse set of gas-phase species. Dust grains are important catalysts for the formation of new molecules through several physical and chemical processes allowing adsorption of landing atoms or molecules from the gas-phase, diffusion and reactions happening on their surfaces. In specific conditions, and namely in the transition from diffuse to dense clouds, the onset of an icy mantle around the grains is also possible thanks to the availability of gas-phase species such as carbon and oxygen, the stabilization and catalytic support that dust provides and the favourable physical conditions present in translucent clouds. The whole PhD project is divided in two parts and this reflects the overall structure of the Thesis and the scientific questions addressed. The experiments were carried out at LERMA-CYU with the FORMOLISM set-up, while the theoretical follow-up with two different codes (`Cloudy` and `Nautilus`) were developed at UGent. This main focus of this thesis are the astrochemical applications of surface physics and chemistry in ISM conditions and for several astrophysical environments. Except for the fourth Chapter that is very relevant for an overview of the experimental procedures and possibilities offered by the powerful equipment located at LERMA-CYU, the Thesis is symmetrically structured with experimental projects and theoretical follow-ups. Chapter 4 is a tangible example of the very diverse uses of FORMOLISM and it represents a valuable first study of the difference between ices and PAH-like surfaces (i.e. graphite), an extremely important topic in astrochemistry in general and for the aims of the following Chapters. In this Chapter, we also demonstrate how we can extract important information (i.e. binding energies) from experimental results. In the main part of the Thesis, we address two main questions regarding the role of carbonaceous dust grains in the experimental formation

of H_2 (Chapter 5) and H_2O (Chapter 6), with relevant astrophysical implications. The effect on the dissociation front location in PDRs of the high temperature H_2 formation on PAHs found experimentally in Chapter 5 has been studied theoretically with `Cloudy` in Chapter 8. Chapter 9 presents instead the study of the interaction of gas-phase oxygen, together with H, C and in translucent clouds, in order to answer some questions already introduced in Chapter 6 regarding O depletion and grain growth. From an experimental point of view, this Thesis provides direct evidence of the catalytic effects of PAH-like surfaces, namely coronene, underlying the extensive chemisorption stabilization provided by such surfaces. This makes it possible for the landing atoms to form new species at higher temperatures than previously thought, opening the door to explain several observed astrochemical phenomena. Chapter 5 reports on the formation of molecular hydrogen on carbonaceous dust grains up to 250 K, while, before, H_2 formation was considered to be efficient only up to grain temperatures of 50 - 100 K. The first important implication is that H_2 could form in dusty clouds with dust temperatures significantly above 20 K, which is especially relevant to explain the efficient H_2 formation and star-formation through cooling in $T_{dust} > 30$ K high redshift galaxies. The other potential major outcome of our experimental results is the one addressed in Chapter 8. If H_2 can form on grains with higher temperatures, this can have a strong impact on the study of the location of the dissociation fronts of PDRs. This is very important in models that aim to reproduce and compare the emission observed from emission line nebula and PDRs like `Cloudy`. Our simple `Cloudy` implementation of the experimental results on the grain-dependent H_2 formation chemistry described in Chapter 5 has not resulted in the expected shift of the DF towards the IF. Several other possibilities can now be assessed to further explore the impact of high-T H_2 formation, such as introducing a density gradient within the PDR and a better description of the chemisorption-dependent sticking coefficient. The last relevant experimental results are reported in Chapter 6. Here, once again, the chemisorption effect and the catalytic role of coronene are the main characters, this time in its interaction with oxygen and hydrogen. While the first idea was to assess the incorporation of O in the PAH surface to study its implications in grain growth, surface oxidation and oxygen depletion, the results reported here confirm the nature of coronene. Solid water is efficiently formed on the grain upon H and O arrival and the real novelty of our study is the efficient H_2O formation at high temperatures. H_2O forms on coronene at temperatures up to 85 K. Among the several applications of those experimental results, we focus on the effect that this could have in the interpretation of the ice mantle onset and its role in the study of oxygen depletion. In translucent clouds, where the icy mantle starts to form around dust grains, having the formation of solid water at T_{grain} higher than the one at which it was thought to be possible, gives new insights into the preliminary incorporation of gas-phase oxygen in ices. This also represents an explanation for the disappearance of

PAHs in transient regions, since they start to be covered by ice layers. The theoretical follow-up for the interaction of oxygen with carbonaceous dust grains in TC is given in Chapter 9 by using the `Nautilus` code. Here we tried to reproduce the observed O depletions by studying its incorporation in the grains with a specific strategy. The results show promising aspects that need to be further optimized and studied, mainly regarding the chemical description of the species used to lock oxygen and carbon.

Future perspectives consider both the experimental and the theoretical sides of the work. Experimentally, the next main and natural points to analyze would be broadening the range of surfaces where similar results to the ones presented in Chapter 5 and 6 could potentially be obtained. In particular, it would be very relevant to investigate with the same set-up and configuration the atomic hydrogen and oxygen interactions with silicates and PAHs of different families. This might help in having more data useful for future and already available observations and models. Since grain growth has been an invisible "common thread", it would be extremely relevant to expose the already used surfaces to the carbon atomic source that is being constructed on the new setup: FORMOLISM 2.0. Coronene, and PAHs in general, provide chemisorption-active sites for the formation of molecules at higher temperatures and this is an important result that should push the community to investigate such surfaces for the study of grain growth. It has been proven [Zhukovska et al., 2018] that grains can grow at lower densities, therefore at higher T, so the scientific works focusing on the role of PAHs and their properties, like the ones presented in this Thesis, represent a small step forward in that direction. The theoretical follow-ups would require more work to further develop the simple strategies that are presented in this Thesis. In both cases, for `Cloudy` and `Nautilus`, some solutions and the very next steps to take are reported in the Conclusions of the respective Chapters (8 and 9).

In general, astrochemistry represent a bridge between several fields able to help and explain the most diverse scientific question marks where each piece of the puzzle is important to unveil precious hidden information. This Thesis represents the effort of a chemist to network across apparently diverse scientific communities: from experimental astrophysics to surface chemistry, from astrochemical models to the need of reproducing observations. This has been an attempt for astrophysicists and astrochemists to work together and become a melting pot of productive scientific ideas with the aim to tackle relevant astrochemical problems. Thus the most important future perspective is the hope and the invitation to collaborate as much as possible and with scientists having the most diverse expertise to achieve unbelievable goals together.

As Caselli and Ceccarelli [2012] once said: "To understand our origins, we cannot work alone!"

Bibliography

[1] S. Paron. The interstellar medium: from molecules to star formation. *Boletin de la Asociacion Argentina de Astronomia La Plata Argentina*, 60:176–182, August 2018. doi: 10.48550/arXiv.1803.02277.

[2] Yohan Dubois, Francisco Rodríguez Montero, Corentin Guerra, Maxime Trebitsch, San Han, Ricarda Beckmann, Sukyoung K. Yi, Joseph Lewis, and J. K. Jang. Galaxies with grains: unraveling dust evolution and extinction curves with hydrodynamical simulations. , 687:A240, July 2024. doi: 10.1051/0004-6361/202449784.

[3] Theodore P. Snow and Benjamin J. McCall. Diffuse Atomic and Molecular Clouds. , 44(1):367–414, September 2006. doi: 10.1146/annurev.astro.43.072103.150624.

[4] Eva Mateo-Marti, Olga Prieto-Ballesteros, Guillermo Muñoz Caro, Cristobal González-Díaz, Victoria Muñoz-Iglesias, and Santos Gálvez-Martínez. Characterizing Interstellar Medium, Planetary Surface and Deep Environments by Spectroscopic Techniques Using Unique Simulation Chambers at Centro de Astrobiologia (CAB). *Life*, 9(3):72, September 2019. doi: 10.3390/life9030072.

[5] B. Draine and F. Bertoldi. Theoretical Models of Photodissociation Fronts. In F. Combes and G. Pineau Des Forets, editors, *Molecular Hydrogen in Space*, page 131, January 2000. doi: 10.48550/arXiv.astro-ph/0008149.

[6] C. C. Popescu, R. J. Tuffs, M. A. Dopita, J. Fischera, N. D. Kylafis, and B. F. Madore. Modelling the spectral energy distribution of galaxies. V. The dust and PAH emission SEDs of disk galaxies. , 527:A109, March 2011. doi: 10.1051/0004-6361/201015217.

[7] A. P. Jones, L. Fanciullo, M. Köhler, L. Verstraete, V. Guillet, M. Bocchio, and N. Ysard. The evolution of amorphous hydrocarbons in the ISM: dust modelling from a new vantage point. , 558:A62, October 2013. doi: 10.1051/0004-6361/201321686.

[8] https://www.collegesidekick.com/study-guides/astronomy/cosmic-dust, 2024.

[9] E. Congiu, H. Chaabouni, C. Laffon, P. Parent, S. Baouche, and F. Dulieu. Efficient surface formation route of interstellar hydroxylamine through NO hydrogenation. I. The submonolayer regime on interstellar relevant substrates. , 137(5):054713–054713, August 2012. doi: 10.1063/1.4738895.

[10] Valentine Wakelam, Emeric Bron, Stephanie Cazaux, Francois Dulieu, Cécile Gry, Pierre Guillard, Emilie Habart, Liv Hornekær, Sabine Morisset, Gunnar Nyman, Valerio Pirronello, Stephen D. Price, Valeska Valdivia, Gianfranco Vidali, and Naoki Watanabe. H_2 formation on interstellar dust grains: The viewpoints of theory,

experiments, models and observations. *Molecular Astrophysics*, 9:1–36, December 2017. doi: 10.1016/j.molap.2017.11.001.

[11] A. Fuente, D. G. Navarro, P. Caselli, M. Gerin, C. Kramer, E. Roueff, T. Alonso-Albi, R. Bachiller, S. Cazaux, B. Commercon, R. Friesen, S. García-Burillo, B. M. Giuliano, J. R. Goicoechea, P. Gratier, A. Hacar, I. Jiménez-Serra, J. Kirk, V. Lattanzi, J. C. Loison, J. Malinen, N. Marcelino, R. Martín-Doménech, G. Muñoz-Caro, J. Pineda, M. Tafalla, B. Tercero, D. Ward-Thompson, S. P. Treviño-Morales, P. Riviére-Marichalar, O. Roncero, T. Vidal, and M. Y. Ballester. Gas phase Elemental abundances in Molecular cloudS (GEMS). I. The prototypical dark cloud TMC 1. , 624:A105, April 2019. doi: 10.1051/0004-6361/201834654.

[12] Jacob C. Laas and Paola Caselli. Modeling sulfur depletion in interstellar clouds. , 624:A108, April 2019. doi: 10.1051/0004-6361/201834446.

[13] Francesco Grieco, Patrice Theulé, Ilse De Looze, and François Dulieu. Enhanced star formation through the high-temperature formation of H_2 on carbonaceous dust grains. *Nature Astronomy*, 7:541–545, May 2023. doi: 10.1038/s41550-023-01902-4.

[14] D. C. B. Whittet. Oxygen Depletion in the Interstellar Medium: Implications for Grain Models and the Distribution of Elemental Oxygen. , 710(2):1009–1016, February 2010. doi: 10.1088/0004-637X/710/2/1009.

[15] Edward B. Jenkins. A Unified Representation of Gas-Phase Element Depletions in the Interstellar Medium. , 700(2):1299–1348, August 2009. doi: 10.1088/0004-637X/700/2/1299.

[16] Joseph C. Weingartner and B. T. Draine. Interstellar Depletion onto Very Small Dust Grains. , 517(1):292–298, May 1999. doi: 10.1086/307197.

[17] T. K. Nguyen, D. P. Ruffle, E. Herbst, and D. A. Williams. The water ice distribution in Taurus determined by gas-grain chemistry. , 329(2):301–308, January 2002. doi: 10.1046/j.1365-8711.2002.04971.x.

[18] Database CDMS. Cdms, database. `https://cdms.astro.uni-koeln.de/classic/molecules`, 2024. Accessed: 05-08-2024.

[19] P. De Vis, A. Jones, S. Viaene, V. Casasola, C. J. R. Clark, M. Baes, S. Bianchi, L. P. Cassara, J. I. Davies, I. De Looze, M. Galametz, F. Galliano, S. Lianou, S. Madden, A. Manilla-Robles, A. V. Mosenkov, A. Nersesian, S. Roychowdhury, E. M. Xilouris, and N. Ysard. A systematic metallicity study of DustPedia galaxies reveals evolution in the dust-to-metal ratios. , 623:A5, March 2019. doi: 10.1051/0004-6361/201834444.

[20] B. Draine. On the Interpretation of the λ 2175 Å Feature. In Louis J. Allamandola and A. G. G. M. Tielens, editors, *Interstellar Dust*, volume 135 of *IAU Symposium*, page 313, January 1989.

[21] Qi Lin, X. J. Yang, and Aigen Li. Polycyclic aromatic hydrocarbon molecules and the 2175Å interstellar extinction bump. , 525(2):2380–2387, October 2023. doi: 10.1093/mnras/stad2405.

[22] E. Herbst. Chemistry in the Interstellar Medium. *Annual Review of Physical Chemistry*, 46:27–54, October 1995. doi: 10.1146/annurev.pc.46.100195.000331.

[23] James Lequeux. *The Interstellar Medium*. 2005. doi: 10.1007/b137959.

[24] Bradley W. Carroll and Dale A. Ostlie. *An introduction to modern astrophysics, Second Edition*. 2017.

[25] Paola Caselli and Cecilia Ceccarelli. Our astrochemical heritage. , 20:56, October 2012. doi: 10.1007/s00159-012-0056-x.

[26] J. F. Corby, B. A. McGuire, E. Herbst, and A. J. Remijan. The molecular chemistry of diffuse and translucent clouds in the line-of-sight to Sgr B2: Absorption by simple organic and inorganic molecules in the GBT PRIMOS survey. , 610:A10, February 2018. doi: 10.1051/0004-6361/201730988.

[27] Eric B. Burgh, Kevin France, and Edward B. Jenkins. Atomic and Molecular Carbon as a Tracer of Translucent Clouds. , 708(1):334–341, January 2010. doi: 10.1088/0004-637X/708/1/334.

[28] Ewine F. van Dishoeck and John H. Black. Interstellar C 2, CH, and CN in Translucent Molecular Clouds. , 340:273, May 1989. doi: 10.1086/167391.

[29] P. M. Solomon and William Klemperer. The Formation of Diatomic Molecules in Interstellar Clouds. , 178:389–422, December 1972. doi: 10.1086/151799.

[30] Eric Herbst and William Klemperer. The Formation and Depletion of Molecules in Dense Interstellar Clouds. , 185:505–534, October 1973. doi: 10.1086/152436.

[31] S. Weinreb, A. H. Barrett, M. L. Meeks, and J. C. Henry. Radio Observations of OH in the Interstellar Medium. , 200(4909):829–831, November 1963. doi: 10.1038/200829a0.

[32] A. Sternberg and A. Dalgarno. Chemistry in Dense Photon-dominated Regions. , 99:565, August 1995. doi: 10.1086/192198.

[33] D. J. Hollenbach and A. G. G. M. Tielens. Photodissociation regions in the interstellar medium of galaxies. *Reviews of Modern Physics*, 71(1):173–230, January 1999. doi: 10.1103/RevModPhys.71.173.

[34] W. W. Duley and D. A. Williams. The infrared spectrum of interstellar dust - Surface functional groups on carbon. , 196:269–274, July 1981. doi: 10.1093/mnras/196.2.269.

[35] L. J. Allamandola, A. G. G. M. Tielens, and J. R. Barker. Polycyclic aromatic hydrocarbons and the unidentified infrared emission bands: auto exhaust along the milky way. , 290:L25–L28, March 1985. doi: 10.1086/184435.

[36] J. L. Puget and A. Leger. A new component of the interstellar matter: small grains and large aromatic molecules. , 27:161–198, January 1989. doi: 10.1146/annurev.aa.27.090189.001113.

[37] A. G. G. M. Tielens. Interstellar polycyclic aromatic hydrocarbon molecules. , 46:289–337, September 2008. doi: 10.1146/annurev.astro.46.060407.145211.

[38] Frédéric Galliano, Angelos Nersesian, Simone Bianchi, Ilse De Looze, Sambit Roychowdhury, Maarten Baes, Viviana Casasola, Letizia P. Cassará, Wouter Dobbels, Jacopo Fritz, Maud Galametz, Anthony P. Jones, Suzanne C. Madden, Aleksandr Mosenkov, Emmanuel M. Xilouris, and Nathalie Ysard. A nearby galaxy perspective on dust evolution. Scaling relations and constraints on the dust build-up in galaxies with the DustPedia and DGS samples. , 649:A18, May 2021. doi: 10.1051/0004-6361/202039701.

[39] Ambra Nanni, Alessandro Bressan, Paola Marigo, and Léo Girardi. Evolution of thermally pulsing asymptotic giant branch stars - II. Dust production at varying metallicity. , 434(3):2390–2417, September 2013. doi: 10.1093/mnras/stt1175.

[40] P. Ventura, M. di Criscienzo, R. Schneider, R. Carini, R. Valiante, F. D'Antona, S. Gallerani, R. Maiolino, and A. Tornambé. Dust formation around AGB and SAGB stars: a trend with metallicity? , 424(3):2345–2357, August 2012. doi: 10.1111/j.1365-2966.2012.21403.x.

[41] M. Maercker, S. Ramstedt, M. L. Leal-Ferreira, G. Olofsson, and H. G. Floren. The detached dust shells around the carbon AGB stars R Sculptoris and V644 Scorpii. , 570:A101, October 2014. doi: 10.1051/0004-6361/201424892.

[42] Jonathan D. Slavin, Eli Dwek, and Anthony P. Jones. Destruction of Interstellar Dust in Evolving Supernova Remnant Shock Waves. , 803(1):7, April 2015. doi: 10.1088/0004-637X/803/1/7.

[43] Alexey Potapov and Martin McCoustra. Physics and Chemistry on the Surface of Cosmic Dust Grains: A Laboratory View. *arXiv e-prints*, art. arXiv:2105.01387, May 2021. doi: 10.48550/arXiv.2105.01387.

[44] B. T. Draine. Interstellar Dust Models and Evolutionary Implications. In T. Henning, E. Grün, and J. Steinacker, editors, *Cosmic Dust - Near and Far*, volume 414 of *Astronomical Society of the Pacific Conference Series*, page 453, December 2009. doi: 10.48550/arXiv.0903.1658.

[45] S. Viaene, M. Baes, G. Bendo, M. Boquien, A. Boselli, L. Ciesla, L. Cortese, I. De Looze, S. Eales, J. Fritz, O. Ł. Karczewski, S. Madden, M. W. L. Smith, and L. Spinoglio. The bolometric and UV attenuation in normal spiral galaxies of the Herschel Reference Survey. , 586:A13, February 2016. doi: 10.1051/0004-6361/201527586.

[46] S. P. Driver, P. D. Allen, Alister. W. Graham, E. Cameron, J. Liske, S. C. Ellis, N. J. G. Cross, R. De Propris, S. Phillipps, and W. J. Couch. The Millennium Galaxy Catalogue: morphological classification and bimodality in the colour-concentration plane. , 368(1):414–434, May 2006. doi: 10.1111/j.1365-2966.2006.10126.x.

[47] A. P. Jones, M. Köhler, N. Ysard, M. Bocchio, and L. Verstraete. The global dust modelling framework THEMIS. , 602:A46, June 2017. doi: 10.1051/0004-6361/201630225.

[48] B. T. Draine, D. A. Dale, G. Bendo, K. D. Gordon, J. D. T. Smith, L. Armus, C. W. Engelbracht, G. Helou, Jr. Kennicutt, R. C., A. Li, H. Roussel, F. Walter, D. Calzetti, J. Moustakas, E. J. Murphy, G. H. Rieke, C. Bot, D. J. Hollenbach, K. Sheth, and H. I. Teplitz. Dust Masses, PAH Abundances, and Starlight Intensities in the SINGS Galaxy Sample. , 663(2):866–894, July 2007. doi: 10.1086/518306.

[49] G. Aniano, B. T. Draine, L. K. Hunt, K. Sandstrom, D. Calzetti, R. C. Kennicutt, D. A. Dale, M. Galametz, K. D. Gordon, A. K. Leroy, J. D. T. Smith, H. Roussel, M. Sauvage, F. Walter, L. Armus, A. D. Bolatto, M. Boquien, A. Crocker, I. De Looze, J. Donovan Meyer, G. Helou, J. Hinz, B. D. Johnson, J. Koda, A. Miller, E. Montiel, E. J. Murphy, M. Relaño, H. W. Rix, E. Schinnerer, R. Skibba, M. G. Wolfire, and C. W. Engelbracht. Modeling Dust and Starlight in Galaxies Observed by Spitzer and Herschel: The KINGFISH Sample. , 889(2):150, February 2020. doi: 10.3847/1538-4357/ab5fdb.

[50] F. X. Desert, F. Boulanger, and J. L. Puget. Interstellar Dust Models for Extinction and Emission. , 237:215, October 1990.

[51] I. De Looze, I. Lamperti, A. Saintonge, M. Relaño, M. W. L. Smith, C. J. R. Clark, C. D. Wilson, M. Decleir, A. P. Jones, R. C. Kennicutt, G. Accurso, E. Brinks, M. Bureau, P. Cigan, D. L. Clements, P. De Vis, L. Fanciullo, Y. Gao, W. K. Gear, L. C. Ho, H. S. Hwang, M. J. Michałowski, J. C. Lee, C. Li, L. Lin, T. Liu, M. Lomaeva, H. A. Pan, M. Sargent, T. Williams, T. Xiao, and M. Zhu. JINGLE - IV. Dust, H I gas, and metal scaling laws in the local Universe. , 496(3):3668–3687, August 2020. doi: 10.1093/mnras/staa1496.

[52] Hiroyuki Hirashita and Huirong Yan. Shattering and coagulation of dust grains in interstellar turbulence. , 394(2):1061–1074, April 2009. doi: 10.1111/j.1365-2966.2009.14405.x.

[53] Florian Kirchschlager, Lars Mattsson, and Frederick A. Gent. Supernova induced processing of interstellar dust: impact of interstellar medium gas density and gas turbulence. , 509(3):3218–3234, January 2022. doi: 10.1093/mnras/stab3059.

[54] Lars Mattsson. Modelling dust processing and the evolution of grain sizes in the ISM using the method of moments. , 133:107–123, November 2016. doi: 10.1016/j.pss.2016.05.002.

[55] Jonathan D. Slavin, Eli Dwek, Mordecai-Mark Mac Low, and Alex S. Hill. The Dynamics, Destruction, and Survival of Supernova-formed Dust Grains. , 902(2):135, October 2020. doi: 10.3847/1538-4357/abb5a4.

[56] A. P. Jones, A. G. G. M. Tielens, and D. J. Hollenbach. Grain Shattering in Shocks: The Interstellar Grain Size Distribution. , 469:740, October 1996. doi: 10.1086/177823.

[57] Devin W. Silvia, B. D. Smith, and J. M. Shull. Numerical Simulations of Dust Destruction in Supernova Remnants. In *American Astronomical Society Meeting Abstracts #215*, volume 215 of *American Astronomical Society Meeting Abstracts*, page 454.02, January 2010.

[58] A. P. Jones and J. A. Nuth. Dust destruction in the ISM: a re-evaluation of dust lifetimes. , 530:A44, June 2011. doi: 10.1051/0004-6361/201014440.

[59] Elisabetta R. Micelotta, Eli Dwek, and Jonathan D. Slavin. Dust destruction by the reverse shock in the Cassiopeia A supernova remnant. , 590:A65, May 2016. doi: 10.1051/0004-6361/201527350.

[60] Gaël Rouillé, Cornelia Jäger, Serge A. Krasnokutski, Melinda Krebsz, and Thomas Henning. Cold condensation of dust in the ISM. *arXiv e-prints*, art. arXiv:1502.00388, February 2015. doi: 10.48550/arXiv.1502.00388.

[61] Gaël Rouillé, Cornelia Jäger, and Thomas Henning. Separate Silicate and Carbonaceous Solids Formed from Mixed Atomic and Molecular Species Diffusing in Neon Ice. , 892(2):96, April 2020. doi: 10.3847/1538-4357/ab7a11.

[62] Florian Kirchschlager, Franziska D. Schmidt, M. J. Barlow, Erica L. Fogerty, Antonia Bevan, and Felix D. Priestley. Dust survival rates in clumps passing through the Cas A reverse shock - I. Results for a range of clump densities. , 489(4):4465–4496, November 2019. doi: 10.1093/mnras/stz2399.

[63] Julia Roman-Duval, Edward B. Jenkins, Kirill Tchernyshyov, Christopher J. R. Clark, Annalisa De Cia, Karl D. Gordon, Aleksandra Hamanowicz, Vianney Lebouteiller, Marc Rafelski, Karin Sandstrom, Jessica Werk, and Petia Yanchulova Merica-Jones. METAL: The Metal Evolution, Transport, and Abundance in the Large Magellanic Cloud Hubble Program. III. Interstellar Depletions, Dust-to-Metal, and Dust-to-Gas Ratios versus Metallicity. , 928(1):90, March 2022. doi: 10.3847/1538-4357/ac5248.

[64] Christopher J. R. Clark, Julia C. Roman-Duval, Karl D. Gordon, Caroline Bot, Matthew W. L. Smith, and Lea M. Z. Hagen. The Quest for the Missing Dust. II. Two Orders of Magnitude of Evolution in the Dust-to-gas Ratio Resolved within Local Group Galaxies. , 946(1):42, March 2023. doi: 10.3847/1538-4357/acbb66.

[65] Christina Konstantopoulou, Annalisa De Cia, Cédric Ledoux, Jens-Kristian Krogager, Lars Mattsson, Darach Watson, Kasper E. Heintz, Céline Péroux, Pasquier Noterdaeme, Anja C. Andersen, Johan P. U. Fynbo, Iris Jermann, and Tanita Ramburuth-Hurt. Dust depletion of metals from local to distant galaxies. II. Cosmic dust-to-metal ratio and dust composition. , 681:A64, January 2024. doi: 10.1051/0004-6361/202347171.

[66] Svitlana Zhukovska, Clare Dobbs, Edward B. Jenkins, and Ralf S. Klessen. Modeling Dust Evolution in Galaxies with a Multiphase, Inhomogeneous ISM. , 831(2): 147, November 2016. doi: 10.3847/0004-637X/831/2/147.

[67] Svitlana Zhukovska, Thomas Henning, and Clare Dobbs. Iron and Silicate Dust Growth in the Galactic Interstellar Medium: Clues from Element Depletions. , 857 (2):94, April 2018. doi: 10.3847/1538-4357/aab438.

[68] E. Dartois, J. A. Noble, P. Caselli, H. J. Fraser, I. Jiménez-Serra, B. Maté, M. K. McClure, G. J. Melnick, Y. J. Pendleton, T. Shimonishi, Z. L. Smith, J. A. Sturm, A. Taillard, V. Wakelam, A. C. A. Boogert, M. N. Drozdovskaya, J. Erkal, D. Harsono, V. J. Herrero, S. Ioppolo, H. Linnartz, B. A. McGuire, G. Perotti, D. Qasim, and W. R. M. Rocha. Spectroscopic sizing of interstellar icy grains with JWST. *Nature Astronomy*, 8:359–367, March 2024. doi: 10.1038/s41550-023-02155-x.

[69] A. Ferrara, S. Viti, and C. Ceccarelli. The problematic growth of dust in high-redshift galaxies. , 463(1):L112–L116, November 2016. doi: 10.1093/mnrasl/slw165.

[70] Michael J. Barlow. The destruction and growth of dust grains in interstellar space - III. Surface recombination, heavy element depletion and mantle growth. , 183: 417–434, May 1978. doi: 10.1093/mnras/183.3.417.

[71] Cecilia Ceccarelli, Serena Viti, Nadia Balucani, and Vianney Taquet. The evolution of grain mantles and silicate dust growth at high redshift. , 476(1):1371–1383, May 2018. doi: 10.1093/mnras/sty313.

[72] D. P. Ruffle, T. W. Hartquist, P. Caselli, and D. A. Williams. The sulphur depletion problem. , 306(3):691–695, July 1999. doi: 10.1046/j.1365-8711.1999.02562.x.

[73] S. Cazaux, H. Carrascosa, G. M. Muñoz Caro, P. Caselli, A. Fuente, D. Navarro-Almaida, and P. Riviére-Marichalar. Photoprocessing of H_2S on dust grains. Building S chains in translucent clouds and comets. , 657:A100, January 2022. doi: 10.1051/0004-6361/202141861.

[74] A. Fuente, P. Rivière-Marichalar, L. Beitia-Antero, P. Caselli, V. Wakelam, G. Esplugues, M. Rodríguez-Baras, D. Navarro-Almaida, M. Gerin, C. Kramer, R. Bachiller, J. R. Goicoechea, I. Jiménez-Serra, J. C. Loison, A. Ivlev, R. Martín-Doménech, S. Spezzano, O. Roncero, G. Muñoz-Caro, S. Cazaux, and N. Marcelino. Gas phase Elemental abundances in Molecular cloudS (GEMS). VII. Sulfur elemental abundance. , 670:A114, February 2023. doi: 10.1051/0004-6361/202244843.

[75] F. D. Priestley, I. De Looze, and M. J. Barlow. The efficiency of grain growth in the diffuse interstellar medium. , 502(2):2438–2445, April 2021. doi: 10.1093/mnras/stab122.

[76] A. C. Adwin Boogert, Perry A. Gerakines, and Douglas C. B. Whittet. Observations of the icy universe. , 53:541–581, August 2015. doi: 10.1146/annurev-astro-082214-122348.

[77] F. Boulanger, P. Cox, and A. P. Jones. Course 7: Dust in the Interstellar Medium. In F. Casoli, J. Lequeux, and F. David, editors, *Infrared Space Astronomy, Today and Tomorrow*, volume 70, page 251, January 2000.

[78] S. Tosi, D. Kamath, F. Dell'Agli, H. Van Winckel, P. Ventura, T. Marchetti, E. Marini, and M. Tailo. A study of carbon-rich post-AGB stars in the Milky Way to understand the production of carbonaceous dust from evolved stars. , 673:A41, May 2023. doi: 10.1051/0004-6361/202245563.

[79] S. Zhukovska and T. Henning. Dust input from AGB stars in the Large Magellanic Cloud. , 555:A99, July 2013. doi: 10.1051/0004-6361/201321368.

[80] Sundar Srinivasan, Franciska Kemper, and Ronny Zhao-Geisler. Identifying the chemistry of the dust around AGB stars in nearby galaxies. *arXiv e-prints*, art. arXiv:1608.00312, July 2016. doi: 10.48550/arXiv.1608.00312.

[81] Ambra Nanni, Alessandro Bressan, Paola Marigo, and Léo Girardi. Evolution of thermally pulsing asymptotic giant branch stars - III. Dust production at supersolar metallicities. , 438(3):2328–2340, March 2014. doi: 10.1093/mnras/stt2348.

[82] P. Ventura, M. Di Criscienzo, R. Carini, and F. D'Antona. Yields of AGB and SAGB models with chemistry of low- and high-metallicity globular clusters. , 431 (4):3642–3653, June 2013. doi: 10.1093/mnras/stt444.

[83] P. Ventura and M. Limongi. Gas and dust from stars. , 85:196, January 2014.

[84] A. Leger and J. L. Puget. Identification of the Unidentified Infrared Emission Features of Interstellar Dust. , 137:L5–L8, August 1984.

[85] Karin M. Sandstrom, Alberto D. Bolatto, B. T. Draine, Caroline Bot, and Snežana Stanimirović. The Spitzer Survey of the Small Magellanic Cloud (S^3MC): Insights into the Life Cycle of Polycyclic Aromatic Hydrocarbons. , 715(2):701–723, June 2010. doi: 10.1088/0004-637X/715/2/701.

[86] Jérémy Chastenet, Karin Sandstrom, I-Da Chiang, Adam K. Leroy, Dyas Utomo, Caroline Bot, Karl D. Gordon, Bruce T. Draine, Yasuo Fukui, Toshikazu Onishi, and Kisetsu Tsuge. The Polycyclic Aromatic Hydrocarbon Mass Fraction on a 10 pc Scale in the Magellanic Clouds. , 876(1):62, May 2019. doi: 10.3847/1538-4357/ab16cf.

[87] Karl D. Gordon, Charles W. Engelbracht, George H. Rieke, K. A. Misselt, J. D. T. Smith, and Jr. Kennicutt, Robert C. The Behavior of the Aromatic Features in M101 H II Regions: Evidence for Dust Processing. , 682(1):336–354, July 2008. doi: 10.1086/589567.

[88] Joris Witstok, Irene Shivaei, Renske Smit, Roberto Maiolino, Stefano Carniani, Emma Curtis-Lake, Pierre Ferruit, Santiago Arribas, Andrew J. Bunker, Alex J. Cameron, Stephane Charlot, Jacopo Chevallard, Mirko Curti, Anna de Graaff, Francesco D'Eugenio, Giovanna Giardino, Tobias J. Looser, Tim Rawle, Bruno Rodríguez del Pino, Chris Willott, Stacey Alberts, William M. Baker, Kristan Boyett, Eiichi Egami, Daniel J. Eisenstein, Ryan Endsley, Kevin N. Hainline, Zhiyuan Ji, Benjamin D. Johnson, Nimisha Kumari, Jianwei Lyu, Erica Nelson, Michele Perna, Marcia Rieke, Brant E. Robertson, Lester Sandles, Aayush Saxena,

Jan Scholtz, Fengwu Sun, Sandro Tacchella, Christina C. Williams, and Christopher N. A. Willmer. Carbonaceous dust grains seen in the first billion years of cosmic time. , 621(7978):267–270, September 2023. doi: 10.1038/s41586-023-06413-w.

[89] Justin S. Spilker, Kedar A. Phadke, Manuel Aravena, Melanie Archipley, Matthew B. Bayliss, Jack E. Birkin, Matthieu Béthermin, James Burgoyne, Jared Cathey, Scott C. Chapman, Hâkon Dahle, Anthony H. Gonzalez, Gayathri Gururajan, Christopher C. Hayward, Yashar D. Hezaveh, Ryley Hill, Taylor A. Hutchison, Keunho J. Kim, Seonwoo Kim, David Law, Ronan Legin, Matthew A. Malkan, Daniel P. Marrone, Eric J. Murphy, Desika Narayanan, Alex Navarre, Grace M. Olivier, Jeffrey A. Rich, Jane R. Rigby, Cassie Reuter, James E. Rhoads, Keren Sharon, J. D. T. Smith, Manuel Solimano, Nikolaus Sulzenauer, Joaquin D. Vieira, David Vizgan, Axel Weiß, and Katherine E. Whitaker. Spatial variations in aromatic hydrocarbon emission in a dust-rich galaxy. , 618(7966):708–711, June 2023. doi: 10.1038/s41586-023-05998-6.

[90] Jérémy Chastenet, Jessica Sutter, Karin Sandstrom, Francesco Belfiore, Oleg V. Egorov, Kirsten L. Larson, Adam K. Leroy, Daizhong Liu, Erik Rosolowsky, David A. Thilker, Elizabeth J. Watkins, Thomas G. Williams, Ashley. T. Barnes, F. Bigiel, Médéric Boquien, Mélanie Chevance, Daniel A. Dale, J. M. Diederik Kruijssen, Eric Emsellem, Kathryn Grasha, Brent Groves, Hamid Hassani, Annie Hughes, Kathryn Kreckel, Sharon E. Meidt, Hsi-An Pan, Miguel Querejeta, Eva Schinnerer, and Cory M. Whitcomb. PHANGS-JWST First Results: Measuring Polycyclic Aromatic Hydrocarbon Properties across the Multiphase Interstellar Medium. , 944(2): L12, February 2023. doi: 10.3847/2041-8213/acac94.

[91] Jessica Sutter, Karin Sandstrom, Jérémy Chastenet, Adam K. Leroy, Eric W. Koch, Thomas G. Williams, Ryan Chown, Francesco Belfiore, Frank Bigiel, Médéric Boquien, Yixian Cao, Mélanie Chevance, Daniel A. Dale, Oleg V. Egorov, Simon C. O. Glover, Brent Groves, Ralf S. Klessen, Kathryn Kreckel, Kirsten L. Larson, Elias K. Oakes, Debosmita Pathak, Lise Ramambason, Erik Rosolowsky, and Elizabeth J. Watkins. The Fraction of Dust Mass in the Form of Polycyclic Aromatic Hydrocarbons on 10–50 pc Scales in Nearby Galaxies. , 971(2):178, August 2024. doi: 10.3847/1538-4357/ad54bd.

[92] Ryan Chown, Ameek Sidhu, Els Peeters, Alexander G. G. M. Tielens, Jan Cami, Olivier Berné, Emilie Habart, Felipe Alarcón, Amélie Canin, Ilane Schroetter, Boris Trahin, Dries Van De Putte, Alain Abergel, Edwin A. Bergin, Jeronimo Bernard-Salas, Christiaan Boersma, Emeric Bron, Sara Cuadrado, Emmanuel Dartois, Daniel Dicken, Meriem El-Yajouri, Asunción Fuente, Javier R. Goicoechea, Karl D. Gordon, Lina Issa, Christine Joblin, Olga Kannavou, Baria Khan, Ozan

Lacinbala, David Languignon, Romane Le Gal, Alexandros Maragkoudakis, Raphael Meshaka, Yoko Okada, Takashi Onaka, Sofia Pasquini, Marc W. Pound, Massimo Robberto, Markus Röllig, Bethany Schefter, Thiébaut Schirmer, Sílvia Vicente, Mark G. Wolfire, Marion Zannese, Isabel Aleman, Louis Allamandola, Rebecca Auchettl, Giuseppe Antonio Baratta, Salma Bejaoui, Partha P. Bera, John H. Black, François Boulanger, Jordy Bouwman, Bernhard Brandl, Philippe Brechignac, Sandra Brünken, Mridusmita Buragohain, Andrew Burkhardt, Alessandra Candian, Stéphanie Cazaux, Jose Cernicharo, Marin Chabot, Shubhadip Chakraborty, Jason Champion, Sean W. J. Colgan, Ilsa R. Cooke, Audrey Coutens, Nick L. J. Cox, Karine Demyk, Jennifer Donovan Meyer, Sacha Foschino, Pedro García-Lario, Lisseth Gavilan, Maryvonne Gerin, Carl A. Gottlieb, Pierre Guillard, Antoine Gusdorf, Patrick Hartigan, Jinhua He, Eric Herbst, Liv Hornekaer, Cornelia Jäger, Eduardo Janot-Pacheco, Michael Kaufman, Francisca Kemper, Sarah Kendrew, Maria S. Kirsanova, Pamela Klaassen, Sun Kwok, Álvaro Labiano, Thomas S. Y. Lai, Timothy J. Lee, Bertrand Lefloch, Franck Le Petit, Aigen Li, Hendrik Linz, Cameron J. Mackie, Suzanne C. Madden, Joëlle Mascetti, Brett A. McGuire, Pablo Merino, Elisabetta R. Micelotta, Karl Misselt, Jon A. Morse, Giacomo Mulas, Naslim Neelamkodan, Ryou Ohsawa, Alain Omont, Roberta Paladini, Maria Elisabetta Palumbo, Amit Pathak, Yvonne J. Pendleton, Annemieke Petrignani, Thomas Pino, Elena Puga, Naseem Rangwala, Mathias Rapacioli, Alessandra Ricca, Julia Roman-Duval, Joseph Roser, Evelyne Roueff, Gaël Rouillé, Farid Salama, Dinalva A. Sales, Karin Sandstrom, Peter Sarre, Ella Sciamma-O'Brien, Kris Sellgren, Sachindev S. Shenoy, David Teyssier, Richard D. Thomas, Aditya Togi, Laurent Verstraete, Adolf N. Witt, Alwyn Wootten, Henning Zettergren, Yong Zhang, Ziwei E. Zhang, and Junfeng Zhen. PDRs4All. IV. An embarrassment of riches: Aromatic infrared bands in the Orion Bar. , 685: A75, May 2024. doi: 10.1051/0004-6361/202346662.

[93] Els Peeters, Emilie Habart, Olivier Berné, Ameek Sidhu, Ryan Chown, Dries Van De Putte, Boris Trahin, Ilane Schroetter, Amélie Canin, Felipe Alarcón, Bethany Schefter, Baria Khan, Sofia Pasquini, Alexander G. G. M. Tielens, Mark G. Wolfire, Emmanuel Dartois, Javier R. Goicoechea, Alexandros Maragkoudakis, Takashi Onaka, Marc W. Pound, Sílvia Vicente, Alain Abergel, Edwin A. Bergin, Jeronimo Bernard-Salas, Christiaan Boersma, Emeric Bron, Jan Cami, Sara Cuadrado, Daniel Dicken, Meriem Elyajouri, Asunción Fuente, Karl D. Gordon, Lina Issa, Christine Joblin, Olga Kannavou, Ozan Lacinbala, David Languignon, Romane Le Gal, Raphael Meshaka, Yoko Okada, Massimo Robberto, Markus Röllig, Thiébaut Schirmer, Benoit Tabone, Marion Zannese, Isabel Aleman, Louis Allamandola, Rebecca Auchettl, Giuseppe Antonio Baratta, Salma Bejaoui, Partha P. Bera, John H. Black, Francois Boulanger, Jordy Bouwman, Bernhard Brandl, Philippe Brechignac,

Sandra Brünken, Mridusmita Buragohain, Andrew Burkhardt, Alessandra Candian, Stéphanie Cazaux, Jose Cernicharo, Marin Chabot, Shubhadip Chakraborty, Jason Champion, Sean W. J. Colgan, Ilsa R. Cooke, Audrey Coutens, Nick L. J. Cox, Karine Demyk, Jennifer Donovan Meyer, Sacha Foschino, Pedro García-Lario, Maryvonne Gerin, Carl A. Gottlieb, Pierre Guillard, Antoine Gusdorf, Patrick Hartigan, Jinhua He, Eric Herbst, Liv Hornekaer, Cornelia Jäger, Eduardo Janot-Pacheco, Michael Kaufman, Sarah Kendrew, Maria S. Kirsanova, Pamela Klaassen, Sun Kwok, Álvaro Labiano, Thomas S. Y. Lai, Timothy J. Lee, Bertrand Lefloch, Franck Le Petit, Aigen Li, Hendrik Linz, Cameron J. Mackie, Suzanne C. Madden, Joëlle Mascetti, Brett A. McGuire, Pablo Merino, Elisabetta R. Micelotta, Karl Misselt, Jon A. Morse, Giacomo Mulas, Naslim Neelamkodan, Ryou Ohsawa, Roberta Paladini, Maria Elisabetta Palumbo, Amit Pathak, Yvonne J. Pendleton, Annemieke Petrignani, Thomas Pino, Elena Puga, Naseem Rangwala, Mathias Rapacioli, Alessandra Ricca, Julia Roman-Duval, Joseph Roser, Evelyne Roueff, Gaël Rouillé, Farid Salama, Dinalva A. Sales, Karin Sandstrom, Peter Sarre, Ella Sciamma-O'Brien, Kris Sellgren, Sachindev S. Shenoy, David Teyssier, Richard D. Thomas, Aditya Togi, Laurent Verstraete, Adolf N. Witt, Alwyn Wootten, Nathalie Ysard, Henning Zettergren, Yong Zhang, Ziwei E. Zhang, and Junfeng Zhen. PDRs4All: III. JWST's NIR spectroscopic view of the Orion Bar. , 685:A74, May 2024. doi: 10.1051/0004-6361/202348244.

[94] Emilie Habart, Els Peeters, Olivier Berné, Boris Trahin, Amélie Canin, Ryan Chown, Ameek Sidhu, Dries Van De Putte, Felipe Alarcón, Ilane Schroetter, Emmanuel Dartois, Sílvia Vicente, Alain Abergel, Edwin A. Bergin, Jeronimo Bernard-Salas, Christiaan Boersma, Emeric Bron, Jan Cami, Sara Cuadrado, Daniel Dicken, Meriem Elyajouri, Asunción Fuente, Javier R. Goicoechea, Karl D. Gordon, Lina Issa, Christine Joblin, Olga Kannavou, Baria Khan, Ozan Lacinbala, David Languignon, Romane Le Gal, Alexandros Maragkoudakis, Raphael Meshaka, Yoko Okada, Takashi Onaka, Sofia Pasquini, Marc W. Pound, Massimo Robberto, Markus Röllig, Bethany Schefter, Thiébaut Schirmer, Benoit Tabone, Alexander G. G. M. Tielens, Mark G. Wolfire, Marion Zannese, Nathalie Ysard, Marc-Antoine Miville-Deschenes, Isabel Aleman, Louis Allamandola, Rebecca Auchettl, Giuseppe Antonio Baratta, Salma Bejaoui, Partha P. Bera, John H. Black, Francois Boulanger, Jordy Bouwman, Bernhard Brandl, Philippe Brechignac, Sandra Brünken, Mridusmita Buragohain, Andrew Burkhardt, Alessandra Candian, Stéphanie Cazaux, Jose Cernicharo, Marin Chabot, Shubhadip Chakraborty, Jason Champion, Sean W. J. Colgan, Ilsa R. Cooke, Audrey Coutens, Nick L. J. Cox, Karine Demyk, Jennifer Donovan Meyer, Sacha Foschino, Pedro García-Lario, Lisseth Gavilan, Maryvonne Gerin, Carl A. Gottlieb, Pierre Guillard, Antoine Gusdorf, Patrick Hartigan, Jinhua He,

Eric Herbst, Liv Hornekaer, Cornelia Jäger, Eduardo Janot-Pacheco, Michael Kaufman, Francisca Kemper, Sarah Kendrew, Maria S. Kirsanova, Pamela Klaassen, Sun Kwok, Álvaro Labiano, Thomas S. Y. Lai, Timothy J. Lee, Bertrand Lefloch, Franck Le Petit, Aigen Li, Hendrik Linz, Cameron J. Mackie, Suzanne C. Madden, Joëlle Mascetti, Brett A. McGuire, Pablo Merino, Elisabetta R. Micelotta, Karl Misselt, Jon A. Morse, Giacomo Mulas, Naslim Neelamkodan, Ryou Ohsawa, Alain Omont, Roberta Paladini, Maria Elisabetta Palumbo, Amit Pathak, Yvonne J. Pendleton, Annemieke Petrignani, Thomas Pino, Elena Puga, Naseem Rangwala, Mathias Rapacioli, Alessandra Ricca, Julia Roman-Duval, Joseph Roser, Evelyne Roueff, Gaël Rouillé, Farid Salama, Dinalva A. Sales, Karin Sandstrom, Peter Sarre, Ella Sciamma-O'Brien, Kris Sellgren, Sachindev S. Shenoy, David Teyssier, Richard D. Thomas, Aditya Togi, Laurent Verstraete, Adolf N. Witt, Alwyn Wootten, Henning Zettergren, Yong Zhang, Ziwei E. Zhang, and Junfeng Zhen. PDRs4All. II. JWST's NIR and MIR imaging view of the Orion Nebula. , 685:A73, May 2024. doi: 10.1051/0004-6361/202346747.

[95] C. Knight, E. Peeters, D. J. Stock, W. D. Vacca, and A. G. G. M. Tielens. Tracing PAH Size in Prominent Nearby Mid-Infrared Environments. , 918(1):8, September 2021. doi: 10.3847/1538-4357/ac02c6.

[96] Valentine Wakelam and Eric Herbst. Polycyclic Aromatic Hydrocarbons in Dense Cloud Chemistry. , 680(1):371–383, June 2008. doi: 10.1086/587734.

[97] M. Rapacioli, C. Joblin, and P. Boissel. Spectroscopy of polycyclic aromatic hydrocarbons and very small grains in photodissociation regions. , 429:193–204, January 2005. doi: 10.1051/0004-6361:20041247.

[98] M. Rapacioli, F. Calvo, C. Joblin, P. Parneix, D. Toublanc, and F. Spiegelman. Formation and destruction of polycyclic aromatic hydrocarbon clusters in the interstellar medium. , 460(2):519–531, December 2006. doi: 10.1051/0004-6361:20065412.

[99] C. Joblin, A. Leger, and P. Martin. Contribution of Polycyclic Aromatic Hydrocarbon Molecules to the Interstellar Extinction Curve. , 393:L79, July 1992. doi: 10.1086/186456.

[100] T. Allain, S. Leach, and E. Sedlmayr. Photodestruction of PAHs in the interstellar medium. I. Photodissociation rates for the loss of an acetylenic group. , 305:602, January 1996.

[101] A. G. G. M. Tielens and W. Hagen. Model calculations of the molecular composition of interstellar grain mantles. , 114(2):245–260, October 1982.

[102] F. Salama, E. L. O. Bakes, L. J. Allamandola, and A. G. G. M. Tielens. Assessment of the Polycyclic Aromatic Hydrocarbon–Diffuse Interstellar Band Proposal. , 458: 621, February 1996. doi: 10.1086/176844.

[103] Y. Oba, N. Miyauchi, H. Hidaka, T. Chigai, N. Watanabe, and A. Kouchi. Formation of Compact Amorphous H_2O Ice by Codeposition of Hydrogen Atoms with Oxygen Molecules on Grain Surfaces. , 701(1):464–470, August 2009. doi: 10.1088/0004-637X/701/1/464.

[104] E. L. Gibb, D. C. B. Whittet, A. C. A. Boogert, and A. G. G. M. Tielens. Interstellar Ice: The Infrared Space Observatory Legacy. , 151(1):35–73, March 2004. doi: 10.1086/381182.

[105] Victor F. Petrenko and Robert W. Whitworth. *Physics of Ice*. 2002. doi: 10.1093/acprof:oso/9780198518945.001.0001.

[106] E. F. van Dishoeck. The Chemistry of Diffuse and Dark Interstellar Clouds. *International Series in Astronomy and Astrophysics*, 4:53, January 1998.

[107] Robert J. Gould and Edwin E. Salpeter. The Interstellar Abundance of the Hydrogen Molecule. I. Basic Processes. , 138:393, August 1963. doi: 10.1086/147654.

[108] J. M. Shull and S. Beckwith. Interstellar molecular hydrogen. , 20:163–190, January 1982. doi: 10.1146/annurev.aa.20.090182.001115.

[109] J. Fischer, T. R. Geballe, Howard A. Smith, M. Simon, and J. W. V. Storey. Molecular Hydrogen Line Emission in Seyfert Galactic Nuclei. , 320:667, September 1987. doi: 10.1086/165584.

[110] Parvinder S. Parmar, John H. Lacy, and Jeffrey M. Achtermann. Detection of Low-J Pure-Rotational Emission from H 2 in the Orion Bar Region: Evidence for Small-Scale Clumpiness. , 372:L25, May 1991. doi: 10.1086/186015.

[111] E. Habart, F. Boulanger, L. Verstraete, C. M. Walmsley, and G. Pineau des Forêts. Some empirical estimates of the H_2 formation rate in photon-dominated regions. , 414:531–544, February 2004. doi: 10.1051/0004-6361:20031659.

[112] Christine Joblin. Experimental Astrophysics: a new window on the Interstellar Matter. In F. Combes, D. Barret, and F. Thévenin, editors, *SF2A-2001: Semaine de l'Astrophysique Francaise*, page 39, May 2001.

[113] Patricia Le Coupanec. *Observations et modelisation des Bandes Diffuses et Bandes Infrarouges dans le milieu interstellaire: Confrontation a l'hypothese PAH*. PhD thesis, Universite Pierre et Marie Curie (Paris VI), France, January 1998.

[114] Emilie Habart, Malcolm Walmsley, Laurent Verstraete, Stephanie Cazaux, Roberto Maiolino, Pierre Cox, Francois Boulanger, and Guillaume Pineau des Forêts. Molecular Hydrogen. , 119(1-4):71–91, August 2005. doi: 10.1007/s11214-005-8062-1.

[115] E. Habart, A. Abergel, F. Boulanger, C. Joblin, L. Verstraete, M. Compiègne, G. Pineau Des Forêts, and J. Le Bourlot. Excitation of H_2 in photodissociation regions as seen by Spitzer. , 527:A122, March 2011. doi: 10.1051/0004-6361/20077327.

[116] P. N. Appleton, P. Guillard, Bjorn Emonts, Francois Boulanger, Aditya Togi, William T. Reach, Katherine Alatalo, M. Cluver, T. Diaz Santos, P. A. Duc, S. Gallagher, P. Ogle, E. O'Sullivan, K. Voggel, and C. K. Xu. Multiphase Gas Interactions on Subarcsec Scales in the Shocked Intergalactic Medium of Stephan's Quintet with JWST and ALMA. , 951(2):104, July 2023. doi: 10.3847/1538-4357/accc2a.

[117] Ewine F. Van Dishoeck, Eric Herbst, and David A. Neufeld. Interstellar Water Chemistry: From Laboratory to Observations. *Chemical Reviews*, 113(12):9043–9085, December 2013. doi: 10.1021/cr4003177.

[118] D. C. B. Whittet, A. M. Cook, Eric Herbst, J. E. Chiar, and S. S. Shenoy. Observational Constraints on Methanol Production in Interstellar and Preplanetary Ices. , 742(1):28, November 2011. doi: 10.1088/0004-637X/742/1/28.

[119] A. P. Jones and N. Ysard. The essential elements of dust evolution. A viable solution to the interstellar oxygen depletion problem? , 627:A38, July 2019. doi: 10.1051/0004-6361/201935532.

[120] Endrik Kruegel. *The physics of interstellar dust*. 2003.

[121] Marco Minissale, Yuri Aikawa, Edwin Bergin, Mathieu Bertin, Wendy A. Brown, Stephanie Cazaux, Steven B. Charnley, Audrey Coutens, Herma M. Cuppen, Victoria Guzman, Harold Linnartz, Martin R. S. McCoustra, Albert Rimola, Johanna G.M. Schrauwen, Celine Toubin, Piero Ugliengo, Naoki Watanabe, Valentine Wakelam, and Francois Dulieu. Thermal desorption of interstellar ices: A review on the controlling parameters and their implications from snowlines to chemical complexity. *ACS Earth Space Chem.*, 6(3):597–630, 2022. doi: 10.1021/acsearthspacechem.1c00357. URL `https://doi.org/10.1021/acsearthspacechem.1c00357`.

[122] M. Minissale, E. Congiu, and F. Dulieu. Direct measurement of desorption and diffusion energies of O and N atoms physisorbed on amorphous surfaces. , 585:A146, January 2016. doi: 10.1051/0004-6361/201526702.

[123] Robert E. Johnson, Robert W. Carlson, Timothy A. Cassidy, and Marcelo Fama. Sputtering of Ices. In Murthy S. Gudipati and Julie Castillo-Rogez, editors, *Astrophysics and Space Science Library*, volume 356 of *Astrophysics and Space Science Library*, page 551, January 2013. doi: 10.1007/978-1-4614-3076-6_17.

[124] Mathieu Bertin, Edith C. Fayolle, Claire Romanzin, Hugo A. M. Poderoso, Xavier Michaut, Laurent Philippe, Pascal Jeseck, Karin I. Öberg, Harold Linnartz, and Jean-Hugues Fillion. Indirect Ultraviolet Photodesorption from CO:N_2 Binary Ices — an Efficient Grain-gas Process. , 779(2):120, December 2013. doi: 10.1088/0004-637X/779/2/120.

[125] K. I. Öberg, E. F. van Dishoeck, and H. Linnartz. Photodesorption of ices I: CO, N_2, and CO_2. , 496(1):281–293, March 2009. doi: 10.1051/0004-6361/200810207.

[126] Karin I. Öberg, Harold Linnartz, Ruud Visser, and Ewine F. van Dishoeck. Photodesorption of Ices. II. H_2O and D_2O. , 693(2):1209–1218, March 2009. doi: 10.1088/0004-637X/693/2/1209.

[127] François Dulieu, Emanuele Congiu, Jennifer Noble, Saoud Baouche, Henda Chaabouni, Audrey Moudens, Marco Minissale, and Stéphanie Cazaux. How micron-sized dust particles determine the chemistry of our Universe. *Sci. Rep.*, 3:1338, February 2013. doi: 10.1038/srep01338.

[128] C. Wang and R. Gomer. Sticking coefficients of CO, O $_2$ and Xe on the (110) and (100) planes of tungsten. *Surface Science*, 84(2):329–354, June 1979. doi: 10.1016/0039-6028(79)90141-9.

[129] Grazyna Antczak and Gert Ehrlich. *Diffusion on one-dimensional surfaces*. Cambridge University Press, 2010.

[130] Nix Roger. *Surface Science*. Open Education Resource (OER) LibreTexts Project.

[131] R. Martinazzo, S. Assoni, G. Marinoni, and G. F. Tantardini. Hot-atom versus Eley-Rideal dynamics in hydrogen recombination on Ni(100). I. The single-adsorbate case. , 120(18):8761–8771, May 2004. doi: 10.1063/1.1695316.

[132] K. Oura, V. G. Lifshits, A. A. Saranin, A. V. Zotov, M. Katayama, and John T. Yates. Surface Science: An Introduction. *Physics Today*, 57(10):79–80, October 2004. doi: 10.1063/1.1825276.

[133] L. Amiaud, F. Dulieu, J. H. Fillion, A. Momeni, and J. L. Lemaire. Interaction of atomic and molecular deuterium with a nonporous amorphous water ice surface between 8 and 30 K. , 127(14):144709–144709, October 2007. doi: 10.1063/1.2746323.

[134] Marco Minissale. *Physics and chemistry at the surface of interstellar dust grains: the influence of O-atom diffusion and chemical desorption on a H-N-C-O reaction network*. PhD thesis, UNIVERSITY OF CERGY PONTOISE, Departement of Physics, LERMA-Cergy, Observatory of Paris, 2014.

[135] D. Williams and E. Herbst. It's a dusty Universe: surface science in space. *Surface Science*, 500(1-3):823–837, March 2002. doi: 10.1016/S0039-6028(01)01538-2.

[136] S. Ferrero, F. Grieco, A. S. Ibrahim Mohamed, F. Dulieu, A. Rimola, C. Ceccarelli, C. Nervi, M. Minissale, and P. Ugliengo. Acetaldehyde binding energies: a coupled experimental and theoretical study. , 516(2):2586–2596, October 2022. doi: 10.1093/mnras/stac2358.

[137] V. Pirronello, Chi Liu, Liyong Shen, and Gianfranco Vidali. Laboratory Synthesis of Molecular Hydrogen on Surfaces of Astrophysical Interest. , 475(1):L69–L72, January 1997. doi: 10.1086/310464.

[138] F. Grieco, F. Dulieu, I. De Looze, and S. Baouche. Experimental H_2O formation on carbonaceous dust grains at temperatures up to 85 K. , 527(4):10604–10614, February 2024. doi: 10.1093/mnras/stad3854.

[139] MOHAMED-IBRAHIM Abdi-Salam. *Études expérimentales de l'interaction de l'oxygène et de l'eau avec des surfaces carbonées d'intérêt astrophysique*. PhD thesis, UNIVERSITY OF CERGY PONTOISE, Departement of Physics, LERMA-Cergy, Observatory of Paris, 2019.

[140] NGUYEN Thanh. *Experimental study of desorption and reactivity of nitrogen bearing species on interstellar dust grains*. PhD thesis, UNIVERSITY OF CERGY PONTOISE, Departement of Physics, LERMA-Cergy, Observatory of Paris, 2018.

[141] Carl A. Gottlieb. Detection of Acetaldehyde in Sagittarius. In M. A. Gordon and Lewis E. Snyder, editors, *Molecules in the Galactic Environment*, page 181, January 1973.

[142] N. Fourikis, M. W. Sinclair, B. J. Robinson, P. D. Godfrey, and R. D. Brown. Microwave emission of the $2_{11} \rightarrow 2_{12}$ rotational transition in interstellar acetaldehyde. *Austral. J. Phys.*, 27:425, June 1974. doi: 10.1071/PH740425.

[143] Geoffrey A. Blake, E. C. Sutton, C. R. Masson, and T. G. Phillips. Molecular Abundances in OMC-1: The Chemical Composition of Interstellar Molecular Clouds and the Influence of Massive Star Formation. , 315:621, April 1987. doi: 10.1086/165165.

[144] T. Csengeri, A. Belloche, S. Bontemps, F. Wyrowski, K. M. Menten, and L. Bouscasse. Search for high-mass protostars with ALMA revealed up to kilo-parsec scales (SPARKS). II. Complex organic molecules and heavy water in shocks around a young high-mass protostar. , 632:A57, December 2019. doi: 10.1051/0004-6361/201935226.

[145] Charles J. Law, Qizhou Zhang, Karin I. Öberg, Roberto Galván-Madrid, Eric Keto, Hauyu Baobab Liu, and Paul T. P. Ho. Subarcsecond Imaging of the Complex Organic Chemistry in Massive Star-forming Region G10.6-0.4. , 909(2):214, March 2021. doi: 10.3847/1538-4357/abdeb8.

[146] S. Cazaux, A. G. G. M. Tielens, C. Ceccarelli, A. Castets, V. Wakelam, E. Caux, B. Parise, and D. Teyssier. The Hot Core around the Low-mass Protostar IRAS 16293-2422: Scoundrels Rule! , 593(1):L51–L55, August 2003. doi: 10.1086/378038.

[147] S. Manigand, J. K. Jørgensen, H. Calcutt, H. S. P. Müller, N. F. W. Ligterink, A. Coutens, M. N. Drozdovskaya, E. F. van Dishoeck, and S. F. Wampfler. The ALMA-PILS survey: inventory of complex organic molecules towards IRAS 16293-2422 A. , 635:A48, March 2020. doi: 10.1051/0004-6361/201936299.

[148] Yao-Lun Yang, Nami Sakai, Yichen Zhang, Nadia M. Murillo, Ziwei E. Zhang, Aya E. Higuchi, Shaoshan Zeng, Ana López-Sepulcre, Satoshi Yamamoto, Bertrand Lefloch, Mathilde Bouvier, Cecilia Ceccarelli, Tomoya Hirota, Muneaki Imai, Yoko Oya, Takeshi Sakai, and Yoshimasa Watanabe. The Perseus ALMA Chemistry Survey (PEACHES). I. The Complex Organic Molecules in Perseus Embedded Protostars. , 910(1):20, March 2021. doi: 10.3847/1538-4357/abdfd6.

[149] L. Chahine, A. López-Sepulcre, R. Neri, C. Ceccarelli, S. Mercimek, C. Codella, M. Bouvier, E. Bianchi, C. Favre, L. Podio, F. O. Alves, N. Sakai, and S. Yamamoto. Organic chemistry in the protosolar analogue HOPS-108: Environment matters. , 657:A78, January 2022. doi: 10.1051/0004-6361/202141811.

[150] Bertrand Lefloch, C. Ceccarelli, C. Codella, C. Favre, L. Podio, C. Vastel, S. Viti, and R. Bachiller. L1157-B1, a factory of complex organic molecules in a solar-type star-forming region. , 469(1):L73–L77, July 2017. doi: 10.1093/mnrasl/slx050.

[151] M. De Simone, C. Codella, C. Ceccarelli, A. López-Sepulcre, A. Witzel, R. Neri, N. Balucani, P. Caselli, C. Favre, F. Fontani, B. Lefloch, J. Ospina-Zamudio, J. E. Pineda, and V. Taquet. Seeds of Life in Space (SOLIS). X. Interstellar complex organic molecules in the NGC 1333 IRAS 4A outflows. , 640:A75, August 2020. doi: 10.1051/0004-6361/201937004.

[152] C. Codella, C. Ceccarelli, E. Bianchi, N. Balucani, L. Podio, P. Caselli, S. Feng, B. Lefloch, A. López-Sepulcre, R. Neri, S. Spezzano, and M. De Simone. Seeds of Life

in Space (SOLIS). V. Methanol and acetaldehyde in the protostellar jet-driven shocks L1157-B0 and B1. , 635:A17, March 2020. doi: 10.1051/0004-6361/201936725.

[153] C. Codella, E. Bianchi, B. Tabone, C. F. Lee, S. Cabrit, C. Ceccarelli, L. Podio, F. Bacciotti, R. Bachiller, E. Chapillon, F. Gueth, A. Gusdorf, B. Lefloch, S. Leurini, G. Pineau des Forêts, K. L. J. Rygl, and M. Tafalla. Water and interstellar complex organics associated with the HH 212 protostellar disc. On disc atmospheres, disc winds, and accretion shocks. , 617:A10, September 2018. doi: 10.1051/0004-6361/201832765.

[154] Chin-Fei Lee, Claudio Codella, Zhi-Yun Li, and Sheng-Yuan Liu. First Abundance Measurement of Organic Molecules in the Atmosphere of HH 212 Protostellar Disk. , 876(1):63, May 2019. doi: 10.3847/1538-4357/ab15db.

[155] A. Bacmann, V. Taquet, A. Faure, C. Kahane, and C. Ceccarelli. Detection of complex organic molecules in a prestellar core: a new challenge for astrochemical models. , 541:L12, May 2012. doi: 10.1051/0004-6361/201219207.

[156] C. Vastel, C. Ceccarelli, B. Lefloch, and R. Bachiller. The Origin of Complex Organic Molecules in Prestellar Cores. , 795(1):L2, November 2014. doi: 10.1088/2041-8205/795/1/L2.

[157] Samantha Scibelli and Yancy Shirley. Prevalence of Complex Organic Molecules in Starless and Prestellar Cores within the Taurus Molecular Cloud. , 891(1):73, March 2020. doi: 10.3847/1538-4357/ab7375.

[158] J. Crovisier, D. Bockelée-Morvan, P. Colom, N. Biver, D. Despois, D. C. Lis, and Teamtarget-of-opportunity radio observations of comets. The composition of ices in comet C/1995 O1 (Hale-Bopp) from radio spectroscopy. Further results and upper limits on undetected species. , 418:1141–1157, May 2004. doi: 10.1051/0004-6361:20035688.

[159] Léna Le Roy, Kathrin Altwegg, Hans Balsiger, Jean-Jacques Berthelier, Andre Bieler, Christelle Briois, Ursina Calmonte, Michael R. Combi, Johan De Keyser, Frederik Dhooghe, Björn Fiethe, Stephen A. Fuselier, Sébastien Gasc, Tamas I. Gombosi, Myrtha Hässig, Annette Jäckel, Martin Rubin, and Chia-Yu Tzou. Inventory of the volatiles on comet 67P/Churyumov-Gerasimenko from Rosetta/ROSINA. , 583:A1, November 2015. doi: 10.1051/0004-6361/201526450.

[160] N. Biver, D. Bockelée-Morvan, J. Boissier, R. Moreno, J. Crovisier, D. C. Lis, P. Colom, M. A. Cordiner, S. N. Milam, N. X. Roth, B. P. Bonev, N. Dello Russo, R. J. Vervack, and M. A. DiSanti. Molecular composition of comet 46P/Wirtanen

from millimetre-wave spectroscopy. , 648:A49, April 2021. doi: 10.1051/0004-6361/202040125.

[161] E. Bianchi, C. Codella, C. Ceccarelli, F. Vazart, R. Bachiller, N. Balucani, M. Bouvier, M. De Simone, J. Enrique-Romero, C. Kahane, B. Lefloch, A. López-Sepulcre, J. Ospina-Zamudio, L. Podio, and V. Taquet. The census of interstellar complex organic molecules in the Class I hot corino of SVS13-A. , 483(2):1850–1861, February 2019. doi: 10.1093/mnras/sty2915.

[162] Maria N. Drozdovskaya, Ewine F. van Dishoeck, Martin Rubin, Jes K. Jørgensen, and Kathrin Altwegg. Ingredients for solar-like systems: protostar IRAS 16293-2422 B versus comet 67P/Churyumov-Gerasimenko. , 490(1):50–79, November 2019. doi: 10.1093/mnras/stz2430.

[163] S. B. Charnley. Acetaldehyde in star-forming regions. *Adv. Space Res.*, 33(1): 23–30, January 2004. doi: 10.1016/j.asr.2003.08.005.

[164] Dimitrios Skouteris, Nadia Balucani, Cecilia Ceccarelli, Fanny Vazart, Cristina Puzzarini, Vincenzo Barone, Claudio Codella, and Bertrand Lefloch. The Genealogical Tree of Ethanol: Gas-phase Formation of Glycolaldehyde, Acetic Acid, and Formic Acid. , 854(2):135, February 2018. doi: 10.3847/1538-4357/aaa41e.

[165] A. I. Vasyunin, P. Caselli, F. Dulieu, and I. Jiménez-Serra. Formation of Complex Molecules in Prestellar Cores: A Multilayer Approach. , 842(1):33, June 2017. doi: 10.3847/1538-4357/aa72ec.

[166] V. Wakelam, E. Herbst, J.-C. Loison, I. W. M. Smith, V. Chandrasekaran, B. Pavone, N. G. Adams, M.-C. Bacchus-Montabonel, A. Bergeat, K. Béroff, and et al. A kinetic database for astrochemistry (kida). , 199(1):21, Mar 2012. ISSN 1538-4365. doi: 10.1088/0067-0049/199/1/21. URL `http://dx.doi.org/10.1088/0067-0049/199/1/21`.

[167] D. McElroy, C. Walsh, A. J. Markwick, M. A. Cordiner, K. Smith, and T. J. Millar. The umist database for astrochemistry 2012. , 550, 2013. ISSN 0004-6361. doi: 10.1051/0004-6361/201220465.

[168] Fanny Vazart, Cecilia Ceccarelli, Nadia Balucani, Eleonora Bianchi, and Dimitrios Skouteris. Gas-phase formation of acetaldehyde: review and new theoretical computations. , 499(4):5547–5561, December 2020. doi: 10.1093/mnras/staa3060.

[169] R. L. Hudson and M. H. Moore. NOTE: Hydrocarbon Radiation Chemistry in Ices of Cometary Relevance. , 126(1):233–235, March 1997. doi: 10.1006/icar.1997.5678.

[170] Chris J. Bennett, Corey S. Jamieson, Yoshihiro Osamura, and Ralf I. Kaiser. A Combined Experimental and Computational Investigation on the Synthesis of Acetaldehyde [$CH_3CHO(X\ ^1A')$] in Interstellar Ices. , 624(2):1097–1115, May 2005. doi: 10.1086/429119.

[171] Karin I. Öberg, Ewine F. van Dishoeck, Harold Linnartz, and Stefan Andersson. The Effect of H_2O on Ice Photochemistry. , 718(2):832–840, August 2010. doi: 10.1088/0004-637X/718/2/832.

[172] Rafael Martín-Doménech, Karin I. Öberg, and Mahesh Rajappan. Formation of NH_2CHO and CH_3CHO upon UV Photoprocessing of Interstellar Ice Analogs. , 894 (2):98, May 2020. doi: 10.3847/1538-4357/ab84e8.

[173] K. J. Chuang, G. Fedoseev, C. Scirè, G. A. Baratta, C. Jäger, Th. Henning, H. Linnartz, and M. E. Palumbo. Formation of complex organic molecules in molecular clouds: acetaldehyde, vinyl alcohol, ketene, and ethanol via the "energetic" processing of C_2H_2 ice. , 650:A85, June 2021. doi: 10.1051/0004-6361/202140780.

[174] R. T. Garrod and E. Herbst. Formation of methyl formate and other organic species in the warm-up phase of hot molecular cores. , 457(3):927–936, October 2006. doi: 10.1051/0004-6361:20065560.

[175] J. Enrique-Romero, A. Rimola, C. Ceccarelli, and N. Balucani. The (impossible?) formation of acetaldehyde on the grain surfaces: insights from quantum chemical calculations. , 459(1):L6–L10, June 2016. doi: 10.1093/mnrasl/slw031.

[176] Albert Rimola, Dimitrios Skouteris, Nadia Balucani, Cecilia Ceccarelli, Joan Enrique-Romero, Vianney Taquet, and Piero Ugliengo. Can Formamide Be Formed on Interstellar Ice? An Atomistic Perspective. *ACS Earth Space Chem.*, 2(7):720–734, July 2018. doi: 10.1021/acsearthspacechem.7b00156.

[177] Joan Enrique-Romero, Albert Rimola, Cecilia Ceccarelli, Piero Ugliengo, Nadia Balucani, and Dimitrios Skouteris. Reactivity of HCO with CH3 and NH2 on Water Ice Surfaces. A Comprehensive Accurate Quantum Chemistry Study. *ACS Earth Space Chem.*, 3(10):2158–2170, October 2019. doi: 10.1021/acsearthspacechem.9b00156.

[178] J. Enrique-Romero, S. Álvarez-Barcia, F. J. Kolb, A. Rimola, C. Ceccarelli, N. Balucani, J. Meisner, P. Ugliengo, T. Lamberts, and J. Kästner. Revisiting the reactivity between HCO and CH_3 on interstellar grain surfaces. , 493(2):2523–2527, April 2020. doi: 10.1093/mnras/staa484.

[179] Thanja Lamberts, Max N. Markmeyer, Florian J. Kolb, and Johannes Kästner. Formation of Acetaldehyde on CO-Rich Ices. *ACS Earth Space Chem.*, 3(6):958–963, June 2019. doi: 10.1021/acsearthspacechem.9b00029.

[180] Joan Enrique-Romero, Cecilia Ceccarelli, Albert Rimola, Dimitrios Skouteris, Nadia Balucani, and Piero Ugliengo. Theoretical computations on the efficiency of acetaldehyde formation on interstellar icy grains. , 655:A9, November 2021. doi: 10.1051/0004-6361/202141531.

[181] A. Gutiérrez-Quintanilla, Y. Layssac, T. Butscher, S. Henkel, Y. A. Tsegaw, D. Grote, W. Sander, F. Borget, T. Chiavassa, and F. Duvernay. iCOM formation from radical chemistry: a mechanistic study from cryogenic matrix coupled with IR and EPR spectroscopies. , 506(3):3734–3750, September 2021. doi: 10.1093/mnras/stab1850.

[182] Gleb Fedoseev, Danna Qasim, Ko-Ju Chuang, Sergio Ioppolo, Thanja Lamberts, Ewine F. van Dishoeck, and Harold Linnartz. Hydrogenation of Accreting C Atoms and CO Molecules-Simulating Ketene and Acetaldehyde Formation Under Dark and Translucent Cloud Conditions. , 924(2):110, January 2022. doi: 10.3847/1538-4357/ac3834.

[183] Reggie L. Hudson and Robert F. Ferrante. Quantifying acetaldehyde in astronomical ices and laboratory analogues: IR spectra, intensities, ^{13}C shifts, and radiation chemistry. , 492(1):283–293, February 2020. doi: 10.1093/mnras/stz3323.

[184] V. Wakelam, J. C. Loison, R. Mereau, and M. Ruaud. Binding energies: New values and impact on the efficiency of chemical desorption. *Mol. Astrophys.*, 6:22–35, March 2017. doi: 10.1016/j.molap.2017.01.002.

[185] Maria Angela Corazzi, John Robert Brucato, Giovanni Poggiali, Linda Podio, Davide Fedele, and Claudio Codella. Thermal Desorption of Astrophysically Relevant Ice Mixtures of Acetaldehyde and Acetonitrile from Olivine Dust. , 913(2):128, June 2021. doi: 10.3847/1538-4357/abf6d3.

[186] G. Molpeceres, J. Kaestner, V.J. Herrero, R.J. Peláez, and B. Maté. Desorption of organic molecules from interstellar ices, combining experiments and computer simulations: Acetaldehyde as a case study. , forthcoming issue, July 2022. doi: 10.1051/0004-6361/202243489.

[187] H. Chaabouni, M. Minissale, S. Baouche, and F. Dulieu. Deuteration of ammonia with D atoms on oxidized partly ASW covered graphite surface. , October 2020.

[188] Robin J. Speedy, Pablo G. Debenedetti, R. Scott Smith, C. Huang, and Bruce D. Kay. The evaporation rate, free energy, and entropy of amorphous water at 150 K. *J.*

Chem. Phys., 105(1):240, 1996. ISSN 00219606. doi: 10.1063/1.471869. URL http://scitation.aip.org/content/aip/journal/jcp/105/1/10.1063/1.471869.

[189] H. Chaabouni, S. Diana, T. Nguyen, and F. Dulieu. Thermal desorption of formamide and methylamine from graphite and amorphous water ice surfaces. , 612:A47, apr 2018. ISSN 14320746. doi: 10.1051/0004-6361/201731006. URL http://arxiv.org/abs/1801.08897%0Ahttp://dx.doi.org/10.1051/0004-6361/201731006.

[190] S. L. Tait, Z. Dohnálek, C. T. Campbell, and B. D. Kay. n-Alkanes on MgO(100). II. Chain length dependence of kinetic desorption parameters for small n-alkanes. *J. Chem. Phys.*, 122:164708, 2005. ISSN 0021-9606, 1089-7690. doi: 10.1063/1.1883629. URL http://aip.scitation.org/doi/10.1063/1.1883630.

[191] Tatsuhiko I. Hasegawa, Eric Herbst, and Chun M. Leung. Models of Gas-Grain Chemistry in Dense Interstellar Clouds with Complex Organic Molecules. , 82:167, September 1992. doi: 10.1086/191713.

[192] Roberto Dovesi, Alessandro Erba, Roberto Orlando, Claudio M Zicovich-Wilson, Bartolomeo Civalleri, Lorenzo Maschio, Michel Rérat, Silvia Casassa, Jacopo Baima, Simone Salustro, et al. Quantum-mechanical condensed matter simulations with crystal. *WIREs Comput. Mol. Sci.*, 8(4):e1360, 2018.

[193] L. Doná, J. G. Brandenburg, and B. Civalleri. Extending and assessing composite electronic structure methods to the solid state. *J. Chem. Phys.*, 151(12):121101, 2019. doi: 10.1063/1.5123627. URL https://doi.org/10.1063/1.5123627.

[194] Axel D Becke. A new mixing of hartree–fock and local density-functional theories. *J. Chem. Phys.*, 98(2):1372–1377, 1993.

[195] Chengteh Lee, Weitao Yang, and Robert G. Parr. Development of the colle-salvetti correlation-energy formula into a functional of the electron density. *Phys. Rev. B*, 37:785–789, Jan 1988. doi: 10.1103/PhysRevB.37.785. URL https://link.aps.org/doi/10.1103/PhysRevB.37.785.

[196] Stefan Grimme, Jens Antony, Stephan Ehrlich, and Helge Krieg. A consistent and accurate ab initio parametrization of density functional dispersion correction (dft-d) for the 94 elements h-pu. *J. Chem. Phys.*, 132(15):154104, 2010.

[197] Stefan Grimme, Stephan Ehrlich, and Lars Goerigk. Effect of the damping function in dispersion corrected density functional theory. *J. Comput. Chem*, 32(7):1456–1465, 2011. doi: https://doi.org/10.1002/jcc.21759. URL https://onlinelibrary.wiley.com/doi/abs/10.1002/jcc.21759.

[198] Stefano Ferrero, Lorenzo Zamirri, Cecilia Ceccarelli, Arezu Witzel, Albert Rimola, and Piero Ugliengo. Binding Energies of Interstellar Molecules on Crystalline and Amorphous Models of Water Ice by Ab Initio Calculations. , 904(1):11, November 2020. doi: 10.3847/1538-4357/abb953.

[199] Revision A Gaussian09. 1, mj frisch, gw trucks, hb schlegel, ge scuseria, ma robb, jr cheeseman, g. scalmani, v. barone, b. mennucci, ga petersson et al., gaussian. *Inc., Wallingford CT*, 121:150–166, 2009.

[200] Ben Hourahine, Bálint Aradi, Volker Blum, F Bonafé, A Buccheri, C Camacho, C Cevallos, MY Deshaye, T Dumitrică, A Dominguez, et al. Dftb+, a software package for efficient approximate density functional theory based atomistic simulations. *J. Chem. Phys.*, 152(12):124101, 2020.

[201] Marcus Elstner, Dirk Porezag, G Jungnickel, J Elsner, M Haugk, Th Frauenheim, Sandor Suhai, and Gotthard Seifert. Self-consistent-charge density-functional tight-binding method for simulations of complex materials properties. *Phys. Rev. B*, 58 (11):7260, 1998.

[202] Eike Caldeweyher, Sebastian Ehlert, Andreas Hansen, Hagen Neugebauer, Sebastian Spicher, Christoph Bannwarth, and Stefan Grimme. A generally applicable atomic-charge dependent london dispersion correction. *J. Chem. Phys.*, 150(15): 154122, 2019.

[203] Eike Caldeweyher, Christoph Bannwarth, and Stefan Grimme. Extension of the d3 dispersion coefficient model. *J. Chem. Phys.*, 147(3):034112, 2017.

[204] Georg Kresse and Jürgen Hafner. Ab initio molecular dynamics for liquid metals. *Phys. Rev. B*, 47(1):558, 1993.

[205] Georg Kresse and Jürgen Hafner. Ab initio molecular-dynamics simulation of the liquid-metal–amorphous-semiconductor transition in germanium. *Phys. Rev. B*, 49 (20):14251, 1994.

[206] Georg Kresse and Jürgen Furthmüller. Efficiency of ab-initio total energy calculations for metals and semiconductors using a plane-wave basis set. *Comput. Materials Sci.*, 6(1):15–50, 1996.

[207] Georg Kresse and Jürgen Furthmüller. Efficient iterative schemes for ab initio total-energy calculations using a plane-wave basis set. *Phys. Rev. B*, 54(16):11169, 1996.

[208] Georg Kresse and Daniel Joubert. From ultrasoft pseudopotentials to the projector augmented-wave method. *Phys. Rev. B*, 59(3):1758, 1999.

[209] Andriy O Lyakhov, Artem R Oganov, Harold T Stokes, and Qiang Zhu. New developments in evolutionary structure prediction algorithm uspex. *Comput. Phys. Commun.*, 184(4):1172–1182, 2013.

[210] Artem R Oganov and Colin W Glass. Crystal structure prediction using ab initio evolutionary techniques: Principles and applications. *J. Chem. Phys.*, 124(24): 244704, 2006.

[211] Artem R Oganov, Andriy O Lyakhov, and Mario Valle. How evolutionary crystal structure prediction works and why. *Acc. Chem. Res.*, 44(3):227–237, 2011.

[212] Pavel V Bushlanov, Vladislav A Blatov, and Artem R Oganov. Topology-based crystal structure generator. *Comput. Phys. Commun.*, 236:1–7, 2019.

[213] J. A. Noble, E. Congiu, F. Dulieu, and H. J. Fraser. Thermal desorption characteristics of CO, O2 and CO2 on non-porous water, crystalline water and silicate surfaces at submonolayer and multilayer coverages. , 421(1):768–779, jan 2012. ISSN 00358711. doi: 10.1111/j.1365-2966.2011.20351.x. URL `http://mnras.oxfordjournals.org.ezproxy.obspm.fr/content/421/1/768`.

[214] T Nguyen, S Baouche, E Congiu, S Diana, L Pagani, and F Dulieu. Astrophysics Segregation effect and N 2 binding energy reduction in CO-N 2 systems adsorbed on water ice substrates. *AA*, 619:111, 2018. doi: 10.1051/0004-6361/201832774. URL `https://doi.org/10.1051/0004-6361/201832774`.

[215] Greg a. Kimmel, K. P. Stevenson, Z. Dohn'alek, R. Scott Smith, and Bruce D. Kay. Control of amorphous solid water morphology using molecular beams. I. Experimental results. *J. Chem. Phys.*, 114(12):5284, 2001. ISSN 00219606. doi: 10.1063/1.1350580. URL `http://scitation.aip.org/content/aip/journal/jcp/114/12/10.1063/1.1350580`.

[216] F. Dulieu, L. Amiaud, S. Baouche, A. Momeni, J.-H. Fillion, and J.L. Lemaire. Isotopic segregation of molecular hydrogen on water ice surface at low temperature. *Chem. Phys. Lett.*, 404(1-3):187–191, mar 2005. ISSN 00092614. doi: 10.1016/j.cplett.2005.01.044. URL `http://www.sciencedirect.com/science/article/pii/S0009261405000746`.

[217] Chenlin Zhou, Charlotte Vastel, Julien Montillaud, Cecilia Ceccarelli, Karine Demyk, Jorma Harju, Mika Juvela, Isabelle Ristorcelli, and Tie Liu. Chemical exploration of Galactic cold cores. *arXiv e-prints*, art. arXiv:2202.02157, February 2022.

[218] E. Dartois, M. Chabot, T. Id Barkach, H. Rothard, B. Augé, A. N. Agnihotri, A. Domaracka, and P. Boduch. Non-thermal desorption of complex organic

molecules. , 627:A55, jul 2019. ISSN 0004-6361. doi: 10.1051/0004-6361/201834787. URL https://www.aanda.org/10.1051/0004-6361/201834787.

[219] S. B. Charnley, A. G. G. M. Tielens, and T. J. Millar. On the Molecular Complexity of the Hot Cores in Orion A: Grain Surface Chemistry as "The Last Refuge of the Scoundrel". , 399:L71, November 1992. doi: 10.1086/186609.

[220] C. Ceccarelli, L. Loinard, A. Castets, A. G. G. M. Tielens, and E. Caux. The hot core of the solar-type protostar IRAS 16293-2422: H_2CO emission. , 357:L9–L12, May 2000.

[221] Ali A. Jaber, C. Ceccarelli, C. Kahane, and E. Caux. The Census of Complex Organic Molecules in the Solar-type Protostar IRAS16293-2422. , 791(1):29, August 2014. doi: 10.1088/0004-637X/791/1/29.

[222] Eleonora Bianchi, Ana López-Sepulcre, Cecilia Ceccarelli, Claudio Codella, Linda Podio, Mathilde Bouvier, and Joan Enrique-Romero. The two hot corinos of the SVS13-A protostellar binary system: counterposed siblings. *arXiv e-prints*, art. arXiv:2203.03412, March 2022.

[223] Yuki Okoda, Yoko Oya, Shotaro Abe, Ayano Komaki, Yoshimasa Watanabe, and Satoshi Yamamoto. Molecular Distributions of the Disk/Envelope System of L483: Principal Component Analysis for the Image Cube Data. , 923(2):168, December 2021. doi: 10.3847/1538-4357/ac2c6c.

[224] Tilman Hartwig, Simon C. O. Glover, Ralf S. Klessen, Muhammad A. Latif, and Marta Volonteri. How an improved implementation of H_2 self-shielding influences the formation of massive stars and black holes. , 452(2):1233–1244, September 2015. doi: 10.1093/mnras/stv1368.

[225] A. G. G. M. Tielens and D. Hollenbach. Photodissociation regions. II. A model for the Orion photodissociation region. , 291:747–754, April 1985. doi: 10.1086/163112.

[226] F. Bigiel, A. Leroy, F. Walter, E. Brinks, W. J. G. de Blok, B. Madore, and M. D. Thornley. The Star Formation Law in Nearby Galaxies on Sub-Kpc Scales. , 136 (6):2846–2871, December 2008. doi: 10.1088/0004-6256/136/6/2846.

[227] Simon C. O. Glover and Paul C. Clark. Molecular cooling in the diffuse interstellar medium. , 437(1):9–20, January 2014. doi: 10.1093/mnras/stt1809.

[228] S. Cazaux and M. Spaans. Molecular Hydrogen Formation on Dust Grains in the High-Redshift Universe. , 611(1):40–51, August 2004. doi: 10.1086/422087.

[229] Hiddo S. B. Algera, Hanae Inami, Pascal A. Oesch, Laura Sommovigo, Rychard J. Bouwens, Michael W. Topping, Sander Schouws, Mauro Stefanon, Daniel P. Stark, Manuel Aravena, Laia Barrufet, Elisabete da Cunha, Pratika Dayal, Ryan Endsley, Andrea Ferrara, Yoshinobu Fudamoto, Valentino Gonzalez, Luca Graziani, Jacqueline A. Hodge, Alexander P. S. Hygate, Ilse de Looze, Themiya Nanayakkara, Raffaella Schneider, and Paul P. van der Werf. The ALMA REBELS survey: the dust-obscured cosmic star formation rate density at redshift 7. , 518(4):6142–6157, February 2023. doi: 10.1093/mnras/stac3195.

[230] Gianfranco Vidali. H2 Formation on Interstellar Grains. *Chem. Rev.*, 113(12): 8752–8782, December 2013. doi: 10.1021/cr400156b.

[231] Vito Mennella. HD Formation by Abstraction of H/D Chemisorbed in Carbon Grains with D/H Atoms under Simulated Interstellar Conditions. , 684(1):L25, September 2008. doi: 10.1086/592001.

[232] Stéphanie Cazaux, Leon Boschman, Nathalie Rougeau, Geert Reitsma, Ronnie Hoekstra, Dominique Teillet-Billy, Sabine Morisset, Marco Spaans, and Thomas Schlathölter. The sequence to hydrogenate coronene cations: A journey guided by magic numbers. *Scientific Reports*, 6:19835, January 2016. doi: 10.1038/srep19835.

[233] Irene Shivaei, Naveen A. Reddy, Alice E. Shapley, Brian Siana, Mariska Kriek, Bahram Mobasher, Alison L. Coil, William R. Freeman, Ryan L. Sanders, Sedona H. Price, Mojegan Azadi, and Tom Zick. The MOSDEF Survey: Metallicity Dependence of PAH Emission at High Redshift and Implications for 24 μm Inferred IR Luminosities and Star Formation Rates at z $\sim$ 2. , 837(2):157, March 2017. doi: 10.3847/1538-4357/aa619c.

[234] Tucker Jones, Ryan Sanders, Guido Roberts-Borsani, Richard S. Ellis, Nicolas Laporte, Tommaso Treu, and Yuichi Harikane. The Mass-Metallicity Relation at z 8: Direct-method Metallicity Constraints and Near-future Prospects. , 903(2):150, November 2020. doi: 10.3847/1538-4357/abb943.

[235] P. Dayal, A. Ferrara, L. Sommovigo, R. Bouwens, P. A. Oesch, R. Smit, V. Gonzalez, S. Schouws, M. Stefanon, C. Kobayashi, J. Bremer, H. S. B. Algera, M. Aravena, R. A. A. Bowler, E. da Cunha, Y. Fudamoto, L. Graziani, J. Hodge, H. Inami, I. De Looze, A. Pallottini, D. Riechers, R. Schneider, D. Stark, and R. Endsley. The ALMA REBELS survey: the dust content of z 7 Lyman break galaxies. , 512(1): 989–1002, May 2022. doi: 10.1093/mnras/stac537.

[236] Darach Watson, Lise Christensen, Kirsten Kraiberg Knudsen, Johan Richard, Anna Gallazzi, and Michał Jerzy Michałowski. A dusty, normal galaxy in the epoch of reionization. , 519(7543):327–330, March 2015. doi: 10.1038/nature14164.

[237] F. Pozzi, F. Calura, Y. Fudamoto, M. Dessauges-Zavadsky, C. Gruppioni, M. Talia, G. Zamorani, M. Bethermin, A. Cimatti, A. Enia, Y. Khusanova, R. Decarli, O. Le Fèvre, P. Capak, P. Cassata, A. L. Faisst, L. Yan, D. Schaerer, J. Silverman, S. Bardelli, M. Boquien, A. Enia, D. Narayanan, M. Ginolfi, N. P. Hathi, G. C. Jones, A. M. Koekemoer, B. C. Lemaux, F. Loiacono, R. Maiolino, D. A. Riechers, G. Rodighiero, M. Romano, L. Vallini, D. Vergani, and E. Zucca. The ALPINE-ALMA [CII] survey. Dust mass budget in the early Universe. , 653:A84, September 2021. doi: 10.1051/0004-6361/202040258.

[238] Dominik A. Riechers, Alexandra Pope, Emanuele Daddi, Lee Armus, Christopher L. Carilli, Fabian Walter, Jacqueline Hodge, Ranga-Ram Chary, Glenn E. Morrison, Mark Dickinson, Helmut Dannerbauer, and David Elbaz. Polycyclic Aromatic Hydrocarbon and Mid-Infrared Continuum Emission in a z ¿ 4 Submillimeter Galaxy. , 786(1):31, May 2014. doi: 10.1088/0004-637X/786/1/31.

[239] L. Sommovigo, A. Ferrara, A. Pallottini, S. Carniani, S. Gallerani, and D. Decataldo. Warm dust in high-z galaxies: origin and implications. , 497(1):956–968, September 2020. doi: 10.1093/mnras/staa1959.

[240] L. Sommovigo, A. Ferrara, A. Pallottini, P. Dayal, R. J. Bouwens, R. Smit, E. da Cunha, I. De Looze, R. A. A. Bowler, J. Hodge, H. Inami, P. Oesch, R. Endsley, V. Gonzalez, S. Schouws, D. Stark, M. Stefanon, M. Aravena, L. Graziani, D. Riechers, R. Schneider, P. van der Werf, H. Algera, L. Barrufet, Y. Fudamoto, A. P. S. Hygate, I. Labbé, Y. Li, T. Nanayakkara, and M. Topping. The ALMA REBELS Survey: cosmic dust temperature evolution out to z 7. , 513(3):3122–3135, July 2022. doi: 10.1093/mnras/stac302.

[241] Andreas L. Faisst, Yoshinobu Fudamoto, Pascal A. Oesch, Nick Scoville, Dominik A. Riechers, Riccardo Pavesi, and Peter Capak. ALMA characterizes the dust temperature of z $\sim$ 5.5 star-forming galaxies. , 498(3):4192–4204, November 2020. doi: 10.1093/mnras/staa2545.

[242] Tom J. L. C. Bakx, Yoichi Tamura, Takuya Hashimoto, Akio K. Inoue, Minju M. Lee, Ken Mawatari, Kazuaki Ota, Hideki Umehata, Erik Zackrisson, Bunyo Hatsukade, Kotaro Kohno, Yuichi Matsuda, Hiroshi Matsuo, Takashi Okamoto, Takatoshi Shibuya, Ikkoh Shimizu, Yoshiaki Taniguchi, and Naoki Yoshida. ALMA uncovers the [C II] emission and warm dust continuum in a z = 8.31 Lyman break galaxy. , 493(3):4294–4307, April 2020. doi: 10.1093/mnras/staa509.

[243] E. Rauls and L. Hornekær. Catalyzed Routes to Molecular Hydrogen Formation and Hydrogen Addition Reactions on Neutral Polycyclic Aromatic Hydrocarbons under Interstellar Conditions. , 679(1):531–536, May 2008. doi: 10.1086/587614.

[244] Azi Lipshtat and Ofer Biham. The effect of grain size distribution on H_2 formation rate in the interstellar medium. , 362(2):666–670, September 2005. doi: 10.1111/j.1365-2966.2005.09356.x.

[245] E. Congiu, E. Matar, L. E. Kristensen, F. Dulieu, and J. L. Lemaire. Laboratory evidence for the non-detection of excited nascent H_2 in dark clouds. , 397(1):L96–L100, July 2009. doi: 10.1111/j.1745-3933.2009.00692.x.

[246] S. Cazaux, S. Morisset, M. Spaans, and A. Allouche. When sticking influences H_2 formation. , 535:A27, November 2011. doi: 10.1051/0004-6361/201117220.

[247] J. D. Thrower, L. Nilsson, B. Jørgensen, S. Baouche, R. Balog, A. C. Luntz, I. Stensgaard, E. Rauls, and L. Hornekær. Superhydrogenated PAHs: Catalytic formation of H_2. In C. Joblin and A. G. G. M. Tielens, editors, *EAS Publications Series*, volume 46 of *EAS Publications Series*, pages 453–460, March 2011. doi: 10.1051/eas/1146047.

[248] L. Hornekær, E. Rauls, W. Xu, Ž. Šljivančanin, R. Otero, I. Stensgaard, E. Lægsgaard, B. Hammer, and F. Besenbacher. Clustering of Chemisorbed H(D) Atoms on the Graphite (0001) Surface due to Preferential Sticking. , 97(18):186102, November 2006. doi: 10.1103/PhysRevLett.97.186102.

[249] J. D. Thrower, B. Jørgensen, E. E. Friis, S. Baouche, V. Mennella, A. C. Luntz, M. Andersen, B. Hammer, and L. Hornekær. Experimental Evidence for the Formation of Highly Superhydrogenated Polycyclic Aromatic Hydrocarbons through H Atom Addition and Their Catalytic Role in H_2 Formation. , 752(1):3, June 2012. doi: 10.1088/0004-637X/752/1/3.

[250] Frederik Doktor S. Simonsen, Pernille A. Jensen, Anders W. Skov, Rijutha Jaganathan, John D. Thrower, and Liv Hornekær. H_2 catalysis through superhydrogenation of interstellar polycyclic aromatic hydrocarbons. In Farid Salama and Harold Linnartz, editors, *Laboratory Astrophysics: From Observations to Interpretation*, volume 350 of *IAU Symposium*, pages 264–266, January 2020. doi: 10.1017/S1743921320000034.

[251] Emilie Habart, Romane Le Gal, Carlos Alvarez, Els Peeters, Olivier Berné, Mark G. Wolfire, Javier R. Goicoechea, Thiébaut Schirmer, Emeric Bron, and Markus Röllig. High-angular-resolution NIR view of the Orion Bar revealed by Keck/NIRC2. , 673:A149, May 2023. doi: 10.1051/0004-6361/202244034.

[252] Steven L. Finkelstein, Micaela B. Bagley, Pablo Arrabal Haro, Mark Dickinson, Henry C. Ferguson, Jeyhan S. Kartaltepe, Casey Papovich, Denis Burgarella,

Dale D. Kocevski, Marc Huertas-Company, Kartheik G. Iyer, Anton M. Koekemoer, Rebecca L. Larson, Pablo G. Pérez-González, Caitlin Rose, Sandro Tacchella, Stephen M. Wilkins, Katherine Chworowsky, Aubrey Medrano, Alexa M. Morales, Rachel S. Somerville, L. Y. Aaron Yung, Adriano Fontana, Mauro Giavalisco, Andrea Grazian, Norman A. Grogin, Lisa J. Kewley, Allison Kirkpatrick, Peter Kurczynski, Jennifer M. Lotz, Laura Pentericci, Nor Pirzkal, Swara Ravindranath, Russell E. Ryan, Jonathan R. Trump, Guang Yang, Omar Almaini, Ricardo O. Amorín, Marianna Annunziatella, Bren E. Backhaus, Guillermo Barro, Peter Behroozi, Eric F. Bell, Rachana Bhatawdekar, Laura Bisigello, Volker Bromm, Véronique Buat, Fernando Buitrago, Antonello Calabrò, Caitlin M. Casey, Marco Castellano, Óscar A. Chávez Ortiz, Laure Ciesla, Nikko J. Cleri, Seth H. Cohen, Justin W. Cole, Kevin C. Cooke, M. C. Cooper, Asantha R. Cooray, Luca Costantin, Isabella G. Cox, Darren Croton, Emanuele Daddi, Romeel Davé, Alexander de La Vega, Avishai Dekel, David Elbaz, Vicente Estrada-Carpenter, Sandra M. Faber, Vital Fernández, Keely D. Finkelstein, Jonathan Freundlich, Seiji Fujimoto, Ángela García-Argumánez, Jonathan P. Gardner, Eric Gawiser, Carlos Gómez-Guijarro, Yuchen Guo, Kurt Hamblin, Timothy S. Hamilton, Nimish P. Hathi, Benne W. Holwerda, Michaela Hirschmann, Taylor A. Hutchison, Anne E. Jaskot, Saurabh W. Jha, Shardha Jogee, Stéphanie Juneau, Intae Jung, Susan A. Kassin, Aurélien Le Bail, Gene C. K. Leung, Ray A. Lucas, Benjamin Magnelli, Kameswara Bharadwaj Mantha, Jasleen Matharu, Elizabeth J. McGrath, Daniel H. McIntosh, Emiliano Merlin, Bahram Mobasher, Jeffrey A. Newman, David C. Nicholls, Viraj Pandya, Marc Rafelski, Kaila Ronayne, Paola Santini, Lise-Marie Seillé, Ekta A. Shah, Lu Shen, Raymond C. Simons, Gregory F. Snyder, Elizabeth R. Stanway, Amber N. Straughn, Harry I. Teplitz, Brittany N. Vanderhoof, Jesús Vega-Ferrero, Weichen Wang, Benjamin J. Weiner, Christopher N. A. Willmer, Stijn Wuyts, Jorge A. Zavala, and Ceers Team. A Long Time Ago in a Galaxy Far, Far Away: A Candidate z $\sim$ 12 Galaxy in Early JWST CEERS Imaging. , 940(2):L55, December 2022. doi: 10.3847/2041-8213/ac966e.

[253] Tom J. L. C. Bakx, Laura Sommovigo, Stefano Carniani, Andrea Ferrara, Hollis B. Akins, Seiji Fujimoto, Masato Hagimoto, Kirsten K. Knudsen, Andrea Pallottini, Yoichi Tamura, and Darach Watson. Accurate dust temperature determination in a z = 7.13 galaxy. , 508(1):L58–L63, November 2021. doi: 10.1093/mnrasl/slab104.

[254] Lichen Liang, Robert Feldmann, Dušan Kereš, Nick Z. Scoville, Christopher C. Hayward, Claude-André Faucher-Giguère, Corentin Schreiber, Xiangcheng Ma, Philip F. Hopkins, and Eliot Quataert. On the dust temperatures of high-redshift galaxies. , 489(1):1397–1422, October 2019. doi: 10.1093/mnras/stz2134.

[255] Marco P. Viero, Guochao Sun, Dongwoo T. Chung, Lorenzo Moncelsi, and Sam S. Condon. The early Universe was dust-rich and extremely hot. , 516(1):L30–L34, October 2022. doi: 10.1093/mnrasl/slac075.

[256] Elisabete da Cunha, Brent Groves, Fabian Walter, Roberto Decarli, Axel Weiss, Frank Bertoldi, Chris Carilli, Emanuele Daddi, David Elbaz, Rob Ivison, Roberto Maiolino, Dominik Riechers, Hans-Walter Rix, Mark Sargent, and Ian Smail. On the Effect of the Cosmic Microwave Background in High-redshift (Sub-)millimeter Observations. , 766(1):13, March 2013. doi: 10.1088/0004-637X/766/1/13.

[257] G. Lagache, M. Cousin, and M. Chatzikos. The [CII] 158 μm line emission in high-redshift galaxies. , 609:A130, January 2018. doi: 10.1051/0004-6361/201732019.

[258] S. N. Longmore, J. Bally, L. Testi, C. R. Purcell, A. J. Walsh, E. Bressert, M. Pestalozzi, S. Molinari, J. Ott, L. Cortese, C. Battersby, N. Murray, E. Lee, J. M. D. Kruijssen, E. Schisano, and D. Elia. Variations in the Galactic star formation rate and density thresholds for star formation. , 429(2):987–1000, February 2013. doi: 10.1093/mnras/sts376.

[259] E. Schinnerer and A. K. Leroy. Molecular Gas and the Star-Formation Process on Cloud Scales in Nearby Galaxies. , 62(1):369–436, September 2024. doi: 10.1146/annurev-astro-071221-052651.

[260] Simon C. O. Glover and Paul C. Clark. Star formation in metal-poor gas clouds. , 426(1):377–388, October 2012. doi: 10.1111/j.1365-2966.2012.21737.x.

[261] Aigen Li. Spitzer's perspective of polycyclic aromatic hydrocarbons in galaxies. *Nature Astronomy*, 4:339–351, March 2020. doi: 10.1038/s41550-020-1051-1.

[262] Dries Van De Putte, Raphael Meshaka, Boris Trahin, Emilie Habart, Els Peeters, Olivier Berné, Felipe Alarcón, Amélie Canin, Ryan Chown, Ilane Schroetter, Ameek Sidhu, Christiaan Boersma, Emeric Bron, Emmanuel Dartois, Javier R. Goicoechea, Karl D. Gordon, Takashi Onaka, Alexander G. G. M. Tielens, Laurent Verstraete, Mark G. Wolfire, Alain Abergel, Edwin A. Bergin, Jeronimo Bernard-Salas, Jan Cami, Sara Cuadrado, Daniel Dicken, Meriem Elyajouri, Asunción Fuente, Christine Joblin, Baria Khan, Ozan Lacinbala, David Languignon, Romane Le Gal, Alexandros Maragkoudakis, Yoko Okada, Sofia Pasquini, Marc W. Pound, Massimo Robberto, Markus Röllig, Bethany Schefter, Thiébaut Schirmer, Benoit Tabone, Sílvia Vicente, Marion Zannese, Sean W. J. Colgan, Jinhua He, Gaël Rouillé, Aditya Togi, Isabel Aleman, Rebecca Auchettl, Giuseppe Antonio Baratta, Salma Bejaoui, Partha P. Bera, John H. Black, Francois Boulanger, Jordy Bouwman, Bernhard Brandl, Philippe Brechignac, Sandra Brünken, Mridusmita Buragohain, Andrew

Burkhardt, Alessandra Candian, Stéphanie Cazaux, Jose Cernicharo, Marin Chabot, Shubhadip Chakraborty, Jason Champion, Ilsa R. Cooke, Audrey Coutens, Nick L. J. Cox, Karine Demyk, Jennifer Donovan Meyer, Sacha Foschino, Pedro García-Lario, Maryvonne Gerin, Carl A. Gottlieb, Pierre Guillard, Antoine Gusdorf, Patrick Hartigan, Eric Herbst, Liv Hornekaer, Lina Issa, Cornelia Jäger, Eduardo Janot-Pacheco, Olga Kannavou, Michael Kaufman, Francisca Kemper, Sarah Kendrew, Maria S. Kirsanova, Pamela Klaassen, Sun Kwok, Álvaro Labiano, Thomas S. Y. Lai, Bertrand Le Floch, Franck Le Petit, Aigen Li, Hendrik Linz, Cameron J. Mackie, Suzanne C. Madden, Joëlle Mascetti, Brett A. McGuire, Pablo Merino, Elisabetta R. Micelotta, Jon A. Morse, Giacomo Mulas, Naslim Neelamkodan, Ryou Ohsawa, Alain Omont, Roberta Paladini, Maria Elisabetta Palumbo, Amit Pathak, Yvonne J. Pendleton, Annemieke Petrignani, Thomas Pino, Elena Puga, Naseem Rangwala, Mathias Rapacioli, Jeonghee Rho, Alessandra Ricca, Julia Roman-Duval, Joseph Roser, Evelyne Roueff, Farid Salama, Dinalva A. Sales, Karin Sandstrom, Peter Sarre, Ella Sciamma-O'Brien, Kris Sellgren, Sachindev S. Shenoy, David Teyssier, Richard D. Thomas, Adolf N. Witt, Alwyn Wootten, Nathalie Ysard, Henning Zettergren, Yong Zhang, Ziwei E. Zhang, and Junfeng Zhen. PDRs4All. VIII. Mid-infrared emission line inventory of the Orion Bar. , 687:A86, July 2024. doi: 10.1051/0004-6361/202449295.

[263] Irene Shivaei and Leindert Boogaard. The tight correlation of PAH and CO emission from z~0-4. *arXiv e-prints*, art. arXiv:2409.05710, September 2024. doi: 10.48550/arXiv.2409.05710.

[264] Edvige Corbelli, Jonathan Braine, Rino Bandiera, Nathalie Brouillet, Françoise Combes, Clément Druard, Pierre Gratier, Jimmy Mata, Karl Schuster, Manolis Xilouris, and Francesco Palla. From molecules to young stellar clusters: the star formation cycle across the disk of M 33. , 601:A146, May 2017. doi: 10.1051/0004-6361/201630034.

[265] Jaeyeon Kim, Mélanie Chevance, J. M. Diederik Kruijssen, Ashley. T. Barnes, Frank Bigiel, Guillermo A. Blanc, Médéric Boquien, Yixian Cao, Enrico Congiu, Daniel A. Dale, Oleg V. Egorov, Christopher M. Faesi, Simon C. O. Glover, Kathryn Grasha, Brent Groves, Hamid Hassani, Annie Hughes, Ralf S. Klessen, Kathryn Kreckel, Kirsten L. Larson, Janice C. Lee, Adam K. Leroy, Daizhong Liu, Steven N. Longmore, Sharon E. Meidt, Hsi-An Pan, Jérôme Pety, Miguel Querejeta, Erik Rosolowsky, Toshiki Saito, Karin Sandstrom, Eva Schinnerer, Rowan J. Smith, Antonio Usero, Elizabeth J. Watkins, and Thomas G. Williams. PHANGS-JWST First Results: Duration of the Early Phase of Massive Star Formation in NGC 628. , 944 (2):L20, February 2023. doi: 10.3847/2041-8213/aca90a.

[266] P. Caselli, E. Keto, L. Pagani, Y. Aikawa, U. A. Yıldız, F. F. S. van der Tak, M. Tafalla, E. A. Bergin, B. Nisini, C. Codella, E. F. van Dishoeck, R. Bachiller, A. Baudry, M. Benedettini, A. O. Benz, P. Bjerkeli, G. A. Blake, S. Bontemps, J. Braine, S. Bruderer, J. Cernicharo, F. Daniel, A. M. di Giorgio, C. Dominik, S. D. Doty, P. Encrenaz, M. Fich, A. Fuente, T. Gaier, T. Giannini, J. R. Goicoechea, Th. de Graauw, F. Helmich, G. J. Herczeg, F. Herpin, M. R. Hogerheijde, B. Jackson, T. Jacq, H. Javadi, D. Johnstone, J. K. Jørgensen, D. Kester, L. E. Kristensen, W. Laauwen, B. Larsson, D. Lis, R. Liseau, W. Luinge, M. Marseille, C. McCoey, A. Megej, G. Melnick, D. Neufeld, M. Olberg, B. Parise, J. C. Pearson, R. Plume, C. Risacher, J. Santiago-García, P. Saraceno, R. Shipman, P. Siegel, T. A. van Kempen, R. Visser, S. F. Wampfler, and F. Wyrowski. Water vapor toward starless cores: The Herschel view. , 521:L29, October 2010. doi: 10.1051/0004-6361/201015097.

[267] Ewine F. van Dishoeck, Eric Herbst, and David A. Neufeld. Interstellar Water Chemistry: From Laboratory to Observations. *Chemical Reviews*, 113(12):9043–9085, December 2013. doi: 10.1021/cr4003177.

[268] Laura Silva, Giovanni Vladilo, Giuseppe Murante, and Antonello Provenzale. Quantitative estimates of the surface habitability of Kepler-452b. , 470(2):2270–2282, September 2017. doi: 10.1093/mnras/stx1396.

[269] L. Ilsedore Cleeves, Edwin A. Bergin, Conel M. O. 'D. Alexander, Fujun Du, Dawn Graninger, Karin I. Öberg, and Tim J. Harries. The ancient heritage of water ice in the solar system. *Science*, 345(6204):1590–1593, September 2014. doi: 10.1126/science.1258055.

[270] S. S. Jensen, J. K. Jørgensen, L. E. Kristensen, K. Furuya, A. Coutens, E. F. van Dishoeck, D. Harsono, and M. V. Persson. ALMA observations of water deuteration: a physical diagnostic of the formation of protostars. , 631:A25, November 2019. doi: 10.1051/0004-6361/201936012.

[271] G. Perotti, V. Christiaens, Th. Henning, B. Tabone, L. B. F. M. Waters, I. Kamp, G. Olofsson, S. L. Grant, D. Gasman, J. Bouwman, M. Samland, R. Franceschi, E. F. van Dishoeck, K. Schwarz, M. Güdel, P. O. Lagage, T. P. Ray, B. Vandenbussche, A. Abergel, O. Absil, A. M. Arabhavi, I. Argyriou, D. Barrado, A. Boccaletti, A. Caratti o Garatti, V. Geers, A. M. Glauser, K. Justannont, F. Lahuis, M. Mueller, C. Nehmé, E. Pantin, S. Scheithauer, C. Waelkens, R. Guadarrama, H. Jang, J. Kanwar, M. Morales-Calderón, N. Pawellek, D. Rodgers-Lee, J. Schreiber, L. Colina, T. R. Greve, G. Östlin, and G. Wright. Water in the terrestrial planet-forming zone of the PDS 70 disk. , 620(7974):516–520, August 2023. doi: 10.1038/s41586-023-06317-9.

[272] Ewine F. van Dishoeck. ISO Spectroscopy of Gas and Dust: From Molecular Clouds to Protoplanetary Disks. , 42(1):119–167, September 2004. doi: 10.1146/annurev.astro.42.053102.134010.

[273] F. Dulieu, L. Amiaud, E. Congiu, J. H. Fillion, E. Matar, A. Momeni, V. Pirronello, and J. L. Lemaire. Experimental evidence for water formation on interstellar dust grains by hydrogen and oxygen atoms. , 512:A30, March 2010. doi: 10.1051/0004-6361/200912079.

[274] Y. Oba, N. Miyauchi, H. Hidaka, T. Chigai, N. Watanabe, and A. Kouchi. Formation of Compact Amorphous H_2O Ice by Codeposition of Hydrogen Atoms with Oxygen Molecules on Grain Surfaces. , 701(1):464–470, August 2009. doi: 10.1088/0004-637X/701/1/464.

[275] S. Ioppolo, H. M. Cuppen, C. Romanzin, E. F. van Dishoeck, and H. Linnartz. Laboratory Evidence for Efficient Water Formation in Interstellar Ices. , 686(2):1474–1479, October 2008. doi: 10.1086/591506.

[276] E. Matar, E. Congiu, F. Dulieu, A. Momeni, and J. L. Lemaire. Mobility of D atoms on porous amorphous water ice surfaces under interstellar conditions. , 492 (1):L17–L20, December 2008. doi: 10.1051/0004-6361:200810434.

[277] H. Mokrane, H. Chaabouni, M. Accola, E. Congiu, F. Dulieu, M. Chehrouri, and J. L. Lemaire. Experimental evidence for water formation via O_3 hydrogenation on a water ice covered surface under interstellar conditions. page 195, November 2009.

[278] C. Romanzin, S. Ioppolo, H. M. Cuppen, E. F. van Dishoeck, and H. Linnartz. Water formation by surface O_3 hydrogenation. , 134(8):084504–084504, February 2011. doi: 10.1063/1.3532087.

[279] C. Ceccarelli, P. Caselli, E. Herbst, A. G. G. M. Tielens, and E. Caux. Extreme Deuteration and Hot Corinos: The Earliest Chemical Signatures of Low-Mass Star Formation. page 47, January 2007. doi: 10.48550/arXiv.astro-ph/0603018.

[280] B. Parise, C. Ceccarelli, and S. Maret. Theoretical HDO emission from low-mass protostellar envelopes. , 441(1):171–179, October 2005. doi: 10.1051/0004-6361:20053081.

[281] L. E. Kristensen, L. Amiaud, J. H. Fillion, F. Dulieu, and J. L. Lemaire. H_2, HD, and D_2 abundances on ice-covered dust grains in dark clouds. , 527:A44, March 2011. doi: 10.1051/0004-6361/200912124.

[282] Y. Oba, N. Watanabe, T. Hama, K. Kuwahata, H. Hidaka, and A. Kouchi. Water Formation through a Quantum Tunneling Surface Reaction, OH + H_2, at 10 K. , 749(1):67, April 2012. doi: 10.1088/0004-637X/749/1/67.

[283] H. M. Cuppen and Eric Herbst. Simulation of the Formation and Morphology of Ice Mantles on Interstellar Grains. , 668(1):294–309, October 2007. doi: 10.1086/521014.

[284] B M McCormac. *Physics and chemistry of upper atmospheres*, volume 35 of *Astrophysics and Space Science Library*. January 1973. doi: 10.1007/978-94-010-2542-3.

[285] N. Miyauchi, H. Hidaka, T. Chigai, A. Nagaoka, N. Watanabe, and A. Kouchi. Formation of hydrogen peroxide and water from the reaction of cold hydrogen atoms with solid oxygen at 10 K. *Chemical Physics Letters*, 456(1-3):27–30, April 2008. doi: 10.1016/j.cplett.2008.02.095.

[286] L. E. Kristensen, L. Amiaud, J. H. Fillion, F. Dulieu, and J. L. Lemaire. H_2, HD, and D_2 abundances on ice-covered dust grains in dark clouds. , 527:A44, March 2011. doi: 10.1051/0004-6361/200912124.

[287] Parise. *phD Thesis*. PhD thesis, CESR (Toulouse, France), 2004.

[288] Yasuhiro Oba, Naoki Watanabe, Akira Kouchi, Tetsuya Hama, and Valerio Pirronello. Experimental studies of surface reactions among OH radicals that yield H2O and CO2 at 40-60 K. *Physical Chemistry Chemical Physics (Incorporating Faraday Transactions)*, 13(35):15792, January 2011. doi: 10.1039/C1CP20596J.

[289] R. Papoular. On water ice formation in interstellar clouds. , 362(2):489–497, September 2005. doi: 10.1111/j.1365-2966.2005.09313.x.

[290] L. E. Kristensen, L. Amiaud, J. H. Fillion, F. Dulieu, and J. L. Lemaire. H_2, HD, and D_2 abundances on ice-covered dust grains in dark clouds. , 527:A44, March 2011. doi: 10.1051/0004-6361/200912124.

[291] Francois Dulieu, Valerio Pirronello, Marco Minissale, Emanuele Congiu, Saoud Baouche, Henda Chaabouni, Audrey Moudens, Mario Accolla, Stephanie Cazaux, and Giulio Manicò. Chemical desorption and diffusive dust chemistry. 40:F3.2-20-14, January 2014.

[292] L. J. Allamandola, A. G. G. M. Tielens, and J. R. Barker. Interstellar Polycyclic Aromatic Hydrocarbons: The Infrared Emission Bands, the Excitation/Emission Mechanism, and the Astrophysical Implications. , 71:733, December 1989. doi: 10.1086/191396.

[293] Farid Salama. PAHs in Astronomy - A Review. 251:357–366, October 2008. doi: 10.1017/S1743921308021960.

[294] H. W. Jochims, H. Baumgärtel, and S. Leach. Structure-dependent Photostability of Polycyclic Aromatic Hydrocarbon Cations: Laboratory Studies and Astrophysical Implications. , 512(1):500–510, February 1999. doi: 10.1086/306752.

[295] Brett A. McGuire, Ryan A. Loomis, Andrew M. Burkhardt, Kin Long Kelvin Lee, Christopher N. Shingledecker, Steven B. Charnley, Ilsa R. Cooke, Martin A. Cordiner, Eric Herbst, Sergei Kalenskii, Mark A. Siebert, Eric R. Willis, Ci Xue, Anthony J. Remijan, and Michael C. McCarthy. Detection of two interstellar polycyclic aromatic hydrocarbons via spectral matched filtering. *Science*, 371(6535): 1265–1269, March 2021. doi: 10.1126/science.abb7535.

[296] Jos Oomens, Boris G. Sartakov, A. G. G. M. Tielens, Gerard Meijer, and Gert von Helden. Gas-Phase Infrared Spectrum of the Coronene Cation. , 560(1):L99–L103, October 2001. doi: 10.1086/324170.

[297] J. A. Noble, C. Jouvet, C. Aupetit, A. Moudens, and J. Mascetti. Efficient photochemistry of coronene:water complexes. , 599:A124, March 2017. doi: 10.1051/0004-6361/201629613.

[298] E. Peeters, A. G. G. M. Tielens, C. van Kerckhoven, S. Hony, L. J. Allamandola, D. M. Hudgins, and C. W. Bauschlicher. ISO Spectroscopy of PAH Features. 267: 403, October 2002.

[299] SeyedAbdolreza Sadjadi, Yong Zhang, and Sun Kwok. A Theoretical Study on the Vibrational Spectra of Polycyclic Aromatic Hydrocarbon Molecules with Aliphatic Sidegroups. , 801(1):34, March 2015. doi: 10.1088/0004-637X/801/1/34.

[300] Max P. Bernstein, Scott A. Sandford, Louis J. Allamandola, J. Se B. Gillette, Simon J. Clemett, and Richard N. Zare. UV Irradiation of Polycyclic Aromatic Hydrocarbons in Ices: Production of Alcohols, Quinones, and Ethers. *Science*, 283: 1135, February 1999. doi: 10.1126/science.283.5405.1135.

[301] Murthy S. Gudipati and Rui Yang. In-situ Probing of Radiation-induced Processing of Organics in Astrophysical Ice Analogs—Novel Laser Desorption Laser Ionization Time-of-flight Mass Spectroscopic Studies. , 756(1):L24, September 2012. doi: 10.1088/2041-8205/756/1/L24.

[302] Zohra Guennoun, Christian Aupetit, and Joëlle Mascetti. Photochemistry of coronene with water at 10 K: first tentative identification by infrared spectroscopy of oxygen containing coronene products. *Physical Chemistry Chemical Physics (Incorporating Faraday Transactions)*, 13(16):7340, January 2011. doi: 10.1039/C0CP01756F.

[303] J. Bouwman, A. L. Mattioda, H. Linnartz, and L. J. Allamandola. Photochemistry of polycyclic aromatic hydrocarbons in cosmic water ice. I. Mid-IR spectroscopy and photoproducts. , 525:A93, January 2011. doi: 10.1051/0004-6361/201015059.

[304] J. A. Noble, E. Michoulier, C. Aupetit, and J. Mascetti. Influence of ice structure on the soft UV photochemistry of PAHs embedded in solid water. , 644:A22, December 2020. doi: 10.1051/0004-6361/202038568.

[305] Amanda M. Cook, Alessandra Ricca, Andrew L. Mattioda, Jordy Bouwman, Joseph Roser, Harold Linnartz, Jonathan Bregman, and Louis J. Allamandola. Photochemistry of Polycyclic Aromatic Hydrocarbons in Cosmic Water Ice: The Role of PAH Ionization and Concentration. , 799(1):14, January 2015. doi: 10.1088/0004-637X/799/1/14.

[306] R. Jaganathan, F. D. S. Simonsen, J. D. Thrower, and L. Hornekær. Enhanced reactivity of oxygen-functionalised PAHs with atomic hydrogen - A route to the formation of small oxygen-carrying molecules. , 663:A136, July 2022. doi: 10.1051/0004-6361/202243312.

[307] John D. Thrower, Emil E. Friis, Anders L. Skov, Bjarke Jørgensen, and Liv Hornekær. Hydrogenation of PAH molecules through interaction with hydrogenated carbonaceous grains. *Physical Chemistry Chemical Physics (Incorporating Faraday Transactions)*, 16(8):3381, January 2014. doi: 10.1039/C3CP54073A.

[308] Francois Dulieu, Sabine Morisset, Abdi-Salam Ibrahim Mohamed, Leon Boshman, Stephanie Cazaux, Dominique Teillet-Billy, Saoud Baouche, and Nathalie Rougeau. Reactivity of coronene with O-atoms, a possible route to ketene in the interstellar medium. *Molecular Astrophysics*, 17:100054, December 2019. doi: 10.1016/j.molap.2019.100054.

[309] Ricardo M. Ferullo, Carolina E. Zubieta, and Patricia G. Belelli. Hydrogenated polycyclic aromatic hydrocarbons (HnPAHs) as catalysts for hydrogenation reactions in the interstellar medium: a quantum chemical model. *Physical Chemistry Chemical Physics (Incorporating Faraday Transactions)*, 21(22):12012–12020, June 2019. doi: 10.1039/C9CP02329A.

[310] Abdi Salam Mohamed Ibrahim, Sabine Morisset, Saoud Baouche, and Francois Dulieu. Desorption of physisorbed molecular oxygen from coronene films and graphite surfaces. , 156(19):194307, May 2022. doi: 10.1063/5.0087870.

[311] H. Chaabouni, M. Minissale, G. Manicò, E. Congiu, J. A. Noble, S. Baouche, M. Accolla, J. L. Lemaire, V. Pirronello, and F. Dulieu. Water formation through O_2 + D pathway on cold silicate and amorphous water ice surfaces of interstellar interest. , 137(23):234706–234706, December 2012. doi: 10.1063/1.4771663.

[312] David Hollenbach, Michael J. Kaufman, Edwin A. Bergin, and Gary J. Melnick. Water, O_2, and Ice in Molecular Clouds. , 690(2):1497–1521, January 2009. doi: 10.1088/0004-637X/690/2/1497.

[313] Rafael Martín-Doménech, Karin I. Öberg, and Mahesh Rajappan. Formation of NH_2CHO and CH_3CHO upon UV processing of interstellar ice analogs. 350:417–419, January 2020. doi: 10.1017/S1743921319007804.

[314] D. C. B. Whittet. Oxygen Depletion in the Interstellar Medium: Implications for Grain Models and the Distribution of Elemental Oxygen. , 710(2):1009–1016, February 2010. doi: 10.1088/0004-637X/710/2/1009.

[315] Valery Le Page, Theodore P. Snow, and Veronica M. Bierbaum. Hydrogenation and Charge States of Polycyclic Aromatic Hydrocarbons in Diffuse Clouds. II. Results. , 584(1):316–330, February 2003. doi: 10.1086/345595.

[316] Valéry Le Page, Theodore P. Snow, and Veronica M. Bierbaum. Molecular Hydrogen Formation Catalyzed by Polycyclic Aromatic Hydrocarbons in the Interstellar Medium. , 704(1):274–280, October 2009. doi: 10.1088/0004-637X/704/1/274.

[317] Alexey Potapov, Cornelia Jäger, and Thomas Henning. Photodesorption of Water Ice from Dust Grains and Thermal Desorption of Cometary Ices Studied by the INSIDE Experiment. , 880(1):12, July 2019. doi: 10.3847/1538-4357/ab25e7.

[318] Charles A. Poteet, Douglas C. B. Whittet, and Bruce T. Draine. The Composition of Interstellar Grains toward ζ Ophiuchi: Constraining the Elemental Budget near the Diffuse-dense Cloud Transition. , 801(2):110, March 2015. doi: 10.1088/0004-637X/801/2/110.

[319] Shu Wang, Aigen Li, and B. W. Jiang. The interstellar oxygen crisis, or where have all the oxygen atoms gone? , 454(1):569–575, November 2015. doi: 10.1093/mnras/stv1900.

[320] Lorenzo Tinacci, Aurèle Germain, Stefano Pantaleone, Cecilia Ceccarelli, Nadia Balucani, and Piero Ugliengo. Theoretical Water Binding Energy Distribution and Snowline in Protoplanetary Disks. , 951(1):32, July 2023. doi: 10.3847/1538-4357/accae8.

[321] Hendrik Christoffel van de Hulst. *The solid particles in interstellar space.* 1949.

[322] H. M. Cuppen, L. J. Karssemeijer, and T. Lamberts. The Kinetic Monte Carlo Method as a Way To Solve the Master Equation for Interstellar Grain Chemistry. *Chemical Reviews*, 113(12):8840–8871, December 2013. doi: 10.1021/cr400234a.

[323] H. M. Cuppen, E. F. van Dishoeck, E. Herbst, and A. G. G. M. Tielens. Microscopic simulation of methanol and formaldehyde ice formation in cold dense cores. , 508(1):275–287, December 2009. doi: 10.1051/0004-6361/200913119.

[324] David J Hollenbach, Michael W Werner, and Edwin E Salpeter. Molecular hydrogen in h i regions. *The Astrophysical Journal*, 163:165, 1971.

[325] M. Röllig, N. P. Abel, T. Bell, F. Bensch, J. Black, G. J. Ferland, B. Jonkheid, I. Kamp, M. J. Kaufman, J. Le Bourlot, F. Le Petit, R. Meijerink, O. Morata, V. Ossenkopf, E. Roueff, G. Shaw, M. Spaans, A. Sternberg, J. Stutzki, W. F. Thi, E. F. van Dishoeck, P. A. M. van Hoof, S. Viti, and M. G. Wolfire. A photon dominated region code comparison study. , 467(1):187–206, May 2007. doi: 10.1051/0004-6361:20065918.

[326] M. Chatzikos, S. Bianchi, F. Camilloni, P. Chakraborty, C. M. Gunasekera, F. Guzmán, J. S. Milby, A. Sarkar, G. Shaw, P. A. M. van Hoof, and G. J. Ferland. The 2023 Release of Cloudy. , 59:327–343, October 2023. doi: 10.22201/ia.01851101p.2023.59.02.12.

[327] G. J. Ferland, K. T. Korista, D. A. Verner, J. W. Ferguson, J. B. Kingdon, and E. M. Verner. CLOUDY 90: Numerical Simulation of Plasmas and Their Spectra. , 110(749):761–778, July 1998. doi: 10.1086/316190.

[328] G. J. Ferland, M. Chatzikos, F. Guzmán, M. L. Lykins, P. A. M. van Hoof, R. J. R. Williams, N. P. Abel, N. R. Badnell, F. P. Keenan, R. L. Porter, and P. C. Stancil. The 2017 Release Cloudy. , 53:385–438, October 2017. doi: 10.48550/arXiv.1705.10877.

[329] Maxime Ruaud, Valentine Wakelam, and Franck Hersant. Gas and grain chemical composition in cold cores as predicted by the Nautilus three-phase model. , 459(4):3756–3767, July 2016. doi: 10.1093/mnras/stw887.

[330] T. I. Hasegawa and E. Herbst. Three-Phase Chemical Models of Dense Interstellar Clouds - Gas Dust Particle Mantles and Dust Particle Surfaces. , 263:589, August 1993. doi: 10.1093/mnras/263.3.589.

[331] F. X. Desert, F. Boulanger, and S. N. Shore. Grain temperature fluctuations - A key to infrared spectra. , 160(2):295–300, May 1986.

[332] B. T. Draine and Aigen Li. Infrared Emission from Interstellar Dust. I. Stochastic Heating of Small Grains. , 551(2):807–824, April 2001. doi: 10.1086/320227.

[333] P. Castellanos, A. Candian, H. Andrews, and A. G. G. M. Tielens. Photoinduced polycyclic aromatic hydrocarbon dehydrogenation. Molecular hydrogen formation in dense PDRs. , 616:A167, September 2018. doi: 10.1051/0004-6361/201833221.

[334] E. Habart, F. Boulanger, L. Verstraete, C. M. Walmsley, and G. Pineau des Forêts. Estimates of the H_2 Formation Rate in PDRs. In Charles L. Curry and Michel Fich, editors, *SFChem 2002: Chemistry as a Diagnostic of Star Formation*, page 26, January 2003.

[335] Mark G. Wolfire, Livia Vallini, and Mélanie Chevance. Photodissociation and X-Ray-Dominated Regions. , 60:247–318, August 2022. doi: 10.1146/annurev-astro-052920-010254.

[336] N. P. Abel, P. A. M. van Hoof, G. Shaw, G. J. Ferland, and T. Elwert. Sensitivity of PDR Calculations to Microphysical Details. , 686(2):1125–1136, October 2008. doi: 10.1086/591505.

[337] J. Meisner, I. Kamp, W. F. Thi, and J. Kästner. The role of atom tunneling in gas-phase reactions in planet-forming disks. , 627:A45, July 2019. doi: 10.1051/0004-6361/201834974.

[338] K. N. Allers, D. T. Jaffe, J. H. Lacy, B. T. Draine, and M. J. Richter. H_2 Pure Rotational Lines in the Orion Bar. , 630(1):368–380, September 2005. doi: 10.1086/431919.

[339] D. Cormier, N. P. Abel, S. Hony, V. Lebouteiller, S. C. Madden, F. L. Polles, F. Galliano, I. De Looze, M. Galametz, and A. Lambert-Huyghe. The Herschel Dwarf Galaxy Survey. II. Physical conditions, origin of [C II] emission, and porosity of the multiphase low-metallicity ISM. , 626:A23, June 2019. doi: 10.1051/0004-6361/201834457.

[340] Xianwei Sha, Bret Jackson, Didier Lemoine, and Bruno Lepetit. Quantum studies of H atom trapping on a graphite surface. , 122(1):014709–014709, January 2005. doi: 10.1063/1.1827601.

[341] B. T. Draine. Photoelectric heating of interstellar gas. , 36:595–619, April 1978. doi: 10.1086/190513.

[342] H. J. Habing. The interstellar radiation density between 912 A and 2400 A. , 19:421, January 1968.

[343] A. G. G. M. Tielens. *The Physics and Chemistry of the Interstellar Medium.* Cambridge University Press, 2010.

[344] D. C. B. Whittet, M. F. Bode, A. J. Longmore, A. J. Adamson, A. D. McFadzean, D. K. Aitken, and P. F. Roche. Infrared spectroscopy of dust in the Taurus dark clouds : ice and silicates. , 233:321–336, July 1988. doi: 10.1093/mnras/233.2.321.

[345] D. C. B. Whittet, A. J. Adamson, W. W. Duley, T. R. Geballe, and A. D. McFadzean. Infrared spectroscopy of dust in the Taurus dark clouds : solid carbon monoxide. , 241:707–720, December 1989. doi: 10.1093/mnras/241.4.707.

[346] R. G. Smith, K. Sellgren, and T. Y. Brooke. Grain mantles in the Taurus dark cloud. , 263:749–766, August 1993. doi: 10.1093/mnras/263.3.749.

[347] A. P. Jones. Dust evolution, a global view: III. Core/mantle grains, organic nanoglobules, comets and surface chemistry. *Royal Society Open Science*, 3(12):160224, December 2016. doi: 10.1098/rsos.160224.

[348] Department of Chemistry Zurich University. Common bond lengths for organic functional groups. `https://www.chem.uzh.ch/en/research/services/xray/bond_lenghts.html`, 2024. Accessed: 05-10-2024.